# Measurement of the Azimuthal Anisotropy for Particle Identified Charged Hadrons in $Au + Au$ Collisions via Long-Range Two-Particle Correlation Method at $\sqrt{s_{NN}} = 200$, 62.4 and 39 GeV

A Dissertation Presented

by

**Yi Gu**

to

The Graduate School

in Partial Fulfillment of the Requirements

for the Degree of

**Doctor of Philosophy**

in

**Physics**

Stony Brook University

May 2014

**Stony Brook University**

The Graduate School

## Yi Gu

We, the dissertation committee for the above candidate for the Doctor of Philosophy degree, hereby recommend acceptance of this dissertation.

Roy Lacey – Dissertation Advisor
Professor, Department of Chemistry

Jiangyong Jia – Dissertation co-Advisor
Associate Professor, Department of Chemistry

Michael Rijssenbeek – Chairperson of Defense
Professor, Department of Physics and Astronomy

Xu Du
Assistant Professor, Department of Physics and Astronomy

Joanna Kiryluk
Assistant Professor, Department of Physics and Astronomy

Xiaorong Wang
Assistant Professor, Department of Physics
New Mexico State University

This dissertation is accepted by the Graduate School.

Charles Taber
Dean of the Graduate School

Abstract of the Dissertation

# Measurement of the Azimuthal Anisotropy for Particle Identified Charged Hadrons in $Au + Au$ Collisions via Long-Range Two-Particle Correlation Method at $\sqrt{s_{NN}}$ = 200, 62.4 and 39 GeV

by

**Yi Gu**

**Doctor of Philosophy**

in

**Physics**

Stony Brook University

2014

Anisotropic flow that stems from an eccentricity-driven hydrodynamic expansion of the matter in the collision zone, is one of the most prominent bulk observables in heavy-ion collisions. Based on long-range two-particle correlation (2PC) method, measurements of azimuthal anisotropy $v_n$ (n = 2,3,4) for particle identified charged hadrons ($\pi^{\pm}$, $K^{\pm}$, and $p\bar{p}$) as a function of centrality, transverse momentum $p_T$, and transverse kinetic energy $KE_T$ within mid-rapidity ($|\eta| < 0.35$) in Au+Au collisions at $\sqrt{s_{NN}}$ = 200, 62.4 and 39 GeV, are presented. Charged hadrons are identified up to $p_T$ = 3.2 GeV/c, 2.8 GeV/c and 3.3 GeV/c for pions, kaons and (anti-)protons, respectively. The scaling properties of measured $v_n$ with the number of valence quarks ($n_q$) have been studied extensively in different centrality classes as a function of transverse

momentum and transverse kinetic energy. The obtained $v_n$ results via 2PC method are compared with those from event plane (EP) method and a good consistency is achieved, suggesting the phase space we are looking at in anisotropy measurements presented in this work, is dominated by collective flow. Comparisons are also performed with the particle identified $v_n$ measured at the LHC. In spite of the striking similarity between RHIC and LHC $v_2(p_T)$ measurements for unidentified charged hadrons, tests for quark number scaling with LHC data for identified charged hadrons, have indicated an apparent breakdown of this scaling. These results provide important inputs for studying the physical properties of the plasma and the initial collision geometry of the hot and dense matter created in Au+Au collisions.

To my parents and my wife.

# Contents

# List of Figures

# List of Tables

# Acknowledgements

First and foremost, I would like to express my deepest gratitude to my advisors, Dr. Roy A. Lacey and Dr. Jiangyong Jia, for the immeasurable support and guidance they have provided throughout my Ph.D. studies at Stony Brook. Dr. Lacey's insights into and patient endurance throughout this research project have been a true blessing for me. I could still remember all those times we were working together, discussing analysis details, exchanging opinion on possible interpretations, figuring out one and another physics puzzle. Dr. Lacey's passion for doing innovative physics greatly inspired me. Dr. Jia also examplifies to me what it means to be an excellent researcher. His creative ideas, passionate interests, diligent working attitude all become a great impetus for me to emulate his greatness.

I would like to thank my PHENIX colleagues, without whom the data employed in my research never have been recorded, processed and produced to use. I feel honered to be a member of this wonderful collaboration. Also I would like to thank my friends in the Nuclear Chemistry group at Stony Brook. Dr. Arkadiy, it was my pleasure to work with you. Thank you for always helping me out with detailed analysis advice and extremely useful suggestions. My fellow graduate students, Xiaoyang (graduated), Soumya (graduated), Damian, Alex, Sooraj, Thomas, thank you all for being there and offering me help when I get stuck in my project. Sometimes, even a simple "how are you doing" would wipe out all the uneasiness and make me realize I do have backups. Your daily laughter and smiles have made my time as a graduate student extremely enjoyable and absolutely unforgettable.

My thanks also goes to my defense committee members, for taking precious time out of their already busy schedule, reading my thesis and coming to my defense. Thank you for your time serving on my committee!

Last but not least, I am especially grateful to my parents and my wife. Thank you for your endless support and love throughout these years.

# Chapter 1

# Introduction

This dissertation presents recent anisotropic flow measurement for identified charged particles in Gold+Gold nuclei ($Au + Au$) collisions at $\sqrt{s_{NN}} = 200$, 62.4 and 39 GeV. The experiment data were taken during run year of 2007 and 2010 by the PHENIX Collaboration at Brookhaven National Laboratory (BNL).

The dissertation is constructed as follows. We start by laying out the underlying theories, relevant background knowledge, basic terminology and the framework within which the phenomenon of anisotropic flow can be understood and studied. The PHENIX detector from which we collect our data and perform physics analysis is introduced in Chapter 2, where sub-detector systems used in our studies as well as the experiment set-up that are pertaining to my physics analysis, are included and explicitly described. We then outline the traditional Event Plane (EP) method for anisotropic flow measurement in Chapter 3. In Chapter 4, we document the particle identified anisotropic flow measurement via long-range two-particle correlation method in PHENIX. We present not only behind-the-scenes analysis details and results obtained, but also the cross-method consistency check with results from EP method, along with a set of comprehensive comparisons with similar measurement at the Large Hadron Collider (LHC) in CERN. In Chapter 5, we discuss the acoustic anisotropic flow and its viscous damping. Multiple "acoustic scaling" properties are included and their possible implications are also discussed. We close this dissertation by summary and conclusions in Chapter 6.

## 1.1 Quantum Chromodynamics (QCD)

The physics discovered after 1900 (*i.e.* twentieth-century physics) is usually called "modern" physics. When it comes to the history of modern physics,

people may think it is, in a general sense, all about the quest for understanding matter in its most fundamental forms and how the basic constituents of matter interact among themselves. The training of problem-solving skill educates us when trying to understand a phenomenon, we need zoom in and dissect out the possible composition factor, and trace the underlying reason down to its sub-level, its sub-sub-level, ..., all the way to the concentrically microscopic nature. The quest for understanding matter is the same. The human organism functions in unit of organ systems, that are made of organs, that are made of tissues, that are made of cells, that are made of molecules, that are made of different atoms, that are made of nucleus and surrounding electrons. The nucleus, known as the core of an atom, only takes $\approx 1/10^{15}$ of the atom space, but is responsible for more than 99.99% of atom's mass. Nucleons (identified as positive-charged protons and charge-neutral neutrons) make up the nucleus, and quarks plus gluons make up the nucleus. In light of the Standard Model, we believe quarks and gluons are truely the most fundamental particles by far.

Quarks and gluons are generally referred to as "partons". A composite subatomic particle that consists of three quarks is called "baryon", and a particle made up of one quark and one antiquark is "meson". Baryons and mesons belong to the hadron family, a collection of all quark-based particles. In particular, protons and neutrons, known as the components of atomic nuclei, are the most stable hadrons in nature.

Each quark carries one of three color charges of the strong interaction, and exhibits "color confinement" phenomenon. Because of color confinement, quarks are never directly observed or found in isolation, but confined within hadrons. There are six types of quarks, distinguished by distinctive "flavors": up (u), down (d), strange (s), charm (c), bottom (b), and top (t). The up and down quarks are particularly noteworthy in that they are thought to form protons and neutrons, and are thus the ones observed in ordinary matter.

One of the most successful physics theories that describe elementary particles and their interactions is Quantum Chromodynamics (QCD), a non-Abelian $SU(3)$ gauge theory of strong interactions between quarks and gluons at $fm$ scale . As formulated in QCD, a new quantum number "color" assigned to each quark is responsible for the strong interaction, and as such most problems with quarks are resolved. The colors red (R), green (G), and blue (B) are introduced to quarks and their opposites, minus-red, minus-green, and minus-blue, to antiquarks. As a metaphor drawn from chromatics, a color neutrality can be achieved from certain combination of quarks, each of which carries specific color property to make the resulting particle have no net color. A baryon, for example, always consists of a combination of one red, one green, and one blue quark. The intrinsic property of color in strong interactions plays a role

that is similar to an electric charge in electromagnetic interactions. Quarks interact via emitting and absorbing gluons. Just as photons carry electromagnetic force, gluons transmit the forces that "glued" quarks together acting as the exchange particles and mediate strong interactions of quarks in Quantum Chromodynamics.

### 1.1.1 Asymptotic Freedom and Color Confinement

Quantum Chromodynamics successfully describes the strong interaction in Standard Model and it exhibits two fundamental phenomena. One is *confinement*, which refers to the observation that quarks and antiquarks are always confined in hadrons and they can never be detected in isolation in nature. The other interesting property of QCD is *asymptotic freedom* or *ultraviolet (UV) asymptotic freedom*, which basically states the interaction between quarks becomes week at large energies (or equivalently at short distances)[46][47].

The strength of the interaction between quarks is characterized by the coupling constant of the strong interaction, $\alpha_s$. In contrast to the electroweak theory, the coupling constant for the strong interactions monotonically decreases as the energy scale increases. In hadrons, the farther two quarks are separated, the stronger interaction between them would be, and hence tends to bind the two quarks back together into a hadronic state to lower system energy. This concept explains the failure to observe free quarks experimentally. A nice summary plot of $\alpha_s$ measurements as a function of energy scale is shown in Figure.1.1, where energy scale has been translated to corresponding momentum transfer $Q$.

In the framework of asymptotic freedom, when interaction is strong and momentum scale of the measurement is large (momentum transfer $Q$ larger than a few $GeV$), the dynamics of QCD can be expediently described via weakly coupled color degrees of freedom. In this scenario, QCD cross section can be expanded by power series in the coupling constant $\alpha_s$. Since the coupling constant $\alpha_s$ is relatively small, contributions from higher order $\alpha_s$ terms are negligible resulting in the perturbative expansion be reduced to summation of the first few leading order terms. Therefore QCD cross section calculation is greatly simplified. This QCD calculation method is called the perturbative QCD (pQCD) method. The asymptotic freedom property of QCD and pQCD method has been extensively tested and verified in collisions of elementary particles, for example, $p$+$p$, $e^-$+$e^+$... collisions[1]. One of the confirmative experiments is the Bjorken scaling observed in Deep Inelastic Scattering (DIS) experiment at the Stanford Linear Accelerator Center (SLAC)[48].

In the opposite low energy limit where running coupling constant $\alpha_s$ grows and interaction becomes strong, the perturbation theory is no longer validated.

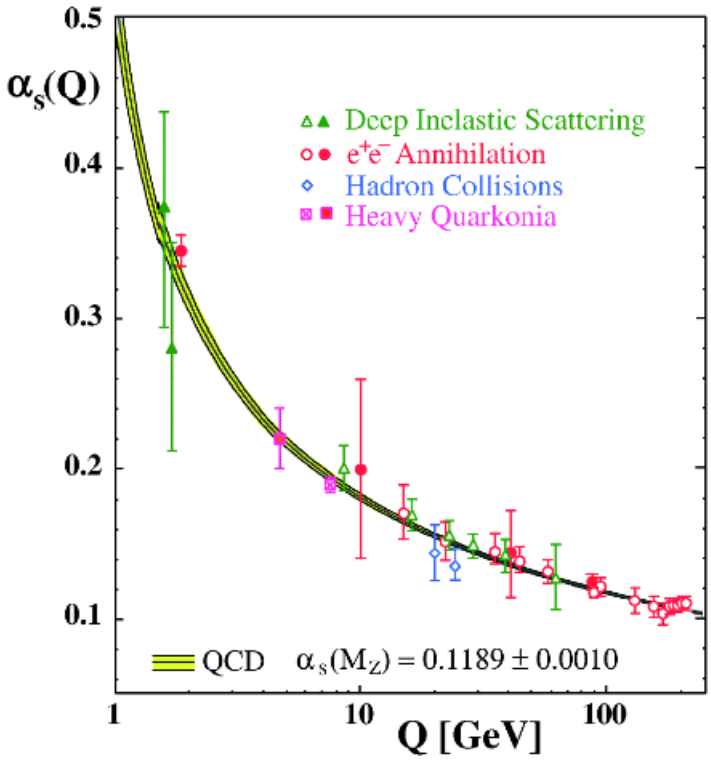


Figure 1.1: Summary of measurements of $\alpha_s(Q)$ as a function of energy scale Q. Open symbols and filled symbols indicate (resummed) NLO and NNLO QCD calculations, respectively[1].

This feature, as the origin of color confinement, is usually called the *infrared (IR) slavery*. QCD exhibits infrared slavery and according to this interesting characteristic, color degrees of freedom must be confined in low energy end. As QCD becomes non-perturbative at low energy, many effective theoretical models and non-perturbative methods are developed, such as chiral perturbation theory[49] and lattice QCD[50]. Fomulated on a lattice of discrete space-time points, lattice QCD allows calculations at high temperature and large coupling strength.

### 1.1.2 QCD Phase Diagram and Deconfinement

The form of existence that a substance exhibits is usually referred to as *phase*. Water can occur in ice, liquid and vapor, three different phases. Just as water phase diagram describes the phase relationships in $H_2O$ system, QCD phase diagram pictures different states of nuclear matter and possible boundary or crossover among them. A contemporary view of the QCD phase diagram showing the expected phase relationships of nuclear matter can be found in Figure.1.2. It is a systematic compliation of theoretical results from conjectured model calculation, experimental observations from nuclear physics (especially heavy-ion physics) studies, outcomes from lattice QCD calculations as well as the success of perturbative handling in asymptotic regimes. The vertical axis of the QCD phase diagram represents system temperature ($T$) that is related to energy density ($\epsilon$) and the horizontal axis represents baryochemical potential ($\mu_B$), which reflects the net baryon density of the matter.

In this expected phase diagram, the vacuum is at the origin $T = 0$, $\mu_B = 0$ and normal nuclear matter exisits around $T \approx 0$ MeV, $\mu_B \approx 1$ GeV. Here, 1 MeV temperature roughly translates to $\approx 10^{10}$ Kelvin, the standard temperature unit. The matter exists in the "hadron gas" phase when system $T$ is low and $\mu_B$ is small, and this corresponds to the lower left region on the phase diagram. At low temperature $T$ and small baryon chemical potential $\mu_B$, strong interaction (and large coupling constant $\alpha_s$) confine quarks and gluons well within hadrons. Because of the color neutrality of hadron, the interactions between hadrons are relatively weak and the whole particle system behaves as a gas.

Because of asymptotic freedom of QCD, the interaction becomes weaker as the momentum scale increases. Therefore, at sufficient high density but low temperature, there exists a Fermi surface of almost free quarks and a state with lower (than a simple Fermi surface) free enregy. That state, which arises from superposition of particle pairs, is usually referred to as "Cooper pairs" state. Since pairs of quarks cannot be color singlets, the resulting condensate will break the local color SU(3) symmetry, and a new "color superconductivity"

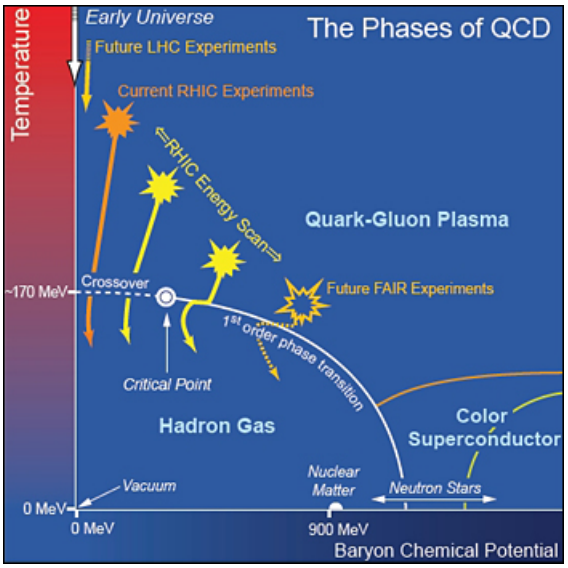


Figure 1.2: Schematic QCD phase diagram for nuclear matter. The solid lines show the phase boundaries for the indicated phases. The solid circle depicts the conjectured critical point. Possible trajectories for systems created in the QGP phase at different accelerator facilities are also shown[2].

state is formed[51][52]. It is generally believed that the physics of compact stars (neutron stars, for example) is also relevant to the phase structure of QCD in this low temperature but large $\mu_B$ domain.

On the other hand, if nuclear matter is heated up (experimentally this can be achieved by colliding two large nuclei - typically Gold or Lead - at very high energy, which will be discussed later in Sec.1.2), asymptotic freedom suggests quarks and gluons become decomfined as the interaction becomes weak and coupling constant $\alpha_s$ becomes small. The state that quarks and gluons are not confined in hadrons but form the degrees of freedom is called *quark-gluon plasma* (QGP). The term "plasma" usually refers to an electrically neutral system of positive and negative particles in which charges are screened due to other mobile charges. In the context of QGP, "charge" bears the color properties of (anti-)quarks and has nothing to do with the electric charge, as in the usual sense. The QGP phase of nuclear matter occupies most of the upper space in QCD phase diagram. Its various properties and the mapping of its first order phase transition with hadron-gas phase has been the most interesting and attractive research topics in the realm of high energy nuclear physics during the past decade.

The solid circle in QCD phase diagram depicts the conjectured critical point that possibly separates the continuous transition (cross-over) and abrupt

phase transition that occurs between hadronic matter and a QGP[53]. For an ideal gas, the energy density is proportional to the fourth power of the temperature with the number of degrees of freedom (NDF) being reflected in the proportionality constant. Recent lattice QCD calculation indicates the energy density divided by the fourth power of temperature ($T^4$) exhibits a dramatic change at temperature around 170 MeV. As shown in Figure.1.3, where temperature has been scaled down by the expected critical temperature $T_c \approx 170$ MeV (*i.e.*, horizontal axis represents $T/T_c$), the strong increase of scaled energy density near the critical temperature $T_c$ suggests that the system undergoes a phase transition from hadronic matter to a QGP with a corresponding large increase in the number of degrees of freedom. Above $T_c$, the QGP is heated while $\epsilon/T^4$ is constant[3, 4, 54].

The lattice QCD calculation of energy density shown here are obtained by extrapolating at $\mu_B = 0$, and they show sharp but rather continuous transition in NDF. In this sense, a crossover instead of phase transition is conjectured. Nevertheless at finite $\mu_B$, the variation in thermodynamic parameter (like temperature, chemical potential, energy density, etc.) at the phase boundary is found to have the discontinuity feature of first order phase transition.

## 1.2 The Quark Gluon Plasma and Relativistic Heavy-ion Collisions

One consequential indication of the asymptotic freedom of QCD is the new state of nuclear matter containing deconfined quakrs and gluons[55, 56]. From our earlier discussion, we may justifiably expect at the proper energy density hadronic matter should undergo a phase transition into strongly coupled partonic matter, or QGP. This decomfined QGP is believed to have existed a few microseconds after the Big Bang, when the system temperature and energy density are so high that presumably this QGP-state matter could form.

### 1.2.1 From "Big Bang" to "Little Bang"

It was once theoretically proposed in mid 70's of last century that this deconfined nuclear matter with partonic degrees of freedoms could be reproduced on earth[57]. "Little Bang" is an amuzing nickname people assign to relativistic heavy-ion collisions in contrast to the "Big Bang". Indeed, by colliding two large nuclei (typically Gold or Lead) at various extremely high energies, people manage to recreate the nuclear matter of deconfined quarks and gluons in laboratory. During the collision process, part of the kinetic energies of the two

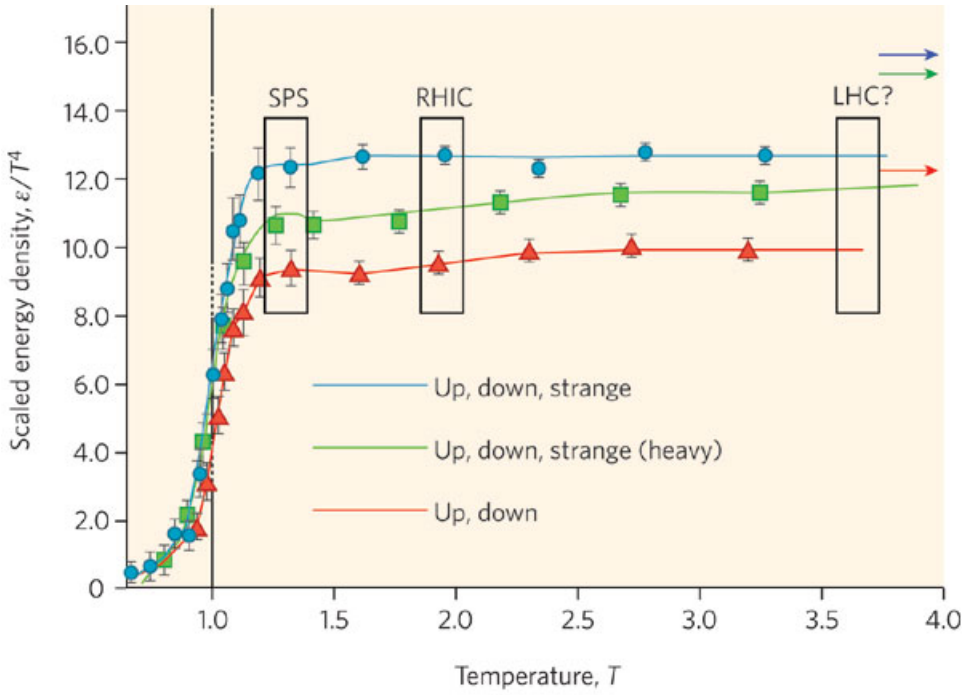


Figure 1.3: Increase of NDF around expected critical temperature $T_c$ ≈170 MeV, predicted by lattice QCD[3]. Scaled energy density $\epsilon/T^4$ (proportional to NDF) is shown as function of $T_c$-scaled temperature ($T/T_c$). The three lines are calculations for two light quark flavors (only up and down; red), three equally light flavors (up, down and strange; blue) and the most realistic case of two light flavors (up and down) and one more massive (strange) flavor (green). Colored arrows show the expected values of scaled energy density at the Stefan-Boltzman limit. The regions labelled by accelerator facilities (to be discussed later in this manuscript) indicate maximum initial temperatures reached there. Figure take from [4].

nuclei are transformed to heat up the QCD vacuum within a super-contracted small volume.

Such heavy-ion collisions are carried out with ever increasing energies at various facilities. The first attempt dates back to early 80's when relativistic heavy-ion program was first implemented at the Bevalac at Lawrence Berkeley Laboratory (with beam energy up to 1 GeV per nucleon)[58]. In 1990's, experiment at BNL (the AGS with $\sqrt{s_{NN}} \sim 5$ GeV) and CERN (the SPS with $\sqrt{s_{NN}} \sim 17$ GeV) brought the collision energy further up to a new level[59]. Although a number of signals from SPS did suggest possible formation of a "new state of matter"[60], it was not until the RHIC program launched at BNL did we eventually confirm the creation and existence of a strongly coupled new state of nuclear matter (known as "QGP")[61–66]. Since the first heavy-ion run started to collect data in November of 2010 at CERN, the collision energy advances to over one order of magnitude higher than the maximum energy achieved at RHIC. With the higher collision energy at CERN (up to 5.02 TeV as of 2013) and thus denser nuclear matter, a set of quite interesting phenomena have been uncovered, some of which "surprisingly" comply with what we have learned at RHIC and some of which appear different and require more careful studies and investigations. Discussions pertaining to this topic will be presented later in Sec.1.2.6.

### 1.2.2 Collision Geometry

Unlike high energy physics experiment where physicists often collide elementary particles ($e^+$+$e^-$ or $p$+$p$), heavy-ion collision experiment is geometrically more complicated in that hundreds of nuclei usually participate in the collision and as such, the nuclear matter created in the collision originates from a non-trivial initial collision profile that may vary event by event. The initial geometry profile undergoes a space-time evolution and will be eventually reflected in the final state particle distribution.

A schematic cartoon illustrating the nucleus-nucleus collision can be found in Fig.1.4. A 2D complementary plot showing collision geometry for an off center collision is presented in Fig.1.5. In this section, we will be discussing the collision geometry associated with a heavy-ion collision.

By convention, z-axis is usually defined along the beam direction, and corresponding xy-plane perpendicular to the beam ($z$) axix is determined following cartesian right hand rule. The grid plane in 1.4 is the *reaction plane (RP)*, which is defined by the beam axis and the vector connecting two centers of the colliding nuclei. The length of such vector reaches its minimum (see Fig.1.5) when it is normal to beam direction, and the shortest length is defined as *impact parameter* (usually denoted by "$b$"). Those nucleons in the

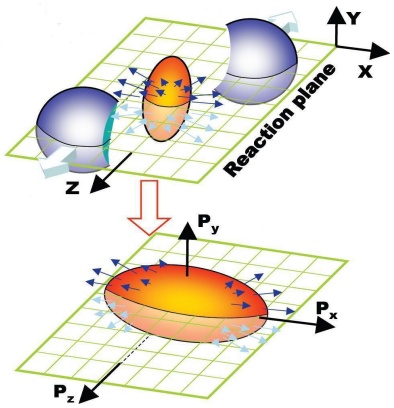


Figure 1.4: A schematic view of the collision ellipse of a heavy-ion collision. Flow is measured in phi (around the beam axis, Z) with respect to the plane indicated, known as the *reaction plane*.

overap region would participate in collisions, thus are called *participants*. The total number of participants in a collision is usually denoted by $N_{part}$. The remaining non-participating nucleons are referred to as *spectators*, which only "spectate" during collision along beam ($z$) axis. The total number of non-participating spectator nucleons is called as $N_{spec}$. The extent to which two colliding nuclei are overlapped is usually described by *centrality*, a numeric parameter ranging from 0 to 1 (100%) with 0 and 100% corresponding to a perfect head-on collision and a barely touched collision, respectively. The more overlapped between colliding nuclei (and thus smaller impact rarameter), the larger $N_{part}$ would be and collision is more central. Otherwise, the collision is more peripheral. In this sense, there exists an one-to-one mapping between centrality and $N_{part}$. Nowadays $N_{part}$ is also being used to reflect how overlapped a collision is. Experimentally, centrality is defined by measuring the multiplicity (the total number of particles produced in a collision) or transverse energy (the energy associated with momentum that is transverse to the beam axis) in a particular detector unit and then quantified into percentile classes. Unlike quantities"velocity","time" or "distances", for which measurement can be performed immediately with proper equipment, observables such as $N_{part}$, $N_{spec}$ may not be directly measured in heavy-ion collision experiment. Therefore centrality definition largely relies on model-dependent characterization of the theoretical quantities (e.g. $N_{part}$) and indirect measurables (e.g. charge or energy deposit within certain detector unit).

The collision region in initial state has an almond-like elliptical shape, as illustrated in Fig.1.4. Such spacial anisotropy could be quantified by an

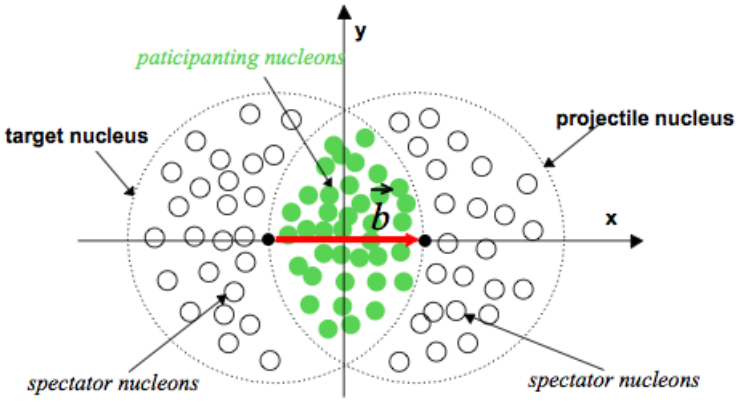


Figure 1.5: The collision geometry for an off-center nucleus-nucleus collision.

*eccentricity* given by

$$\epsilon = \frac{< y^2 - x^2 >}{< y^2 + x^2 >} \tag{1.1}$$

where $x$ and $y$ are the transverse positions of the participating nucleons about the center of mass, with the x-axis in the reaction plane, and the averaging is performed over all participating nucleons. Such spacial anisotropies are driven by anisotropic pressure gradient (as the "arrows" illustrated in Fig.1.4), which is caused by collision geometry and event-by-event fluctuations in its initial density distribution. The intial state spacial anisotropies are then transformed into final state momentum space anisotropies and eventually being measured.

For convenience purpose, the cylindrical coordinate is also used to describe the spacial information. The z-axis is defined along beam axis as what we have in cartesian case, $\phi$ angle (azimuthal angle) is within the plane perpendicular to z-axis. The angle that describes the deviation a projectile particle travels with respect to z-axis is denoted by $\theta$. However, instead of $\theta$, the pseudorapitidy $\eta = -ln[tan(\frac{\theta}{2})]$ of a particle is usually employed. By definition, $\eta = 0$ corresponds to a direction perpendicular to z-axis ($\theta = \frac{\pi}{2}$); the more $\eta$ value off zero, the closer a particle is to a direction that is parallel with z-axis.

### 1.2.3 Time Evolution of Heavy-ion Colllisions

In this subsection, we will be introducing different time evolution stages in ultra-relativistic heavy-ion collisions. The conjectured stages that a heavy-ion collision possibly goes through are shown in Fig.1.6. Detailed descriptions for these stages are presented below:

1. Initial State: As one of the effects of near-lightspeed travel, incoming

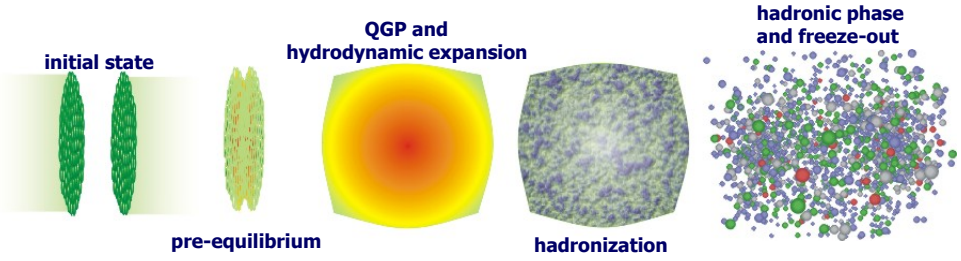


Figure 1.6: The conjecture of time evolution stages in heavy-ion collisions, with leftmost corresponding to earliest occurrence and rightmost latest occurrence. [Courtesy S.Bass]

nuclei are Lorentz contracted to appear "pancake" shapes in the lab frame. Take $Au + Au$ collisions at $\sqrt{s_{NN}} = 200$ GeV for example, the correpsonding contraction factor $\gamma$ is around 100. In other words, two semi-spherical Au nuclei are Lorentz contracted by a factor of $\sim$100 colliding each other. Those participating nucleons are scattered resulting in an anisotropic entropy and energy density distribution. The profile of produced nuclear matter with extremly high density is determined at this stage. Interestingly, this initial state geometry profile can be theoretically modeled by dense gluon walls known as the Color Glass Condensate (CGC) [67, 68] or alternatively understood within the framework of Glauber[69]. Important quantities including the number of participants $N_{part}$, the number of binary collisions involved $N_{coll}$ as well as the eccentricity are also determined.

2. Pre-equilibrium and thermalization: A QCD vacuum followed by a hot dense matter consisting of abundant quarks, anti-quarks and gluons is created. Before the pre-equilibrium bulk nuclear matter achieves local thermalization and forms quark-gluon plasma, "hard probes" with either large mass or large $p_T$ (transverse momentum) are generated in this very early pre-equilibrium stage. These "probes" include high $p_T$ quarks and gluons (which form jets later during hadronization stage), heavy quarks ($c\bar{c}$ and $b\bar{b}$) and vector bosons, all of which are generated and embedded in hard scatterings during an energetic heavy nuclei collision. At the same time, entropy of the system becomes quite large. Those hard processes are followed by a production of much softer particles with $p_T \sim \mathcal{O}(1)$ GeV. Such soft processes occur when most of the entropy (multiplicity) is produced in the collision.

Initially the produced matter is not in thermal equilibrium, however partons interact among themselves, and according to hydrodynamics calculations, it would take the system around $\tau_o \leq 1fm/c$ to approach thermal equilibirum[70, 71]. Please note the thermalization process is really fast with the characteristic proper time of QGP $\tau_o \leq 1fm/c$ at RHIC.

3. QGP and hydrodynamic expansion: The scatterings of partons lead to a local thermalization in the bulk matter and eventually the formation of deconfined QGP. Driven by thermal pressure gradients arising from large pressure difference inside and ouside the matter, the quark-gluon plasma (QGP) expands and cools down very quickly. Because of the anisotropic nature of the pressure gradients, the expansion is also asymmetric. This process has been well studied in the framework of relativistic hydrohynamics with a very small shear viscosity to entropy density ratio $\eta/s$[72–74]. The system exhibits strong collective flow behaviors[75] and large opacity to the fast moving partons[76].

4. Hadronization: As the QGP cools down rapidly, the energy density and temperature of the bulk nuclear matter drops to a critical temperature $T_c \simeq 170MeV$ where the interactions among partons become so strong that they tend to confine those partons and form a bound state, *i.e.* hadrons. Such hadronization process occurs continuously at the edge of the QGP fireball during the entire expansion period. Take central $Au + Au$ collisions at $\sqrt{s_{NN}} = 200$ GeV for example, the possible time scale for the QGP fireball to completely convert into hadronic matter is around $10fm/c$. Some extremely energetic partons might also fragment into hadrons before they can be directly detected, becoming jets. A *jet* is a bunch of hadrons and other particles produced by the hadronization of quarks or gluons travelling within a narrow cone region, therefore hadronization is also referred to as *jet fragmentation* in this case.

5. Hadronic phase and freeze-out: A transition (or crossover) to the hadronic phase takes place while QGP further expands and cools down. At this stage, the energy density of matter is still large enough, hence the produced hadrons might continue scattering among themselves, *i.e. hadronic rescattering*. As the hadronic matter expands, system becomes quite dilute and resembles a gaseous state, where hadrons interact weakly. One prevailing model that well describes the features of this stage is Ultra-relativistic Quantum Molecular Dynamics model (UrQMD). During the expansion, system's local thermal equilibrium will no longer be maintained and hadrons do not display collective behaviors. Eventually, particles are sufficiently separated as free particles. This

stage is usually known as "freeze-out" and particles could stream freely to the detector.

Our major interests lie in the QGP stage. The studies of its properties and measurements of its signatures are the main topics of this thesis and will be presented in the following sections and chapters.

### 1.2.4 QGP Signatures

During the past decade, much efforts have been geared to invetigate the possible signals and probes for the quark-gluon plasma (QGP). Since quarks and gluons can not be directly measured, experiments have to rely on indirect observables that are sensitive to the transient QGP matter. For this reason, the existence of the QGP can only be varified by a collection of indirect evidences from many observables. These observables, known as QGP signatures, include: dilepton emission, $J/\psi$ and other charmonium production and suppression, radial and collective elliptic flow, the Hanbury-Brown-Twiss (HBT) effect, strangeness enhancement and jet quenching.

In this subsection, we will be focusing on two really impressive QGP signatures discovered at RHIC within the past decade.

One significant finding of the strongly coupled QGP is the strong collective flow. Its precise measurement along with its description from ideal hydronamics indicates that the quark-gluon plasma created at RHIC behaves like a nearly perfect liquid with small viscosity.

Another striking discovery of QGP at RHIC is its opaqueness to high $p_T$ particles passing through it. Unlike the strong enhancement of high $p_T$ hadrons found at Super Proton Synchrotron (SPS), this important property of observed suppression of fast moving particles in QGP's dense medium is known as *jet quenching*[77].

It was not until 2005 did the nuclear physics community announce the discovery of QGP at RHIC. Since QGP signals may get contaminated during evolution process from very early pre-equilibrium to later hadronic matter stage, a comprehensive study of all possible signatures, including strong anisotropic collective flow, the number of constituent quark scaling for elliptic flow $v_2$ (or "elliptic flow", "$v_2$" for short) and jet quenching, finally confirms the existence and discovery of QGP at RHIC[78, 79].

- **Collective flow and its hydrodynamics representation**

One of the most important discoveries at RHIC is that the QGP medium exhibits strong collective behavior - flow. As elaborated in previous sections,

the asymmetry of initial collision profile is reflected in the final anisotropic distributions of particles. For an ellipsoid collision profile (see Fig.1.4), the pressure gradient is stronger along the minor axis (x-axis) of the ellipsoid in initial state. Because the minor axis is within the reaction plane, this direction with stronger pressure gradient is also called the "in-plane" direction. On the other hand, the direction along longer axis of the ellipsoid (y-axis) is the "out-of-plane" direction with smaller pressure gradient. Driven by pressure gradient, the expansion of collision profile is therefore faster along the in-plane direction resulting in the azimuthal distributions of particles having the largest density along this (in-plane) direction.

Since the pressure gradient in the in-plane direction is stronger than the out-of-plane direction, the outward collective flow predominantly drives particle emission along the in-plane direction. As time evolves, the stronger expansion in plane than out of plane will thereby reduce the initial anisotropy and eventually lead to an overshoot such that the nuclear profile appears elongated along in-plane direction at the every end of its existence (cf. Fig.1.4). Rapid thermalization in the early stage transforms the spatial anisotropy into a final state momentum anisotropy, known as elliptic flow depicted in lower panel of Fig.1.4. Other than the eccentricity definition in Eqn.1.1, the elliptic flow $v_2$ follows

$$v_2 \equiv \frac{< p_x^2 - p_y^2 >}{< p_x^2 + p_y^2 >} \tag{1.2}$$

Equivalently, starting from azimuthal distributions of the particles in final state momentum space,

$$\frac{dN}{d\phi} \propto 1 + 2v_2 \cos(2(\phi - \Phi)) + 2v_4 \cos 4(\phi - \Phi) + \dots \tag{1.3}$$

the elliptic flow $v_2 = \langle \cos 2(\phi - \Phi) \rangle$ is defined as the $2^{nd}$ Fourier coefficient of the azimuthal distribution of hadron spectra. This definition can be easily extended to other orders as well $v_n = \langle \cos n(\phi - \Phi) \rangle$. Since $v_n$, in this case, indicates the strength of its corresponding $n^{th}$ order Fourier component contributes in spectra, $v_n$ are commonly called *flow harmonics* to signify the hydrodynamic nature of its development during expansion. $\Phi$ is the azimuthal direction where maximum particle yield is achieved.

Because of the elliptic overlap region, the final distribution of particles inherits the symmetries from such initial geometry, and consequently only even-order harmonics are present in the final distribution. In this scenario, $\Phi$ coincides with the shorter axis of the ellipsoid region, and $v_2$ is expected to be much larger than any other $v_n (n = 4, 6, \dots)$ due to the elliptic symmetry. However, this situation does not always occur (actually rarely happen) in

reality. I would like to defer this discussion as well as higher-order ($n > 2$) flow measurements to later Sec.1.3 of this thesis.

The finding of sizable elliptic flow $v_2$ in $Au+Au$ collisions is thought to be one of the most remarkable discoveries at RHIC. Fig.1.7 is a comprehensive plot that shows elliptic flow $v_2$ measurements for different particle species by PHENIX and STAR collaboration using minimum bias $Au+Au$ collisions at $\sqrt{s_{NN}} = 200$ GeV data collected in run year 2004 and 2005. In Fig. 1.7, $v_2$ is plotted as a function of transverse momentum $p_T = \sqrt{p_x^2 + p_y^2}$ and transverse kinetic energy $KE_T = \sqrt{m^2 + p_T^2} - m$.

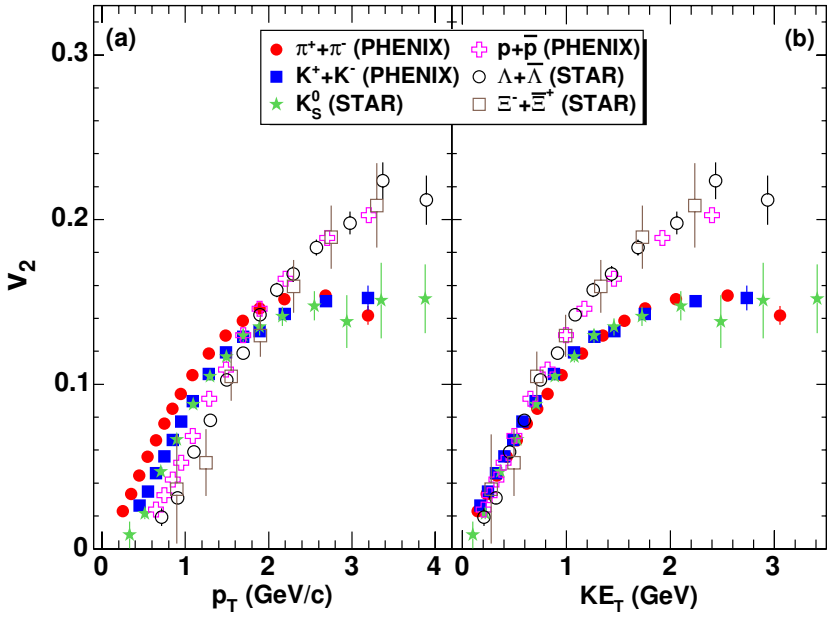


Figure 1.7: (a) $v_2$ vs. $p_T$ (transverse momentum) and (b) $v_2$ vs. $KE_T$ (transverse kinetic energy) for identified particle species obtained in minimum bias $Au+Au$ collisions at $\sqrt{s_{NN}} = 200$ GeV. Figure taken from [5].

The magnitude of $v_2$ bears the information on QGP's capability of transforming initial spatial asymmetry into final state momentum anisotropy, hence it is sensitive to the initial condition, equation of state (EoS) as well as the degree of medium thermalization. The $v_2$ value can go as large as 20% at around 3 GeV/c, which translates into approximately $(1+2\times0.2)/(1-2\times0.2) \sim 2.3$ more yield in the in-plane direction than in the out-of-plane direction.

The interesting feature that the relatively "complicated" dependence of azimuthal anisotropy $v_2$ on centrality, transverse momentum, rapidity, particle type, etc can be scaled to a single function is thought to be an evidence in

support of hydrodynamic description of the QGP at low $p_T$. Within hydrodynamic framework, the collision medium is characterized as an almost thermalized relativistic fluid with some additional macroscopic properties such as viscous effects and equilibrium EoS, subject to initial conditions and a particular"freeze-out" prescription at the end of the evolution. As shown in panel (b) of Fig.1.7, the $v_2$ data exhibit a universal scaling property with transverse kinetic energy $KE_T$ for $KE_T < 1$ GeV at mid-rapidity, which is an important prediction of perfect fluid hydrodynamics [80, 81]. When $kE_T > 1$ GeV, there is a clear separation of $v_2$ values for hadrons and baryons.

Although subject to ingredients such as initial conditions, EoS and decoupling prescriptions, hydrodynamics that models the strongly coupled QGP shows good agreements with experimental data, which indicates that the bulk of the matter behaves like a nearly perfect fluid. In the framework of ideal hydrodynamics, hydrodynamic equations are initialized by the Glauber model and are solved toward T∼100 MeV. This pure hydrodynamic model gives a comparable result with the data at midrapidity(Fig.1.8,1.9). However at forward and backward rapidities, it overshoots the data significantly. Instead, If a hadron gas model is employed to incorporate a hadron cascade, $v_2$ is significantly reduced in both the forward and backward region. In this hybrid model, the hadrons have a finite mean free path, which results in an effective shear viscosity in the hadron phase[8].

In Fig.1.8, the solid blue curve shows the calculation from ideal hydrodynamics and the dotted red curve reflects the hybrid model calculation, where Glauber type initial conditions followed by a perfect fluid QGP and a dissipative hadronic gas evolution are included and utilized. It is noteworthy that hydrodynamic models can also reproduce the mass ordering pattern for $v_2$ as a function of $p_T$ that is observed experimentally for different identified hadron species as shown in Fig.1.9. Especially in the low $p_T$ region, the $v_2$ for different hadron species are well described by hydrodynamic modeling of the QGP.

Further development of hydrohynamics allows us to better understand the transport properties of the nearly perfect fluid-like QGP. A dimensionless quantity $\eta/s$ is introdueced to quantify the viscosity of QGP. $\eta$ denotes the shear viscosity, while $s$ is the entropy density. Mapping strongly coupled quantum field theories to gravity via the AdS/CFT correspondence, theorists have conjectured a lower bound for $\eta/s$ of $1/4\pi \approx 0.08$[82], which in turn implies that the QGP can not be a perfect fluid with zero viscosity.

Figure.1.10 presents the comparison of various hydro-model calculations with experiment data, where different viscosity values in conjuction with Glauber (left) or CGC (right) initial conditions are applied to reproduce data. The line thickness for the hydrodynamic model curves reflects an estimate of the accu-

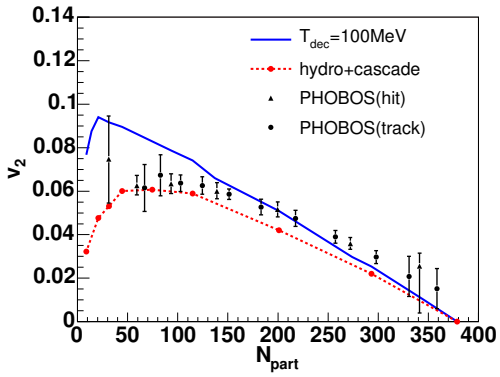


Figure 1.8: PHOBOS $v_2$ as a function of centrality[6] compared to different model calculations[7]. Figure taken from [8].

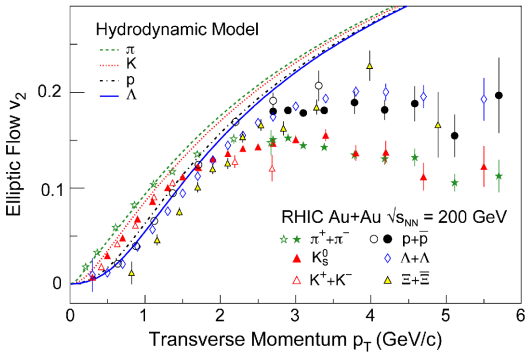


Figure 1.9: Model calcuations compared with differential $v_2$ results. Figure taken from [9].

mulated numerical error (for example, due to finite grid spacing). The data points are from the PHOBOS experiment for $Au$+$Au$ collisions at $\sqrt{s_{NN}} = 200$ GeV. The associated errors, which include 90% confidence level systematic uncertainties, are indicated in error bars. It is clearly shown in the two plots that in order to best describe the data trend, the models starting from a CGC initial conditions requires much stronger viscosity. This is because CGC profile folds in a larger eccentricity so that a greater viscosity effect is needed to lower down the model predicted values of elliptic flow coefficient $v_2$[83]. Although best description of data requires different values of viscosity for different initial geometry profiles, the viscosity values in both initial conditions are quite small. Apparently, the $\eta/s$ values determined by Glauber model description of data is closer to the conjectured lower bound.

- **Quark degrees of freedom and partonic collectivity**

As shown in panel (a) of Fig.1.7, the elliptic flow $v_2$ exhibits a well-known particle identification (PID) ordering (*mass ordering*) at low $p_T$ values. In the low $p_T$ region ($p_T$ lower than 2 GeV/c), those heavier baryons are influenced more from the hydrodynamic flow expansion so that they are pushed further towards higher $p_T$ end resulting in a smaller elliptic flow $v_2$ values. This mass ordering pattern of hadron $v_2$ in turn serves to support the hydrodynamic mechanism of the fireball expansion in heavy-ion collisions within this low $p_T$ region. When it comes to intermediate $p_T$ region where $p_T$ is $2-4$ GeV/c, the mass ordering is broken and what we see from Fig.1.7(a) is a stronger dependence of $v_2$ on the quark composition of the particles than on their

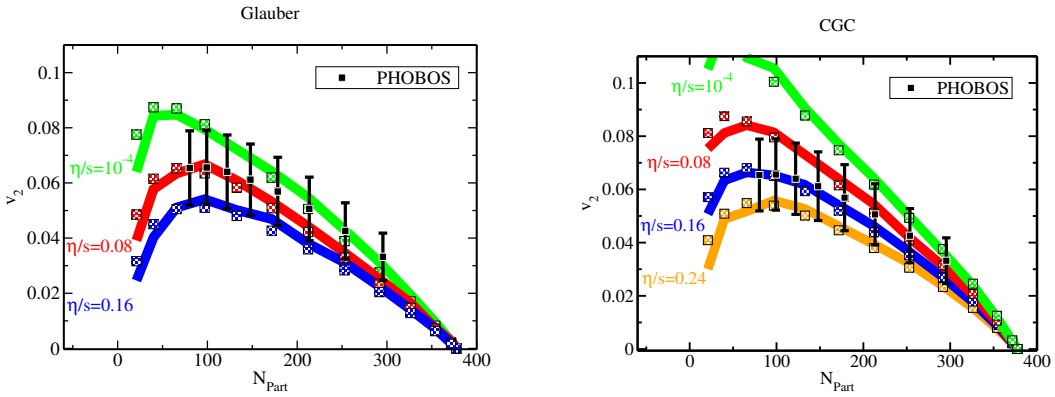


Figure 1.10: Comparison of hydrodynamic models to experimental data on charged hadron integrated elliptic flow by PHOBOS [10].

mass, which has been attributed to the dominance of the quark coalescence (recombination) mechanism for $p_T \sim 2-4$ GeV/c[84, 85].

On the other hand, if elliptic flow is indeed driven by a hydrodynamic pressure gradient, the differential $v_2$ values observed for each particle species should scale with transverse kinetic energy $KE_T$ in that $KE_T$ not only reflects the collective kinetic energy of the emitted particles but also links directly to the pressure gradient that drives the particles to expand to form elliptic flow. As seen from $KE_T$ definition, this physics quantity is particularly useful in flow studies for various particle species because it takes into account relativistic effects, which are especially important for the lightest particles. From panel (b) of Fig.1.7, the elliptic flow $v_2$ all scale to a common curve for $KE_T \lesssim 1$ GeV. This interesting phenomenon furthur confirms the dominance of hydrodynamic mechanism where pressue gradients drive the flow. For $KE_T \gtrsim 0.8$ GeV, this mass scaling feature fails, resulting in a clear splitting into a lower $v_2$ branch (meson branch) and a higher $v_2$ branch (baryon branch).

According to the quark coalescence model, baryons and mesons elliptic flow coefficients are first expressed in terms of the quark elliptic flow in $p_T$ coordinates[86],

$$v_{2,Meson}(p_T) \approx 2v_{2,q}\left(\frac{p_T}{2}\right) \; v_{2,Baryon}(p_T) \approx 3v_{2,q}\left(\frac{p_T}{3}\right). \tag{1.4}$$

Following this thread, Figure.1.11 (a) (b) presents the same elliptic flow $v_2$ values in Fig.1.7 but scaled down by the number of constituent quarks. This is usually referred to as *constituent quark number ($n_q$) scaling*. In Fig.1.11, $v_2$, $p_T$ and $KE_T$ are divided by number of consituent/valance quarks $n_q$ for

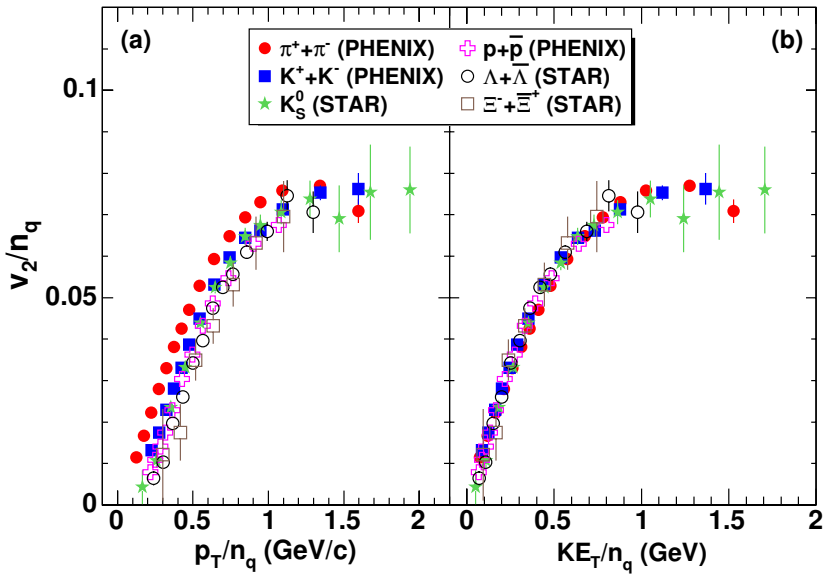


Figure 1.11: The elliptic flow per constituent quark ($n_q$) vs. transverse momentum per $n_q$ (left, panel (a)), transverse kinetic energy per $n_q$ (right, panel (b)) for different hadron species at RHIC. Figure taken from [5].

mesons ($n_q = 2$) and baryons ($n_q = 3$). In Fig.1.11(a), it shows relatively poor scaling feature for $p_T/n_q \lesssim 1$ GeV/c and the quark scaling $v_2$ seems to scale slightly better above 1.3 GeV/c even if the results carry large error bars. In contrast to panel (a), Fig.1.11(b) exhibits a universal curve which indicates an excellent scaling feature achieved over the full range of $KE_T/n_q$ (up to $\sim$ 1.5 GeV). Please note the results shown here are for minimum bias $Au + Au$ collision at $\sqrt{s_{NN}} = 200$ GeV.

The phenomenon that quark-scaling $v_2$ lies in a universal curve is thought to be an indication of the inherent quark-like degrees of freedom in the flowing matter that exhibits strong partonic collectivity. As shown in Fig.1.7, these quark degrees of freedom are not revealed from the dominant hydrodynamic mass scaling at low $KE_T$, but gradually appear when $KE_T$ becomes larger than 1 GeV (cf. Fig.1.7(b)). The finding that quark scaling $v_2$ shows a good universal pattern over the entire range of $KE_T/n_q$ but not for $p_T/n_q$ is considered as a compelling argument for the fact that hydrodynamic mass scaling is preserved over the domain of the linear increase in transverse kinetic energy $KE_T$[5].

Similar but more detailed $n_q$ scaling studies for different hadron species (charged pions, kaons and protons/anti-protons) in both central and noncentral $Au+Au$ collisions at $\sqrt{s_{NN}} = 200$ GeV is shown in Fig.1.12. The $v_2$ of all

species for centrality 0−20% has been scaled up by a factor of 1.6 for better comparison with results of 20−60% centrality. On top of the message conveyed in Fig.1.11 for minimum bias $Au + Au$ collisions, a quite different $n_q$ scaling behavior is found in central (Fig.1.12(c)) and in noncentral (Fig.1.12(d)) collisions. Similar to what is shown in Fig.1.11(b), a universal behavior of quark scaling $v_2$ is observed in the central (0-20% centrality) collisions within the statistical and systematic uncertainties, but not in the noncentral (20-60% centrality) collisions, where the measured $v_2/n_q$ of (anti-)protons falls off from the mesons branch for $KE_T/n_q$ greater than 1 GeV. Interestingly, the onset of falling for (anti-)protons shown in panel (d) coincides with the range where the (anti-)proton elliptic flow $v_2(p_T)$ drops in noncentral collisions but remains relatively constant in central collisions (cf. Fig.1.12(a)(b)). Similar breaking of $v_2/n_q$ occurs when we shift our x-axis from $KE_T/n_q$ to $p_T/n_q$. Since the changes in $v_2$ are relatively small in higher $p_T$ region, the pattern of curves does not vary significantly as we go from panel (c) (d) to panel (e) (f). The breaking of $n_q$ scaling indicates that quark recombination mechanism is clearly violated at high $p_T$ region.

Some theoretical models are proposed to explain such breaking of $n_q$ scaling. One possible interpretation for the breaking is the occurrence of transition from purely thermal to thermal+shower recombination mechanism[87]. Further measurements of the nuclear modification factors ($R_{AA}$) that are used to quantify the partonic energy loss in medium are found consistent among charged pions and (anti-)protons within high $p_T$ region ($p_T \gtrsim 5$ GeV/c)[88, 89]. Such consistency of $R_{AA}$ among mesons and baryons suggests additional mechanisms other than quark coalescence and jet energy loss be needed to explain the $v_2$ and $R_{AA}$ of pions and protons in $Au + Au$ collisions in this $p_T$ region.

Another intriguing probe to the QCD phase diagram is the $\phi-$mesons. STAR has performed a set of $\phi-$mesons elliptic flow measurements (cf. Fig.1.13). Because of its zero net strangeness, $\phi-$mesons production is not sensitive to Canonical suppression effects, hence relative to p+p collisions, the observed enhancement of $\phi(s\bar{s})$ production in Cu+Cu and $Au+Au$ collisions clearly indicates the formation of a dense partonic medium in these heavy-ion collisions. Phenomenological study has suggested a relatively small hadronic interaction cross section for $\phi-$meson[90–92], which indicates $\phi-$mesons decouple early from the system and do not participate strongly in hadronic interactions. The sizable $v_2$ of $\phi-$mesons provides a convincing evidence that flow develops in a partonic phase.

A beam energy scan study of hadron elliptic flow is shown in Fig.1.14, where a universal trend for most of particles is achieved and $\phi-$meson $v_2$ clearly deviates from other hadron species in $Au + Au$ collisions at $\sqrt{s_{NN}} =$

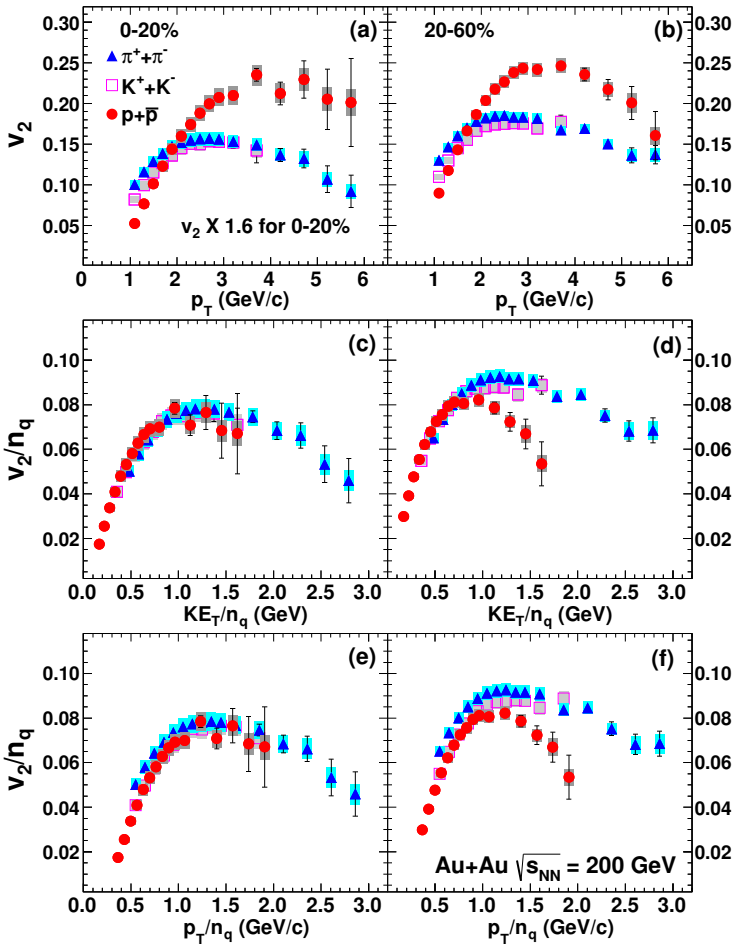


Figure 1.12: Elliptic flow $v_2$ for various hadron species in central (0−20% centrality, left panels) and noncentral (20−60%, right panels) $Au + Au$ collisions at $\sqrt{s_{NN}} = 200$ GeV as as a function of transverse momentum $p_T$ (a)(b). The $n_q$ scaled $v_2$ ($v_2/n_q$) is shown as a function of kinetic energy per quark $KE_T/n_q$ (c)(d) and transverse momentum per quark $p_T/n_q$ (e)(f). The $v_2$ of all species for centrality 0−20% is scaled up by a factor of 1.6 for better comparison with results of 20−60% centrality. The error bars (shaded boxes) represent the statistical (systematic) uncertainties. Figure taken from [11].

11.5 GeV. The small or zero $v_2$ for $\phi-$meson might suggest the formation of partonic matter had not occurred and hadronic interactions might be dominant as collision energy drops below 11.5 GeV. Therefore, the mechanism such as $K\bar{K}$ coalescence in $\phi-$meson production might not dominant in this energy region.

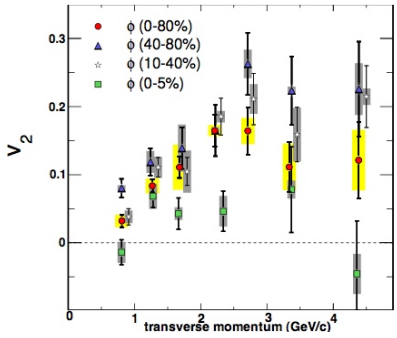


Figure 1.13: $\phi-$mesons $v_2$ as a function of $p_T$ in $Au+Au$ collisions at $\sqrt{s_{NN}}$ = 200 GeV for different centrality classes. Figure taken from [12].

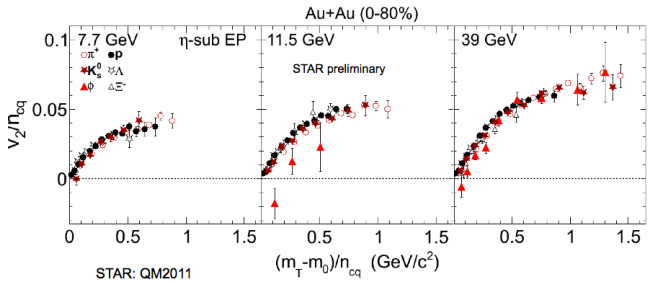


Figure 1.14: $n_q$ scaled $v_2$ as a function of transverse kinetic energy per quark $(m_T - m_0)/n_q$ in $Au + Au$ collisions at different collision energies for 0-80% centrality class. Figure taken from [13].

- **Jet quenching & suppression of high$-p_T$ particles**

Another important property of the QGP discovered at RHIC is a strong suppression of high$-p_T$ hadrons in central $Au + Au$ collisions, compared with $p + p$ collisions. Originated from energetic partons that are generated and fragmented in initial hard processes, these energetic high$-p_T$ particles interact with the QGP medium and lose their energies. To quantify the modification effect in nucleus-nucleus $(Au + Au)$ collisions with respect to nucleon-nucleon collisions, *the nuclear modification factor,* $R_{AA}$, is introduced. $R_{AA}$ is defined as ratio between the yield per $Au + Au$ event and the yield scaled by the average number of binary nucleon-nucleon collisions ($\langle N_{coll} \rangle$) in p+p events. In particular,

$$R_{AA}(p_T) = \frac{(1/N_{AA}^{evt}) d^2N_{AA}/dp_T dy}{\langle T_{AA} \rangle \times d^2\sigma_{pp}/dp_T dy}$$

Figure.1.15 shows $R_{AA}$ for serveral particle species observed in $Au + Au$ colllisions at RHIC. The dotted reference line at 1 indicates a situation where no nuclear modification effect is found, that is, the absence of medium effects is expected and the particle yield in $Au+Au$ collisions can be viewed as simple

superposition of multiple ($N_{coll}$) yields in $p+p$ collisions at the same $\sqrt{s_{NN}}$. From the plot, we observe the high$-p_T$ spectra for baryons and mesons are strongly suppressed in heavy-ion collisions. It is noteworthy that $R_{AA}$ for direct photons $\gamma$ is found consistent around 1, which is due to the charge neutral nature of photons. The phenomenon that high$-p_T$ particles lose their energies and are strongly suppressed in QGP medium is also referred to as *jet quenching*.

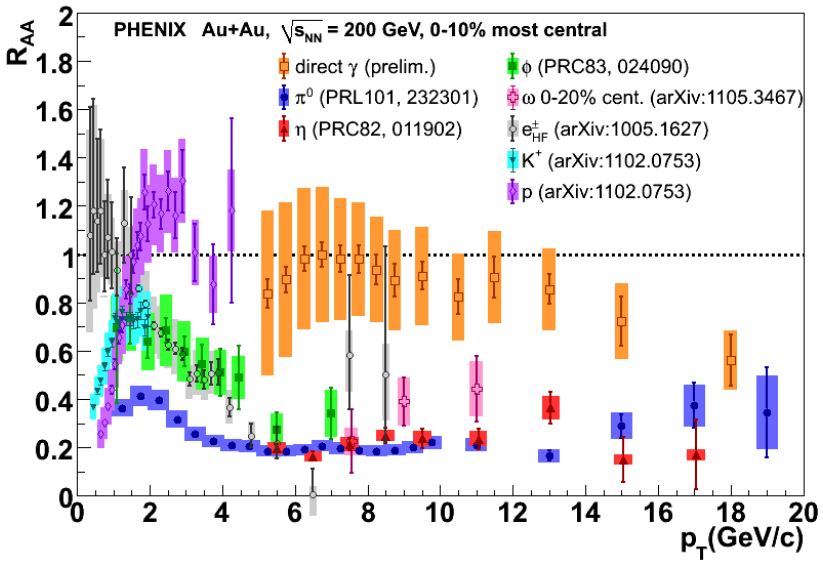


Figure 1.15: $R_{AA}$ for several identified particle species in $0-10\%$ central $\sqrt{s_{NN}} = 200$ GeV $Au+Au$ collisions[14–19].

### 1.2.5 RHIC & PHENIX

The Relativistic Heavy Ion Collider (RHIC) is located at Brookhaven National Laboratory (BNL), about 80 miles east to NYC on Long Island, NY. Currently, there are two active experiments at RHIC; Pioneering High Energy Nuclear Interaction eXperiment (PHENIX), and the Solenoidal Tracker at RHIC (STAR). These two experiments exist to independently address fundamental questions about the QGP state of nuclear matter. Because they are having fundamentally different detector designs, the two experiments serve to make complementary measurements and cross check results with each other. Since RHIC came into being, the two major experiments together with two

other experiments, PHOBOS and BRAHMS, have produced hundreds of scientific papers, successfully addressing many challenging questions from different perspetives.

RHIC is a well-rounded nuclear experiment facility because of its capability of performing head-on collision experiments based on various particle species and at different collision energies. In terms of collision species, RHIC has accelerated and collided $Au+Au$, $p+p$, $Cu+Cu$, $d+Au$ and $U+U$ systems; In terms of collision energies, RHIC has conducted experiments at $\sqrt{s_{NN}}$ =7.7 GeV, 11.5 GeV, 19.6GeV, 22.5 GeV, 27 GeV, 39 GeV, 62.4 GeV, 130 GeV, 200 GeV and 510 GeV. The great versatility of RHIC allows physicists to perform the beam energy scan (BES) study over a broad region on the QCD phase diagram to better understand the nuclear matter we have created.

The data used in this thesis are from $Au+Au$ collisions at $\sqrt{s_{NN}}$ =200, 62.4 and 39 GeV, collected by PHENIX collaboration.

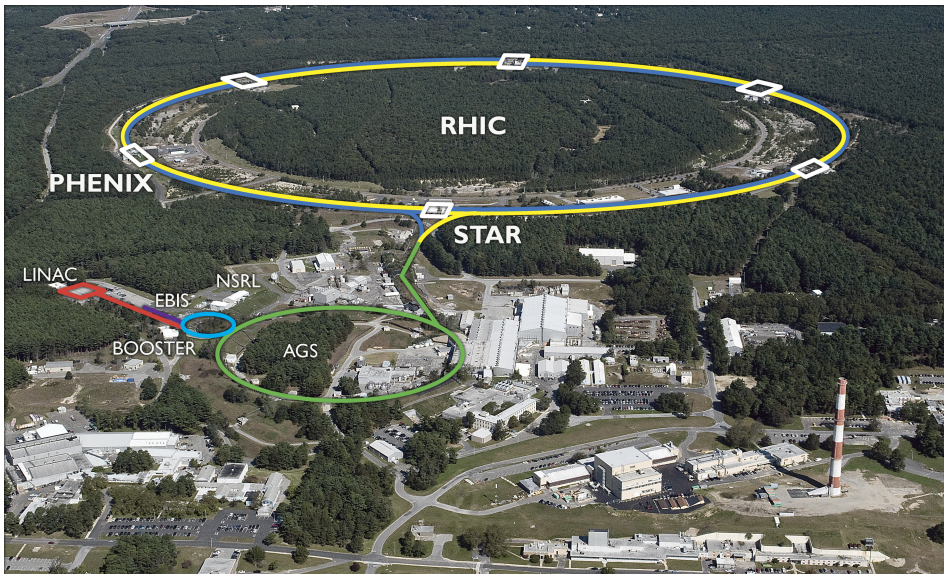


Figure 1.16: RHIC at BNL. PHENIX is at 8:00 o'clock on the RHIC collider ring. picture courtesy to http://www.rhip.utexas.edu/experiments.php

### 1.2.6 From RHIC to LHC

The extremely hot and dense matter discovered at RHIC has shown a number of surprisingly interesting properties. Its opaqueness to colored particles (such as quarks and gluons) gives rise to the striking jet quenching phenomenon observed at RHIC. Comprehensive measurements of the elliptic flow of different

hadron species clearly indicate that the QGP matter created at RHIC is a liquid with extremely low viscosity. Despite the success of heavy-ion experiments at LHC, the beam energy scan (BES) program launched at RHIC is expected to provide details of the QCD phase diagram not accessible at the LHC.

On the other hand, when heavy-ion experiments enter the LHC era, more than a factor of ten increase in collision energy at LHC extends the kinematic reach in rapidity and $p_T$ of previous measurements at RHIC to an unprecedented level. The observations at LHC are expected to uncover the temperature dependence of various observables.

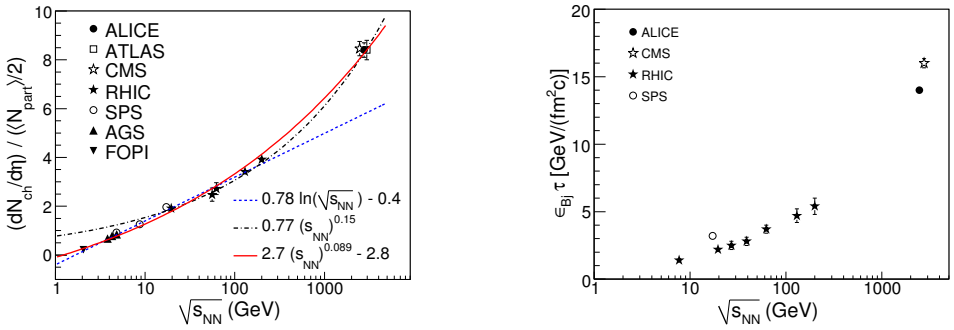


Figure 1.17: $dN_{ch}/d\eta$ per participating nucleon pair at midrapidity in central heavy-ion collisions as a function of $\sqrt{s_{NN}}$ (left); The product of Bjorken energy density, $\epsilon_{Bj}$[20], and the formation time $\tau$ in central heavy-ion collisions at midrapidity as a function of $\sqrt{s_{NN}}$[21–26] (right).

Much higher collision energies at LHC is expected to produce much denser nuclear matter. Fig.1.17 presents the multiplicity per participating nucleon pair (left panel) and the product of Bjorken energy density $\epsilon_{Bj}$ and formation time $\tau$ (right panel) at midrapidity in central heavy-ion collisions as a function of $\sqrt{s_{NN}}$. $\epsilon_{Bj} = \frac{1}{A_\perp \tau} dE_T/dy$, where $A_\perp$ is the transverse overlap area of the nuclei and $E_T$ is the transverse energy[20].

As shown in the left panel of Fig.1.17, the charged particle multiplicity density per participating nucleon pair at midrapidity ($dN_{ch}/d\eta$) in central heavy-ion collisions increases by a factor of two as the energy advances from RHIC to LHC. Three fitting functions are employed to reflect the trend. It is quite interesting to notice that the data seem to prefer a power law type of dependence on $\sqrt{s_{NN}}$ and clearly exclude the logarithmic dependence of particle production with $\sqrt{s_{NN}}$. The red solid curve turns out to well describe the data in full energy range.

From right panel of Fig.1.17, the product of energy density and the formation time at LHC is believed to be a factor three larger compared to those at RHIC. If $\tau_0(= 1fm/c)$ is presumably same for LHC and RHIC, the Bjorken energy density is about three times larger at the LHC compared to that at RHIC in central collisions.

Because of the denser and hotter matter created at LHC, it is intriguing and natural to ask what the properties of transporting particles, energy, momentum and charge are going to change, if any, compared with those found at RHIC, whose collision energy is at least one order lower than LHC? For those transporting properties of nuclear matter created at LHC, do they change, if any, by the same amount as the collision energy does from RHIC to LHC, that is by a factor over ten? Of course, to address these questions, we need to perform extensive, high precision measurements. The discussions pertaining to this topic will be included in Chapter 4 and 5 of this manuscript.

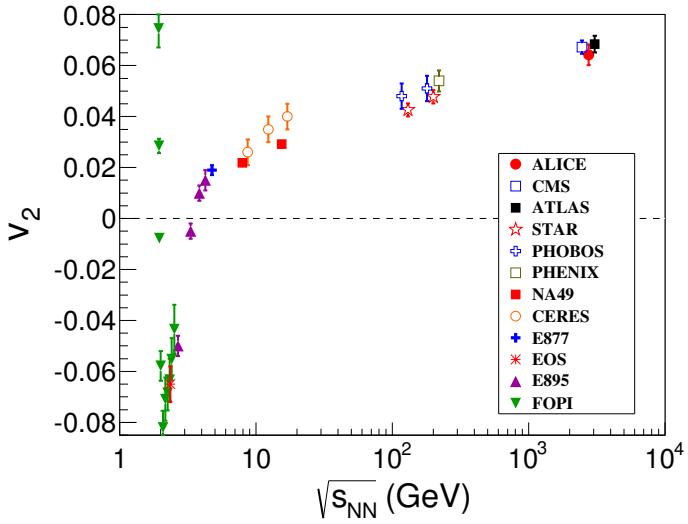


Figure 1.18: Transverse momentum integrated $v_2$ close to midrapidity for charged (Z = 1) particles with around 20-30% centrality as a function of $\sqrt{s_{NN}}$. Figure taken from [27].

Figure.1.18 displays the $p_T-$integrated $v_2$ close to midrapidity of charged particles for collision centralities around 20-30% as a function of center of mass energy $\sqrt{s_{NN}}$. Since average transverse momentum $\langle p_T \rangle$ of pions (dominant particles after hadronization) increases by about 30% from RHIC to LHC, the magnitude of observed $p_T-$integrated $v_2$ increases by roughly the same amount ($\sim$ 30%) from top RHIC heavy-ion collision energy ($\sqrt{s_{NN}}$ = 200 GeV) to

LHC energy ($\sqrt{s_{NN}}$ = 2.76 TeV, as of early 2013). Note that the data at beam energy less than 10AGeV are from fixed target experiments, while the $v_2$'s beyond 10AGeV are from head-on collision experiments. The increase of $p_T-$integrated $v_2$ at beam energy above 10AGeV follows a logarithmic trend in $\sqrt{s_{NN}}$, which can be understood from the pressure gradient-driven nature of the fireball expansion[93]. For $v_2$'s at lower beam energies, the dependence observed can be attributed to the subtle interplay of passing time of spectators and time scale of system expansion. The negative $v_2$ arises from a "squeeze-out" pattern that in-plane particle emission is blocked by spectators and out-of-plane emission is "preferred" at relatively low beam energies.

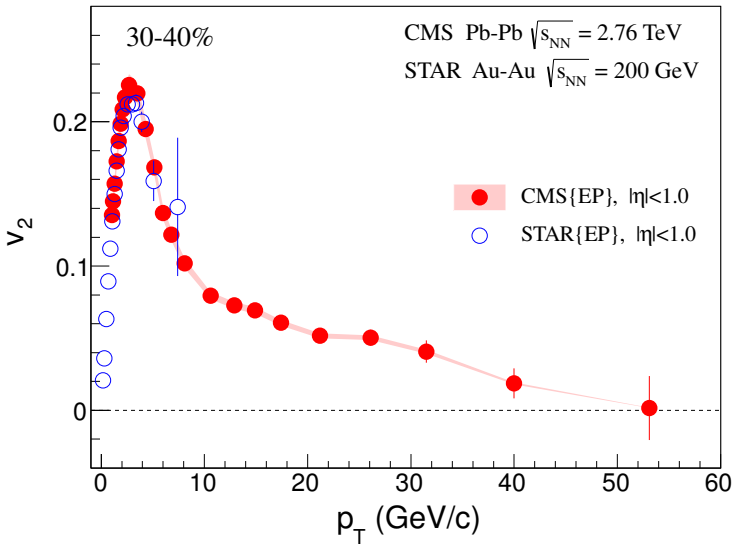


Figure 1.19: $v_2(p_T)$ at midrapidity for 30-40% collision centrality in Au+Au collisions at RHIC ($\sqrt{s_{NN}}$ =200 GeV from STAR experiment) and in Pb+Pb collisions at LHC ($\sqrt{s_{NN}}$ =2.76 TeV from CMS experiment). The shaded band represents CMS systematic uncertainties and error bars represent statistical uncertainties. Figure taken from [27].

Figure.1.19 shows the inclusive charged hadron elliptic flow coefficient $v_2(p_T)$ for 30-40% centrality class in Au+Au collisions at $\sqrt{s_{NN}}$ =200 GeV and Pb+Pb collisions at $\sqrt{s_{NN}}$ =2.76 TeV for $|\eta|$ <1[94]. The higher kinematic reach at LHC allows us to study the flow pattern of particle emission in the $p_T$ range that has been never touched in heavy-ion collisions at RHIC. The negligible $v_2$ for $p_T$ > 40 GeV/c suggests the absence of pressure gradient-driven flow and the near-zero $v_2$ indicates that those particles must have been emitted well before collective effects come into play. The extremely high$-p_T$

$v_2$ is also helpful in understanding the role of initial geometry and path-length dependence of various properties associated with parton modification inside the hot QCD medium[27].

Another quite striking observation from Fig.1.19 is the comparable $v_2$ found at LHC. Even $v_2(p_T)$ seems to be 10-20% smaller at RHIC compared to the corresponding LHC results when $p_T \gtrsim 3$ GeV/c, in low $p_T$ region, results are somewhat consistant from RHIC to LHC in this 30-40% centrality. This interesting finding might suggest the nuclear matter created at LHC be possibly governed by the similar rules to behave like a nearly perfect fluid. The models within hydrodynamic framwork that first proposed to explain RHIC data might also hold in LHC domain, subject to additional tuning of parameters to accommodate the much denser and hotter environment at LHC. Further detailed comparison of RHIC and LHC elliptic, as well as high-order harmonic flow results in low and intermediate $p_T$ region, will be presented in Chapter 4 of this manuscript. I would like to defer the discussions within this topic to then.

## 1.3 Harmonic Flow Measurements

The QGP medium created in relativistic heavy-ion collisions exhibits strong collective behavior. Flow is an observable that provides crucial information on the equation of state (EoS) and the transport properties of the created QGP. Experimentally, the most direct evidence of collective flow activity is the observation of anisotropy in particle distribution in momentum space correlated with the reaction plane. This anisotropic flow has been interpreted as evidence of a low viscosity, nearly perfect fluid being created in heavy-ion experiments.

### 1.3.1 An Overview

Two different methods are employed in harmonic flow measurements at PHENIX, one of which is event plane (EP) method and the other is multi-particle correlation method (in most cases, two particle correlations). Even though these two methods are technically quite distinct, from methodological point of view, they share some similarity.

In EP method, particle hits in reaction plane detectors are used to estimate event plane and other particle tracks are correlated with the estimated reaction plane (referred to as event plane) to find the distributions of azimuthal angle difference. With additional correction factors that account for the dispersion effect due to limited detector resolutions, the second order (and higher order) coefficients of Fourier expansion of correlation functions are extracted.

In the two-particle correlation method that I use in my work at PHENIX, qualified good particle tracks are selected from both the same and different collision events in order to eliminate the acceptance effect of detectors. Tracks are used in pair to build correlation functions (cf. Eqn.4.1). These two methods will be introduced in great details in following chapters of this manuscript.

Event Plane (EP) method is a traditional and mature method in flow measurement, however it requires the determination of event plane angle and the estimate of its resolution to account for the dispersion effect. This process usually demands multiple scan of the whole dataset, which may take quite long to obtain relatively reliable results. To avoid the process of event plane determination, the multi-particle correlation method is proposed, in which particles are correlated directly without knowing the estimated reaction plane. However, there is always an introduced uncertainty from correlation not associated with the reaction plane (non-flow contribution) in the correlation analysis. In general, the non-flow contributions in the correlatioin analysis are not negligible, and included in non-flow effects are various long- or short-range correlations among clusters of particles, such as momentum conservation, Hanbury-Brown Twis (HBT) effect, resonance decay and jets[95]. The reliable flow measurement requires accurate discrimination of flow signal from non-flow contributions. Unfortunately, a general and rigorous way to separate flow from non-flow correlations has not been found[96].

Various methods to evaluate and suppress non-flow contributions have been proposed and performed. Among them, the so called cumulants method is quite successful. Although this method is indeed a correlation-based analysis, it is quite different from what I use at PHENIX. In cumulants method, particles can be selected within the same rapidity window, where non-flow effects from any short-range correlations are thought to come into play. Since non-flow correlations are mainly few-particle effects, from the combinatorics it is easy to show that such non-flow contribution scales as the inverse of the multiplicity (this is true under assumption that the relative strengths of non-flow effects are not dependent on centrality), that is $\propto 1/M$, where $M$ is the multiplicity. Therefore, the $v_2$ from second order cumulants (obtained from correlating two particles) is a good estimate when $v_2 \gg 1/\sqrt{M}$, $v_2$ from fourth order cumulants (obtained from correlating four particles) is a good estimate if $v_2 \gg 1/M^{3/4}$ and $v_2$ from infinite-particle correlation is already a good estimate when $v_2 \gg 1/M$. This basically says that for a typical Pb+Pb collision at the LHC with $M \sim 10^2$, the possible non-flow contributions can be significantly reduced by more than an order of magnitude using higher order cumulants.

Another proposal to suppress non-flow contributions is to correlate particles in pair with as large pseudorapidity gap as possible to build correlation func-

tions. The long-range two-particle correlation method I use to measure harmonic flow signals at PHENIX is within this category. Actually, EP method's great success of obtaining reliable $v_n$ is mainly due to its implementation process (e.g. two sub-event technique), in which tracks with huge pseudorapidity gap are usually used to build azimuthal distributions and/or determine detector resolutions.

### 1.3.2 Initial Geometry Fluctuations and Higher Order Flow Harmonics $v_n(n > 2)$

The initial geometry of the collision profile encodes information about the particle distributions in the final momentum space. If the collision zone (overlap region) is smooth as shown in Fig.1.4, there would be only even order (n=2,4,...) flow harmonics in the final particle distributions. In particular, if the overlap region in initial state is a perfect ellipsoid, the anisotropy flow would be $2^{nd}$ order only. In this scenario, Fourier decomposition up to $2^{nd}$ order would be good enough to describe the azimuthal distribution of the emitted particles in final state. However, due to a finite number of nucleons participating in the collisions, their positions may vary event-by-event, which results in fluctuations in the initial collision geometry. Figure.1.20 shows participants that are randomly distributed in the overlap region. This particular configuration of participating nucleons defines a participant plane $\Psi_{PP}$[1] which fluctuates, for each event, around the reaction plane $\Psi_{RP}$.

These fluctuations in the initial collision geometry can be well modeled and computed within the framework of, for instance, Glauber conditions. To quantify such spatial anisotropy in initial collision geometry, the quantity *participant eccentricity* is introduced,

$$\begin{aligned} \epsilon_{part} &= \frac{\sqrt{(\sigma_y^2 - \sigma_x^2)^2 + 4\sigma_{xy}^2}}{\sigma_y^2 + \sigma_x^2} = \frac{\sqrt{\langle r^2 \cos 2\phi \rangle^2 + \langle r^2 \sin 2\phi \rangle^2}}{\langle r^2 \rangle} \\ tan(2\Psi_{PP}) &= \frac{2\sigma_{xy}}{\sigma_y^2 - \sigma_x^2} = \frac{\langle r^2 \sin 2\phi \rangle}{\langle r^2 \ cos 2\phi \rangle} \end{aligned} \tag{1.5}$$

where, $\sigma_y^2 = \langle y^2 \rangle - \langle y \rangle^2$, $\sigma_x^2 = \langle x^2 \rangle - \langle x \rangle^2$, $\sigma_{xy}^2 = \langle x^2 y^2 \rangle - \langle xy \rangle^2$ are the variance in the positions of participating nucleons, $r$ and $\phi$ denote the transverse positions of the participating nucleons in polar cooridnates about the center of mass. $\Psi_{PP}$ gives the orientation of the particpant-eccentricity plane. It is noteworthy that the participant eccentricity defined in Eqn.1.5, compared with

[1]Sometimes it is also referred to as (observed) event plane.

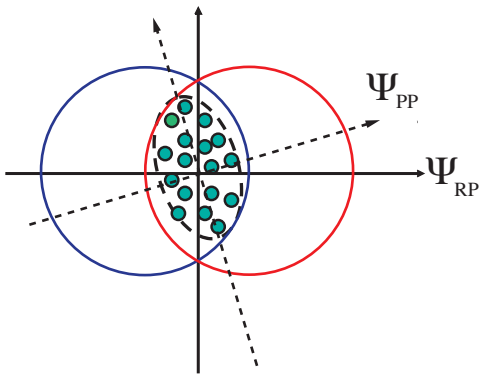


Figure 1.20: Transverse view of a heavy-ion collision showing fluctuations in the initial geometry. The "participant eccentricity" is computed based on participating nucleons, which form an actual collision zone with its own orientation that is not necessarily along the reaction plane. Figure taken from [28]

Eqn.1.1, makes more sence in that this quantity better describes the event-by-event fluctuations of the participating nucleons in initial collision geometry that drives the anisotropic flow.

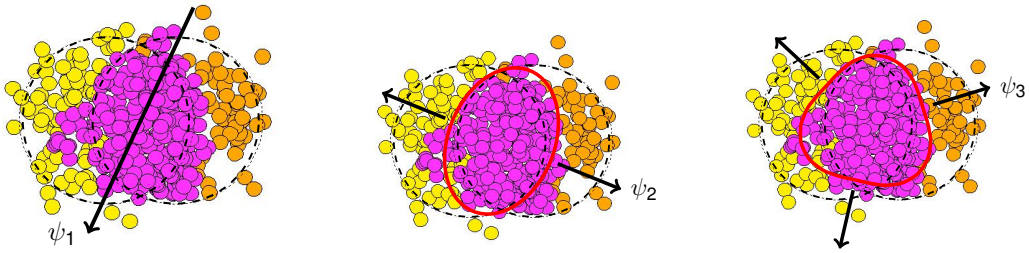


Figure 1.21: Schematic diagram illustrating the orientations of directed ($\Psi_1$), elliptic ($\Psi_2$) and triangular flow ($\Psi_3$) with respect to the initial distributions of participating nucleons in a single event from Glauber model[29].

The symmetry of initial collision geometry will be broken by any event-by-event fluctuations. Flow fluctuations are thought to play an important role and have been carefully studied for several years, however much efforts are initially allocated to examine its influences on elliptic flow $v_2$[97]. An breakthrough idea is that such event-by-event fluctuations of initial collision geometry imply other flow coefficients, especially $v_3$, should not be neglected[98]. It was not until 2010 did the entire heavy ion community realize these fluctuations would lead to the presence of odd order eccentricities with its own orientation that

drives higher (than $2^{nd}$) order anisotropic flow (cf. Fig.1.21). The $n^{th}$ order eccentricity is a generalization of Eqn.1.5, for $n > 1$,

$$\begin{aligned} \epsilon_n &= \frac{\sqrt{\langle r^n \cos n\phi \rangle^2 + \langle r^n sinn\phi \rangle^2}}{\langle r^n \rangle} \\ tan(n\Psi_{PP,n}) &= \frac{\langle r^n \sin n\phi \rangle}{\langle r^n \cos n\phi \rangle} \end{aligned} \tag{1.6}$$

Note that the $n^{th}$ order participant plane ($\Psi_{PP,n}$) has an intrinsic $2\pi/n$ symmetry (n-fold degeneracy) and it orients along the major axis of the $n^{th}$ order eccentricity. Because of the possible presence of multiple orders of eccentricities in the initial collision geometry, Eqn.1.3 needs to be generalized,

$$\frac{dN}{d\phi} \propto 1 + \sum_{n=1}^{\infty} 2v_n \cos n(\phi - \Phi_n) \tag{1.7}$$

to reflect the independent orientation of each order eccentricity (and thus participant event plane) component. $N$ is the number of particles, $\phi$ denotes azimuthal angles for emitted particles and $\Phi_n$ is the phase angle of the $n^{th}$ order component. $\Phi_n$ also represents the orientation of $n^{th}$ order participant event plane.

Experimentally, the fluctuations-induced higher order flow harmonics (higher order components in Fourier decomposition) have been systematically studied as a function of transverse momentum $p_T$, transverse kinetic energy $KE_T$, centrality class and rapidity $\eta$ at different collision energies, at both RHIC and LHC by many collaborations. As an example, Figure.1.22 shows $v_n$ measurements as a function of rapidity $\eta$ and transverse momentum $p_T$ at ATLAS in $Pb+Pb$ collisions at $\sqrt{s_{NN}} = 2.76$ TeV. A weak $\eta$ dependence is observed for all $v_n(n >= 2)$ within $|\eta| < 2.5$. All measured harmonics have a similar $p_T$ dependence in both central and mid-central collisions. $v_2$ values first increase rapidly up to $p_T \sim 3-4$ GeV/c, then decrease but remain positive even at high $p_T$. This $p_T$ dependence can be well understood by the pressure gradient-driven mechanism of flow development in low and intermediate $p_T$ region as well as the path-length dependent jet-medium interactions-driven machanism of flow development in high $p_T$ region.

As collisions become more peripheral, $v_2$ values increase by a factor of three from the most central to mid-central collisions, whereas higher order flow harmonics show very weak centrality dependence. This observation is consistent with our understanding of $v_n$'s origin, because $v_2$ is mainly driven by the pressure gradient from the elliptical shape of initial collision geometry

and $v_n$ $(n > 2)$, however, originates from fluctuations in collision geometry. Therefore, $v_2$ must be very sensitive to the collision geometry (*i.e.* the centrality dependence of $2^{nd}$ order eccentricity, $\epsilon_2$, determines $v_2$ trend), while $v_n$ $(n > 2)$ does not exhibit strong dependence on the shape of initial overlap region.

Moreover, because the anisotropic flow coefficients $v_5$ and above were found to have a very small hydrodynamic response and very large viscous suppression (cf. Fig.1.22) [99], significant contribution from collective flow should not be expected for flow harmonics that is $5^{th}$ order and beyond.

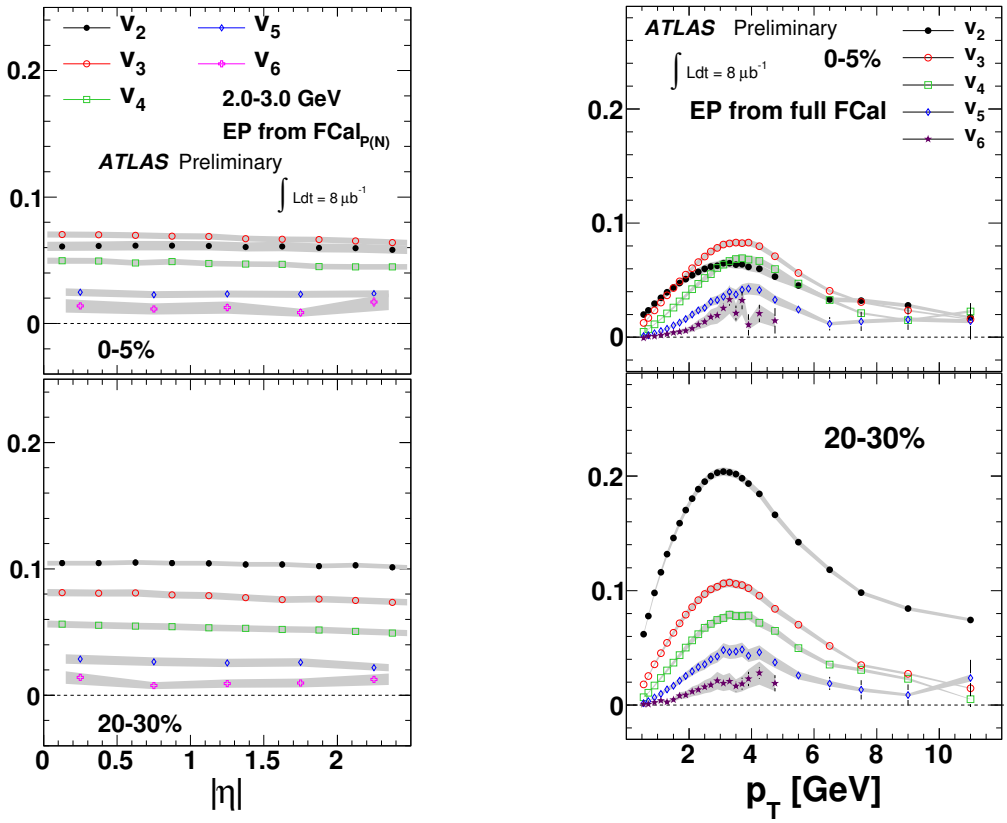


Figure 1.22: $\eta$ dependence of $v_n(n >= 2)$ for inclusive charged hadrons within $2 < p_T < 3$ GeV/c from $FCal_{P(N)}$ at ATLAS (left); $p_T$ dependence of $v_n(n >= 2)$ at ATLAS (right).

The measurement of higher order harmonics $v_n$ $(n > 2)$ yields additional constraints on initial geometry models and $\eta/s$ extraction of the created QGP matter[100]. On the other hand, fluctuations in initial collision geometry, the origin of $v_n$ $(n > 2)$, open a window for event-by-event (EbyE) studies of flow

measurements. Recently, the EbyE hydro calculations have been found quite successful in describing the experiment findings[101].

## 1.4 Di-hadron Correlation in Flow Measurement

Correlations among particles detected in heavy-ion collisions is a powerful tool in understanding the properties and dynamics of the collision system. As stated in previous section, the spacial anisotropy in initial state plus its fluctuations would evolve into a momentum anisotrpy that manifests itself in correlations among the final particles.

A correlation function $C(\Delta\phi, \Delta\eta)$ in di-hadron correlation studies is defined as

$$C(\Delta\phi, \Delta\eta) = \frac{N_{pair,same}(\Delta\phi, \Delta\eta)}{N_{pair,mix}(\Delta\phi, \Delta\eta)} \tag{1.8}$$

where $\Delta\phi$ is the azimuthal angle separation between the selected two hadrons and $\Delta\eta$ is the pseudorapidity difference between them. $N_{pair,same}(\Delta\phi, \Delta\eta)$ in numerator represents the $(\Delta\phi, \Delta\eta)-$distribution of correlated hadron pairs from the same collision event. In contrast, $N_{pair,mix}(\Delta\phi, \Delta\eta)$ in denominator represents the distribution of uncorrelated hadron pairs, in which two hadrons are selected from different events (known as "mixed-event" correlations) but with similar event character as same-event correlations, such as centrality and collision vertex position. Note that the mixed-event pair distribution in denominator reflects the pair $(\Delta\phi, \Delta\eta)$ acceptance of detector, but it does not have any physical correlations embedded. Since both numerator and denominator are affected by the pair efficiency, the ratio of the two distributions will have such acceptance effect canceled out. Therefore, the correlation function $C(\Delta\phi, \Delta\eta)$ in Eqn.4.1 contains only meaningful physical correlations. It is noteworthy that we may integrate out the $\Delta\eta$ dependence in both same- and mixed-event correlations if our analysis is not sensitive to pseudorapidity within a certain $\Delta\eta$ range. In this case, numerator and denominator is reduced to $N_{pair,same}(\Delta\phi)$ and $N_{pair,mix}(\Delta\phi)$ respectively, resulting in an azimuthal correlation function $C(\Delta\phi)$.[2]

Following a two-source ansatz, the correlation function is assumed to come from a jet-induced source and an underlying harmonic modulation that origi-

[2]In my work at PHENIX presented later by this manuscript, an azimuthal correlation function $C(\Delta\phi)$ is built by looking at particle pairs with fixed and large pseudorapidity gap.

nates from collective flow.

$$C(\Delta\phi, \Delta\eta) = C_{flow}(\Delta\phi, \Delta\eta) + C_{jet}(\Delta\phi, \Delta\eta) \tag{1.9}$$

A jet is known as a spray of energetic hadrons moving in a narrow cone. As explained in earlier section of this manuscript, it is usually formed in the hadronization phase when energetic parton pairs interact with QGP medium and hadronize through fragmentations. Jet contributions are often considered as short-range effects and they are usually localized in a narrow window of $\Delta\eta \sim 0$ and $\Delta\phi \sim 0$ or $\pi$. It might be interesting to point out that jets of $\Delta\phi \sim \pi$ are also known as "back-to-back" jets or "di-jet".

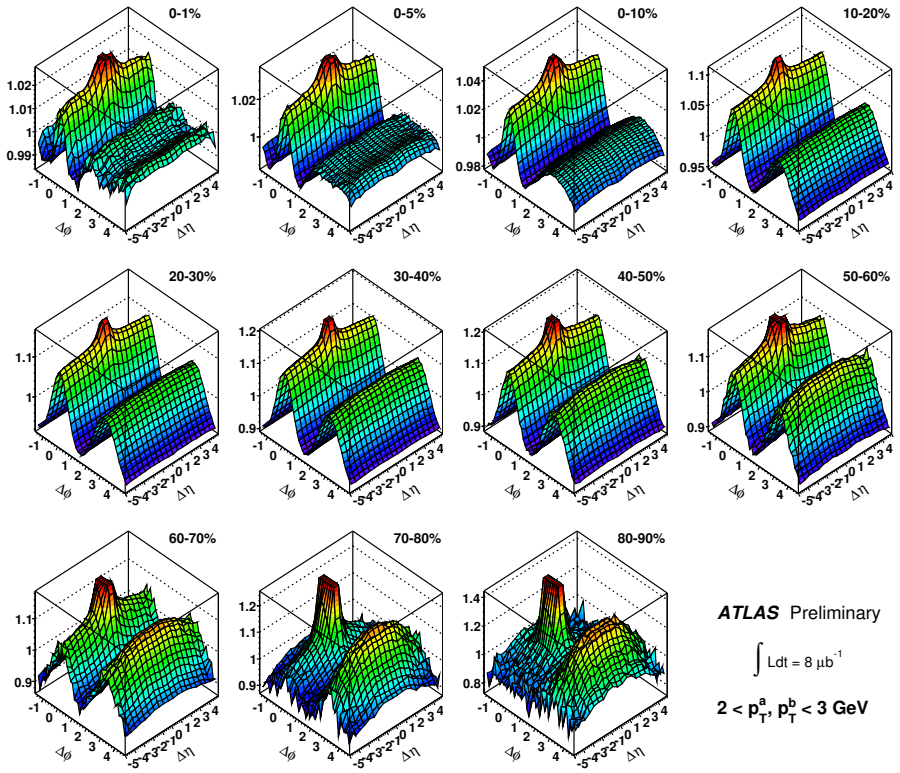


Figure 1.23: Two-particle correlation 2D data for charded hadrons in $Pb+Pb$ collisions at $\sqrt{s_{NN}} = 2.76$ TeV from the ATLAS collaboratioin.

Figure 1.23 shows the evolution of di-hadron (two-particle) correlation structure from most central (0-1% centrality) to peripheral (80-90% centrality) collisions. Data are collected by the ATLAS collaboration. Several impoartant phenomena of great interest to the whole community are found in this figure:

1. For most central collisions, there exists a clear "double-hump" structure in the away side ($\Delta\phi \sim \pi$) of correlation function. The collision zone, rather than an elliptical shape, is quite symmetric in most central collisions and $v_2$ values are comparable with or even smaller than fluctuations-induced $v_3$. The competing nature of pressure gradient-driven and profile fluctuations-driven mechanism is manifested in the detailed interplay between the odd harmonics ($v_3$ and $v_5$) and even harmonics ($v_2$,$v_4$,...), which results in the away-side "double-hump" structure obtained in the correlation function[44].

2. The near-side ($\Delta\phi \sim 0$) "ridge" structure along wide range of $\Delta\eta$ is seen from most central to peripheral collisions. Such "ridge" structure can be understood as a global response from flow contributions and the peak structure observed on the "ridge" near $\Delta\phi \sim 0$, $\Delta\eta \sim 0$ is considered as the near-side jet contribution, which can be largely suppresed by applying $\Delta\eta$ cut.

3. As collisions become more and more peripheral, the long-range structures from flow contributions gradually disappear. Instead, clear jet-related peaks are observed on the away side. These peaks are presumably coming from recoil jet fragmentation and soon dominate the correlation structure in high $p_T$ region.

Another important study from ATLAS collaboration implies that a transition in $p_T$ from flow-dominated to jet-dominated correlations possibly occurs somewhere around 6-8 GeV/c[44]. This finding indicates the similar correlation analysis performed at PHENIX is legitimate, where $C(\Delta\phi) \approx C_{flow}(\Delta\phi)$ is presumably true in low and intermediate $p_T$ region from central to mid-central collisions, upon additional pseudorapidity gap ($\Delta\eta$) requirement imposed to suppress near-side jet contributions and any other unwanted short-range effects. The correlation function, $C_{flow}(\Delta\phi)$, is further analyzed to extract flow harmonics. The comparison of flow results obtained from long-range two-particle correlation (2PC) method and event plane (EP) method will be presented in later chapters of this manuscript. The good consistency achieved in such comparison implies the structure of di-hadron correlation at relatively large $\Delta\eta$ can be largely accounted for by collective flow contributions.[3]

[3]The away-side (back-to-back) jet contribution can be a left-over in correlation function, however a small fraction of it is suggested based on the consistency of results from 2PC and EP method.

## 1.5 Physics Movitation for This Work

The collective flow behavior is an important probe to investigate the properties of QGP matter we have created in collision experiments. To name a few aspects, the second order flow harmonic reflects the geometric information about the post-collision fireball expansion; higher order flow harmonics could serve to constrain the initial geometry conditions and make precise extraction of hydrodynamic parameters (such as specific viscosity) become potentially possible; the viscous damping of even order flow signals in nuclear matter helps us better understand the acoustic nature of themselves; the number of constituent quark scaling feature of harmonic flow suggests its development in partonic phase and an underlying partonic collectivity... Of course, successfully addressing each of these questions must be accompanied by extensive, high precision flow measurements.

During the past decade, extensive studies are performed in hope of extracting the flow signals to our best accuracy. Most of the existing flow results are obtained via event plane (EP) method at PHENIX. At the same time, an intensive discussion as to how much non-flow (mostly, jet-related) effects are involved in the extracted flow signal has never come to an end. Therefore, the multi-particle correlation analysis quickly re-draws people's attention since it was first introduced in early 00's[102] because of its particular advantages of suppressing jet contributions. It was not until recently did we notice the long-range two-particle correlation (2PC) method applied at PHENIX obtains a set of harmonic flow results that are consistent with those from traditional EP method within investigated $p_T$ and centrality range. Without knowing raction plane orientation and detector resolutions, the 2PC method directly correlates track pairs of large pseudorapidity gap and is thought to greatly suppress jet contributions (particularly near-side jets), which are the major source of non-flow contributions in flow signal extraction.

Comprehensive understanding of the flow pattern in particle expansion also includes its energy dependence study. Thanks to the beam energy scan (BES) program launched at RHIC, in which Au nuclei are accelerated and colided at several center of mass energies below 200 GeV. Although detector performance would deteriorate with the drop of overall multiplicity as $\sqrt{s_{NN}}$ decreases, fortunatley flow observables are still measurable down to $\sqrt{s_{NN}} = 7.7$ GeV. A systematic study of flow observables in terms of their collision energy dependence can be very crucial to identify the change, if any, of properties of the QGP matter.

Large Hadron Collider (LHC) has been running at unprecedented center of mass energies since its first heavy-ion collision in year 2010. With bjorken density that is about three times larger than RHIC, the nuclear matter created

at LHC is very likely to exhibit quite different phenomena. As discussed earlier in Sec.1.2.6, a detailed comparison of flow observables obtained at LHC and RHIC would allow us to study the change, if any, of particles' collective behaviors at beam energies across three orders of magnitude.

# Chapter 2

# The PHENIX Detector

PHENIX is known for Pioneering High Energy Nuclear Interaction eXperiment, a collaboration of over 400 physicists conducting frontier experiments on nuclear physics. PHENIX can be also referred to as the complex detector system that is designed and operated by the collaboration. In this chapter, a brief introduction to the complex PHENIX detector system will be presented. In particular, I have categorized the PHENIX sub-detectors relevant to my analysis into three groups, that is, PHENIX global detectors, PHENIX central arm tracking detectors and central arm particle identification (PID) detectors. These three groups of detectors will be talked explicitly following an overview of the entire PHENIX detector system.

## 2.1 Overview of PHENIX Detector

Figure.2.1 illustrates the beam view (upper panel) and side view (lower panel) of the entire PHENIX detector system as of year 2010.

The "layer structure" of the central arm detectors can be seen from the beam view of PHENIX detector in upper panel of Fig.2.1. Two central arms (west arm, east arm[1]) are constructed (colored green), each of which covers $\sim \pi/2$ azimuthal angle and $|\eta| < 0.35$ pseudorapidity range. The gray shaded area represents the central magnet[103]. The innermost layer of central arm detector systems is the Drift Chamber[31] (DC), followed by layer 1 of Pad Chamber[31] (PC1) and Ring Cherenkov Detector[33] (RICH) as we go further outward. These detectors are basically symmetric around collision vertex and located in both west and east arm. As we move further away from collision center, the layer 2 of Pad Chamber (PC2) followed by aerogel and Time-

[1]In PHENIX, beam direction is defined along z-axis pointing to North or South, hence two central arms are located in West or East side accordingly.

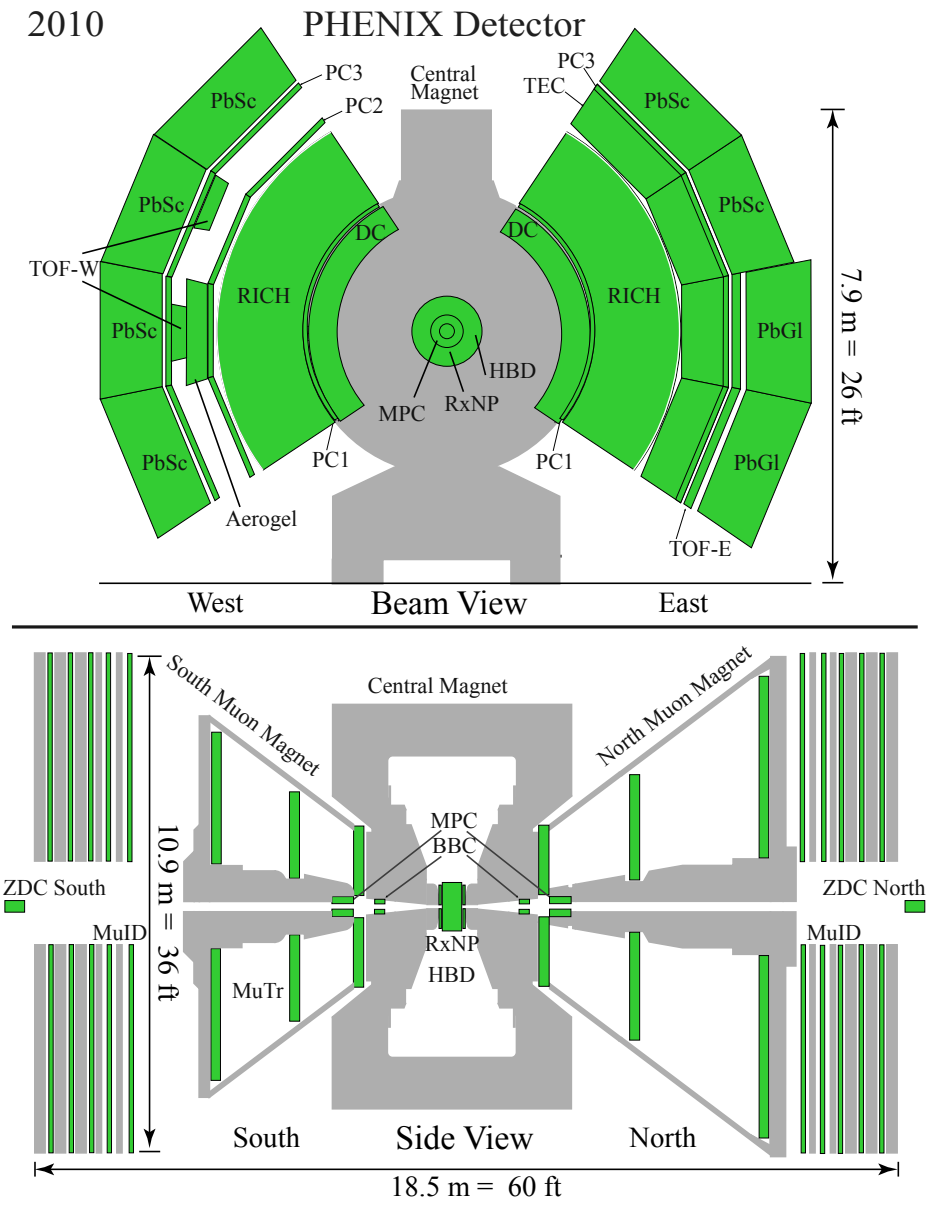


Figure 2.1: The PHENIX detector as of year 2010.

Of-Flight detector[104] (TOF-W) are installed in west arm, whereas Time Expansion Chamber (TEC) followed by layer 3 of Pad Chamber (PC3) and Time-Of-Flight detector[33] (TOF-E) are found in east arm. Both west and east central arm are having Electromagnetic Calorimeter[105] (EMCal) in their outmost layer, however, EMCal in the west side consists of four lead scintillator (PbSc) sectors yet in east side, two PbSc sectors plus two lead glass (PbGl) sectors. Note that Time-Of-Flight detector in west arm (TOF-W) and east arm (TOF-E) are designed differently with distinct technologies. Among these detectors, PC, DC are usually categorized as *tracking detectors* since they are generally used to provide trajectory information for emitted particles; RICH, TOF, EMCal are usually considered as *Particle Identifying (PID) detectors*, because they are respectively capable of identifying one particular type of particles.

The Muon Piston Calorimeter[106] (MPC), Beam-Beam Counter[107] (BBC), Reaction Plane Detector[30] (RxNP), Zero Degree Calorimeter[108] and Hadron Blind Detector[109] (HBD) are located along beam direction within different rapidity range. This can be easily seen from lower panel of Fig.2.1. BBC, RxNP, ZDC and MPC are sometimes called *global detectors* in that they are usually used to characterize the global information for collision events[2], such as global timing, reaction plane, centrality, etc. At forward rapidity, two muon arms are located on both South and North side, where Muon Trackers[110] (MuTr) and Muon Identifiers[110] (MuID) are installed. They are usually used together to perform $\mu-$related analysis. Detectors that are pertaining to the work presented in this manuscript include BBC ($3.1 < |\eta| < 3.9$), RxNP. As will be shown later in this chapter, RxNP is composed of an inner ring (RXI, $1.0 < |\eta| < 1.5$) and an outer ring (RXO, $1.5 < |\eta| < 2.8$), each of which could work independently and can be treated separately if needed.

A brief summery of PHENIX sub-detector systems can be found in Table.2.1

## 2.2 PHENIX Global Detectors

In PHENIX, two sets of detectors are installed at both forward and backward rapidity that is far away from the mid-rapidity region where physics analysis usually focus on. These detectors help to determine the global information of collision events and are usually referred to as global detectors. A schematic plot showing the azimuthal as well as the pseudorapidity acceptance of these global detectors can be found in Fig.2.2. A wide separation in $\eta$ between central arm

[2]An event is usually referred to as one nucleus-nucleus collision.

| **Detectors** | **Azimuthal ($\Delta\phi$) Coverage** | **Pseudorapidity ($\Delta\eta$) Coverage** | **Feature & Purpose** |
|---|---|---|---|
| ZDC | $2\pi$ | $\pm 2$ mrad | Luminosity measurement & Minimum bias trigger |
| BBC | $2\pi$ | $3.0 < \|\eta\| < 3.9$ | Global timing & Reaction plane measurement |
| DC | $2 \times \frac{\pi}{2}$ | $\|\eta\| < 0.35$ | Good mass and momentum resolution |
| PC | $2 \times \frac{\pi}{2}$ | $\|\eta\| < 0.35$ | Trajectory reconstruction and pattern recognition |
| RICH | $2 \times \frac{\pi}{2}$ | $\|\eta\| < 0.35$ | Electron detection |
| TOF-E | $\sim \frac{\pi}{4}$ | $\|\eta\| < 0.35$ | Hadron identification |
| TOF-W | $\sim \frac{1}{9}\pi^*$ | $\|\eta\| < 0.35$ | Hadron identification |
| PbGl | $\frac{\pi}{4}$ | $\|\eta\| < 0.35$ | Good $e^{\pm}/\pi^{\pm}$, $K^{\pm}/\pi^{\pm}$ separation |
| PbSc | $\frac{\pi}{2} + \frac{\pi}{4}$ | $\|\eta\| < 0.35$ | Photon and electron detection |
| RxNP | $2\pi$ | $1.0 < \|\eta\| < 2.8$ | Reaction plane measurement with good resolution |
| MPC | $2\pi$ | $3.0 < \|\eta\| < 3.9$ | Photon detection at forward rapidity & reaction plane measurement |

* $\phi$ coverage: (-0.061,0.110) $\cup$ (0.503,0.674) in rad.

Table 2.1: A brief summary of PHENIX sub-detector systems

detectors and these global detectors allows us to greatly suppress substantial amount of jet contributions in correlation analysis. It is also noteworthy that all the global detectors that are usually employed to determine reaction planes have full $2\pi$ coverage in azimuth, which is also indicated in Tab.2.1. Other global information includes, for example, the event centrality and multiplicity, global timing, collision vertex, etc.

Global information provided by these global detectors is crucial to most of the physics analysis, because these global observables serve to characterize the collision event. Answers to questions such as, how overlapped the initial two nuclei are, where the collision occurred (*i.e.*, where is the nominal vertex), are all strongly dependent on the global information given by these global detectors. Moreover, some of the information may also be badly needed by other detector systems. For example, the global timing resolution is extremely important to PHENIX trigger system and particle identification via TOF detector replies on precise timing info provided by BBC.

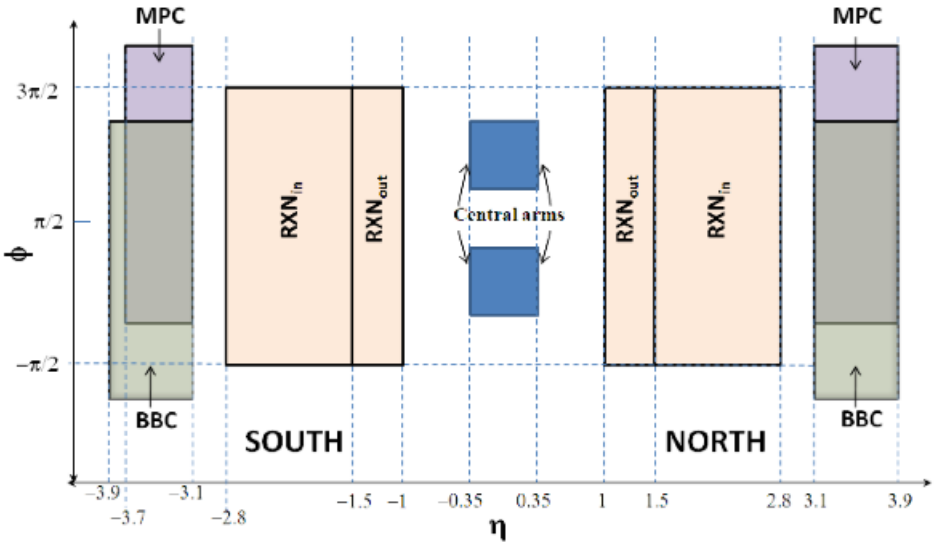


Figure 2.2: The azimuthal and pseudorapidity coverage of global detectors in PHENIX. The BBC and MPC are shifted on purpose to avoid overlap and improve visibility.

In this subsection, I will be introducing few important global detectors in PHENIX. All of these sub-detector systems are either directly or indirectly employed in my analysis.

### 2.2.1 Beam-Beam Counter (BBC)

Beam-Beam Counter (BBC) is mainly used to characterize centrality and collision vertex position, two fundamental pieces of event information that are of great importance to our analysis. As stated in Sec.1.2.2 of Chapter 1, "centrality" describes the extent of overlap of the initial collision zone. Vertex position tells us where the collision takes place. In most cases, beam offset in $x$ and $y$ direction is quite small, however, vertex position along beam pipe may vary significantly, which results in a sizable offset in $z$ coordinate of vertex point. $z = 0$ indicates a collision occurs right in the middle point between south and north arm. Nevertheless, this is not always true in real world. Therefore, to accurately determine $z$ is necessary for timing the entire PHENIX detector system and is essential to subsequent track reconstruction process, in which $z$ is considered as the origin of all charged particle tracks.

Two BBC units are located in both north and south sides of the collision zone, 144.35 cm ($L$) away from the center of the interaction point. Each BBC unit covers a full $2\pi$ azimuth and a pseudorapidity range of $3.0 < |\eta| < 3.9$. One beam-beam counter consists of 64 elements. Each element is made of a hexagonal quartz Cherenkov radiator part and a one-inch diameter mesh-dynode photomultiplier tube (PMT). Figure.2.3 includes a snapshot of one such element in BBC, along with a picture of one entire BBC unit.

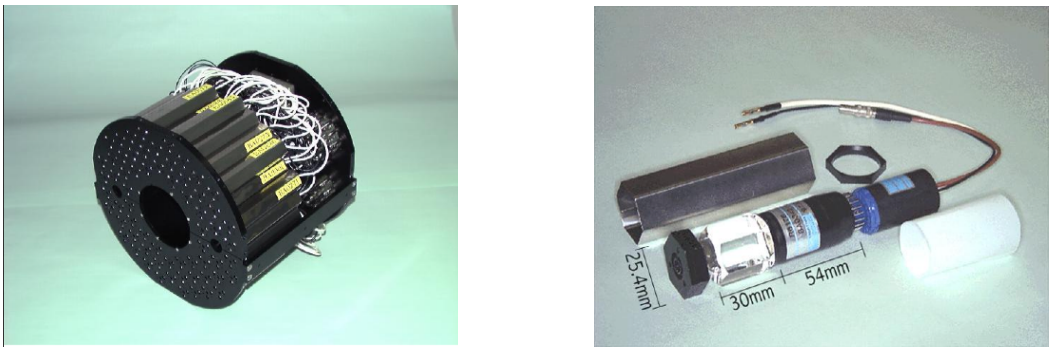


Figure 2.3: Layout of one BBC unit that consists of 64 basic elements (left); photo of one element that contains one hexagonal quartz Cherenkov radiator and a mesh-dynode photomultiplier tube (right).

The averaged arrival time is calculated based on particle arrival time in the $i^{th}$ element of BBC, $t_i$ ($i = 1, 2, \ldots, 64$). We use $T_{BBCN}$ and $T_{BBCS}$ to denote the averaged arrival time in north and south BBC unit, then the vertex position

$z$ and global starting time $T_0$ can be computed via

$$z = \frac{T_{BBCN} - T_{BBCS}}{2} \times c, \;\; T_0 \;\; = \;\; \frac{T_{BBCN} + T_{BBCS} - 2L/c}{2} \qquad (2.1)$$

where $c$ is the speed of light, and $L$ is the distance between each BBC unit and the center of the interaction point, 144.35 cm. $T_0$ is regarded as the global starting time, which signals the occurrence of one collision event. Hence it is treated as the "zero" in time and is being used by other sub-detector systems that require a timing input (e.g. TOF and EMCal). Due to the multiple granularity structure of BBC, its timing resolution is highly dependent on the multiplicity. Typically, it is in order of $\sim$ 10 ps for $T_0$. Consequently, the position resolution for $z$ is about 0.5 cm.

### 2.2.2 Zero Degree Calorimeter (ZDC)

The RHIC Zero Degree Calorimeters (ZDC) are hadron calorimeters. They are installed close to the beam pipe, about 18 meters away from the nominal interaction point in both north and south arm. The ZDC detectors are sitting behind the DX magnet so that all other charged particles are already swept away, allowing only neutron spectators to travel into the detectors. By counting the number of free neutrons, ZDCs are used to measure neutral energy within a 2 mrad cone about the beam direction. This measurement, in conjunction with the BBC, can be applied for event-by-event characterization. During early years, BBC and ZDC are used together to provide the minimum bias trigger and help in centrality determination. For data collected after run year 2007, however, the BBC percentile method is employed without using ZDC any longer. This is because large RMS width in the $N_{part}$ and $N_{coll}$ is introduced when including ZDC in the centrality definition, especially for pheripheral collisions.

Another important role of ZDC is for luminosity monitoring.

### 2.2.3 Reaction Plane Detector (RxNP)

Reaction Plane Detector (RxNP) is uniquely designed for reaction plane construction. Two symmetric RxNP units are located $\sim$ 39 cm away from the nominal vertex position along beam pipe in both north and south side. Each RxNP unit consists of a set of 24 scintillators. Right panel of Fig.2.4 illustrates the layout of these 24 scintillators in one arm. As seen from the figure, these 24 scintillators are arranged in two concentric rings (inner and outer) that surround the beam pipe and perpendicular to it, twelve in the inner ring

and twelve in the outer ring. Numbers in the diagram indicate the dimensions (in cm) of each segment. The two RxNP units are attached to the nosecone of PHENIX's central magnet, which is shown in the left panel of Fig.2.4.

Each ring has been subdivided into 12 trapezoidal-shape segments of equal size, and the 12 segments in total cover a full $2\pi$ azimuth. The inner ring has a pseudorapidity coverage of $1.5 < |\eta| < 2.8$ with its edges positioned at radial distances of 5 and 18 cm from the beam pipe. Pesudorapidity coverage may further extend to $|\eta| = 1.0$ as we move continuously outward, with the edge of outer ring positioned at 33 cm along radial direction. It may be interesting to know that each ring of RxNP is working independently and can be treated as a separate detector if needed.

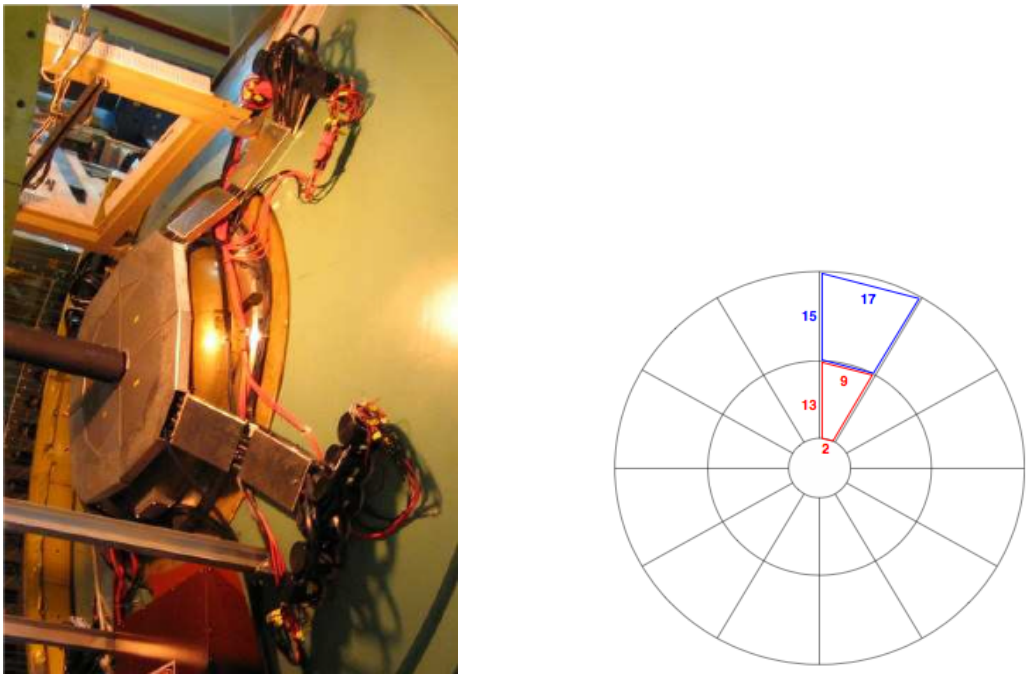


Figure 2.4: RxNP unit on the nosecone of PHENIX's central magnet before the installation of HBD (left); Schematic diagram showing the arrangement of the 24 scintillators, twelve in inner ring and twelve in outer ring. The length of each scintillator side is shown in cm (right).

RxNP has relatively fine azimuthal angle separation among the 12 segments in both inner and outer ring, hence it is good for azimuthal correlation analysis. However, it lacks the ability to register momentum information for detected tracks. It might be also valuable to notice that, had the azimuth been partitioned into more than 12 segments, RxNP's ability of higher order

flow measurements would have been much improved. The "12-paddle" design strategy is rooted in the simulation study, which is illustrated in Fig.2.5. It shows clearly in the figure that resolution of second order event plane resolution, the targeting quantity to be measured at that time, improves only marginally above 8 segments. Back then, 12 segmentations in $\phi$ is a fairly safe plan even from the perspective of protecting any potential dead segments. It was not until recent years did we realize the measurement of higher order flow harmonics is extremely useful in constraining our models of initial conditions as well as viscosity extraction. Although RxNP is optimized to have excellent performance in second order reaction plane ($\psi_2$) measurement, the limited granularity in transverse plane makes reaction plane measurement beyond $4^{th}$ order suffer from deteriorating resolutions.

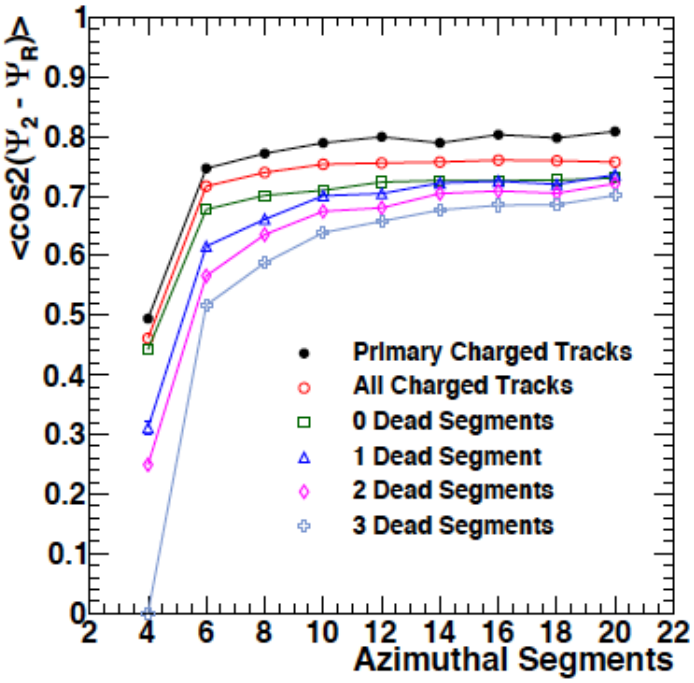


Figure 2.5: Simulation studies of the dependence of the 2nd harmonic event plane resolution in mid-central collisions on the azimuthal segmentation of the RXNP scintillator. Figure taken from [30]

### 2.2.4 Muon Piston Calorimeter (MPC)

The Muon Piston Calorimeter (MPC) is a small lead-tungstate ($PbWO_4$) based electromagnetic calorimeter with Avalanche Photodiode (APD) readout, covering a pseudorapidity range $-3.7 < \eta < -3.1$ and $3.1 < \eta < 3.9$ in the south and north sides of PHENIX.

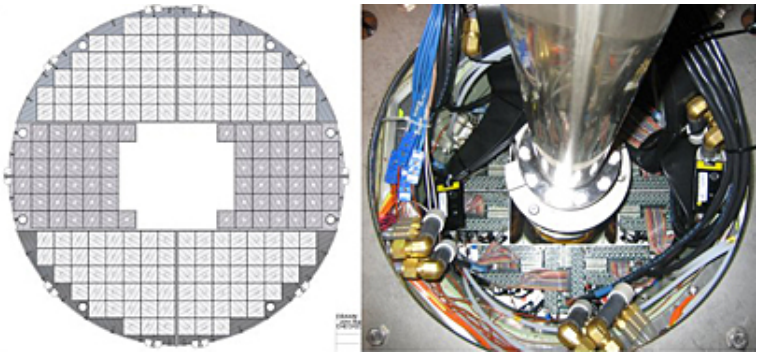

Figure 2.6: The schematic structure diagram (left) and snapshot (right) of south arm MPC.

Two MPC pieces are installed in the small cylindrical holes in the front face of the muon piston behind the beam-beam counters, however, they are not exactly identical. Figure.2.6[3] shows the structure (left panel) and a snapshot (right panel) of the south arm MPC piece, which is composed of 192 $PbWO_4$ crystals, whereas the north arm MPC piece has 216 crystals.

Unlike BBC that sits in the similar pseudorapidity window, MPC is sensitive to both charged and neutral particles. One of the areas that MPC has unique ability to contribute is the low-x physics. Because of its ability to measure netrual pions at forward region, MPC gives us great sensitivity to partons at low x. Another area in which MPC plays an important role is the single spin asymmetries at very high $x_F$ in transversely polarized proton collisions. However, neither of these topics are closely pertaining to the work presented in this dissertation. On the other hand, because of its large granularity, MPC can be used as a reaction plane detector and is expected to improve reaction plane resolutions.

[3]Figure courtesy to http://www.bnl.gov/rhic/news/121608/story1.asp

## 2.3 PHENIX Central Arm Detectors & Charged Particle Detection

PHENIX central arm detectors can be categorized into tracking detectors (DC, PC, ...) and particle identifying detectors (TOF, EMCal, RICH, ...). The tracking detectors are used to reconstruct charged particle trajectory based on the nominal collision vertex, the multiple hits registered on its path as well as the momentum information. The particle identifying detectors can be functioning quite differently from each other, depending on which type of particles the detector is capable of identifying. The electromagnetic calorimeter identifies neutral particles and measures their energy deposit, whereas time-of-flight detectors are responsible for identifying charged hadrons according to gathered path length and time of flight informaiton.

Some of the hadrons decay fairly quick, therefore can hardly be measured directly. At PHENIX, charged particles that can be detected directly by central arm detectors are pions ($\pi^{\pm}$), kaons ($K^{\pm}$), protons ($p$), antiprotons ($\bar{p}$), positrons ($e^{+}$) and electrons ($e^{-}$). Another important ubiquitous particles after collisions, muons ($\mu^{\pm}$), are not detected in central arm but in muon arms.

In this subsection, I will be talking about two major tracking detectors and two major particle identifying detectors that are related to my physics analysis at PHENIX. Let us start with Drift Chamber and Pad Chamber, two gaseous tracking detectors, and then move to the time-of-flight detectors in both east and west arm.

### 2.3.1 Drift Chamber (DC)

The PHENIX tracking system is built for efficiently reconstructing low-momentum particle tracks. Because of particle decays and multiple scatterings that are lingering in low$-p_T$ region, the track reconstruction process may be difficult. Moreover, the discontinuity in azimuthal acceptance of PHENIX detector would potentially introduce a large number of particles entering the active central arm detector region without traversing the Drift Chamber (DC). Therefore, DC should be used in conjunction with other tracking detectors (e.g. pad chamber) to ascertain accurate tracking reconstruction and pattern recognition.

The PHENIX Drift Chambers are made of two independent cylindrically shaped gas volumes located in both east and west arm (cf. Fig.2.1). The left panel of Fig.2.7 illustrates the structure and dimensions of one DC piece. Drift Chamber detector, as the innermost layer of PHENIX tracking system, is 2.5 meters along the beam direction and takes the cylindrical region with

inner(outer) surface 2.02(2.46) meters away from the beam pipe ($z$ axis). DC in each arm covers an azimuthal angle of $\pi/2$ and contains 20 equal sectors, each of which has a $4.5^o$ span in azimuth.

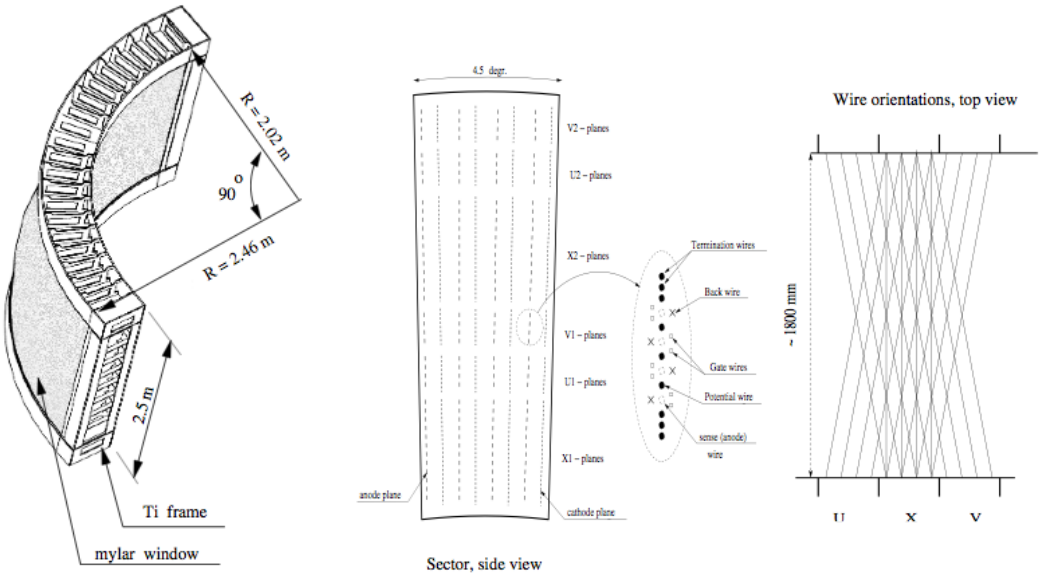


Figure 2.7: The construction of DC frame showing structure and dimensions (left); The side view of wire arrangement within one sector and inside the anode plane (middle); A top view of the $X, U, V$ wire orientation (right). Figure taken from [31]

Six types of wire modules are stacked along radial direction in each sector: $X1$, $U1$, $V1$, $X2$, $U2$ and $V2$. The layout of these wire cells are illustrated in rightmost panel of Fig.2.7. In particular, two types of $X$ wire module ($X1$, $X2$) are parallel to beam axis and they provide trajectory information in the transverse plane. $U$, $V$ wire modules are constructed in a way that are $6^o$ tilted with respect to the $X$ wires, and they measure the $z$ coordinate of the track. For each $X$ module, there are six separate wires to work collaboratively. When it comes to $U$ and $V$ module, there are four separate wires in each $U$ or $V$ module.

Within one sector, there are four anode-cathode plane pairs, as seen in the middle panel of Fig.2.7. An external high voltage is applied across each anode-cathode pair to create a strong electrical field. Charged particles that pass through the gas volume would interact with gas molecules and ionize them to free more electrons and create positve ions. Under strong electrical field, freed electrons drift to the anode wires and induce an avalance of charge

separation, which turns into a signal registered on the wire.

As stated above, $X$ wires are expected to provide trajectory information in the transverse plane. If a wire in $X$ module is triggered, the azimuthal angle of the fired wire would tell us a suspect azimuthal angle (in $x-y$ plane) for the hit. However, we cannot determine where the wire is triggered (by charged particle) along $z$ direction solely based on $X$ wire cells. Please note that there are two types of X modules, each of which consists of 6 separate wires. So we expect that six $X1$ and six $X2$ hits would provide twelve $(x, y)$ coordinate measurements in total. The $z$ coordinate can be measured with $U$ and $V$ wires, where $U, V$ modules are paired first to seek for their intersection points. These intersection points are considered as the potential $z$ coordinate measurements. Again, please recall there are four separate wires in both $X$ and $V$ modules. So we expect that four $UV1$ and four $UV2$ hits would provide eight $z$ coordinate measurements in total. These $12 \oplus 8$ coordinate options are then further refined with the help of one PC1 hit. Eventually, we end up with one $(x, y, z)$ location measurement.

### 2.3.2 Pad Chamber (PC)

The PHENIX Pad Chambers (PC) are multiwire proportional chambers with three separate layers, labeled PC1, PC2 and PC3 respetively. All of these three layers are included in the PHENIX west arm, but only two in the east arm. The PCs are the only nonprojective detectors in the central tracking system and hence are essential for pattern recognition. The locations of these layers in PHENIX central arm detector system can be found in Fig.2.1, and a nice overiew of the Pad Chambers is shown in Fig.2.8.

Each layer of PC consists of a single plane of anode wires inside a gas volume, which is sandwiched between two cathode planes, as illustrated in Fig.2.9. The cathode on top (cf. Fig.2.9) is segmented into an array of pixels. Whenever a charged particle enters the detecor and ionizes gas molecules to induce an avalanche on an anode wire, it will be picked up in form of charge (signal) induced on a few pixels. The signals are then amplified and read out via the ReadOut Card (ROC). Unlike DC, the ROC on PC is a 2D readout.

The combination use of DC and PC1 would help to determine the trajectory that passes through RICH (cf. Fig.2.1), while PC2 and PC3 can be used to resolve the ambiguities in the outer detectors (e.g. EMCal). Not all the entering tracks in outer detectors are coming from collisions at nominal vertex (*primary track*) or the very first post-collision interactions. It is suggested that nearly 1/3 of the total incoming tracks in EMCal are not primary tracks but tracks coming from either secondary interactions and decays outside the aperture of the DC and PC1, or the curved low-momentum primary tracks

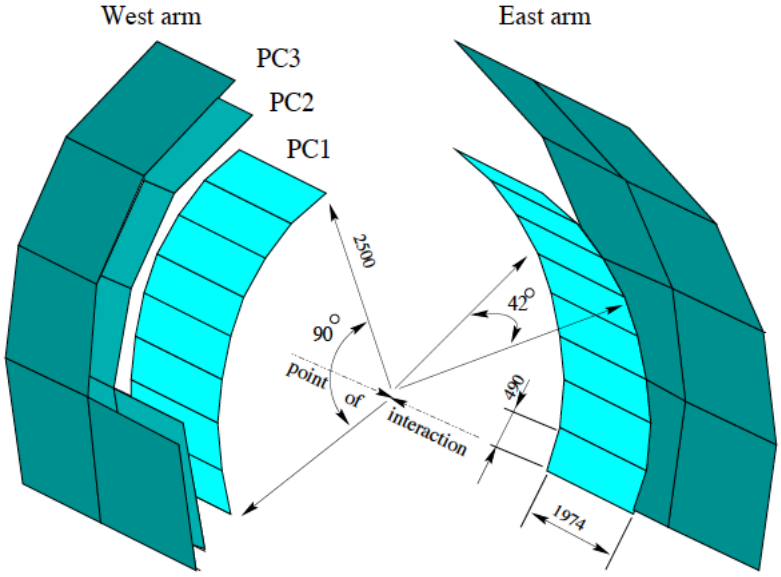


Figure 2.8: PHENIX Pad Chamber. Several sectors of PC3 and PC2 in the West arm are intentionally removed for clarity purpose. Figure taken from [32].

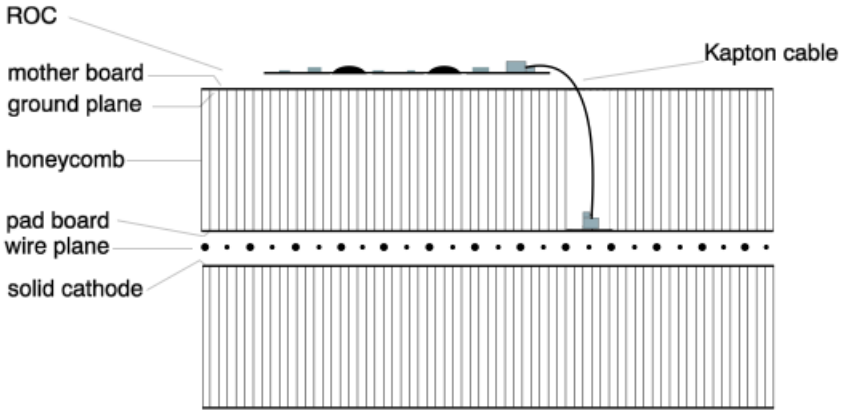


Figure 2.9: Side view of one layer of Pad Chamber. Figure taken from [31]

that bypass PC1 due to the magnetic field and hit PC2, PC3.

Thereofre, PC is essential for track reconstruction and background suppression (by imposing matching cut on PC layers).

### 2.3.3 Time-of-Flight Detector in East Arm (TOF-E)

The PHENIX Time-Of-Flight detector in east arm (TOF-E[4]), together with its western counterpart, Ring-Imaging Cherenkov (RICH) and Electromagnetic Calorimetor (EMCal) are composing the major PHENIX PID system in central arm. RICH is the primary detector for identifying electrons among large number of charged pions. The TOF is mainly applied to identify hadrons, including charged pions ($\pi^{\pm}$), kaons ($K^{\pm}$), protons ($p$) and antiprotons ($\bar{p}$). The reason for measurement of identified hadrons in a relatively wide transverse momentum ($p_T$) range is rooted in the fact that hadron production carries the fundamental information of the properties of the created nuclear matter. In this sense, TOF is crucial for the identified hadron flow analysis presented in this manuscript.

TOF basically measures the time of flight of the particle, and compare it with the momentum. Therefore, accurate measurement of the time of flight and momemtum for charged particles is essential to any subsequent PID analysis. The TOF-E is designed to have intrinsic timing resolution $\sigma \simeq 115$ ps, which allows for a $3\sigma$ $\pi/K$ separation up to 2.5 GeV/c and $3\sigma$ $K$/(anti-)proton separation up to 4 GeV/c.

The TOF-E is located between the outermost layer of the pad chambers, PC3, and the electromagnetic calorimeter (EMCal), as illustrated in Fig.2.1. It is $\sim$ 5.1 m away from the collision vertex and consists of 10 panels of TOF walls. Each wall is segmented into 96 counters and each counter includes a plastic scintillator slat and PMTs to read out at both ends. The toal 960 slats of scintillators are oriented in the $r-\phi$ direction (perpendicular to beam direction) and each of them provides time and longitudinal position information of particles that hit the slat.

### 2.3.4 Time-of-Flight Detector in West Arm (TOF-W)

Installed in Summer 2006, the west arm Time-Of-Flight (TOF-W[5]) detector adopts Multi-Gap Resistive Plate (MRPC) technology with much improved timing resolution. Compared with its counterpart, the scintillator based TOF-E detector, the timing resolution of TOF-W could reach as fast as 79 ps, over

[4]Also denoted as TOFE later in this manuscript.

[5]Also denoted as TOFW later in this manuscript.

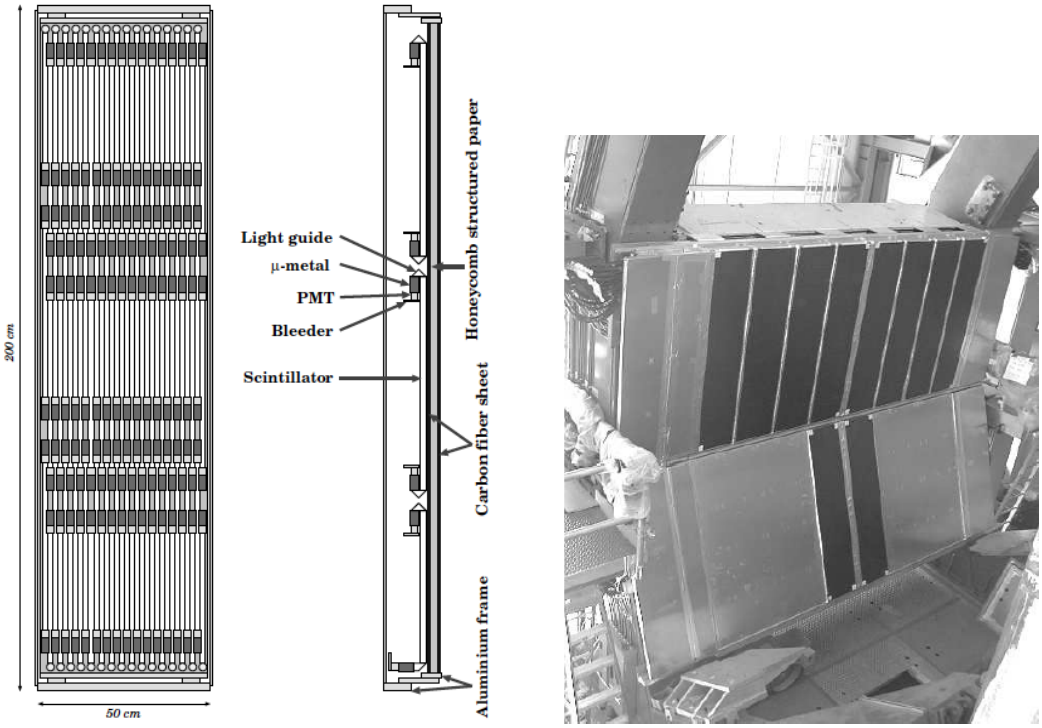


Figure 2.10: A schematic diagram of the layout of one panel of TOF wall (left); One couter cell that contains a plastic scintillator and photomultiplier tubes at both ends, light guides and supports (middle); A picture of TOF-E detector in PHENIX east arm (right). Figure taken from [33].

20 ps faster than TOF-E timing resolution, and it expands PHENIX particle identification (PID) capability up to 9 GeV.

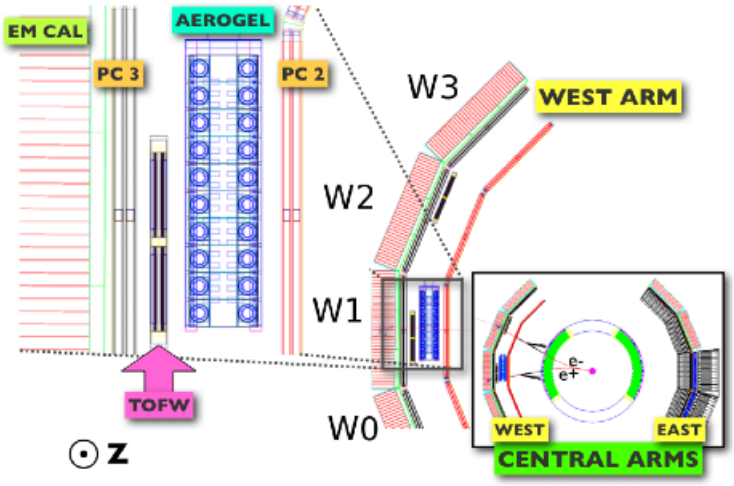


Figure 2.11: Beam view plot showing the location of west arm TOF (TOF-W) detector. Figure courtesy to B. Love.

MRPC is a gaseous ionization chamber with parallel plate structure, where track signals are fired from the charge separation of ion-induced Townsend avalanches[111]. As shown in Fig.2.12, the MRPC consists of a gaseous ion chamber that is divided into several independent gas gaps. When charged track passes through the MRPC gas chamber, charge separation is induced by minimum ionizing particles. These particles, in turn, generate clusters of electron-ion pairs by interacting with the gas molecules. A high-voltage electric field (usually $14 - 15$ kV) is applied on the active gas volume to accelerate these freed electrons (and remaining positive ions) towards the direction of the anode (and cathode). Under strong electric field, the accelerated electrons further interact with gas molecules, liberating more electrons (and positive ions). As a results, one incident ionizing particle would induce an avalanche of charge separation. Such avalanche of moving charge fires a signal. These signals, amplified with on-board electronics, are eventually extracted using pairs of copper readout pads that are positioned around the gas volume.

Since west arm TOF detector is designed and constructed fundamentally different than its east arm counterpart, it allows us to perform hadron identification in parallel within both west and east arm, using independent measurements of path length and time of flight of the charged particles. The TOF-W, in conjunction with TOF-E, provides a well-rounded extraction of hadron PID

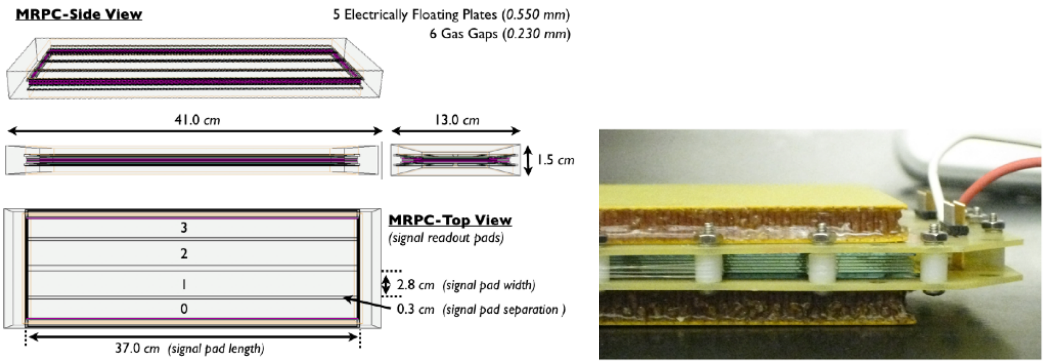


Figure 2.12: Schematic view of the active volume of the detector, which consists of six 230 $\mu m$ gas-gaps separated by five 550 $\mu m$ glass plates (left); A snapshot of MRPC (right).

information, which will surely improve the reliability of hadron flow results at PHENIX.

### 2.3.5 Charged Hadron Identification

Charged hadron identification is performed based upon calculation of particle mass via the measurements of its time of flight and momentum. Such calculated particle mass is then compared with well-accepted standard value.

Experimentally, charged hadron identification at PHENIX uses the combination of three measurements: time-of-flight from the BBC and TOF, momentum from the DC, and flight-path length from the collision vertex point to the TOF hit position. The square of mass can be calculated as

$$m^2 = \frac{p^2}{c^2}\left[\left(\frac{t_{tof}}{L/c}\right)^2 - 1\right] \tag{2.2}$$

where $p$ is the momentum, $t_{tof}$ is the time of flight, $L$ is the flight path length, and $c$ is the speed of light. The charged hadron identification is then performed using cuts in $m^2$ and momentum space, that is, $2\sigma$ standard deviation PID cuts for each particle species. Such PID cut is based on a parameterization of the measured $m^2$ width as a function of momentum.

Figure.2.13 is a 2D plot of Charge×Momentum and Mass Squared, where each hadron species is identified and framed with solid curve. It is noteworthy that three hadron branches are well separated in low momentum region. However, such separation becomes obscure for high-momentum particles, es-

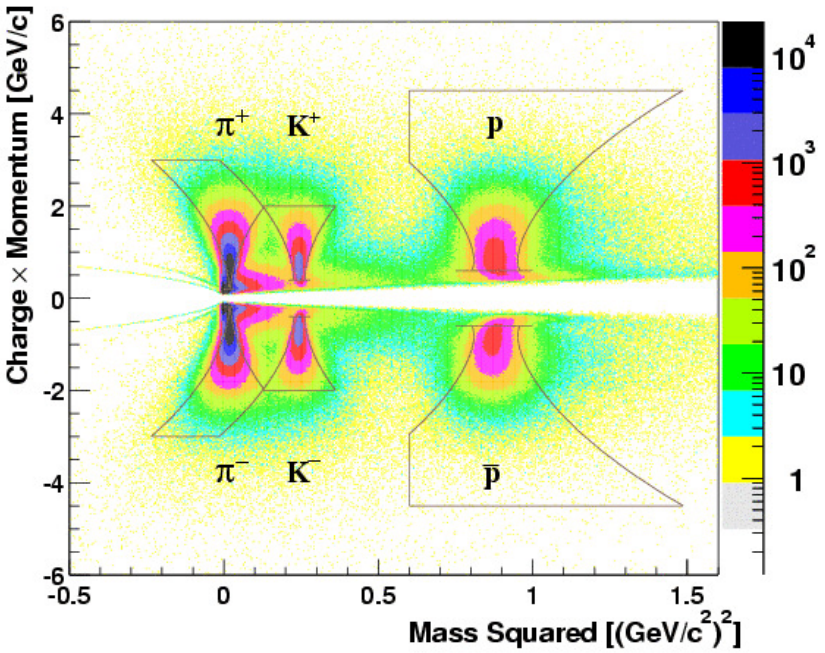


Figure 2.13: Charged hadron identification in TOF. Figure taken from [34].

pecially for charged pions and kaons. Therefore, the identifcation of charged pions and kaons are more challenging.

# Chapter 3

# Hadron Flow Measurement via Event Plane Method

Just by looking at the title of this chapter, it is fairly reasonable to think I may have digressed a little from the main subject this manuscript is presenting.

As a relatively mature approach, event plane (EP) method is widely used to measure harmonic hadron flow in PHENIX. It has developed since it was first introduced in PHENIX's earliest set of publications on flow measurements. In this sense, it deserves a chapter of discussion. Furthermore, centrality information (and other global information) is crucial for any physics analysis. It might be valuable to get ourselves acquainted with the empirical determination of these fundamental parameters, which is included in this chapter. Lastly, the flow results via EP method serve as a good base line and cross-check for the same set of results from long-range two-particle correlation method (to be presented in later chapter). Therefore, this chapter appears in this manuscript, as it is now.

This chapter is organized as follows. I will start by introducing the procedure for centrality determination, which is followed by a necessary discussion on reaction plane construction. Since event plane calibration is essential to accurate extraction of event plane orientation as well as flow signals, we will be talking briefly on that too. A set of beautiful flow results obtained via event plane (EP) method are to be presented in the end of this chapter.

## 3.1 How to Determine Centrality

One of the fundamental event signatures, centrality, can not be directly measured in experiments. In this section, we will discuss how centrality is determined experimentally. In RHIC experiments, two nuclei are having head-on

collisions at fixed center of mass collision energy. However, there is no way to control how the collision will happen (*i.e.* colllision geometry) or where the collision is going to take place (*i.e.* collision vertex). Other important quantities, such as the number of binary collisions ($N_{coll}$), the number of participating nucleons ($N_{part}$), also need to be determined in order to further concretize the collision events. Therefore, theoretical models are badly needed to help determine these geometric quantities and map them to the more abstract concept, centrality.

Among many theoretical studies, the Glauber model [69] is a powerful Monte Carlo simulation tool that successfully pictures heavy ion collisions. In the next section, we will discuss the Glauber Monte Carlo Model.

### 3.1.1 Glauber Monte Carlo Model

In the Glauber model, nucleons are assumed to travel in straight line, parallel to the trajectory of the nucleus. It is also assumed the nucleons are not scattered after colliding with other nucleons. Moreover, the wounded nucleons collide with other nucleons with the same inelastic nucleon-nucleon cross section $\sigma_{inel}$ as ordinary nucleon-nucleon collision does, *i.e.* the same cross section is used for all successive collisions.

Nucleons are populated in each nucleus following the Wood-Saxon nucleon density profile,

$$\rho(r) = \frac{\rho_0}{1 + e^{\frac{r-R}{a}}} \tag{3.1}$$

where parameter $r$ is the distance between nucleon and the gravity center of the nucleus. $\rho_0$ reflects the overall depth of the density well, which is usually fixed for all nucleons. $R$ is the radius of the nucleus. For gold (Au) nucleus, we treat it as a perfect sphere with $R$ =6.55 fm. $a$ is the diffusion coefficient and by default, it is set 0.535 fm.

In the Monte Carlo (MC) framework, the nucleons of the two Au nuclei are populated with a probability proportional to Eqn.3.1 and then simulated to "collide" by varying impact parameter $b$ randomly. A collision of two nucleons is considered as "occurred" if the distance between them, $d$, satisfies

$$\pi d^2 < \sigma_{inel}$$

Such "yes-or-no" binary treatment of collision occurrence can be softened by alternatively imposing, for example, a continuous probability function in the form of $1 - [1 - 0.755e^{-0.89b^2}]^2$ or a discrete probability of $\sigma_{inel}/\sigma_{total}$ if $d < \sqrt{\sigma_{total}/\pi}$ [112].

The variability in judgment of collision occurrence introduces additional

factors that need to be taken into account when estimating systematic uncertainties in our simulations. As such, we assign a ±3 mb uncertainty in the cross section of nucleon-nucleon inelastic collision, $\sigma_{inel}$. It is noteworthy that due to different center of mass collision energies, $\sigma_{inel}$ can vary accordingly. $\sigma_{inel}$ is found as 34 mb, 37mb, 42 mb at $\sqrt{s_{NN}}$ = 39, 62.4 and 200 GeV, respectively [35, 36].

$N_{part}$ can be further determined by the total number of wounded nucleons (the nucleons that have suffered from at least one inelastic nucleon-nucleon collision) and $N_{coll}$ is just the total number of participating nucleon pairs that are involved in one simulation event. Other geometric quantities, such as standard eccentricity, participant eccentricity (cf. Eqn.1.5) can also be computed.

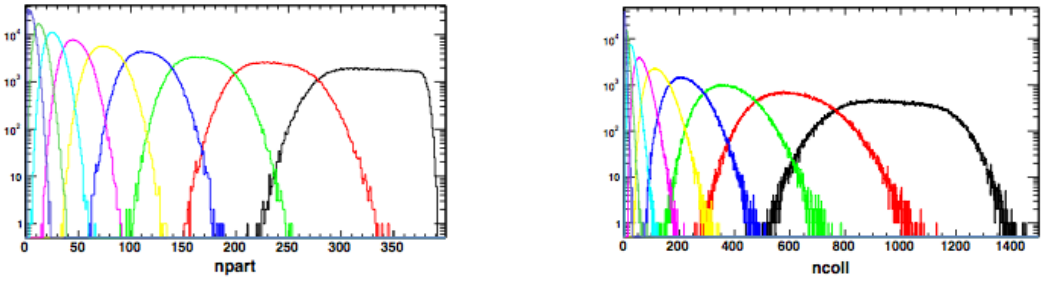


Figure 3.1: $N_{part}$ distributions in 10% centrality step at $\sqrt{s_{NN}}$ = 200 GeV (left); $N_{coll}$ distributions in 10% centrality step at $\sqrt{s_{NN}}$ = 200 GeV (right) [35].

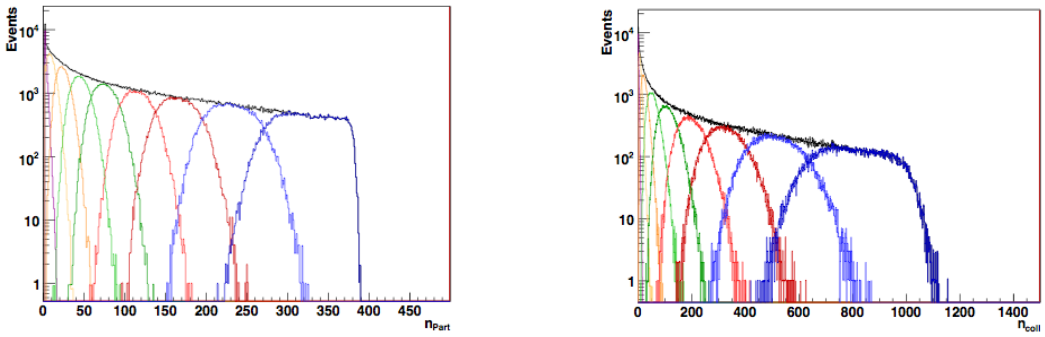


Figure 3.2: $N_{part}$ distributions in 10% centrality step at $\sqrt{s_{NN}}$ = 62 GeV (left); $N_{coll}$ distributions in 10% centrality step at $\sqrt{s_{NN}}$ = 62 GeV (right) [36].

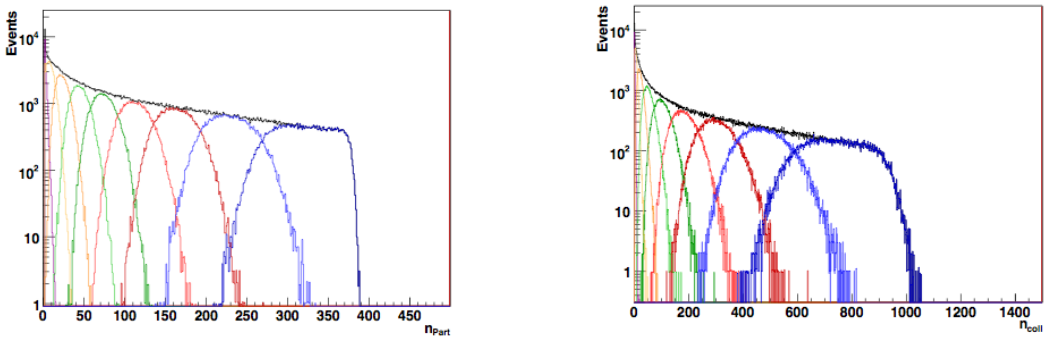


Figure 3.3: $N_{part}$ distributions in 10% centrality step at $\sqrt{s_{NN}} = 39$ GeV (left); $N_{coll}$ distributions in 10% centrality step at $\sqrt{s_{NN}} = 39$ GeV (right) [36].

The MC Glauber simulation results are necessary for subsequent trigger efficiency study and centrality definition (cf. Sec.3.1.2, 3.1.3). In particular, the MC Glauber simulated charge distributions or $N_{hit}$ distributions in different detectors[1] are to be tuned to match experiment data, hence the integrated trigger efficiency can be found and will be treated as maximum centrality value. When centrality is defined, each simulated event can be categorized into certain centrality class (e.g. 10-20% centrality class) and centrality-averaged geometric quantities, such as $\langle N_{part} \rangle$ and $\langle N_{coll} \rangle$, can also be computed accordingly over events tagged with the same centrality class.

Figure.3.1 - 3.3 show the $N_{part}$ and $N_{coll}$ distributions in 10% centrality step for $\sqrt{s_{NN}} = 200$, 62.4 and 39 GeV, respectively. Each color represents the geometric quantity in one centrality class, from the most central (corresponds to largest $N_{part}$ value range) to the most peripheral case. It is noteworthy that both $N_{part}$ and $N_{coll}$ distributions may overlap in neighboring centrality bins, which is due to the fluctuations embedded in collision profile.

The averaged Glauber parameter values are tabulated in Table.3.1-3.3 for $Au + Au$ collisions at $\sqrt{s_{NN}} = 200$, 62.4 and 39 GeV, respectively. One remark on $\langle N_{part} \rangle$ is its great usefulness in describing centrality. Since $\langle N_{part} \rangle$ directly links to centrality, it is widely used as an alternative representation of centrality in many physics results showing observable's centrality dependence.

[1]For $Au + Au$ collisions at $\sqrt{s_{NN}}$ =200 GeV, BBC charge distributions are used. However, at $\sqrt{s_{NN}}$ =62.4 and 39 GeV, PC1-hits, PC3-hits, RXI-charge and RXO-charge distributions are used because of our assumption that number of hits in the detector is only dependent on centrality. This is not true for BBC at low beam energies of 39 and 62.4 GeV.

| centraltiy | $\langle N_{coll} \rangle \pm S.E_{N_{coll}}$ | $\langle N_{part} \rangle \pm S.E_{N_{part}}$ | $\langle T_{AuAu} \rangle (mb^{-1}) \pm S.E_{T_{AuAu}}$ |
|---|---|---|---|
| 0-5% | 1067±107.7 | 350.8±3.092 | 25.4±1.855 |
| 5-10% | 857.8±85.45 | 301.7±4.655 | 20.42±1.466 |
| 10-15% | 680.2±67.26 | 255.7±5.426 | 16.19±1.136 |
| 15-20% | 538.7±52.39 | 216.4±5.619 | 12.83± 0.8909 |
| 20-25% | 424.4±40.37 | 182.4±5.743 | 10.11±0.7354 |
| 25-30% | 330.9±32.68 | 152.7±5.903 | 7.879± 0.6079 |
| 0-10% | 960.2±96.14 | 325.8±3.81 | 22.86±1.642 |
| 10-20% | 609.5±59.81 | 236.1±5.517 | 14.51±1.012 |
| 20-30% | 377.6±36.39 | 167.6±5.811 | 8.991±0.6677 |
| 30-40% | 223.9±23.2 | 115.5±5.841 | 5.332±0.4564 |
| 40-50% | 124.6±14.94 | 76.15±5.502 | 2.968±0.322 |
| 50-60% | 63.9±9.359 | 47.07±4.726 | 1.521±0.2123 |
| 60-70% | 29.75±5.41 | 26.72±3.669 | 0.7083 ±0.1264 |
| 70-80% | 12.55±2.822 | 13.67±2.492 | 0.2988±0.06695 |
| 80-93% | 4.688±1.252 | 6.153±1.359 | 0.1116±0.02998 |

Table 3.1: Glauber parameters with systematic uncertainties for different centralities in $Au + Au$ collision at $\sqrt{s_{NN}} = 200$ GeV [35].

| centraltiy | $\langle N_{coll} \rangle \pm S.E_{N_{coll}}$ | $\langle N_{part} \rangle \pm S.E_{N_{part}}$ | $\langle T_{AuAu} \rangle (mb^{-1}) \pm S.E_{T_{AuAu}}$ |
|---|---|---|---|
| 0-10% | 843±100.5 | 319.6±4.093 | 22.78±2.062 |
| 10-20% | 535.8±58.1 | 229.7±4.501 | 14.48±1.204 |
| 20-30% | 337.2±32.89 | 163.8±4.99 | 9.113±0.6774 |
| 30-40% | 203.3.±20.07 | 113.4±4.711 | 5.496±0.4193 |
| 40-50% | 114.3±11.83 | 74.64±3.659 | 3.09±0.2636 |
| 50-60% | 57.78±6.693 | 45.19±3.358 | 1.561±0.1783 |
| 60-70% | 25.2±3.538 | 24.06±2.559 | 0.6811 ±0.1022 |
| 70-86% | 6.608±0.7984 | 8.034±0.7579 | 0.1786±0.02448 |

Table 3.2: Glauber parameters with systematic uncertainties for different centralities in $Au + Au$ collision at $\sqrt{s_{NN}} = 62$ GeV [36].

| centraltiy | $\langle N_{coll} \rangle \pm S.E_{N_{coll}}$ | $\langle N_{part} \rangle \pm S.E_{N_{part}}$ | $\langle T_{AuAu} \rangle (mb^{-1}) \pm S.E_{T_{AuAu}}$ |
|---|---|---|---|
| 0-10% | 777.2±94.99 | 316.6±4.346 | 22.86±2.032 |
| 10-20% | 496.7±54.84 | 227.2±5.273 | 14.61±1.171 |
| 20-30% | 313.8±31.91 | 161.7±5.377 | 9.23±0.6879 |
| 30-40% | 191±21.16 | 112.2±4.491 | 5.619±0.4666 |
| 40-50% | 108.1±12.74 | 73.77±4.181 | 3.18±0.3117 |
| 50-60% | 55.39±6.291 | 44.83±3.17 | 1.629±0.1833 |
| 60-70% | 24.15±4.385 | 23.68±3.298 | 0.7104 ±0.1369 |
| 70-86% | 6.198±1.404 | 7.71±1.362 | 0.1823±0.04345 |

Table 3.3: Glauber parameters with systematic uncertainties for different centralities in $Au + Au$ collision at $\sqrt{s_{NN}} = 39$ GeV [36].

### 3.1.2 Trigger Efficiency Study

The major step in determining centrality is to map Monte Carlo simulations onto collected data, where trigger efficiency needs to be studied first and centrality can be defined afterwards.

In experiments, only events considered "useful" for physics analysis are recorded because of hardware and storage space limitations in data acquisition (DAQ) system. As such, event triggers are necessary to help select those "good" physics events from a large number of collision events. At PHENIX, triggers are existing in both global and local level, that is, Global Level 1 trigger (GL1) and many Local Level 1 (LL1) triggers. Among the local triggers, LL1 trigger on BBC and ZDC are the most important ones for event selection. For example, BBC LL1 is triggered when one or more hits detected in both south and north arm of the BBC, which is a crucial requirement in selecting meaningful events.

| Run Year | Collision Energy | MB Event Requirements |
|---|---|---|
| Run 10 | $\sqrt{s_{NN}} = 62.4$ GeV | 1) at least two hits in both arms of the BBC |
| | $\sqrt{s_{NN}} = 39$ GeV | 2) vertex position $\lvert z \rvert < 30$ cm |
| Run 7 | $\sqrt{s_{NN}} = 200$ GeV | 1) at least two hits in both arms of the BBC<br>2) ZDC hits required Level 1 live bit |

Table 3.4: Minimum bias (MB) event requirements in $Au + Au$ collisions from run year 2010 and 2007 at PHENIX.

Trigger efficiencey is defined based on the minimum bias (MB) events. As you can tell from the name, MB events are those collisions with no bias from

restricted trigger conditions. For Run7 $Au+Au$ collisions at $\sqrt{s_{NN}}$ =200 GeV and Run 10 $Au+Au$ collisions at $\sqrt{s_{NN}}$ = 62.4 and 39 GeV, a MB event is defined by the requirements listed in Table.3.4.

Since the integrated trigger efficiency for all MB events is considered as the upper bound of centrality (*i.e.* maximum centrality among all collisions), the determination of trigger efficiency is essential to centrality definition. In trigger efficiency study, the following steps are needed,

1. Hit distributions in PC1, PC3 or charge distribution in the inner/outer ring of RxNP (RXI, RXO) and BBC are obtained from experiments[2].

2. Simulate to obtain the hit distributions in correponding detectors.

   (a) In Monte Carlo Glauber model, we first simulate to have $N_{part}$ distributions. These $N_{part}$ distributions are further normalized to obtain the probability distributions of $N_{part}$, *i.e.* the probability of an event whose number of participants equals $N_{part}$ is known.

   (b) We assume that the number of hits in detectors follows the statistics of negative binomial distribution (NBD) [113].

   (c) The simulated hit distribution is the convolution of the probability distribution of $N_{part}$ and NBD, that is, for each simulated event of $N_{part}$ with probility $P(N_{part})$, the total number of hits $N_{hit} = \Sigma_{i=1}^{N_{part}} h_i$, where $h_i$ is the hits from the $i^{th}$ nucleon generated from NBD.

3. Tune NBD parameters to have the simulated $N_{hit}$ distributions reproduce data at the large $N_{hit}$ region.

4. Calculate the integrated trigger efficiency as the ratio of the total number of events from real data (with missing events) and total number of events from simulation (without missing events).

Following this prescription, one remark on its underlying assumptions might be worth mentioning:

- The simulated $N_{part}$ distribution is assumed to reflect real $N_{part}$ distribution from experiment and is used as an input to subsequent trigger efficiency study.

[2]Hereinafter, I shall not explicitly distinguish between hit and charge distribution, since they are, in principle, pointing to the same object, $N_{part}$, and the procedure for trigger efficiency study based on them are same.

- Each nucleon incurs hits in the detector independently from any other participanting nucleons.
- The number of total hits of an event is just the linear sum of hits incurred by each individual nucleons.
- The number of hits ($N_{hit}$) created by a single participating nucleon follows NBD statistics with parameters $\mu$ and $k$, where $\mu$ is the mean of the distribution and variance of NBD is given by $\sigma_{NBD} = \mu + \frac{\mu^2}{k}$.
- The $\eta-$distribution does not vary significantly with centrality, *i.e.* $N_{hit}$ is dependent on centrality.

Another remark I would like to address is in step (3) above, the matching is done at high $N_{hit}$ (or high charge, similarly hereinafter), where we have assumed that all collisions are picked up by the detector at high enough multiplicity, that is, efficiency is 100% in central collisions. Note that when matching is performed in high $N_{hit}$ region, the MC Glauber simulations will end up with higher values (than experiment data) in small $N_{hit}$ region. The reason is that in low $N_{hit}$ end, current interested detector does not have 100% efficient and thus misses some fraction of events. This is where trigger efficiency calculation in step (4) comes in.

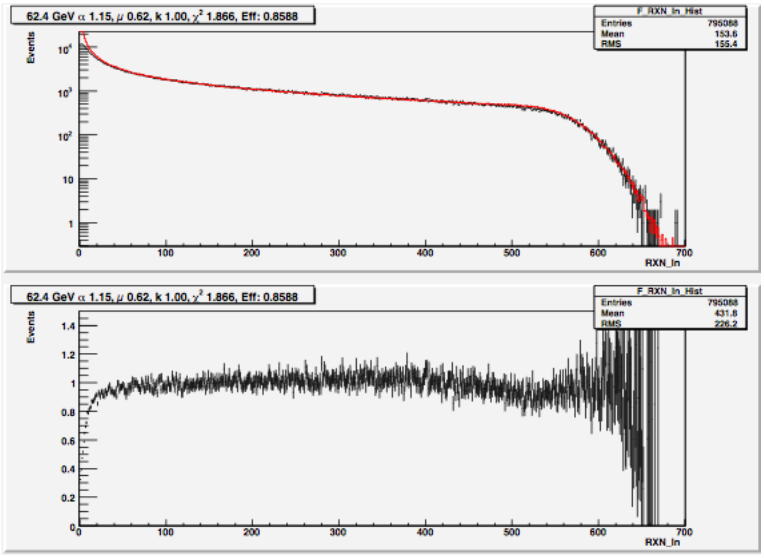


Figure 3.4: An example of a NBD-fit to the scaled summary charge distribution in RXI detector for BBC-Z vertex cut $|z| < 5$ cm and BBCLL1 ($> 1$ tubes) (upper); the resulting efficiency function (bottom) [37].

The upper panel of Fig.3.4 includes an example of NBD-fit to the scaled summary charge distribution in the inner ring of RxNP detector for BBC $z-$vertex cut $|z| < 5$ cm and BBCLL1 ($> 1$ tubes). The bottom panel shows the correponding efficiency function plotted vs. RXI scaled summary charge. The red curve in upper panel represents MC simulation result and clearly overshoots the black curve from experiment in the lower charge end. Consequently, the trigger efficiency in bottom panel illustrates the ratio is consistent with 1 in large charge region, however it drops in the lower end too, which indicates the loss of efficiency and possible event missing in this region.

The total trigger efficiency (or integrated trigger efficiency) in different detectors may vary a little. The overall percentage efficiency value is estimated from these trigger efficieny studies. The systematic uncertainties are evaluated based on the variation of the inelastic scattering cross-section and the Woods-Saxon radius and diffusiveness parameters. In summary, the percentage efficiency values are $85.9 \pm 2.0$ for $\sqrt{s_{NN}}$ =39 GeV and $85.7 \pm 2.0$ for $\sqrt{s_{NN}}$ =62.4 GeV, and $93 \pm 2.0$ for $\sqrt{s_{NN}}$ =200 GeV.

### 3.1.3 Centrality Determination for Experiment Data

MC Glauber simulation study provides us with a great baseline as to what the largest possible centrality value would be in experiments, a very important piece of information that, by no means, could ever be directly measured. In light of Glauber simulations and subsequent trigger efficiency study, the integral trigger efficiency obtained is rounded to integer as the maximum centrality value and total number of centrality divisions. For $\sqrt{s_{NN}}$ =39 and 62.4 GeV, the total number of centrality divisions is 86, and for $\sqrt{s_{NN}}$ =200 GeV, the value is 93.

The centrality definition is fairly straightforward via BBC percentile method. Figure.3.5 shows the BBC total charge distribution from $Au + Au$ collisions at $\sqrt{s_{NN}}$ =62.4 GeV in run year 2010. The total charge distribution in BBC is obtained from MB events. It is then chopped evenly into many slices, each of which includes roughly the same number of events. For $\sqrt{s_{NN}}$ =39 GeV and 62.4 GeV, the total BBC charge distribution is divided into 86 slices, for $\sqrt{s_{NN}}$ =200 GeV, into 93 slices. The partition process is going "backwards" on BBC charge distribution, that is, starting from the rightmost bin with the highest BBC charge value all the way to the leftmost bin with lowest BBC charge value. To be more specfic, event counts are summed up bin by bin on BBC charge distribution from the highest charge bin towards lower charge bin, until the accumulated number of events reaches 1/86 of the total number of events. Then the current bin and its BBC charge value is recorded so that any events with BBC charge higher than this value will be tagged with centrality

1%. This process continues untill all the delimiters are found.

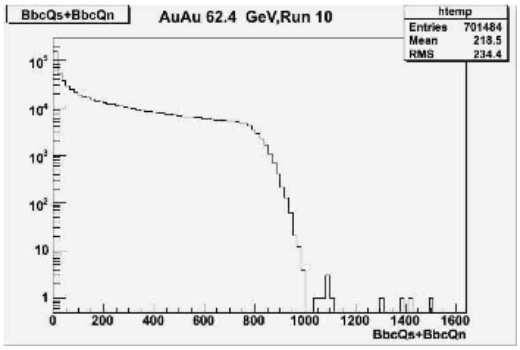


Figure 3.5: BBC total charge distribution for $Au$+$Au$ collisions at $\sqrt{s_{NN}}$ =62.4 GeV, with $|z| < 5$ cm [37].

To reduce discretization error associated with the partition process, the BBC charge distribution is usually built on very fine binning canvas. For $\sqrt{s_{NN}}$ =200 GeV, an acceptable bin width of 0.1 is suggested. Because of charge signal deposited in BBC at lower beam energies is less, bin width of 0.01 is reasonable at $\sqrt{s_{NN}}$ =39 and 62.4 GeV.

Another important heads up is that BBC charge distributions may vary as the collision vertex $z$ changes from -30 to 30 cm. Therefore, centrality definition needs be done separately for each vertex $z$ class. The $z$ values for all MB events are within ±30 cm of the nominal collision vertex, and usually this range is chopped into 12 equally spaced vertex class, each of 5 cm length. Centrality definition is then performed for events in each of these 12 vertex classes.

## 3.2 The Reconstruction of Reaction Plane - Event Plane

A schematic view of reaction plane can be found in Fig.1.4 from Chapter One. The reaction plane[3] (usually denoted by $\Psi_n$ or $\Psi_{RP}$) is defined as the plane of the impact parameter and beam axis. Under pressure gradient, the initial spatial anisotropy of the collision profile is quickly converted into final momentum space anisotropy of particle production if the medium is rapidly thermalized. It is found that usually more particles are emitted along the in-plane direction than the out-of-plane direction, resulting in the so called anisotropic flow. The

[3]Sometimes interchangeably referred to as *true event plane* or *true reaction plane*.

ansiotropic flow observable reflects the correlation between individual tracks (emitted particles) and the direction of the impact parameter (represented as reaction plane angle) in a collision. Unfortunately, reaction plane can not be directly measured. Moreover, due to limited number of participating nucleons, fluctuations of colllision profile would induce a rather "lumpy" structure that consists of a few components, each with its own orientation and tagged with corresponding order (cf. Fig.1.21 in Chapter One). Therefore, the concept of (observed) event plane $\Phi_n$ is introduced as a reconstruction/estimation of reaction plane.

In this section, the principles and procedures for $\Phi_n$ construction are going to be discussed.

### 3.2.1 Event Planes in Experiments

The (observed) event plane (EP) orientation $\Phi_n$ can be measured from the detected particles in a certain rapidity range or the response of a particular detector. To reduce possible auto-correlations in flow measurement for central arm tracks, particles used to construct event planes are usually tracks at large $|\eta|$.

The $n^{th}-$order EP angle $\Phi_n$ is estimated using the so-called "flow vector" ($Q$-vector), which is a two-component vector defined in the transverse plane [114].

$$\begin{aligned} \boldsymbol{Q_n} &= (Q_{n,x}, Q_{n,y}) \\ &= (Q_n \cos(n\Psi_n), Q_n \sin(n\Psi_n)) \\ &= \left( \sum_i \omega_i \cos(n\phi_i), \sum_i \omega_i \sin(n\phi_i) \right) \end{aligned} \tag{3.2}$$

and the $n^{th}$-order event plane angle $\Phi_n$ is

$$\Phi_n = \tan^{-1}\left(\frac{Q_{n,y}}{Q_{n,x}}\right)/n = \tan^{-1}\left(\frac{\sum_i \omega_i \sin(n\phi_i)}{\sum_i \omega_i \cos(n\phi_i)}\right)/n \tag{3.3}$$

where the sum runs over all possible tracks, towers (cells grouped into a narrow $\eta - \phi$ region) or all detector segments/pixels; $\phi_i$ is the azimuthal angle of the $i^{th}$ element and $\omega_i$ is the associated weighting factor chosen to optimize the event plane resolution, which might be just "1" or the $p_T$ for a track, the gain for a detector segment or the transverse kinetic energy for a tower in certain detector. By construction, flow vector $\boldsymbol{Q_n}$ has an intrinsic $n-$fold symmetry, thus the event plane angle $\Phi_n$ determined from the $n^{th}-$order harmonic is in

the range $-\phi/n \leq \Phi_n < \pi/n$.

### 3.2.2 Event Plane Resolution Corrections

As stated above, the estimated reaction plane is defined as the event plane. Due to finite multiplicity in nuclear collisions, the event plane can be different from the reaction plane. Therefore, understanding the dispersion is essential to $v_n$ measurement. On the other hand, the observed raw $v_n$, $v_{n,raw}$, for a given centrality range must always be corrected up by the event plane resolution to account for the difference between reaction plane and event plane.

The event plane resolution factor comes in when we correlate individual tracks with observed event plane, which can be seen from the following trivial trigonometric manipulation,

$$\begin{aligned}
& \langle \cos\left(n(\phi - \Phi_n)\right)\rangle \\
= \; & \langle \cos\left(n(\phi - \Psi_n) - n(\Phi_n - \Psi_n)\right)\rangle \\
= \; & \langle \cos\left(n(\phi - \Psi_n)\right)\cos\left(n(\Phi_n - \Psi_n)\right)\rangle + \langle \sin\left(n(\phi - \Psi_n)\right)\sin\left(n(\Phi_n - \Psi_n)\right)\rangle \\
= \; & \langle \cos\left(n(\phi - \Psi_n)\right)\rangle \langle \cos\left(n(\Phi_n - \Psi_n)\right)\rangle + \langle \sin\left(n(\phi - \Psi_n)\right)\rangle \langle \sin\left(n(\Phi_n - \Psi_n)\right)\rangle \\
= \; & \langle \cos\left(n(\phi - \Psi_n)\right)\rangle \langle \cos\left(n(\Phi_n - \Psi_n)\right)\rangle \qquad (3.4)
\end{aligned}$$

where the average "$\langle\ \rangle$" runs over all tracks in all collision events and we have assumed the absence of auto-correlations between $\phi$ and $\Phi_n$ so that

$$\langle \cos\left(n(\phi - \Psi_n)\right)\cos\left(n(\Phi_n - \Psi_n)\right)\rangle = \langle \cos\left(n(\phi - \Psi_n)\right)\rangle \langle \cos\left(n(\Phi_n - \Psi_n)\right)\rangle$$

can be valid. This is assumption roughly holds if $\phi$ and $\Psi_n$ are measured with large $\eta$ separation.

The real $v_n$ is then obtained by re-arranging Eqn.3.4,

$$v_n = \langle \cos\left(n(\phi - \Psi_n)\right)\rangle = \frac{\langle \cos\left(n(\phi - \Phi_n)\right)\rangle}{\langle \cos\left(n(\Phi_n - \Psi_n)\right)\rangle} = \frac{v_{n,raw}}{Res\{\Phi_n\}} \qquad (3.5)$$

where, the estimated $n^{th}$-order *event plane resolution* is defined as

$$Res\{\Phi_n\} = \langle \cos\left(n(\Phi_n - \Psi_n)\right)\rangle \qquad (3.6)$$

Note that the $v_{n,raw} = \langle \cos\left(n(\phi - \Phi_n)\right)\rangle$ can be directly measured and of course, reliable extraction of the flow harmonic coefficients requires accurate determination of event plane resolution ($Res\{\Phi_n\}$), which is usually estimated from the correlation of the planes of independent sub-events.

### 3.2.3 Sub-events & Event Plane Construction

Because of the limited resolution in the angle of measured event plane, the raw flow harmonic coefficients $v_n$ must be corrected up to what they would be relative to the real reaction plane. Such correction factor is known as event plane resolution (cf. Eqn.3.6). The key step in event plane construction is to find its resolution factor, which is usually done by the correlation from the planes of independent sub-events.

A sub-event refers to a sub-group of the particles used for the event plane determination. It could be a collection of tracks in a certain rapidity range, such as the hits in the south/north arm of RxNP, or the hits in south/north arm of BBC.

The event plane resolution [115] can be expressed as

$$Res\{\Phi_n\} = \frac{\sqrt{\pi}}{2\sqrt{2}}\chi_n e^{-\chi_n^2/4} \times \left[ I_{(k-1)/2}\left(\frac{\chi_n^2}{4}\right) + I_{(k+1)/2}\left(\frac{\chi_n^2}{4}\right)\right] \tag{3.7}$$

where $\chi$ is a real parameter that characterizes the accuracy of the reaction plane determination, and scales with $N$ (multiplicity) like $\sqrt{N}$ [116]. $I_k$ is the modified Bessel function of order $k$. Usually, $k = 1$ for BBC and RxNP events. It is suggested that for the ZDC-SMD[4] event plane the resolution is estimated with both $k = 1$ and $k = 2$ [117]. It is noteworthy that $Res\{\Phi_n\}$ is a monotonically increasing function of $\chi_n$, which guarantees the feasibility of resolution extraction at a given known $\chi_n$.

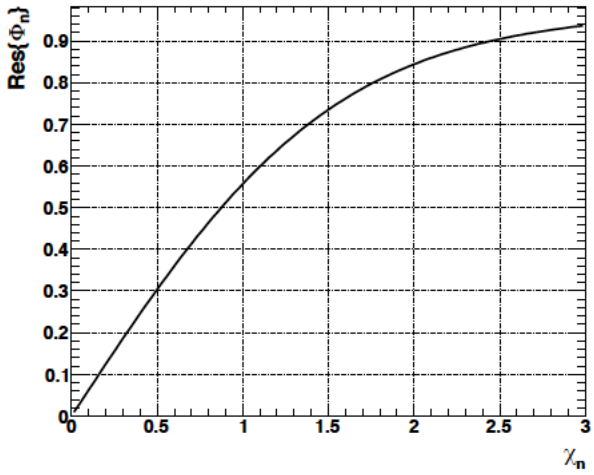


Figure 3.6: Event plane resolution as a function of $\chi_n$ [38].

[4]Abbreviation for shower maximum detector.

A nice plot showing how EP resolution varies with $\chi_n$ can be found in Fig.3.6. An almost linear increasing trend of $Res\{\Phi_n\}$ is observed when $\chi_n$ is small (weak flow end), and $Res\{\Phi_n\}$ slowly approaches 100% as $\chi_n$ increases (strong flow end).

### Two-subevents Method

The event plane resolution for $v_n$ can be evaluated by the two-subevents method. To this end, $\chi_n$ needs to be determined first. The most widely used method to find $\chi_n$ is to divide each event randomly into two subevents, each of which contains half of the total particles. This is particularly prevalent in PHENIX. Since most of the detectors used to determine reaction plane in PHENIX (e.g. RxNP, BBC, ZDC-SMD, etc) have both south and north arm with approximately same $|\eta|$ coverage, the event plane constructed based upon each sub-event is roughly the same. Consequently, if the performances of the two sub-detectors are same, the event plane resolution of each sub-detector (sub-event) is expected to be the same too, that is, $Res\{\Phi_n^{north}\} = Res\{\Phi_n^{south}\}$. Thus, the sub-event resolution for South and North event planes can be written as

$$Res\{\Phi_n^{south(north)}\} \equiv \left\langle \cos\left(n(\Phi_n^{south(north)} - \Psi_n)\right)\right\rangle = \sqrt{\langle \cos\left(n(\Phi_n^{south} - \Phi_n^{north})\right)\rangle} \tag{3.8}$$

where, $\Phi_n^{south(north)}$ denotes the event plane determined by the sub-event in south (north) arm. From Eqn.3.8, the subevent resolution $Res\{\Phi_n^{south(north)}\}$ can be obtained, which is further used to extract $\chi_n^{sub}$ via Eqn.3.7. Since $\chi_n$ scales like $\sqrt{N}$, $\chi_n$ for the full event is just $\chi_n^{full} = \sqrt{2}\chi_n^{sub}$. This is then plugged back into Eqn.3.7 to give the full event resolution, $Res\{\Phi_n\}$ .

Alternatively, $\chi_n^{sub}$ can be extracted by fitting the measured distribution of $\Delta\Phi_n = |\Phi_n^{south} - \Phi_n^{north}|$. The distribution of $\Delta\Phi_n$ follows,

$$\frac{dN}{d(n\Delta\Phi_n)} = \frac{e^{-\chi_n^{sub^2}}}{2}\left\{\frac{2}{\pi}\left(1+\chi_n^{sub^2}\right) + z\left[I_0(z)+L_0(z)\right] + \chi_n^{sub^2}\left[I_1(z)+L_1(z)\right]\right\} \tag{3.9}$$

where $z = \chi_n^{sub^2}\cos(n\Delta\Phi_n)$, $I_n$ is the $n^{th}$-order modified Bessel function and $L_n$ is the modified Struve function. Note that $\Delta\Phi_n$ is defined in $[-2\pi/n, 2\pi/n)$. Usually a normalization is performed so that the distribution becomes probability density function. Once $\chi_n^{sub}$ is obtained, the full $\chi_n$ and the resolution factor of full event can be subsequently found.

An example of $\Delta\Phi_n$ distribution contructed by south and north arm of RxNP along with the fit by Eqn.3.9 can be found in Fig.3.7. The data from 0-5% most central collisions are well represented by the analytical expres-

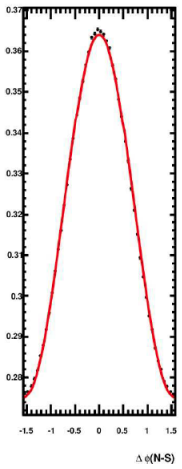


Figure 3.7: Distribution of $\Delta\Phi_2$ measured from south and north arm of RxNP in $Au + Au$ 0-5% collisions at $\sqrt{s_{NN}}$ =62.4 GeV. Red curve indicates the fit by Eqn.3.9. [38].

sion, except it undershoots the probability at $|\Delta\Phi_n| \sim 0$ and overshoots at $|\Delta\Phi_n| \sim \pi/2$. It is also found such deviation becomes more notable in mid-central collisions (20-40%) and diminishes back as the collisions turn into more peripheral. Interestingly, this trend is similar to what is observed in centrality dependence of resolution factor. It is expected that the lower beam energy, the less multiplicity there is, hence the worse event plane resolution factor would be and accordingly, the deviation between the fit (by Eqn.3.9) and data becomes less prominent.

The two methods serve to provide supplementary measurement of $\chi_n^{sub}$ for event plane resolution study and the agreement there is impressive.

### Further Discussions

Since two-subevent method relies on the assumption of equal resolution contributions from both sub-detectors and the validity of Gaussian fluctuations (*i.e.* Eqn.3.7), it may be useful to have it cross checked with other methods. Other than the two-subevents method mentioned above, a so-called **three-subevents method** which includes more than two subevents in determining event plane resolution is also employed, and it gives consistent resolution measurement. The three-subevent is used to find $Res\{\Phi_n^A\}$ of a given detector $A$ by correlating its estimated event plane with two other reference detectors ($B$

and $C$) that sit at different $\eta$ window,

$$Res\{\Phi_n^A\} = \sqrt{\frac{\langle\cos(n(\Phi_n^A - \Phi_n^B)\rangle \langle\cos(n(\Phi_n^A - \Phi_n^C)\rangle}{\langle\cos(n(\Phi_n^B - \Phi_n^C)\rangle}} \tag{3.10}$$

The three-subevents method allows us to calculate any sub-detector resolution factor directly without prior knowledge of $\chi_n^{sub}$, hence it is model independent. Moreover, for a given sub-detector $A$, $B$ and $C$ can be chosen freely so that independent estimates of $Res\{\Phi_n^A\}$ from different combinations of $B$ and $C$ leads to a fairly robust measurement of $Res\{\Phi_n^A\}$. However, there are two caveats worth mentioning:

1. Accurate extraction of $Res\{\Phi_n^A\}$ requires careful choice of $B$ and $C$. Poor resolution of reference detectors may result in large uncertainties in $Res\{\Phi_n^A\}$.

2. To avoid unwanted correlations (e.g. auto-correlations) and suppress non-flow effects (e.g. jet-bias), there should be sufficiently large $\eta$ separation between any two sub-detectors.

Since jet clusters in a sizable azimuth and rapidity range, particles with small $\phi - \eta$ separation are very likely from the same jet cone and thus are correlated. The two-subevents method usually selects two sub-detectos that are well separated in $\eta$ (e.g. from south and north arm components of a detector), hence jet-biased correlation is considered negligibly small. In the three-subevents method however, two of the three sub-detectors are located in the same arm, therefore large $\eta$ gap between them is badly needed and jet correlation has to be carefully assessed.

The two-subevents and three-subevents method for measuring event plane resolution have been widely used in PHENIX, where $Res\{\Phi_n^{north}\} = Res\{\Phi_n^{south}\}$ is generally assumed for detectors having both south and north arm components. However, we have already known from Chapter Two that some of the important global detectors in PHENIX (e.g. MPC) do not have completely same design for their south and north sub-detector. Additionally, due to dead segment or detector glitch, some part of the detector may not fully function as expected, hence $Res\{\Phi_n^{north}\} = Res\{\Phi_n^{south}\}$ sometimes does *not* hold.

To take into account the possible performance difference in south and north arm component of a detector, a so-called **effective three-subevents method** is developed. This method introduces the event plane in central arm (CNT),

$Res\{\Phi_n^{CNT}\}$, as an intermediate. It is not difficult to show that

$$\frac{\left\langle \cos\left(n(\Phi_n^{south} - \Phi_n^{CNT})\right)\right\rangle}{\left\langle \cos\left(n(\Phi_n^{north} - \Phi_n^{CNT})\right)\right\rangle} = \frac{Res\{\Phi_n^{south}\}Res\{\Phi_n^{CNT}\}}{Res\{\Phi_n^{north}\}Res\{\Phi_n^{CNT}\}} = \frac{Res\{\Phi_n^{south}\}}{Res\{\Phi_n^{north}\}} \quad (3.11)$$

where the first equality comes from trigonometric manipulation following the same manner as shown in Eqn.3.4.

Both $\left\langle \cos\left(n(\Phi_n^{south} - \Phi_n^{CNT})\right)\right\rangle$ and $\left\langle \cos\left(n(\Phi_n^{north} - \Phi_n^{CNT})\right)\right\rangle$ are directly measurable and the ratio of $Res\{\Phi_n^{south}\}$ and $Res\{\Phi_n^{north}\}$ is thus obtained. Note that $\left\langle \cos\left(n(\Phi_n^{south} - \Phi_n^{north})\right)\right\rangle = Res\{\Phi_n^{south}\}Res\{\Phi_n^{north}\}$, the multiplication of $Res\{\Phi_n^{south}\}$ and $Res\{\Phi_n^{north}\}$ is also known. Consequently, both $Res\{\Phi_n^{south}\}$ and $Res\{\Phi_n^{north}\}$ are determined. After $\chi_n^{south}$ and $\chi_n^{north}$ is found separately for each arm according to Eqn.3.7, the full event $\chi_n$ is $\chi_n^{full} = \sqrt{\chi_n^{south\,2} + \chi_n^{north\,2}}$. Eventually, resolution factor for the full detector is obtained via Eqn.3.7.

The variation from different methods is treated as an important source of systematic uncertainties for event plane resolution determination.

### 3.2.4 Event Plane Calibration

In our earlier discussions, perfect detector with flat reaction plane angle distribution is assumed. In other words, the constructed $\Phi_n$ should be, in principle, uniform within $[-\pi/n, \pi/n)$. Nevertheless, the event plane angle $\Phi_n$ distribution can be influenced by many factors, such as finite acceptance, sudden detector glitch, dead channel or segment, etc. In this sense, the calibration process is necessary for precise measurement of $v_{n,raw}$ and $Res\{\Phi_n\}$.

The orientation of event plane, $\Phi_n$, largely depends on the initial collision profile. Therefore, the event plane calibration should be done for each centrality class. Moreover, both two-subevents and three-subevents method adopt sub-detectors that sit respectively in south and north arm, therefore the resolution determination as well as $\Phi_n$ construction are also sensitive to the $z-$vertex of the collision. Considering these facts, the calibration is performed with fine centrality bin (usually 5% step) and 5 cm z-vertex increment for all MB events in each run of data.

The calibration process takes two major steps,

1. re-centering of the flow vector (Q vector);
2. flattening of the $\Phi_n$ distributions.

In this section, we will be discussing on these two steps.

**Re-centering**

Ideally, the flow vector distribution should be uniform in azimuth, that is, a perfect circle in $Q_x$-$Q_y$ plane with rotational symmetry around the origin. Due to imperfect detector with possible dead segment (e.g. the inner ring of RxNP south arm since run year 2007), the flow vector distribution could have a pattern that is "stretched" along the direction opposite to the dead segment area. The off-centered flow vector distribution need to be manually "adjusted" so that detector effects are minimized.

The procedure is to normalize the distributions $(Q_{n,x}, Q_{n,y})$ by subtracting the mean $(\langle Q_{n,x}\rangle, \langle Q_{n,y}\rangle)$ averaged over all events, and dividing by the standard deviation $(\sigma(Q_{n,x}), \sigma(Q_{n,y}))$,

$$Q^c_{n,x} = \frac{Q_{n,x} - \langle Q_{n,x}\rangle}{\sigma(Q_{n,x})}, \quad Q^c_{n,y} = \frac{Q_{n,y} - \langle Q_{n,y}\rangle}{\sigma(Q_{n,y})} \tag{3.12}$$

**Flattening**

Based on the re-centered flow vector $(Q^c_{n,x}, Q^c_{n,y})$, event plane angle $\Phi^c_n$ is calculated via Eqn.3.3. In addition, quantities

$$A_{n,k} = -\frac{2}{nk}\langle \sin(nk\Phi^c_n)\rangle, \quad B_{n,k} = +\frac{2}{nk}\langle \cos(nk\Phi^c_n)\rangle \tag{3.13}$$

are obtained. The average "$\langle\ \rangle$" runs over all events; $k$ is selected to go from 1 to a certain order, usually 8.

Then the fully calibrated event plane angle is

$$\Phi^{calib}_n = \Phi^c_n + \Delta\Phi_n, \tag{3.14}$$

where

$$\Delta\Phi_n = \sum_k \left[A_{n,k}\cos(nk\Phi^c_n) + B_{n,k}\sin(nk\Phi^c_n)\right] \tag{3.15}$$

After these two steps, the measured event plane angle distribution is flatten as expected. As an example, Fig.3.8 shows various $2\Phi_2$ distributions after each calibration step for outer ring of RxNP in south (left panel) and north (right panel) arm. After calibration, $(Q_{2,x}, Q_{2,y})$ is not distorted any more, and the distribution (in blue) appears flat.

### 3.2.5 Results of Event Plane Resolutions

After event plane calibration, the calibrated $\Phi_n$ is used to measure raw $v_n$ and construct event plane resolution. The resolution of various detectors for

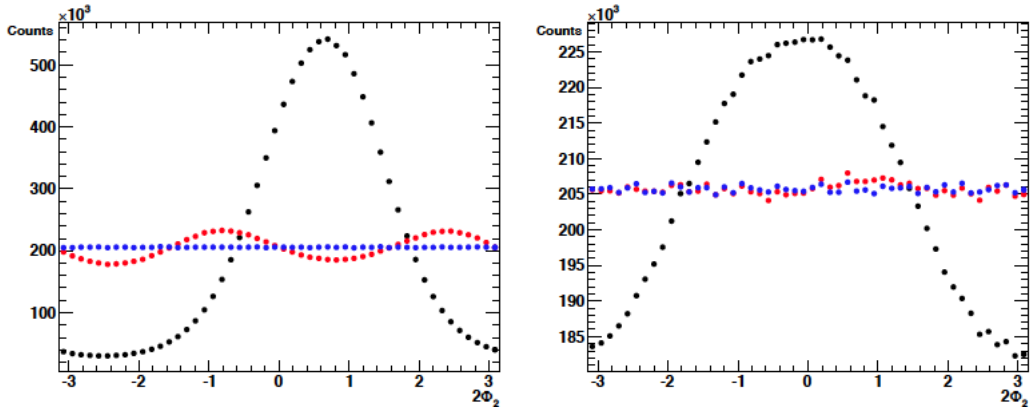


Figure 3.8: Raw $2\Phi_2$ distribution (black) and the distribution after re-centering (red) and flattening (blue) for outer ring of RxNP. Left panel is for south arm RxNP, right panel is for north arm RxNP [38].

$Au + Au$ collisions at $\sqrt{s_{NN}}$ =200 GeV and 62.4, 39 GeV can be found in Fig.3.9 and Fig.3.10, respectively.

It is not hard to see from Fig.3.9, 3.10 that, at certain beam energy, event plane resolution deteriorates as $n$ increases. As shown in Fig.3.9, the resolution factor for RxNP detector is obviously better than MPC and BBC. When it comes to lower collision energy of 62.4 or 39 GeV where much less multiplicity is expected, only RxNP is available for event plane construction. The resolution factors for $2^{nd}$-, $3^{rd}$- and $4^{th}$-order event plane all exhibit similar trend at $\sqrt{s_{NN}}$ =200 GeV, that is, the resolution reaches its maximum in mid-central collisions and deteriorates as collision becomes more central or peripheral. Similar story is for lower energies, however the $4^{th}$-order resolution factor is relatively flat among all centralities. The not so impressive resolution for $4^{th}$-order event plane ($< 0.1$) at lower energies suggests that flow anisotropy measurement beyond $4^{th}$-order might not be realistic at $\sqrt{s_{NN}} = 62.4$ and 39 GeV using event plane method.

## 3.3 Selected $v_n$ Results

The anisotropic flow can be measured via Eqn.3.5 after we find raw $v_n$ and event plane resolution. Figure.3.11, 3.12 illustrate the inclusive charged hadron $v_n$ w.r.t $\Phi_n$ (n=2,3,4) as well as particle identified elliptic flow $v_2$ w.r.t $\Phi_2$ in $Au+Au$ collisions at $\sqrt{s_{NN}} = 39$ and 62.4 GeV, respectively. Sizable $v_3$ and $v_4$ are observed in these low beam energies, and the clear centrality dependence of elliptic flow $v_2$ is expected as a result of initial anisotropic geometry and the

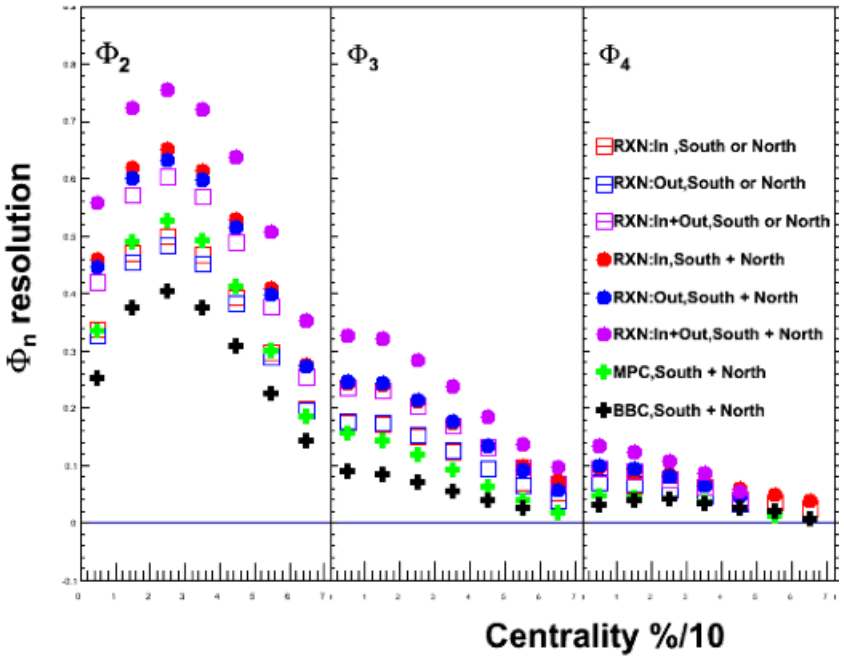


Figure 3.9: Resolution factors $Res\{\Phi_n\}$ (n=2,3,4) for various detectors in $Au + Au$ collisions at $\sqrt{s_{NN}}$ =200 GeV [118].

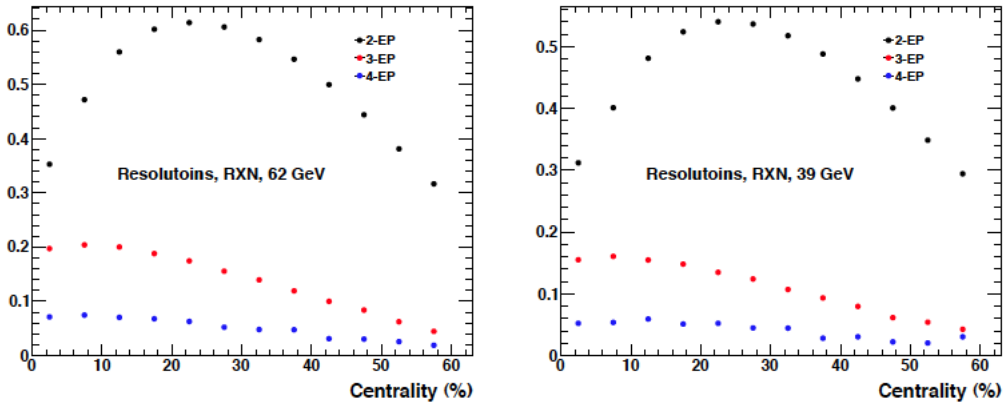


Figure 3.10: Resolution factors $Res\{\Phi_n\}$ (n=2,3,4) for RxNP in $Au + Au$ collisions at $\sqrt{s_{NN}}$ =62.4 (left) and 39 GeV (right) [38].

pressure-driven nature. Triangular flow $v_3$ does not seem to vary much with centrality, which is consistent with its fluctuation-based fomation mechanism. $v_4$ mesurements do suffer from both statistics and limited detector resolution.

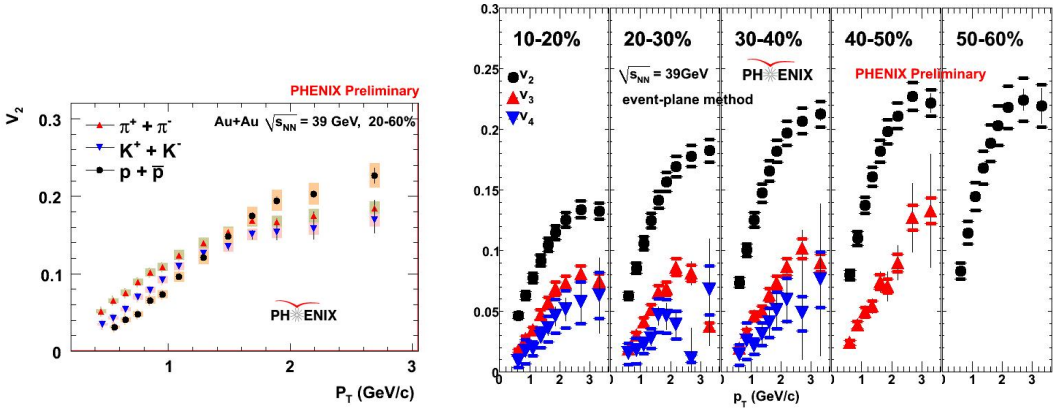


Figure 3.11: Particle identified hadron $v_2$ (left) and inclusive charged hadron $v_n$ (n=2,3,4, right panel) in $Au + Au$ collision at $\sqrt{s_{NN}} = 39$ GeV.

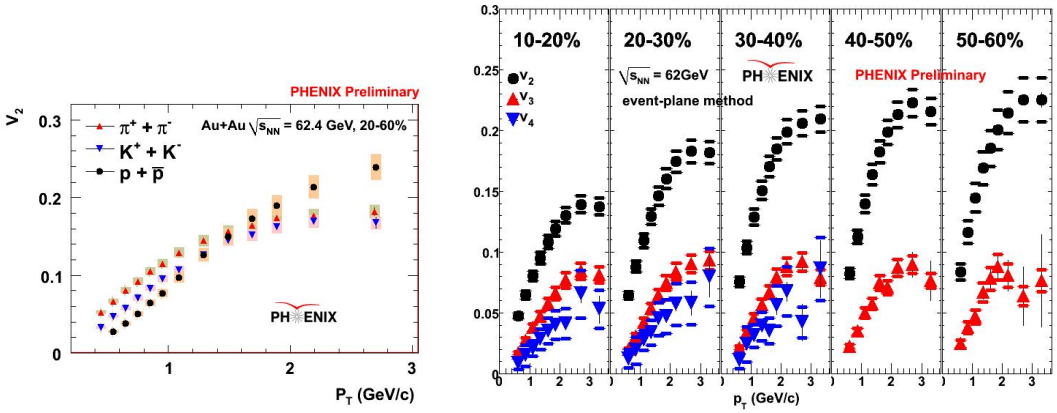


Figure 3.12: Particle identified hadron $v_2$ (left) and inclusive charged hadron $v_n$ (n=2,3,4, right panel) in $Au + Au$ collision at $\sqrt{s_{NN}} = 62.4$ GeV.

The particle identified $v_n$ (n=2,3,4) versus $p_T$ in 10% centrality step for $Au + Au$ collisions at $\sqrt{s_{NN}} = 200$ GeV is shown in Fig.3.13. The top three rows include the $v_n$ w.r.t $\Phi_n$ (n=2,3,4) as a function of transverse momentum $p_T$. Note that the last row is the measured $v_4$ with respect to the $2^{nd}$-order event plane. The sizeable $v_4\{\Phi_2\}$ is attributed to the positive correlation between $\Phi_4$ and $\Phi_2$ [100], which is rooted in the initial geometry correlation between the corresponding eccentricities, $\epsilon_4$ and $\epsilon_2$.

The harmonic flow measurement via EP method serve as a good base line for long-range two-particle (2PC) correlation method to compare with. A detailed study of flow measurements via 2PC method will be presented in following chapter.

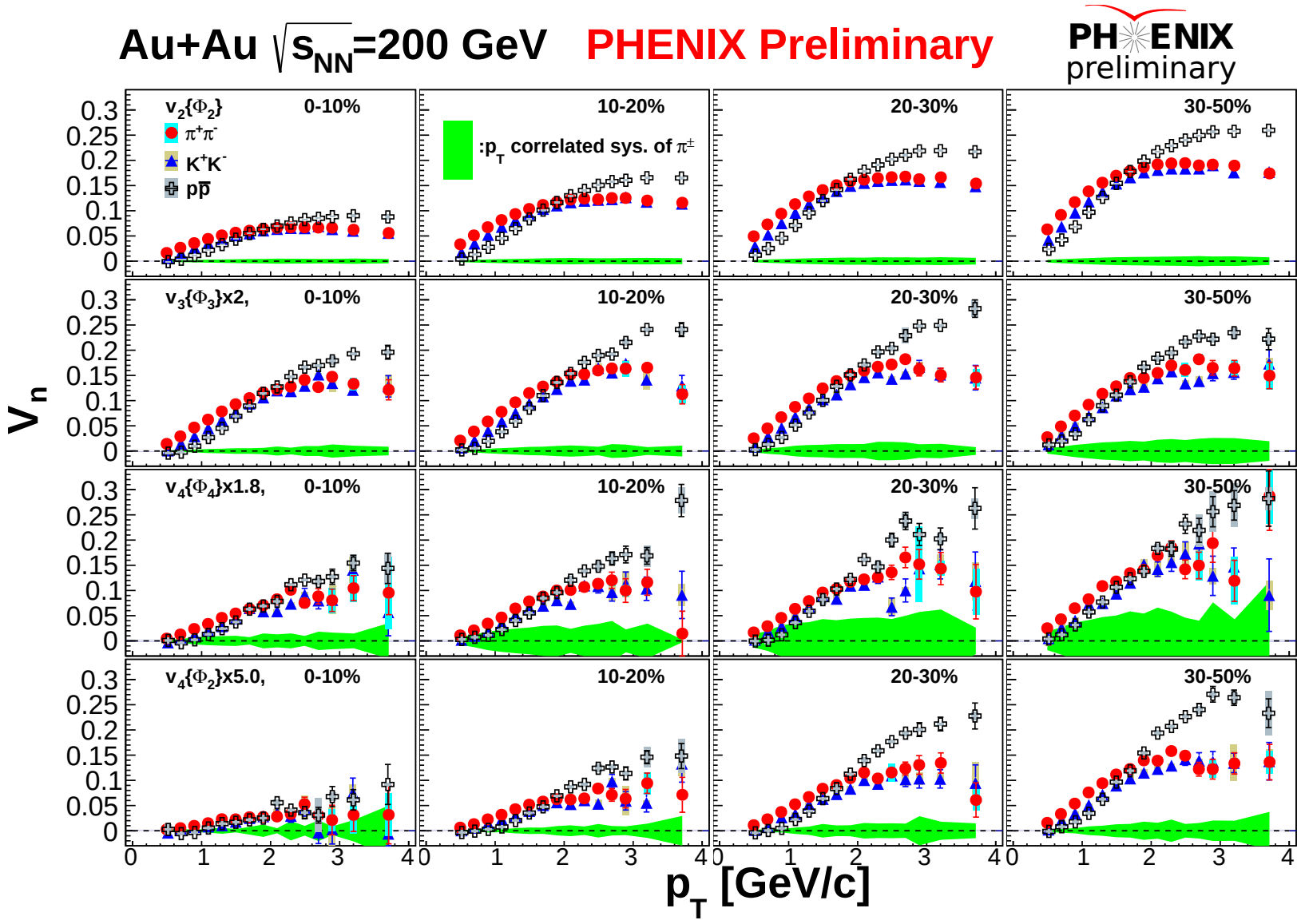


Figure 3.13: Particle Identified $v_n$ (n=2,3,4) vs. $p_T$ in 10% centrality step for $Au + Au$ collisions at $\sqrt{s_{NN}}$ = 200 GeV.

# Chapter 4

# Hadron Flow Measurement via Long-range Two-Particle Correlation Method

In this chapter, correlations between charged particle pairs are studied. Such correlations can be due to global flow collectivity, that is, individual tracks correlate with event planes $\Phi_n$. They can be also attributed to other interesting phenomena, such as back-to-back di-jets, jet-medium interactions etc, depending on where the two hadron tracks that form correlation pair come from.

The methodology of long-range two-particle correlation (2PC) method as well as analysis details are going to be presented in this chapter. As complementary measurements, particle identified $v_n$ obtained via 2PC method are compared with existing EP results. Physics implications and necessary discussions pertaining to such comparisons are also included. In the end of this chapter, RHIC $v_n$ results are compared with corresponding LHC results. Physics message from the cross-experiment comparisons will also be presented.

This chapter is organized as follows. In Section 4.1, an overview of the methodology of long-range two-particle correlation method is discussed. Following which, general features of charged hadron analysis in PHENIX are briefly discussed. In Section 4.4, detailed analysis procedure is included, where necessary QA, track selection, cross-method comparisons and evaluation of systematic uncertainties are discussed. A summary of 2PC $v_n$ results are presented in Section 4.4.1,4.5. Finally in Section 4.6, comparisons between RHIC $v_n$ results and LHC results are discussed.

## 4.1 Overview of Two-particle Correlations

Two particle azimuthal correlations provide special insights into jet-medium interactions. As introduced in Section 1.4 of Chapter One, a correlation function $C(\Delta\phi, \Delta\eta)$ in di-hadron correlation studies is defined as

$$C(\Delta\phi, \Delta\eta) = \frac{N_{pair,same}(\Delta\phi, \Delta\eta)}{N_{pair,mix}(\Delta\phi, \Delta\eta)} \tag{4.1}$$

where $\Delta\phi$ is the azimuthal angle separation between the selected two hadrons and $\Delta\eta$ is the pseudorapidity difference between them. $N_{pair,same}(\Delta\phi, \Delta\eta)$ in numerator represents the $(\Delta\phi, \Delta\eta)-$distribution of correlated hadron pairs from the same collision event (known as "same-event" correlations). In contrast, $N_{pair,mix}(\Delta\phi, \Delta\eta)$ in denominator represents the distribution of uncorrelated hadron pairs, in which two hadrons are selected from different events (known as "mixed-event" correlations) but with similar event character as same-event correlations, such as centrality and collision vertex position. Note that the mixed-event distribution reflects detector inefficiencies and its effects of non-uniformity but contains no physical correlations, while the same-event distribution includes both physical correlations and detector acceptance effects. Among the two particles in pair, usually the one with higher $p_T$ is called *trigger particle*, the other one with lower $p_T$ is denoted as *partner* or *associated particle*.

In $p+p$ collisions, for example, jet fragmentation peaks are found at both $\Delta\phi = 0$ (near side, when particles come from the same jet cone) and $\Delta\phi = \pi$ (away side, when particles originate from back-to-back di-jet). In $Au+Au$ collisions however, a much more bulky medium is created and different phenomena are observed. Figure.1.23 in Chapter One shows centrality evolution of the correlation functions for trigger and partner particle $p_T \in (2, 3)$ GeV. In contrast to what is observed in $p+p$ collisions, an away-side "double-hump" structure appears in most central collisions (0-5%) but soon disappears in 0-10% centrality. As collisions become more non-central, the double peak shoulder-like structure gradually evolves into an away-side "ridge" that is similar to the near-side structure but with smaller magnitude. In all cases, a near-side jet peak sitting at $(\Delta\phi, \Delta\eta) = (0, 0)$ is observed. A long range correlation along $\Delta\eta$ dimension at $\Delta\phi = 0$, known as *ridge*, can be also found in central and mid-central events. Moreover, a noticeable increase in magnitude is observed for the near-side ridge as collisions turn into mid-central from central, and the magnitude decreases for peripheral collisions. Interestingly, the magnitude of away-side ridge also increases from central to mid-central collisions, and becomes comparable to its near-side counterpart for events over

50-60% centrality. As collisions are more into the peripheral end, an away-side peak structure even starts to emerge, which is believed to orignate from back-to-back dijets.

## 4.2 Flow Dominated Phase Space

The long range structure at the near- and away-side could be attributed to global flow collectivity and medium modification of jet fragmentation. To further investigate the two-particle correlations with removed near-side and substantially suppressed away-side jet constribution, 1D correlations of hadron pairs with relatively large rapidity separation are built. The upper panel of Figure.4.1 shows the two-particle azimuthal correlations with $p_T^a, p_T^b \in (3, 4)$ GeV and $2 < |\Delta\eta| < 5$ radipity gap in several centrality classes. Individual contributions from each order of harmonics $v_{n,n}$ (to be discussed later in Sec.4.2.1 and Sec.4.2.2) are illustrated by different curves. The larger magnitude of near-side peak suggests the dominant flow contributions. The away-side jet contributions come into play significantly as collisions become over $\sim 50\%$ centrality.

A similar study for $p_T$ dependence of the long-range correlations is shown in the bottom-left panel of Fig.4.1. In the upper two plots where transverse momentum $p_T < 6$ GeV for both trigger and partner particle, the magnitude of near-side peak is significantly larger than the away-side peak, indicating strong flow contributions to the $C(\Delta\phi)$. When $p_T > 6$ GeV, The near-side peak completely goes away while the away-side peak continues to develop, suggesting the away-side jet and other non-flow correlations already take over in this phase space.

It is fairly safe to draw our conclusion that the long-range correaltion structure is largely dominated by global flow contribution in central and mid-central events for particle of up to intermediate transverse momentum ($\lesssim 4$ GeV). It is important to stress that the influence from away-side jet can hardly be completely removed by applying $|\Delta\eta|$ cut, that is, the effects of away-side jet exist in all collision events for all particles. Nevertheless, for lower $p_T$ particles in central up to mid-central ($\lesssim 60\%$) collisions, the effects of azimuthal anisotropy (flow) appear to dominate the correlation functions. Similarly, the effects of azimuthal anisotropy do not vanish in peripheral events, however the jet correlations dominate. It is also noteworthy that the onset of jet correltions' takeover from anisotropies is not abrupt or sudden in terms of centrality and $p_T$. The transition from flow- to jet-dominated phase space is rather smooth.

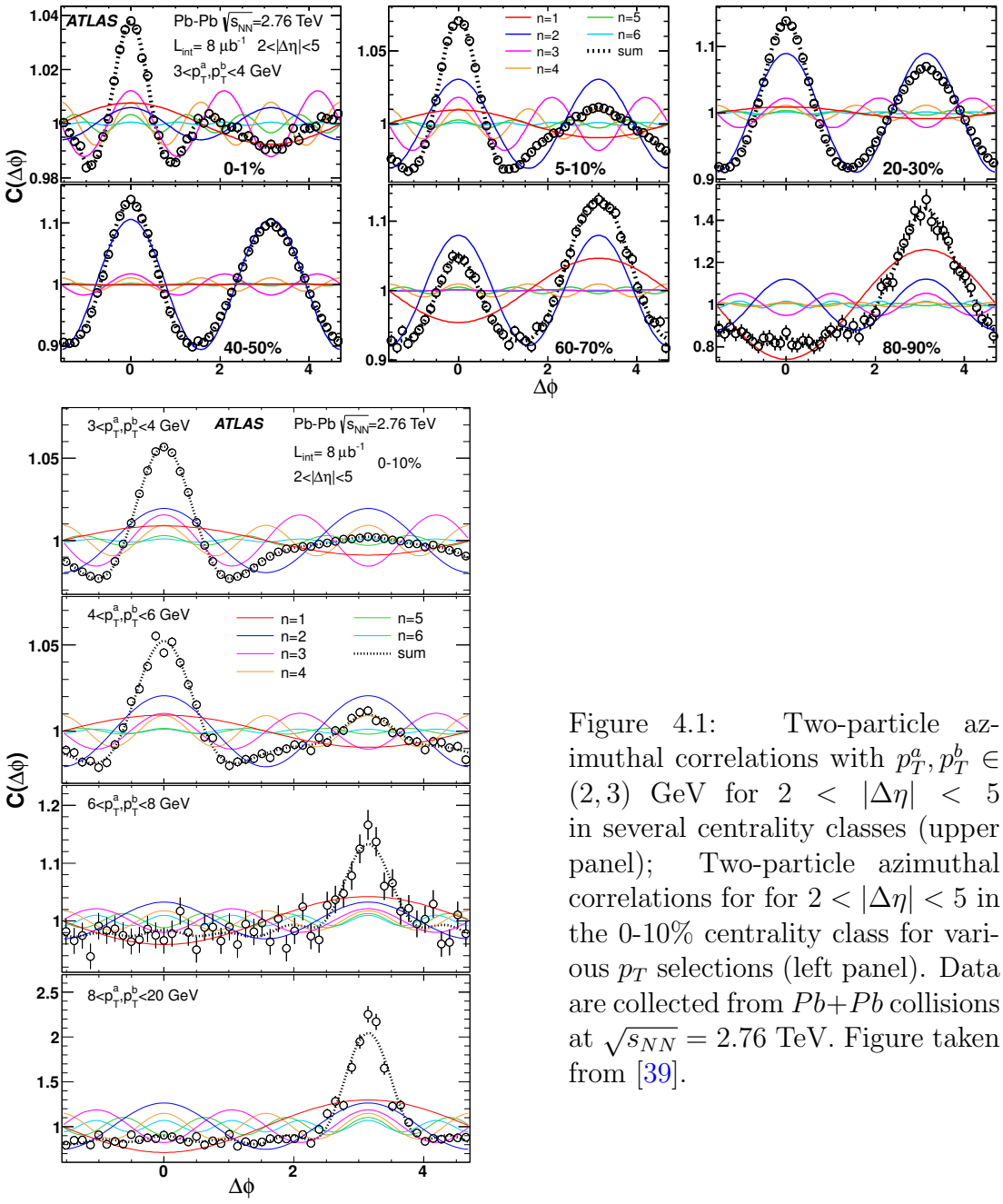


Figure 4.1: Two-particle azimuthal correlations with $p_T^a, p_T^b \in (2,3)$ GeV for $2 < |\Delta\eta| < 5$ in several centrality classes (upper panel); Two-particle azimuthal correlations for for $2 < |\Delta\eta| < 5$ in the 0-10% centrality class for various $p_T$ selections (left panel). Data are collected from $Pb$+$Pb$ collisions at $\sqrt{s_{NN}} = 2.76$ TeV. Figure taken from [39].

### 4.2.1 Long-range Two-particle Correlation Method

In light of prior study, we now discuss the long-range two-particle correlation method in PHENIX, which is performed safely within the flow-dominated

phase space.

In addition to classical event plane method, the anisotropy of particle production, characterized by flow coefficients, has also been made via the pair-wise distribution in the azimuthal angle difference ($\triangle\phi = \phi_1 - \phi_2$) between particles

$$\frac{dN^{pairs}}{d\triangle\phi} \propto \left(1 + \sum_{n=1} 2v_{n,n}(p_T^a, p_T^b)cos(n\triangle\phi)\right) \tag{4.2}$$

where the coefficients $v_{n,n}$ are symmetric functions with respect to $p_T^a$ and $p_T^b$. The harmonics $v_n$ also contribute to this distribution:

$$\frac{dN^{pairs}}{d\triangle\phi} \propto \left(1 + \sum_{n=1} 2v_n(p_T^a)v_n(p_T^b)cos(n\triangle\phi)\right) \tag{4.3}$$

where the global direction (the phase of $n^{th}$ harmonic flow $\psi_{RP}$, known as the reaction plane or RP) drops out in the convolution. Thus if the anisotropy is driven by collective flow expansion, $v_{n,n}$ should factorize into the product of two single-particle harmonic coefficients:

$$v_{n,n}(p_T^a, p_T^b) = v_n(p_T^a)v_n(p_T^b). \tag{4.4}$$

Such factorization may also be valid if the anisotropies of the two particles are independently driven by collective expansion and path-length dependent jet energy loss (both are associated with the same initial spatial asymmetries). This factorization relation has been used to calculate the single-particle $v_n$.

The analysis presented in this chapter, based on Eqn.4.2, 4.3, 4.4, utilizes two-particle azimuthal angle correlation functions across a relatively large rapidity ($\eta$) gap to suppress the near-side jet contributions as well as to minimize away-side jet contributions and other short-range non-flow effects (such as decays, etc).

It is known [39] that the near-side jet tends to increase the $v_{n,n}$, but its limited influence is localized around $\Delta\eta \sim 0$. The influence from away-side correlation on $v_{n,n}$ at large $\Delta\eta$ is also negligible in central and mid-central collisions for particles with up to intermediate transverse momentum. As will be shown later in this chapter, the long-range two-partcie correlation presented in this work selects one track from central arm with $|\eta| < 0.35$ and the other hit from RxNP ($1.0 < |\eta| < 2.8$). Because of resolution limitation of RxNP detector and capability of particle identification in TOF[1], the main phase space

[1]In this work, particle identification is carried out in TOF only, without help of aerogel and EMCal.

we are looking at in PHENIX is about correlations in central to mid-central collisions ($\lesssim 60\%$) for particles of low and intermediate $p_T$.

### 4.2.2 How to determine Single Particle $v_n$ from Two-particle Correlations

If correlation function is dominated by collective flow contributions, the factorization in Eqn.4.4 holds, then the single particle $v_n$ can be calculated afterwards. To be more specific, we extract $v_n$ for hadron track in central arms in two steps. Note that there is no $p_T$ information registered for RxNP hits.

1) $\triangle\phi$ correlation functions are generated for the hits in the north and south reaction plane detector (RxNP), without $p_T$ selection.

2) the azimuths of the charged particles in the central arms are used in concert with the hits in the RxNP detector to generate $\triangle\phi$ correlation functions. Each of these correlation functions was Fourier analyzed to obtain the associated $v_{n,n}$ values (*i.e.* Fourier coefficients). In this case, we obtain $v_{n,n}^{RxNP,RxNP}$ and $v_{n,n}^{central,RxNP}$ respectively. Subsequently, the $v_n^{central}(centrality, p_T)$ values for charged hadrons from central arms are extracted using Eqn.4.4 as well as the $v_n^{RxNP}(centrality)$ values obtained from the Fourier decomposition of the correlation functions generated in step 1 (assuming South and North part of RxNP contributes evenly, *i.e.* $v_n^{RxNP} = \sqrt{v_{n,n}^{RxNP,RxNP}}$ holds in step 1).

#### The Validity of Factorization

It must be stressed that the factorization relation described in Eqn.4.4 is valid if and only if the correlation function is dominated by collective flow. From experiment point of view, as long as radipity gap $|\Delta\eta|$ between the two paticles is reasonably large, such factorization will hold for two-particle correlations in central to mid-central collisions from particle pair with $p_T$ up to intermediate range ($\lesssim 4$ GeV).

In a more general case, trigger (labelled "a", of transverse momentum $p_T^a$) and partner (labelled "b", of transverse momentum $p_T^b$) particles are selected with reasonably large $|\Delta\eta|$ separation to isolate the long-range structures and to suppress any short-range correlations as well as non-flow effects. According to Eqn.4.4, by choosing trigger and partner particles from the same $p_T$ bin[2],

[2]Such correlations of trigger and partner particle from the same $p_T$ bin is usually called *fixed-$p_T$ correlations*, in constrast to *mixed-$p_T$ correlations* where trigger and partner particle

the $v_n(p_T^a)$ can be calculated as the square root of $v_{n,n}(p_T^a, p_T^b)$, that is,

$$v_n(p_T^a) = \sqrt{v_{n,n}(p_T^a, p_T^a)} \tag{4.5}$$

Once the single particle $v_n(p_T^a)$ is obtained, the $v_n(p_T^b)$ of the other particle from another $p_T$ bin can be calculated as,

$$v_n(p_T^b) = \frac{v_{n,n}(p_T^a, p_T^b)}{v_n(p_T^a)} \tag{4.6}$$

It is found [39] the $v_n(p_T^b)$ (n=2,3,4,5,6) obtained via Eqn.4.6 by correlating particles in different $p_T^a$ bins are almost identical when $|\Delta\eta| \gtrsim 1$ and the reference $p_T^a \lesssim$ (3-4) GeV/c. This is true for both central and mid-central events. For 0-10% most central events, possible deviation found in the extracted $v_n(p_T^b)$ for $|\Delta\eta| \ll 1$ when using reference $p_T^a \in (3, 4)$ GeV/c is largely due to non-flow bias. However, such deviation becomes much smaller in 20-30% $Pb + Pb$ collisions [119].

As an example, Fig.4.2 shows $v_n(p_T^b) = \frac{v_{n,n}(p_T^a, p_T^b)}{v_n(p_T^a)}$ vs. $|\Delta\eta|$ (n=1–6) for $p_T^b \in (1, 1.5)$ GeV/c, calculated from a reference $v_n$ in four $p_T^a$ bins (0.5-1, 1-2, 2-3, 3-4 GeV/c) for $Pb + Pb$ 10-20% events. Good agreement among the extracted $v_n(p_T^b)$ is achieved for $|\Delta\eta| \gtrsim 1$.

In summary, the factorization relation in Eqn.4.4 holds well in central and mid-central events for particles of up to intermediate transverse momentum if additional $|\Delta\eta|$ cut is applied. As for the domain we are looking at in PHENIX within this work, the rapidity gap between central arm and RxNP satisfies $|\Delta\eta| \gtrsim 1$, hence the factorization is safely valid, which is essential to the long-range two-particle correlation method presented here.

It has to be emphasized that the factorization relation needs careful scrutiny when it comes to $n = 1$. The factorization is clearly broken for $v_{1,1}$ as shown in upper-left panel of Fig.4.2. This is because $v_{1,1}$ is largely affected by global momentum conservation effects for a system with finite multiplicity [120] and in fact, $v_{1,1}$ does not factorize for any $p_T$ or centrality.

## 4.3 Features of Charged Hadron Analysis

In experiment, most of the detected charged hadrons are $\pi^{\pm}$, $K^{\pm}$ and $p(\bar{p})$. They are abundant throughout each stage of heavy ion collisions and can be detected directly by detectors. The construction of charged hadron tracks is

are from different $p_T$ bins.

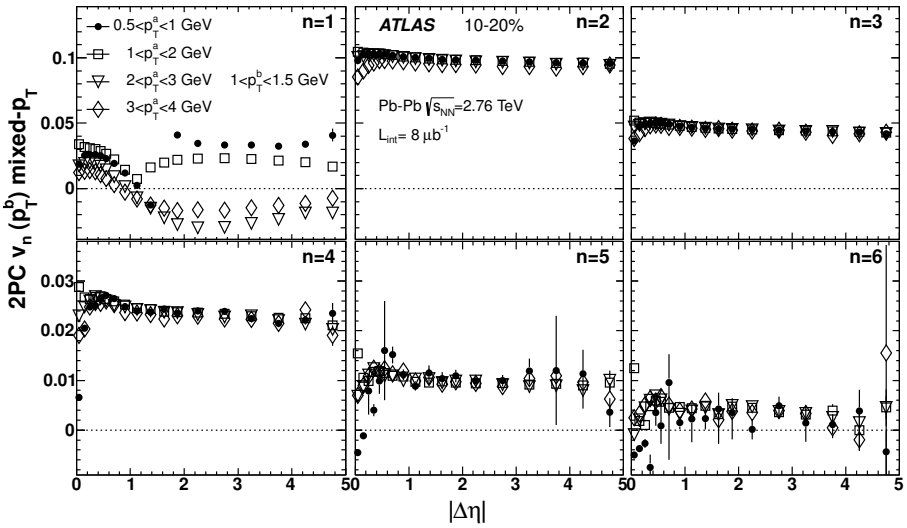


Figure 4.2: $v_n(p_T^b) = \frac{v_{n,n}(p_T^a, p_T^b)}{v_n(p_T^a)}$ vs.$|\Delta\eta|$ (n=1,2,3,4,5,6) for $p_T^b \in (1, 1.5)$ GeV/c, calculated from a reference $v_n$ in four $p_T^a$ bins (0.5-1, 1-2, 2-3, 3-4 GeV/c). Results are for $Pb + Pb$ collisions in 10-20% centrality class [39].

done with help of drift chamber (DC) and pad chamber (PC). Ring-Imaging Cherenkov (RICH) is used to suppress conversion particles with wrong reconstructed momentum, mostly electrons. The particle identification is performed in both east and west arm TOF.

In this section, features of charged hadron analysis are discussed, including momentum measurement, track construction and particle identification.

### 4.3.1 Track Construction and Background Suppression

As stated in Section 2.3.1 of Chapter Two, a track candidate includes 12 hits of $(x, y)$ measurement and 8 hits of $z$ measurement in drift chamber (DC), along with 1 hit of $(x, y, z)$ measurement in first layer of pad chamber (PC).

In a typical heavy ion collisions, hundreds of tracks would leave thousands of hits in DC and PC. To further screen all the possible associations of hits, we use "combinatorial Hough transformation", a general technique that translates a list of points into a particular space that makes the extraction of correlations between points straightforward. The coordinates to describe tracks in the X1 and X2 modules of DC under Hough tranformation are $\phi$ and $\alpha$, as shown in Fig.4.3. $\phi$ is defined as the azimuthal angle at the intersection of the track and the reference circle (together with the collision vertex), while $\alpha$ is defined as the inclination of the track relative to the intersection. In particular, the $z$ coordinate of the intersection point, is denoted by $zed$ or $z_{dc}$. The $(\phi, \alpha)$

pairs are then plotted in a 2D histogram, in which peaks emerging from the background correspond to the tracks, hence are extracted and read from the histogram of hits.

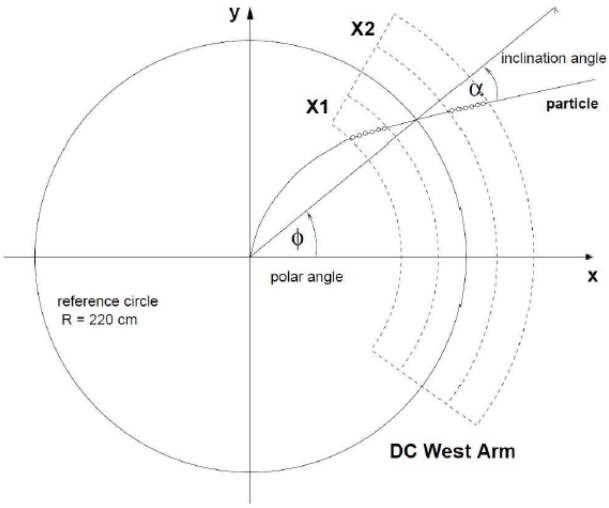


Figure 4.3: Illustration of the Hough transformation for drift chamber hadron track reconstruction. The reference circle is $R = 220$ cm. The open dots represent the X1 and X2 hits in the drift chamber (DC) along the particle trajectory.

However, the track candidates selected from Hough transformation may also contain combinatorial background or any accidental associations of hits. These candidates are then further "filtered" by applying matching cut, which basically requires additional registered hits on outer detectors (e.g. RICH, PC3, TOF etc) that match the reconstructed hadron trajectory in DC. By imposing matching cut, the background may be well suppressed.

The matching variable (M.V) that describes the distance between a track projection point and a registered detector hit is usually decomposed into two components, one is along beam ($z$) direction and the other is in azimuth ($\phi$). Such variable, usually normalized by its root mean square (RMS) value[3], is directly used in matching cut. It is suggested that by requiring $2\sigma$ matching cut, that is, to demand $\sqrt{(M.V_{\Delta z})^2 + (M.V_{\Delta \phi})^2} < 2.0$, the combinatorial background can already be largely suppressed.

Fig.4.4 shows the $p_T$ spectrum for tracks reconstructed with DC and PC1 (red dots) as well as applying additional $2\sigma$ PC2-PC3 matching cut (blue open

[3]A calibration process is also needed so that the mean value of the $z$-direction component is zero for each matching variable.

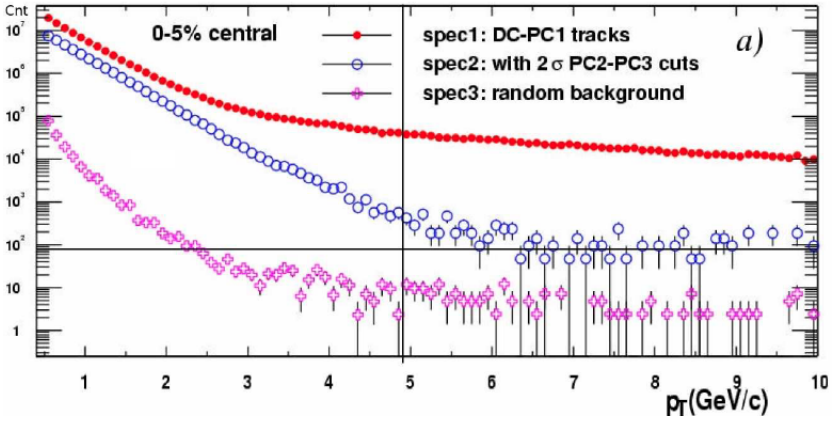


Figure 4.4: The effectiveness of matching on $p_T$ spectrum.

circles) and random background (magenta cross). After applying matching cut, a steep drop of constructed tracks is observed in the $p_T$ spectra for $p_T$ up to 5 GeV/c, which indicates a substantial amount of fake tracks are rejected by imposing such matching requirement. For charged particles with $p_T > 5$ GeV/c, due to possible secondary process (hadron decay, etc) that can be quite prevalent, a significant amount of fake tracks from background remain in this high $p_T$ region even after matching cut is applied.

### 4.3.2 Beam Offset, Momentum Measurement and Corrections

Under magnetic field, the momentum measurement for charged particle depends upon the $\alpha$ angle that describes the curvature of each track. In fact, the charged particle momentum, to its first order, is approximately inverse proportional to $\alpha$, subject to a constant that reflects the overall configuration of magnetic field. Moreover, beam offset corrections and momentum scale determination also largely rely on the $\phi$ and $\alpha$ info in DC. In this sense, after introducing the track construction algorithm and $(\phi, \alpha)$ coordinates, it is worthwhile reviewing the basic idea of the beam offset and momentum correction in this section.

In experiment, the primary collision vertex does not necessarily center inside the beam pipe. The off-centered bunch of heav ion beam could induce error in $\alpha$ measurement. Since $\alpha$ is defined based on zero beam offset assumption, such error in $\alpha$ would propagate to subsequent momentum determination and physics analysis. Therefore, correction is needed to the $\alpha$ angle in order to remove the effects of beam shift and its possible influence on momentum

calculation. To this end, the beam position is determined from zero field runs, where magnetic field is switched off on purpose to have charged particles travel without being bent by Lorentz force. Free of megnatic field, $\alpha$ should be zero if beam centers inside the pipe. Nevertheless, a shift of the beam position from the nominal origin of PHENIX detector will produce a systematic offset in mean $\alpha$ value, which is parameterized as a function of azimuthal angle as

$$\alpha = \frac{dx}{R_{DC}} \cos\phi + \frac{dy}{R_{DC}} \sin\phi \tag{4.7}$$

where $R_{DC}$ is the radius of the reference circle (220 cm). Note that with no beam offset or magnetic field, the tracks are straight and would produce a $\phi$-independent $\alpha$ distribution. The plots of $\alpha$ vs $\phi$ are then fitted for east and west arms to extract the beam offsets $dx$ and $dy$. Since the location of beam center may vary from time to time, $(dx, dy)$ values are usually calculated within relatively small run groups.

Once beam offsets have been corrected, the momentum scale can be determined by the position of (anti-)protons mass peaks, which are calculated as $m^2$ via Eqn.2.2 in Chapter Two. By comparing the $m^2$ peak of (anti-)protons to the standard value (e.g. mass value from PDG), the momentum scale correction, $f$, is found as

$$f = \sqrt{\frac{m^2_{PDG}}{m^2}} \tag{4.8}$$

For a beam shift of $\sim 1$ mm, the effect on the momentum scale is $\sim 0.5\%$.

### 4.3.3 Particle Identification

Charged particle are identified using the combination of three measurements: time-of-flight from the BBC and TOF, momentum from the DC, and flight-path length from the collision vertex point to the TOF hit position. As shown in Eqn.2.2, the square of mass is derived from

$$m^2 = \frac{p^2}{c^2}\left[\left(\frac{t_{tof}}{L/c}\right)^2 - 1\right]$$

where $p$ is the momentum, $t_{tof}$ is the time of flight, $L$ is the flight path length, and $c$ is the speed of light. The charged particle identification is performed using cuts in $m^2$ and momentum space, that is, $2\sigma$ standard deviation PID cuts in $m^2$ and momentum space for each particle species. In addition, we also require $3\sigma$ "veto" cut to reduce the contamination from other particles.

The PID selections are performed by applying momentum-dependent cuts

in mass-squared [11]. The mass-squared distributions are fitted with a 3-Gaussian function corresponding to pions, kaons, and protons. At lower transverse momenta ($p_T < 2.5$ GeV/c), the $2\sigma$ bands centered around each particles $m^2$ separate out from each other and do not overlap, thus symmetric cuts, $m_0^2 - 2\sigma < m^2 < m_0^2 + 2\sigma$, allow for PID with high purity. In the range 2.5 GeV/c $< p_T <$ 3 GeV/c, the $\pi/K$ separation is achieved by excluding the particles that lie within $2\sigma$ of the centroid of the mass-squared distribution of another particle. For illustrative purpose, an example of $m^2$ distribution within different $p_T$ bins in TOFW and TOFE for $Au$+$Au$ collisions at $\sqrt{s_{NN}} =$ 200 GeV is shown in Figure.4.5.

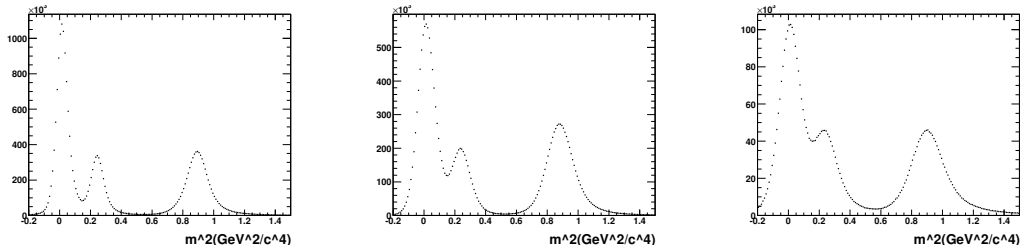


Figure 4.5: $m^2$ distribution in TOFW and TOFE within different $p_T$ range. $m^2$ in TOFW, 1.9GeV/c $< p_T <$2.1GeV/c (left); $m^2$ in TOFE, 1.9GeV/c $< p_T <$2.1GeV/c (middle); $m^2$ in TOFW, 2.7GeV/c $< p_T <$3.0GeV/c (right).

The timing resolution for hadrons can be estimated by measuring the width of the distribution for the difference between the measured time-of-flight and expected time-of-flight for pions of large transverse momentum. An example of such time difference distribution for high $p_T$ pions within run 232839 ($Au$+$Au$ collisions from $\sqrt{s_{NN}} = 200$ GeV) in TOF-W and TOF-E is shown in Figure. 4.6.

Similar to Fig.4.6, an example of time difference distribution for $1.2 < p_T <$ 1.6 GeV/c pions in run 311728 from $Au + Au$ collisions at $\sqrt{s_{NN}} = 62.4$ GeV and in run 314950 from $Au + Au$ collisions at $\sqrt{s_{NN}} = 39$ GeV are shown in Fig.4.7 and 4.8, respectively. The first panel is for west arm TOF (TOF-W), right panel is for east arm TOF (TOF-E).

After Gaussian fitting the width of near-zero peak in the "measured–expected" time difference distribution for each run and applying correction for TOF-E and TOF-W, we obtained the run-by-run dependence of the timing resolution for $Au + Au$ collisions at $\sqrt{s_{NN}} = 200$ GeV in Figure.4.9, at $\sqrt{s_{NN}} = 62.4$ GeV in Figure.4.10 and at $\sqrt{s_{NN}} = 39$ GeV in Figure.4.11, respectively.

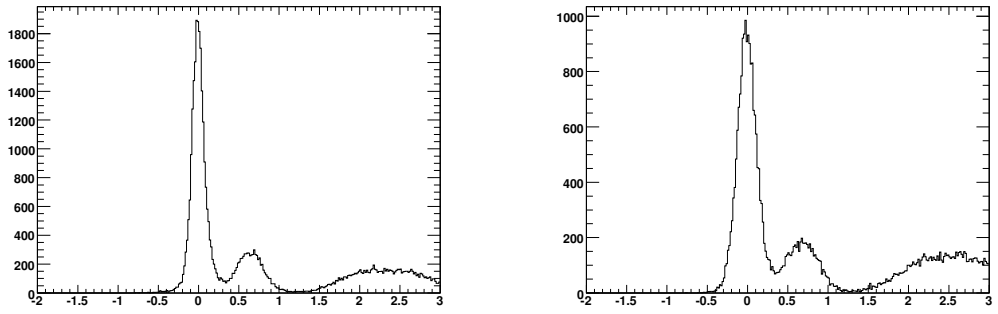

Figure 4.6: Example of distribution for the difference between measured and expected time-of-flight for charged pions with momentum 1.3< $p_T$ <1.6 GeV/c in TOF-W (left) and TOF-E (right) at $\sqrt{s_{NN}} = 200$ GeV.

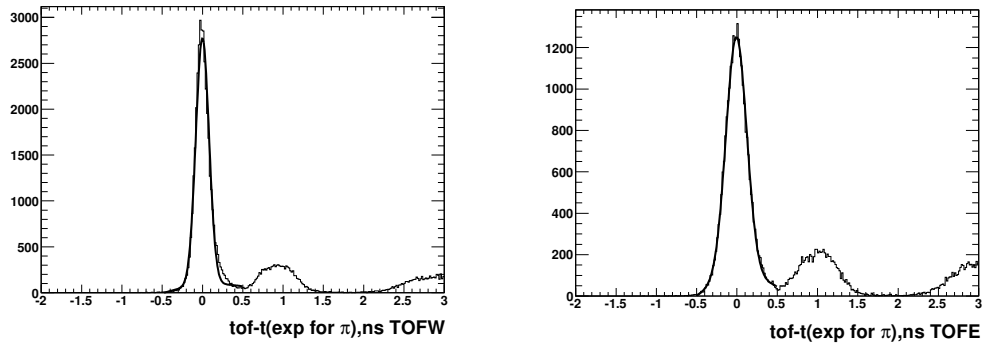


Figure 4.7: Calibrated distribution for difference between measured and expected time for charged pions with momentum 1.2 < $p_T$ < 1.6 GeV/c in TOF-W (left) and TOF-E (right) at $\sqrt{s_{NN}} = 62.4$ GeV.

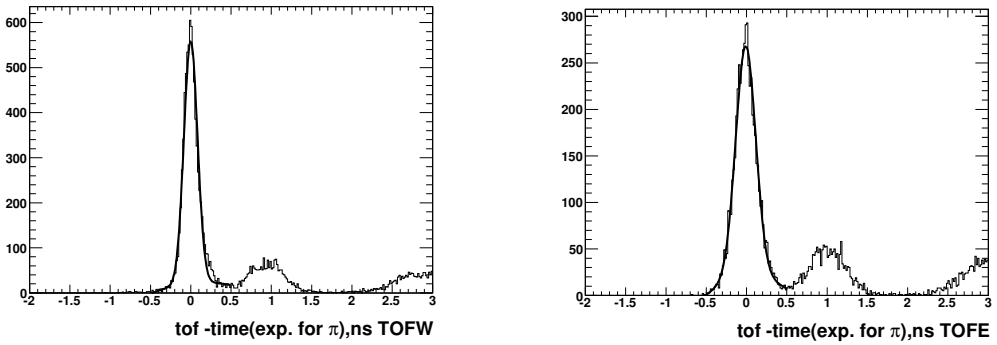


Figure 4.8: Calibrated distribution for difference between measured and expected time for charged pions with momentum $1.2 < p_T < 1.6$ GeV/c in TOF-W (left) and TOF-E (right) at $\sqrt{s_{NN}} = 39$ GeV.

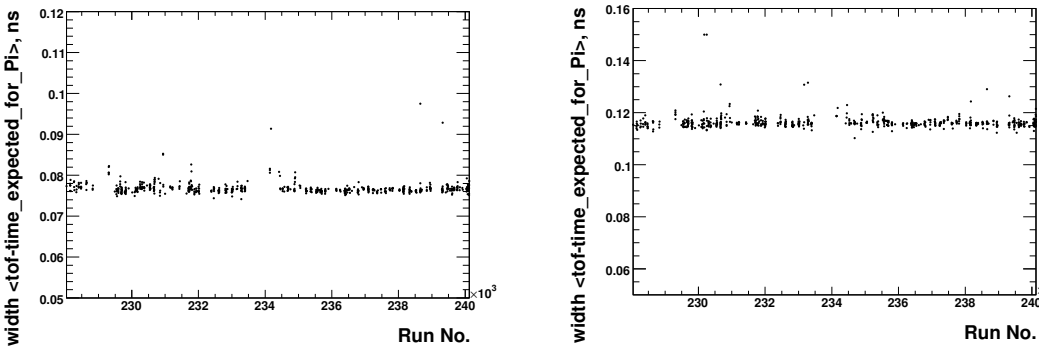


Figure 4.9: Run-by-run dependence of the timing resolution (width of near-zero peak) after correction for TOF-W (left) and TOF-E (right) for $Au + Au$ collisions at $\sqrt{s_{NN}} = 200$ GeV.

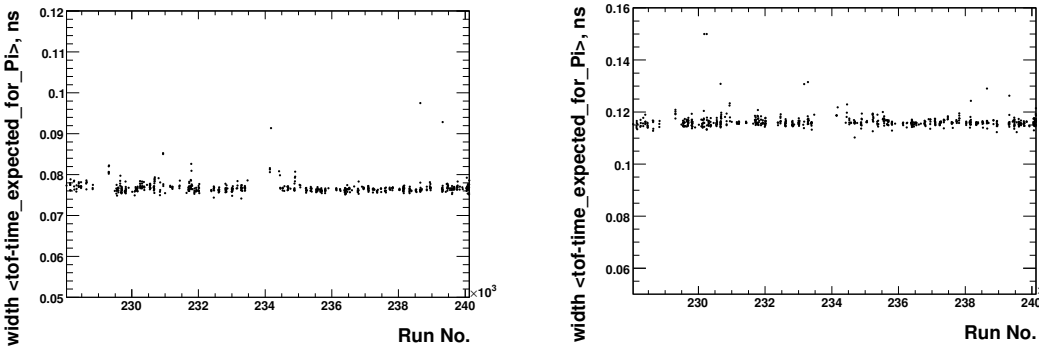


Figure 4.10: Run-by-run dependence of the timing resolution (width of near-zero peak) after correction for TOF-W (left) and TOF-E (right) at $\sqrt{s_{NN}} =$ 62.4 collisions

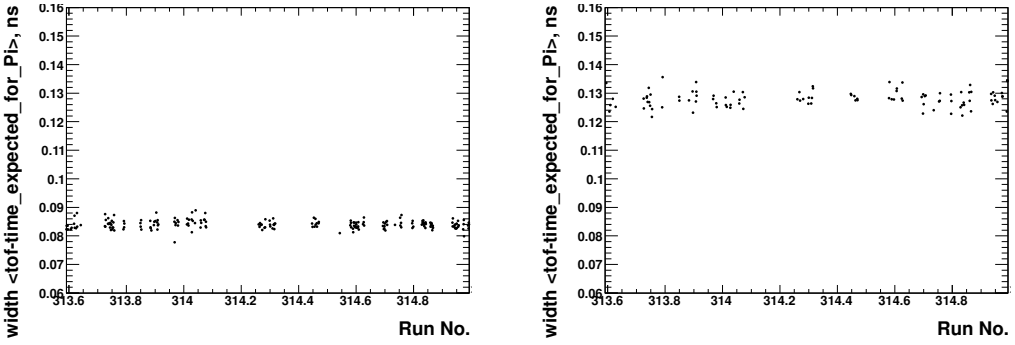


Figure 4.11: Run-by-run dependence of the timing resolution (width of near-zero peak) after correction for TOF-W (left) and TOF-E (right) at $\sqrt{s_{NN}} =$ 39 GeV collisions

The center of the near-zero peak in the "measured –expected" time difference distribution vs. run number can be found in Figure.4.12 for $Au + Au$ collisions at $\sqrt{s_{NN}} = 39$ GeV, and in Figure.4.13 for $Au + Au$ collisions at $\sqrt{s_{NN}} = 62.4$ GeV.

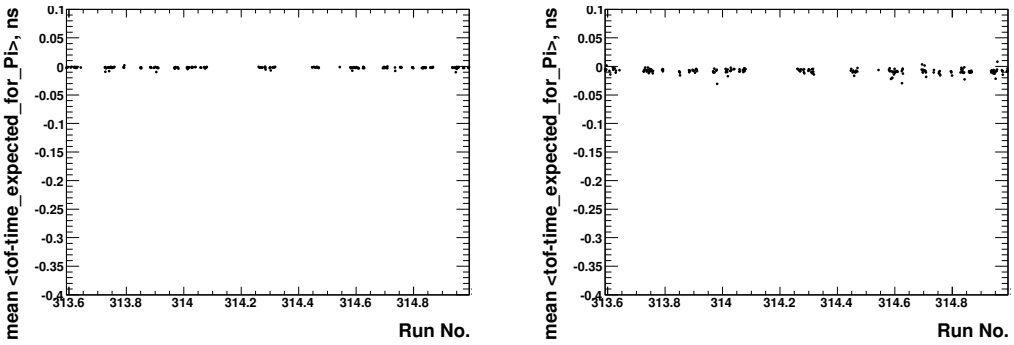


Figure 4.12: Run-by-run dependence of the timing resolution (center of near-zero peak) after correction for TOF-W (left) and TOF-E (right) at $\sqrt{s_{NN}} = 39$ GeV collisions

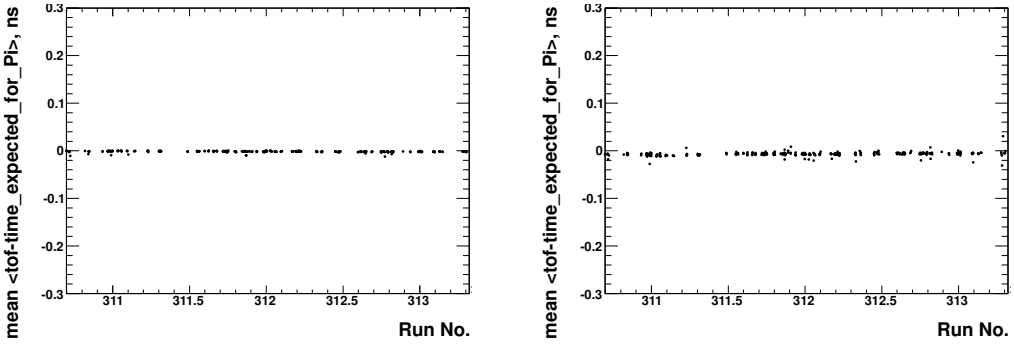


Figure 4.13: Run-by-run dependence of the timing resolution (center of near-zero peak) after correction for TOF-W (left) and TOF-E (right) at $\sqrt{s_{NN}} = 62.4$ GeV collisions

## 4.4 Analysis of $Au + Au$ Collisions

In this section, I will be discussing some of the analysis details, including the dataset, quality assurance (QA) check, event and track selection, many

correlation functions and estimate of systematic uncertainties. The $v_n$ results via long-range two-particle correlation method will be shown following this section.

### 4.4.1 Collisions at $\sqrt{s_{NN}} = 200$ GeV

The analysis presented in this subsection was performed with minimum bias (MB) $Au + Au$ events at $\sqrt{s_{NN}} = 200$ GeV from run year 2007 (Run7). A total of $\sim 3.6$ B events were used subsequent to the rejection of "bad" runs based on QA studies, and a $\pm$ 30 cm BBC Z-vertex cut.

#### QA

The particle identification was performed using both west and east arm TOF detectors. The present analysis is looking at the flow coefficients $v_n$ (n=2,3,4), based on long-range two-particle correlation method, as a function of $p_T$ and centrality.

The number of events in Run7 $Au + Au$ collisions is $\sim 3.6$ B. All the data collected are used in this analysis except the following runs:

- ♢ Zero field runs (7): 229545, 231156, 236137, 238530, 238531, 238971, 239312
- ♢ (++) field runs (15): 235889, 235890, 235891, 235892, 235893, 235894, 235895, 235900, 235901, 235902, 236004, 236005, 236007, 236008, 236009
- ♢ Converter runs (9): 238682, 238683, 238684, 238698, 238843, 238845, 238846, 238847, 238848
- ♢ Bad centrality runs (22) [121]: centrality distributions are plotted and fitted as a function of run number. The $\chi^2/ndf$ is calculated for the fits. It is shown by extensive studies that small deviations ($5 < \chi^2/ndf < 100$) will not affect the extracted $v_n$ via EP method. I will follow the same criterion to reject those "bad" centrality runs that appear to have $\chi^2/ndf > 100$. They are: 232996, 233474, 233475, 235032, 235050, 235658, 235659, 235660, 235684, 235686, 235690, 235699, 235794, 235795, 235796, 235797, 235798, 235801, 235802, 235805, 235807, 235809
- ♢ Runs with missing west arm (3): 232377, 232378, 232379

### Event and Track Selection

Event and track selection are listed below:

Event Selection

♢ Centrality range: 0-60%

♢ $|bbcz|$ <30 cm - BBC vertex cut

Track Selection

♢ Momemtum cut: 0.1–6.0 GeV/c

♢ DCH Track Quality: 31 or 63

♢ $|zed| < 75$cm

♢ $n_0 \leq 0$ – RICH veto cut, to suppress conversion particles with wrong reconstructed momentum

♢ Track is projected to its expected hit location on TOF. We require tracks to have a hit on TOF within $\pm 2\sigma$ ("radial" matching cut) of the expected hit location in both the azimuthal and beam direction

♢ $\pm 2\sigma$ radial matching on PC3, which is used to further suppress residual background

♢ Energy/Charge cut: $E_{tof}$ >0.002 for TOF-E and 60 <SumQ<600 for TOF-W

### Correlation Functions

Correlation functions were constructed following our standard practice of taking the ratio of two distributions:

$$C\left(\triangle\phi\right) = \frac{N_{pair,same}\left(\triangle\phi\right)}{N_{pair,mix}\left(\triangle\phi\right)}$$

where the numerator is the distribution of correlated pairs and the denominator is the distribution of uncorrelated pairs from mixed events. These pairs were selected so as to have the same centrality, zvtx bin, etc, as for the correlated pairs. In current analysis, the bbcz vertex is chopped into 10 bins within $|bbcz| < 30$ cm range, *i.e.*, 6 cm per zvtx bin. The centrality bin is selected at 10% increment.

- **Forward Track-Forward Track Correlations**

In this subsection, we will present the correlation functions from pair tracks from South-North forward detector (the RxNP detector in our analysis). The inner south ring of RxNP detector was found to be pathologic when we performed 2PC analysis for inclusive charged hadron $v_n$. Therefore, this problematic $S_{in}$[4] sector in RxNP is always excluded in this analysis. Since RxNP has inner and outer ring mirrored about collision vertex along beam axis, and given the fact that south inner ring is eliminated, there are three possible combinations of RxNP sectors for correlation function build-up, *i.e.*,

1. $RxNP_{S_{out}}$ with $RxNP_{N_{in+out}}$
2. $RxNP_{S_{out}}$ with $RxNP_{N_{out}}$
3. $RxNP_{S_{out}}$ with $RxNP_{N_{in}}$

The possible differences in Fourier coefficients extracted from correlation functions built with these three opposite-arm combinations are taken into account for systematic estimate, which will be further discussed in later part of this section. The correlations functions with harmonic fit built from these three RxNP sector combinations in $Au + Au$ collisions at $\sqrt{s_{NN}} = 200$ GeV are shown in Fig.4.14–4.16.

It must be emphasized again, the red solid curves indicate a Fourier fit to the data. All of the correlation functions show an asymmetry which reflects the contributions from the odd harmonics.

- **Central Track-Forward Track Correlations**

We build the correlation function according to Eqn.4.1 for different charged hadron species in central arm, that is, to correlate $\Delta\phi$ between hadron track in central arm with hit in the forward detector (RxNP in our case). The correlation functions as a function of $p_T$ and centrality are shown explicitly in this subsection. In each figure, the results are shown in $p_T$ increasing order from left to right and then top to bottom. The most upper left panel is the correlation function for specific hadron species at $p_T$ bin=1, to its right is for $p_T$ bin=2,... The $p_T$ bins in current analysis are defined in Table.4.1.

For illustration purpose, the correlation functions built from charged pions in central arm (CNT) and RxNP particle hits in 20-30% centrality bin are shown in Fig.4.17–4.19.

[4] $S_{in(out)}$ denotes the inner(outer) ring in the South arm of RxNP. Similarly, $N_{in(out)}$ denotes the inner(outer) ring in the North arm of RxNP. Similarly thereafter.

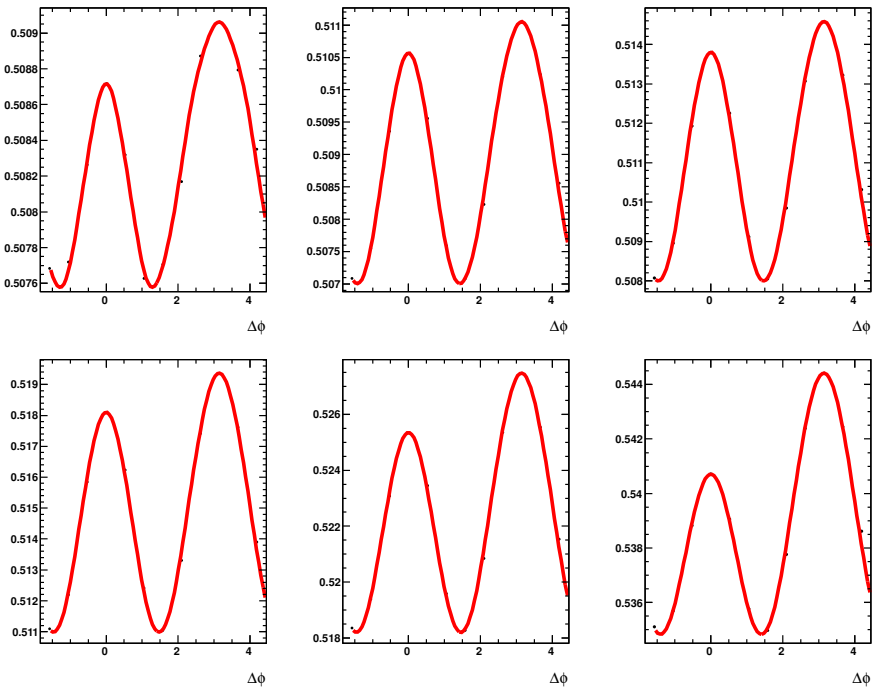


Figure 4.14: $RxNP_{Sout} - RxNP_{Nin+out}$ azimuthal angle correlation functions for the hits in the RxNP detector in $Au + Au$ collisions at $\sqrt{s_{NN}} = 200$ GeV. Results are shown in 10% centrality increments from left to right and then top to bottom. Red curve in each panel is the harmonic fit to its correlation function

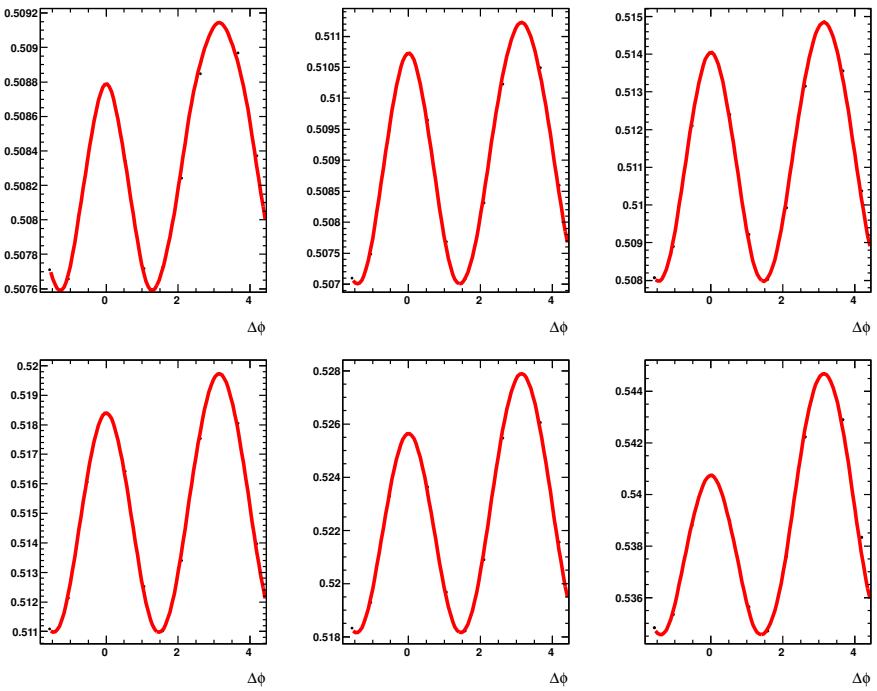


Figure 4.15: Similar to Fig.4.14, $RxNP_{Sout} - RxNP_{Nout}$ azimuthal correlation functions for the hits in the RxNP detector in $Au + Au$ collisions at $\sqrt{s_{NN}} =$ 200 GeV.

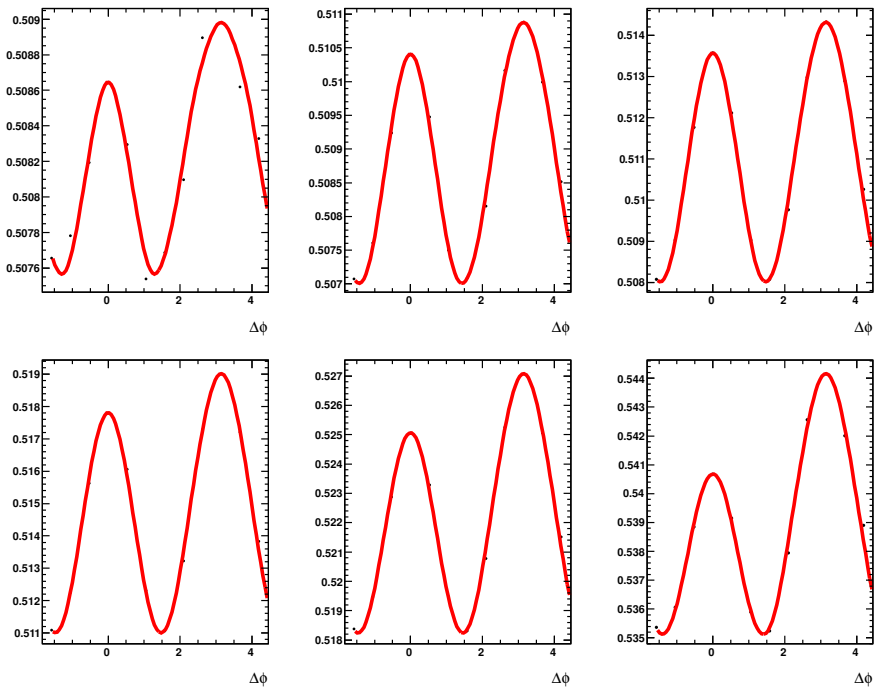


Figure 4.16: Similar to Fig.4.14, $RxNP_{Sout}$ – $RXN_{Nin}$ azimuthal correlation functions for the hits in the RxNP detector in $Au + Au$ collisions at $\sqrt{s_{NN}} =$ 200 GeV.

| $p_T$ | **bin no.** |
|---|---|
| 0.3 GeV/c< $p_T$ <0.5 GeV/c | 1 |
| 0.5 GeV/c< $p_T$ <0.7 GeV/c | 2 |
| 0.7 GeV/c< $p_T$ <0.9 GeV/c | 3 |
| 0.9 GeV/c< $p_T$ <1.1 GeV/c | 4 |
| 1.1 GeV/c< $p_T$ <1.3 GeV/c | 5 |
| 1.3 GeV/c< $p_T$ <1.5 GeV/c | 6 |
| 1.5 GeV/c< $p_T$ <1.7 GeV/c | 7 |
| 1.7 GeV/c< $p_T$ <1.9 GeV/c | 8 |
| 1.9 GeV/c< $p_T$ <2.1 GeV/c | 9 |
| 2.1 GeV/c< $p_T$ <2.3 GeV/c | 10 |
| 2.3 GeV/c< $p_T$ <2.5 GeV/c | 11 |
| 2.5 GeV/c< $p_T$ <2.7 GeV/c | 12 |
| 2.7 GeV/c< $p_T$ <3.0 GeV/c | 13 |
| 3.0 GeV/c< $p_T$ <3.5 GeV/c | 14 |
| 3.5 GeV/c< $p_T$ <6.0 GeV/c | 15 |

Table 4.1: $p_T$ bins in the analysis of $Au + Au$ collisions at $\sqrt{s_{NN}}$ = 200, 62.4 and 39 GeV.

In particular, to study the independent contributions to correlation functions from East and West arm, the charged pions from central arm are collected in the following three cases to build CentralTrack-ForwardTrack Correlations:

1. in East plus West arm TOF,
2. in East arm TOF only,
3. in West arm TOF only

which correspond to plot in 4.17, 4.18 and 4.19, respectively.

The correlation functions built from charged kaons and (anti-)protons in combined TOF-W+TOF-E and RxNP hits in 20-30% centrality bin are shown in Fig.4.20 and 4.21, respectively. Please note that $p\bar{p}$ are selected with minimum $p_T$ of 0.5 GeV/c. The middle panel in the top row of Fig.4.21 is the minimum $p_T$ bin (=2) for $p\bar{p}$, and the upper left panel is "missing".

### Systematic Uncertainties & 2PC $v_n$ Results

The Fourier coefficients $v_n$ are extracted as a function of $p_T$ and centrality after careful evaluations for a potential bias from detector acceptance($\eta$). Here, it is important to note that it is well known one of the sectors on the inner part

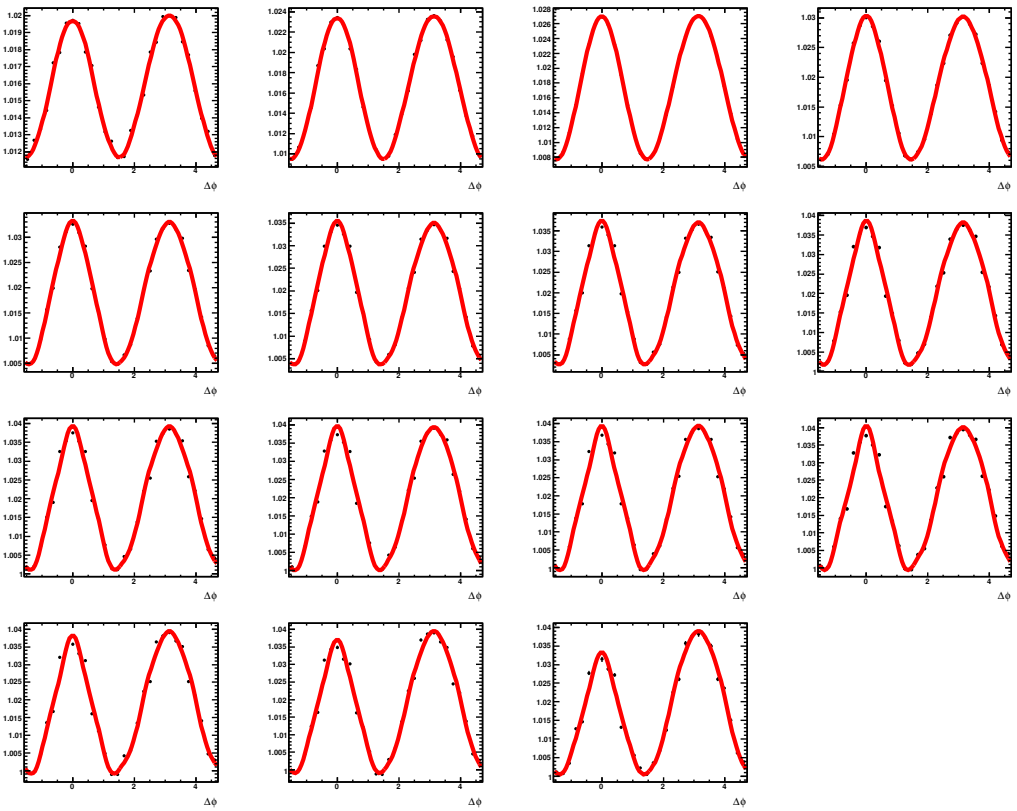

Figure 4.17: CNT-RxNP azimuthal correlation functions for charged **Pions** in **TOF-W+TOF-E** in **20-30%** centrality, in $Au + Au$ collisions at $\sqrt{s_{NN}} =$ 200 GeV. Results are shown in $p_T$ increments from left to right and then top to bottom. Red curve in each panel is the harmonic fit to its correlation function. Full RxNP acceptance is used, excluding $RxNP_{S_{in}}$.

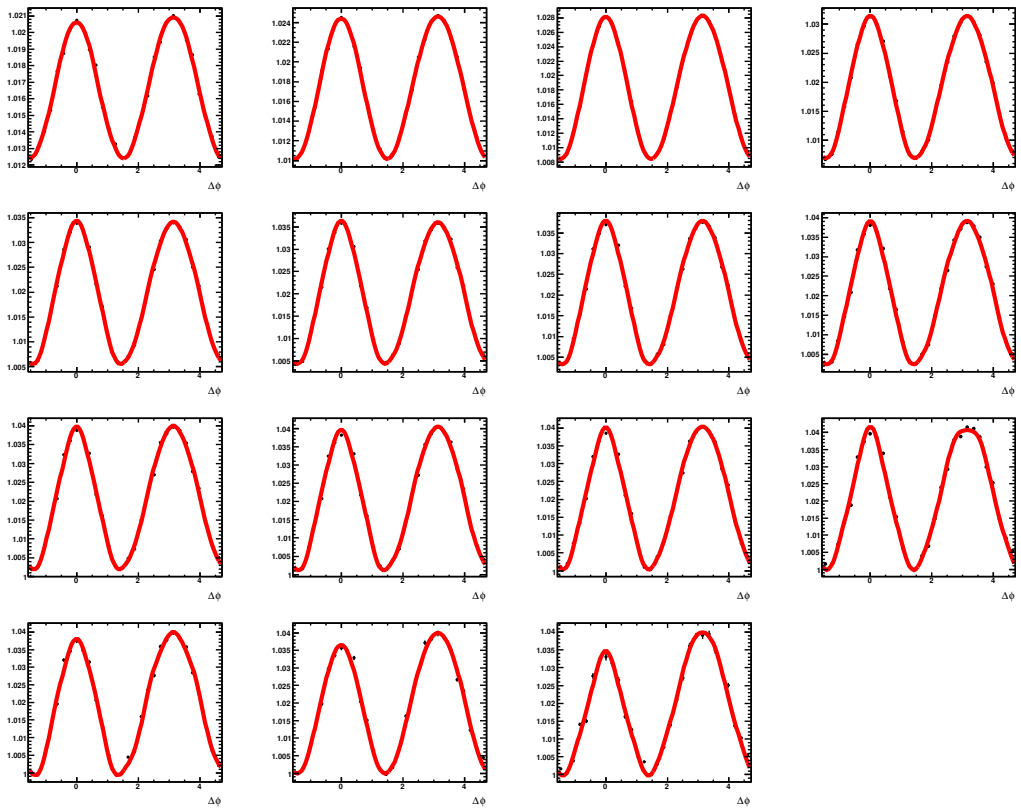

Figure 4.18: Similar to Fig.4.17, but for pions in TOF-E only.

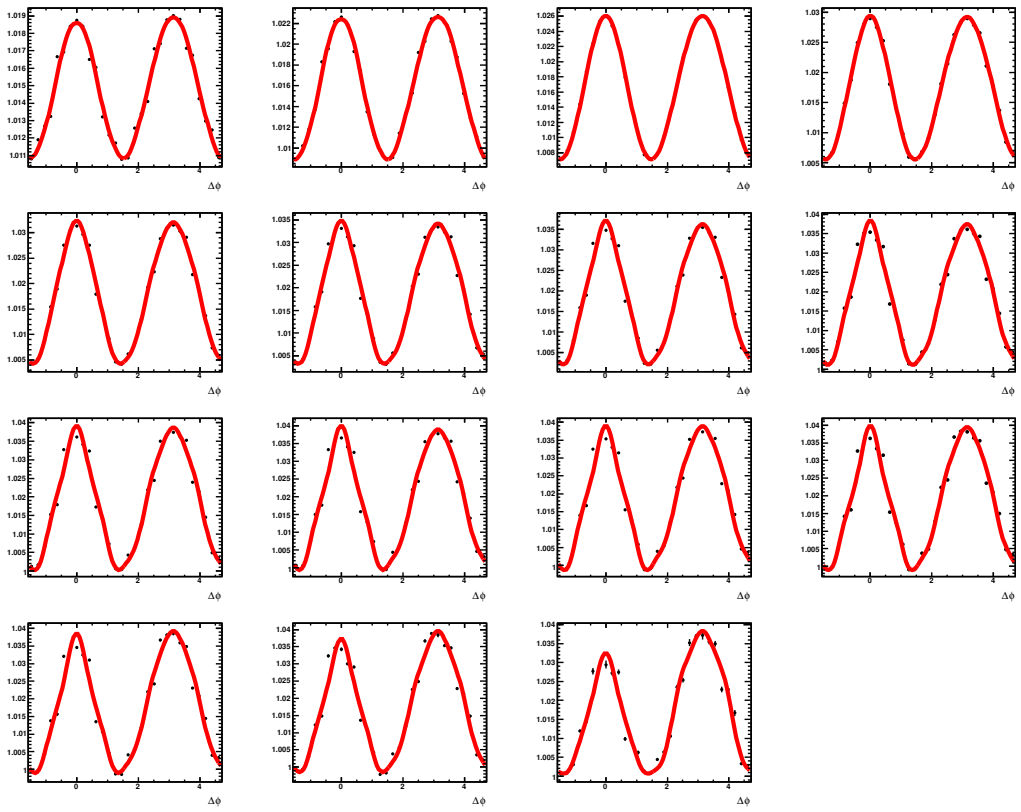

Figure 4.19: Similar to Fig.4.17, but for pions in TOF-W only.

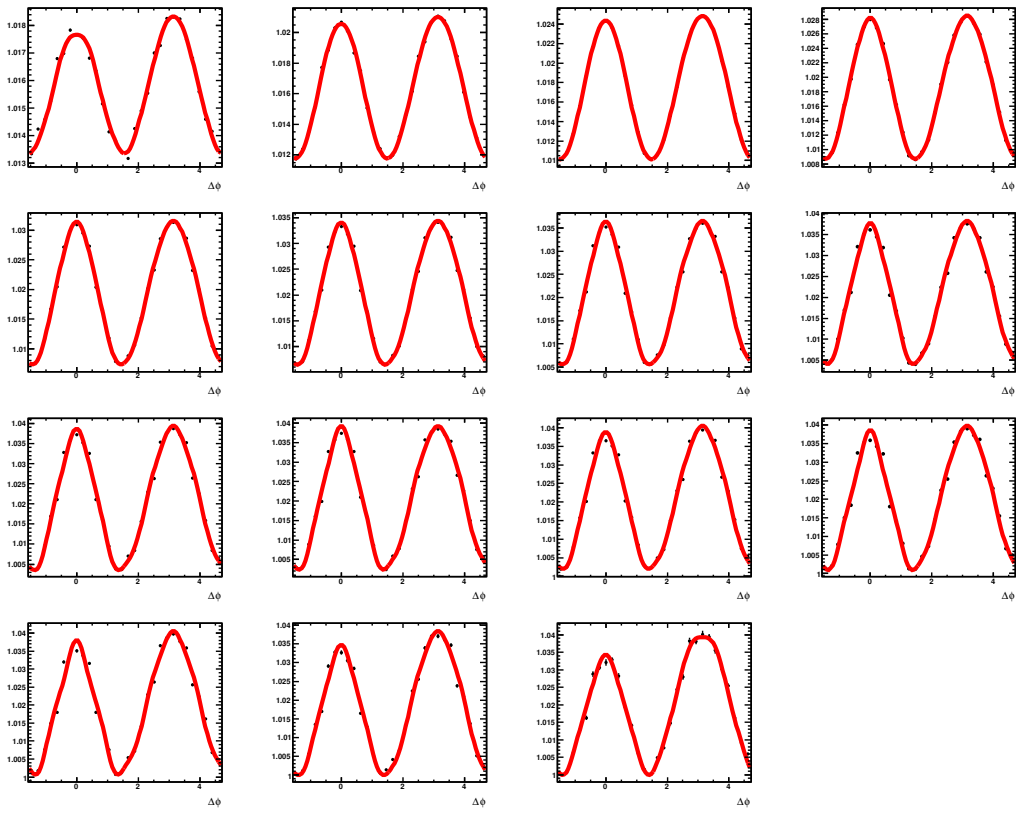

Figure 4.20: CNT-RxNP azimuthal angle correlation functions for charged **Kaons** in **TOFW+TOFE** in **20-30%** centrality, in $Au + Au$ collisions at $\sqrt{s_{NN}} = 200$ GeV. Results are shown in $p_T$ increments from left to right and then top to bottom. Red curve in each panel is the harmonic fit to its correlation function. Full RxNP acceptance is used, excluding $RxNP_{S_{in}}$.

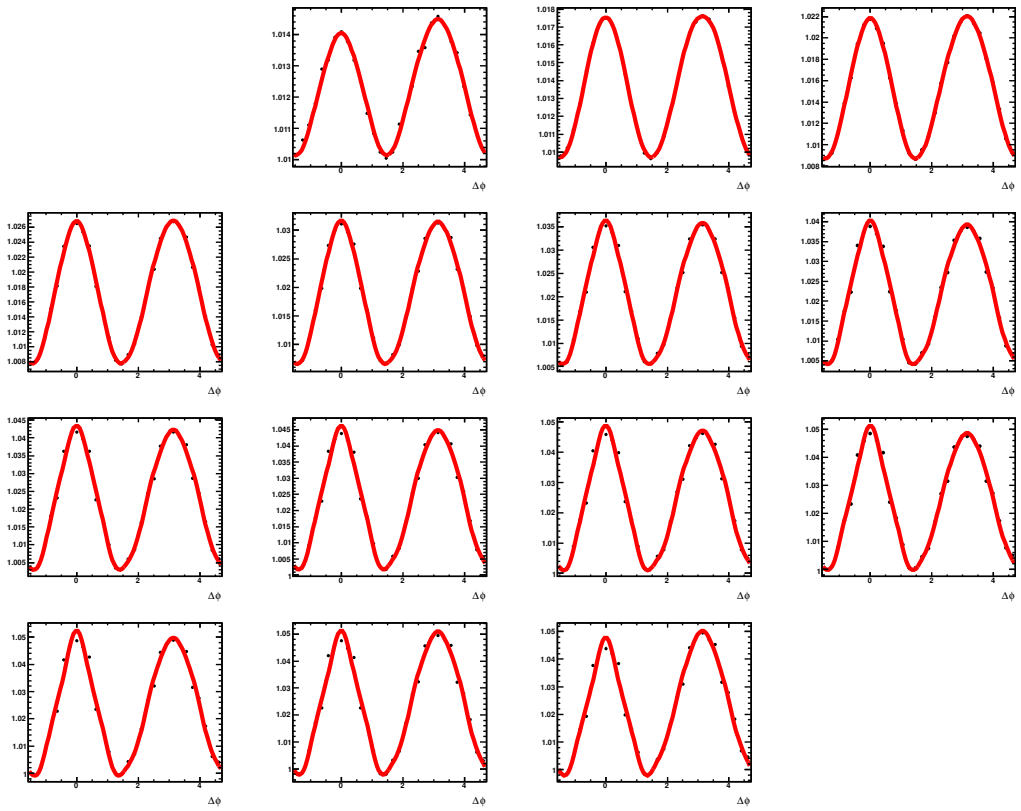

Figure 4.21: CNT-RxNP azimuthal angle correlation functions for **protons(and anti-protons)** in **TOFW+TOFE** in **20-30%** centrality, in $Au+Au$ collisions at $\sqrt{s_{NN}} = 200$ GeV. Results are shown in $p_T$ increments from left to right and then top to bottom. Red curve in each panel is the harmonic fit to its correlation function. Full RxNP acceptance is used, excluding $RxNP_{S_{in}}$.

of RxNP (South inner ring) did not function reliably during the run 2007. We also checked the sensitivity of the results to TOF-W/E acceptance.

In this section, we are going to discuss the systematic uncertainties of $v_n$ for different charged hadron species, and estimate the possible uncertainties induced from different RxNP segment combinations and different TOFE or TOF-W acceptance.

Since inclusive charged hadron $v_n$ are just weighted sum of identified charged hadron $v_n$, and we use both TOF-W and TOF-E as the PID detector, we would start off with the inclusive charged hadron $v_n$ in TOF acceptance, and study the possible variations induced from different detector $\eta$ acceptance(*i.e.* difference RXN segment combinations) and TOF-E/W acceptance. The Figure. 4.22, 4.23 and 4.24 are for $v_2$, $v_3$ and $v_4$ of inclusive charged hadron in TOF acceptance. The values obtained from various types of correlation functions are indicated in legend, which is also explicitly listed below:

* red: central arm track in TOF-W correlated with hits in RxNP $South_{out}-North_{in+out}$
* blue: central arm track in TOF-E correlated with hits in RxNP $South_{out}-North_{in+out}$
* green: central arm track in TOF-W correlated with hits in RxNP $South_{out}-North_{out}$
* magenta: central arm track in TOF-E correlated with hits in RxNP $South_{out} - North_{out}$
* grey: central arm track in TOF-W correlated with hits in RxNP $South_{out}-North_{in}$
* black: central arm track in TOF-E correlated with hits in RxNP $South_{out}-North_{in}$
* light blue (default): central arm track in TOF-W + TOF-E correlated with hits in RxNP $South_{out} - North_{in+out}$

The ratio plots for inclusive charged hadron $v_n$ (n=2,3,4) in TOF acceptance are shown in the Figure.4.25, 4.26 and 4.27 . To illustrate the possible statistical errors and to avoid making the plot too busy, here we just indicate the associated errors when taking the ratio of TOFE-$RxNPS_{out}N_{out}$ to our default setting.

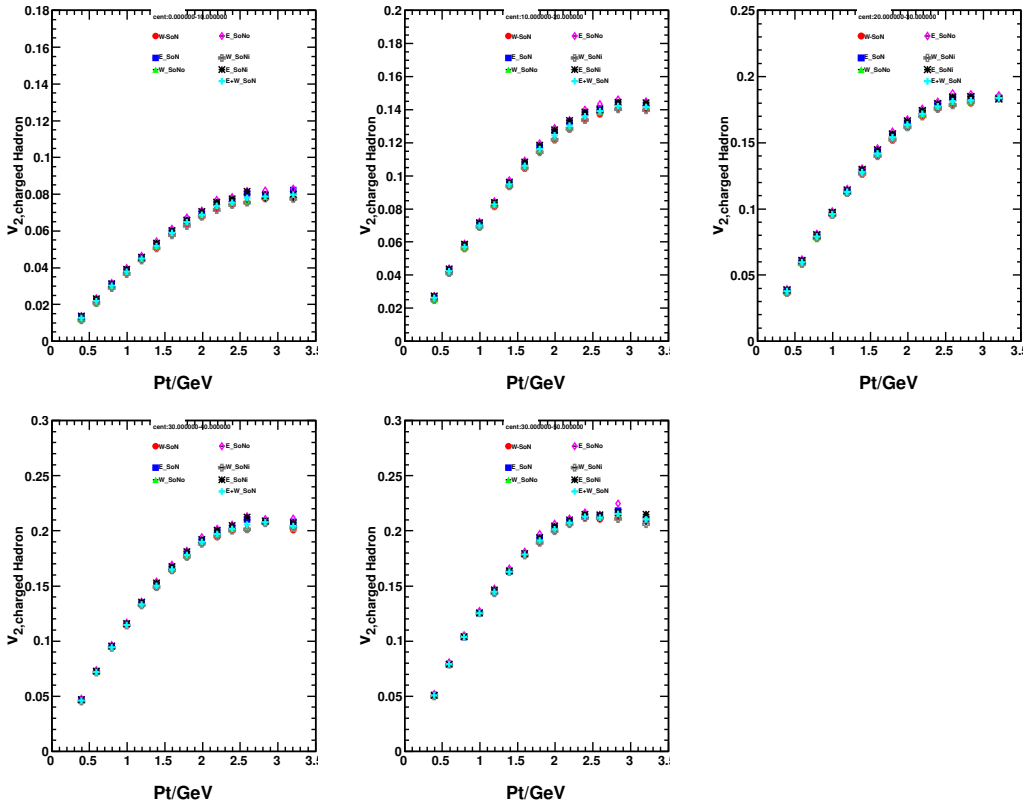


Figure 4.22: $v_2$ of inclusive charged hadron in TOF acceptance. Results are shown in 10% centrality increments from left to right and then top to bottom, starting from 0-10% at top-left panel. Error bars are for statistical only, same below

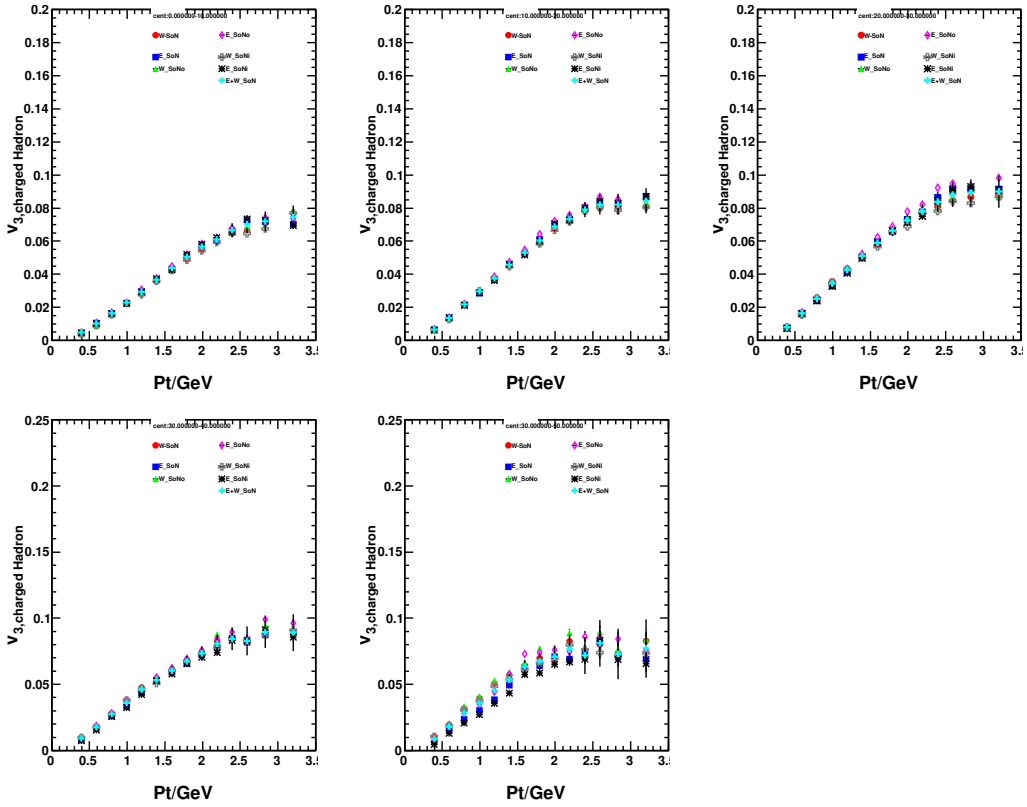


Figure 4.23: $v_3$ of inclusive charged hadron in TOF acceptance. Results are shown in 10% centrality increments from left to right and then top to bottom,starting from 0-10% at top-left panel.

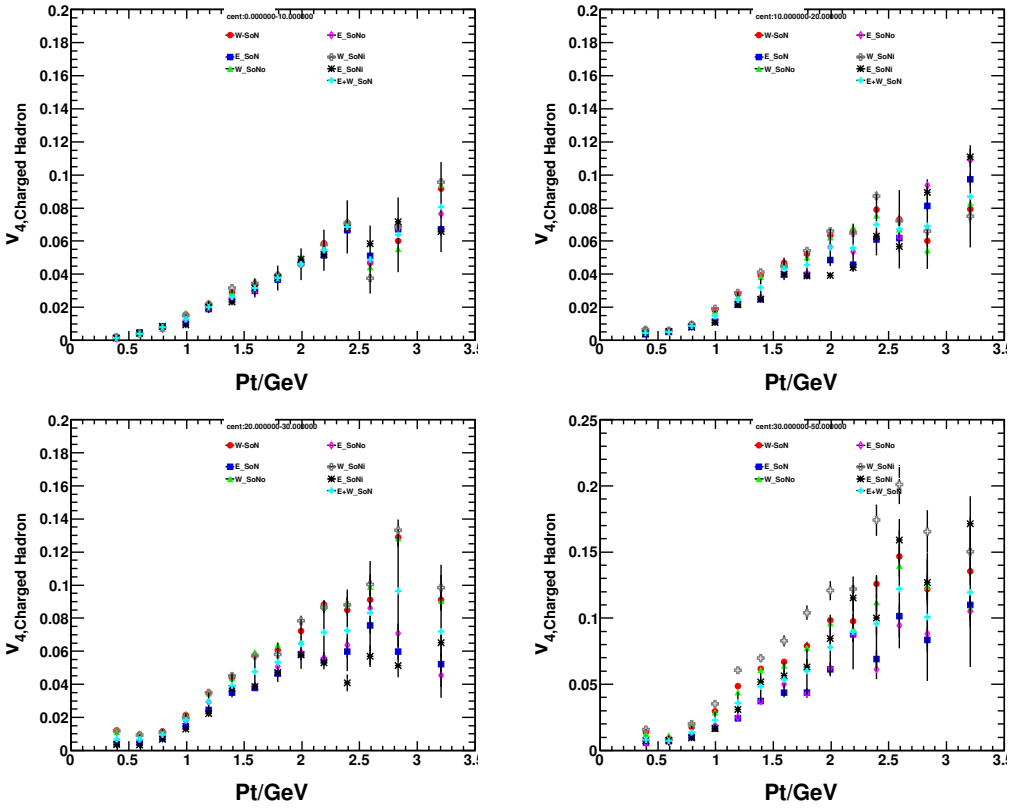


Figure 4.24: $v_4$ of inclusive charged hadron in TOF acceptance. Results are shown in 10% centrality increments from left to right and then top to bottom,starting from 0-10% at top-left panel. **Note**: the bottom-right panel is for 30-50%.

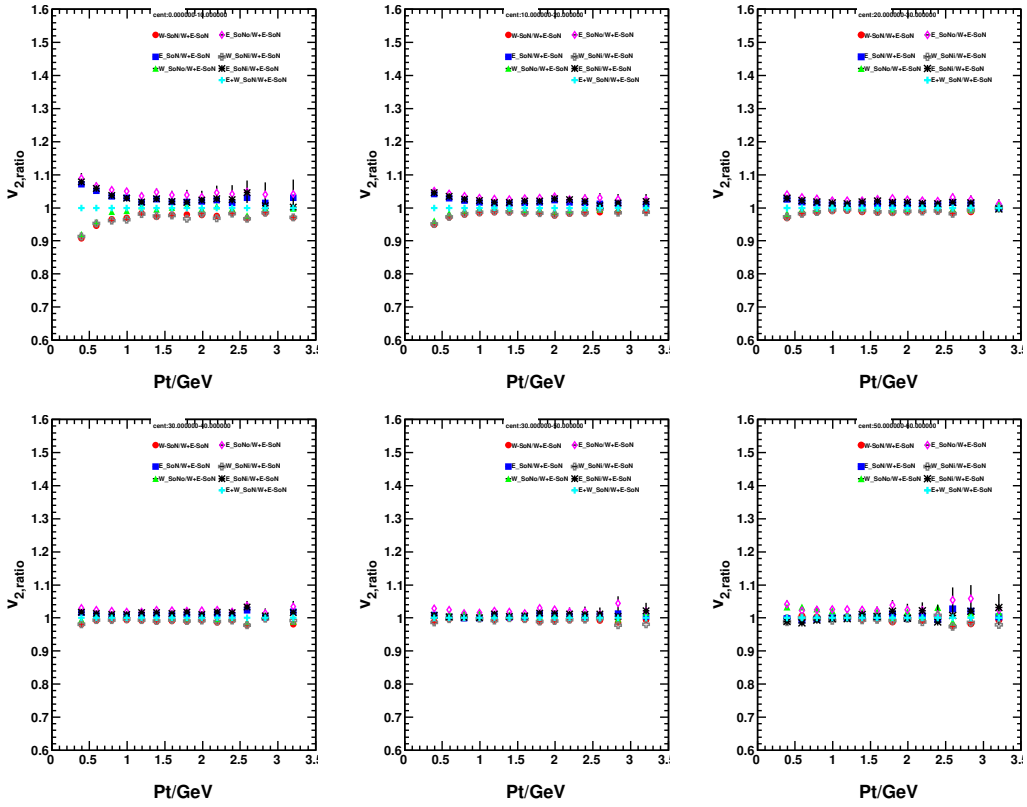


Figure 4.25: Ratio of inclusive charged hadron $v_2$ in various TOF acceptance w.r.t $v_2$ from default TOFE+W with $RxNPS_{out}N_{in+out}$. Results are shown in 10% centrality increments from left to right and then top to bottom, starting from 0-10% at top-left panel. Error bars are for statistical only, same below

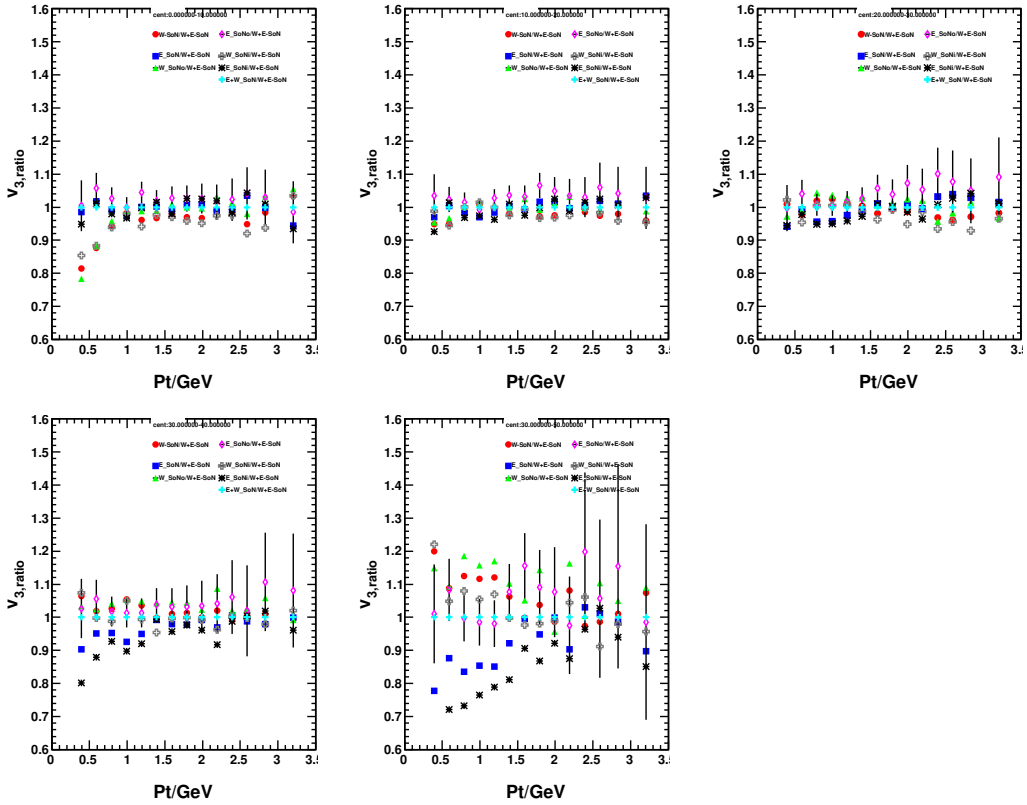


Figure 4.26: Ratio of inclusive charged hadron $v_3$ in various TOF acceptance w.r.t $v_3$ from default TOFE+W with $RxNPS_{out}N_{in+out}$. Results are shown in 10% centrality increments from left to right and then top to bottom, starting from 0-10% at top-left panel.

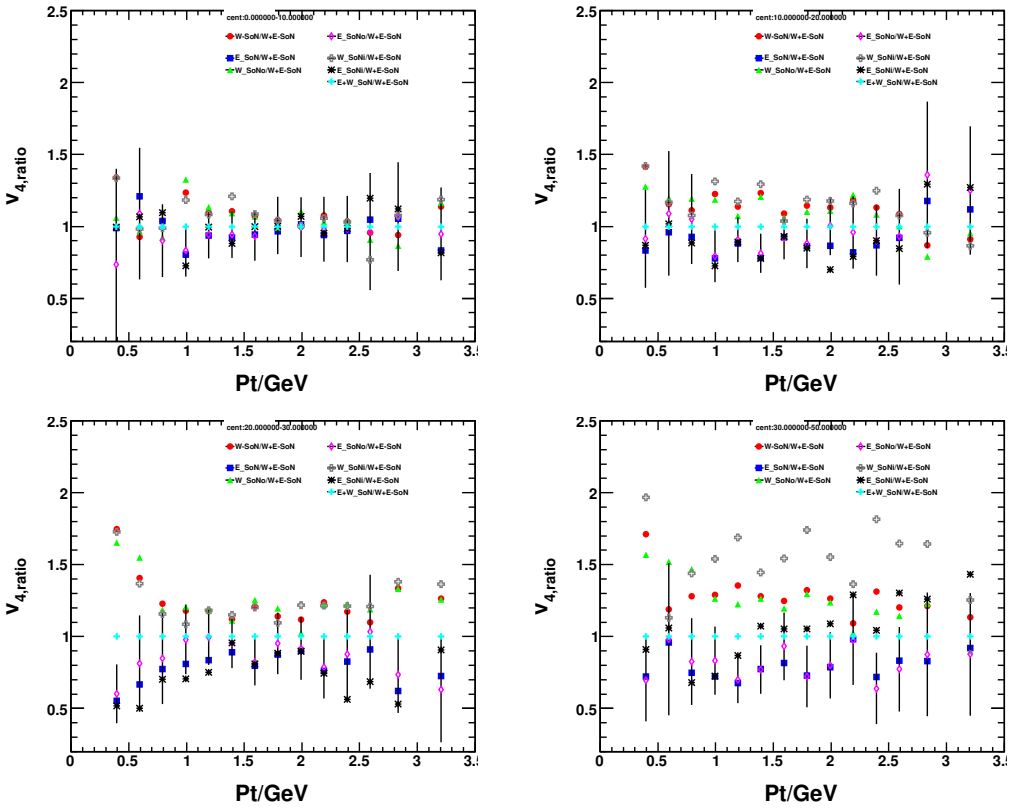


Figure 4.27: Ratio of inclusive charged hadron $v_4$ in various TOF acceptance w.r.t $v_4$ from default TOFE+W with $RxNPS_{out}N_{in+out}$. Results are shown in 10% centrality increments from left to right and then top to bottom, starting from 0-10% at top-left panel. **Note**: the bottom-right panel is for 30-50%.

Note that again *in* and *out* select different $\eta$ gaps. The comparison show relatively good agreement between the different measurements. What is important is the fact that the observed deviation increases with the value $n$ of the harmonic.

Systematic error estimates were obtained primarily via study of the dependence of $v_n$ on the separate TOF-W/E acceptance as well as on the choice of the RxNP sub-detector used to generate the correlation functions. Note that $RxNPSouth_{in}$ is not used in these evaluations because of its pathological nature. Since the inclusive charged hadron flow can be considered as the source of systematic uncertainties for PIDed case, and it is common to each particle species, the uncertainties associated with it can be viewed as the systematic errors that further propagate to pions, kaons and $p\bar{p}$. The ratio plots above show very little difference ($\sim$ 3-5%) for $v_2$ but do show variations of $\sim$8–12% and $\sim$20–25% for $v_3$ and $v_4$ respectively, depending on centrality.

For $v_2$, based on results of inclusive charged hadrons in TOF acceptance, as shown in figures 4.22 and 4.25, we assign 5% for points $< 1$ GeV/c in 0-10% and 10-20%. For all the other $p_T$ points in these two centrality slices and in 20-30%, 30-40% and 40-50% centralities, we assign 3%; For 50-60%, we assign 5%.

For $v_3$, based on results of inclusive charged hadrons in TOF acceptance, as shown in figures 4.23 and 4.26, we assign 8% for 0-10%, 10-20%, 20-30%. We assign 10% for 30-40%. For 40-50%, we assign 12%.

For $v_4$, based on results of inclusive charged hadrons in TOF acceptance, as shown in figures 4.24 and 4.27, we assign 20% for 0-10%, 10-20%. We assign 25% for 20-30%, 30-40% and 40-50%.

For $v_n$ measurements in a relatively broad centrality range, for example, 0-50%, we performed the same studies on inclusive charged hadron in TOF acceptance among various RxNP segment combinations. The actual value and corresponding ratio plots can be found at Fig.4.28 and 4.29. The 0-50% results are multiplicity-scaled from $p_T$ spectra in each centrality and $p_T$ bin. To be explicitly, for each particle species, the $v_n$ of 0-50% for certain $p_T$ bin can be obtained from:

$$\frac{\sum_{icent=0,1,2,3,4} v_n(icent, p_T) \times Multiplicity(icent, p_T)}{\sum_{icent=0,1,2,3,4} Multiplicity(icent, p_T)} \tag{4.9}$$

Based on results of inclusive charged hadrons in TOF acceptance, as shown in figures 4.28 and 4.29, we assign 3% systematic uncertainties for $v_2$, 6% for $v_3$ and 20% for $v_4$, in $Au+Au$ collisions at $\sqrt{s_{NN}} = 200$ GeV, 0-50% centrality bin.

In summary, the observations from the studies are quoted as systematic uncertainty and tabulated in Table.4.2.

Table 4.2: Systematic uncertainties for PIDed $v_n$ results in $Au + Au$ collision at $\sqrt{s_{NN}} = 200$ GeV.

| Centraltiy (%) | 0–10 | 10–20 | 20–30 | 30–40 | 40–50 | 50–60 | 0-50 |
|---|---|---|---|---|---|---|---|
| $v_2$ (% err.) | 3–5* | 3–5* | 3 | 3 | 3 | 5 | 3 |
| $v_3$ (% err.) | 8 | 8 | 8 | 10 | 12 | N/A | 6 |
| $v_4$ (% err.) | 20 | 20 | 25 | 25 | 25 | N/A | 20 |

* 5% for points $< 1$ GeV/c in 0-10% and 10-20%. For all the other $p_T$ points in these two centrality slices, systematic uncertainty is 3%

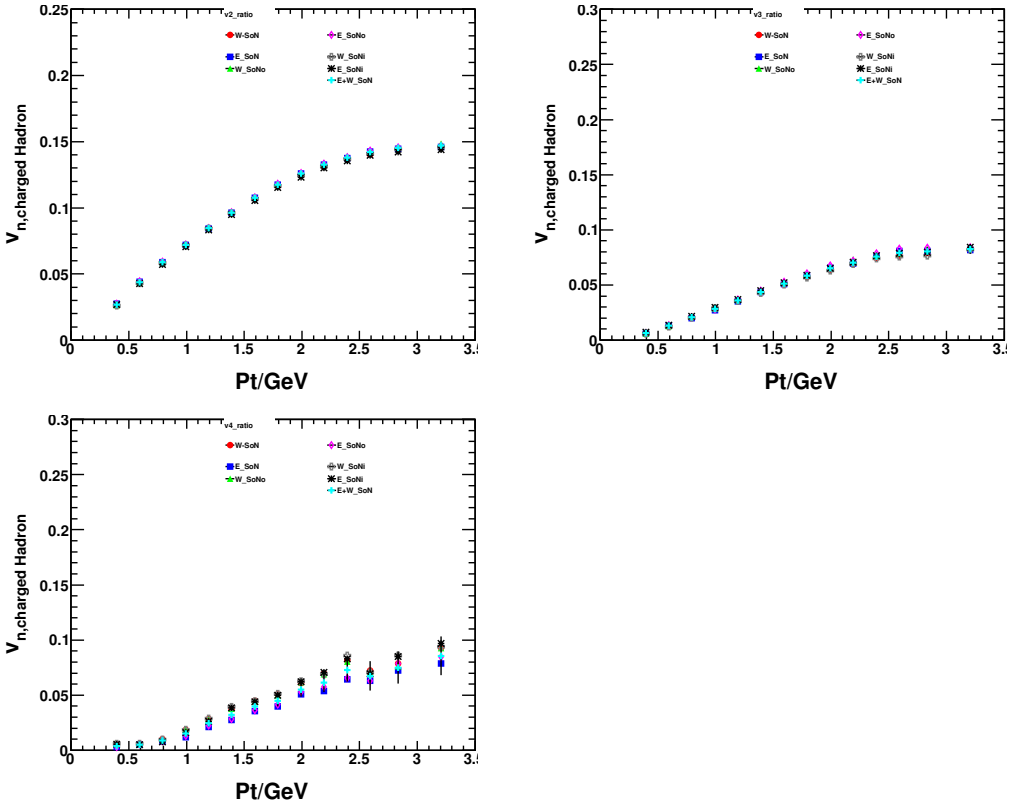


Figure 4.28: Inclusive charged hadron $v_n$ in various TOF acceptance correlated with various RxNP segment combinations, in $Au + Au$ collisions at $\sqrt{s_{NN}} =$ 200 GeV, 0-50% centrality bin. Results are shown in sequence of $v_2$ to $v_4$ from left to right and then top to bottom, starting from $v_2$ at top-left panel.

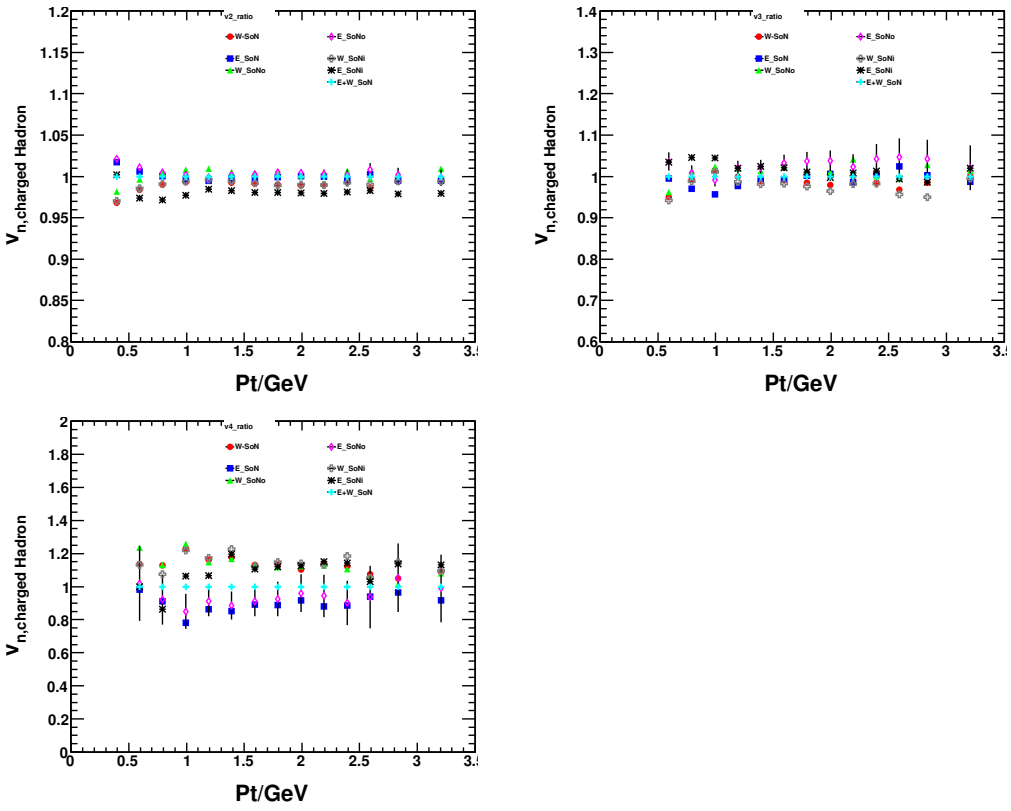


Figure 4.29: Ratio of inclusive charged hadron $v_n$ in various TOF acceptance w.r.t $v_n$ from default TOF-E + TOF-W with $RxNPS_{out}N_{in+out}$, in $Au + Au$ collisions at $\sqrt{s_{NN}}$ = 200 GeV, 0-50% centrality bin. Results are shown in sequence of $v_2$ to $v_4$ from left to right and then top to bottom, starting from $v_2$ at top-left panel.

Upon acquiring the systematic uncertainties, the harmonic coefficients $v_n$ as a function of $p_T$ in various centrality bins via 2PC method are shown in Fig.4.30–4.33.

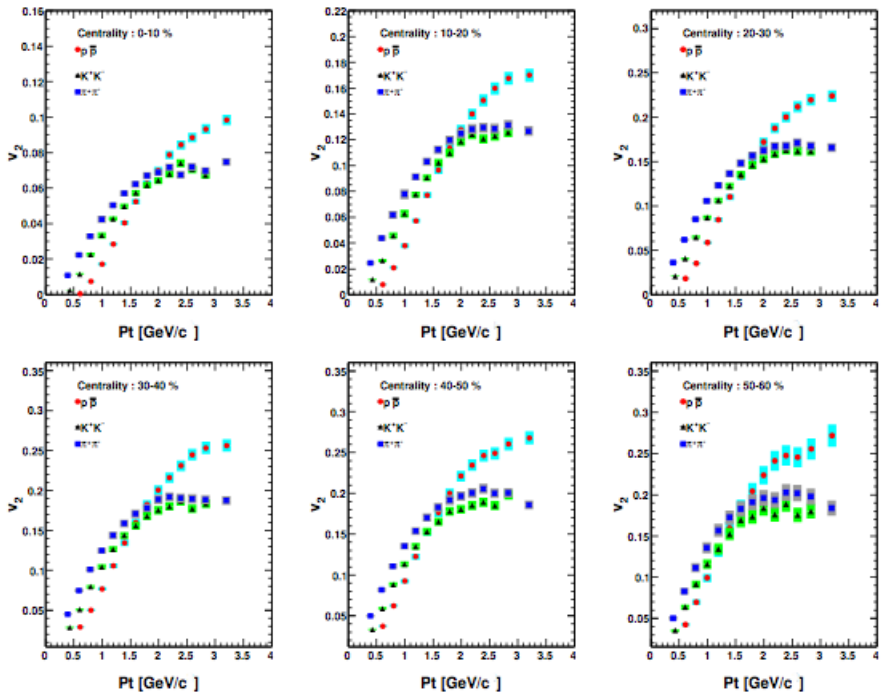


Figure 4.30: Particle IDentified $v_2$ results as a function of $p_T$ in various centrality slices for $Au + Au$ collision at $\sqrt{s_{NN}} = 200$ GeV. Results are shown in 10% centrality increments from left to right and then top to bottom, starting from 0-10% at top-left panel. Shaded bands are for systematic uncertainties associated with data points.

The error bars in Fig.4.30–4.32 indicate statistical uncertainties and shaded bands represent systematic uncertainties associated with data points. The cyan curves in Fig.4.33 indicate the $p_T$-dependent systematic uncertainties for charged pions. In all these measurements, for second order harmonic coefficient, $v_2$, a clear centrality dependence is observed for all particle species. In low $p_T$ region, mass ordering is seen. As stated in Chapter One, such mass splitting in $v_2$ is considered as the result of hydrodynamic behavior of flow expansion. For $v_3$, due to its fluctuation-induced nature, the magnitude does not seem to vary too much with centrality. $v_4$ suffers from the systematic uncertainty, which is root in the azimuthal resolution of RxNP detector (cf. Section 2.2.3 of Chapter Two).

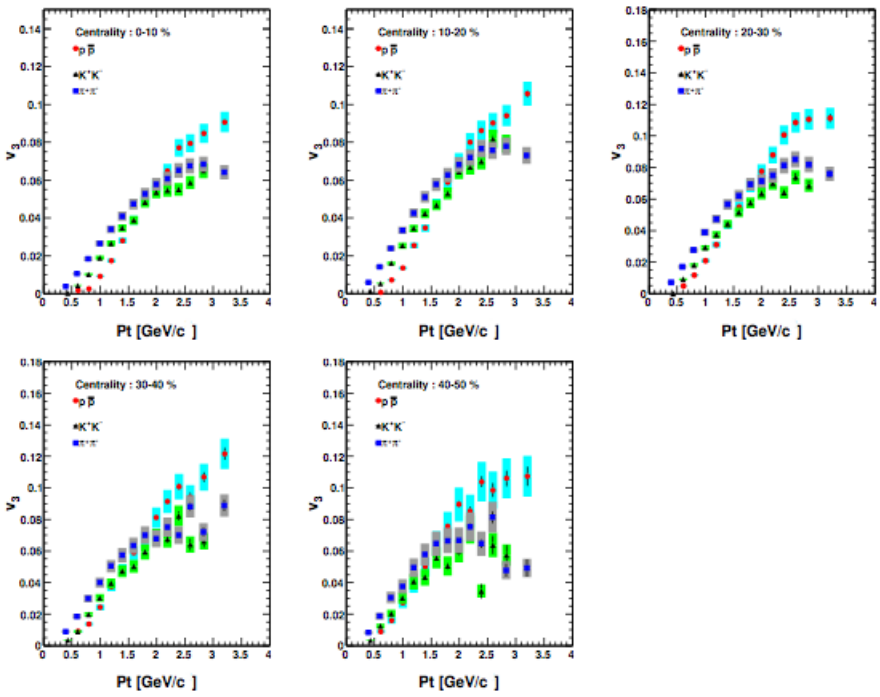


Figure 4.31: Particle IDentified $v_3$ results as a function of $p_T$ in various centrality slice for $Au + Au$ collision at $\sqrt{s_{NN}} = 200$ GeV. Results are shown in 10% centrality increments from left to right and then top to bottom, starting from 0-10% at top-left panel. Shaded bands are for systematic uncertainties associated with data points.

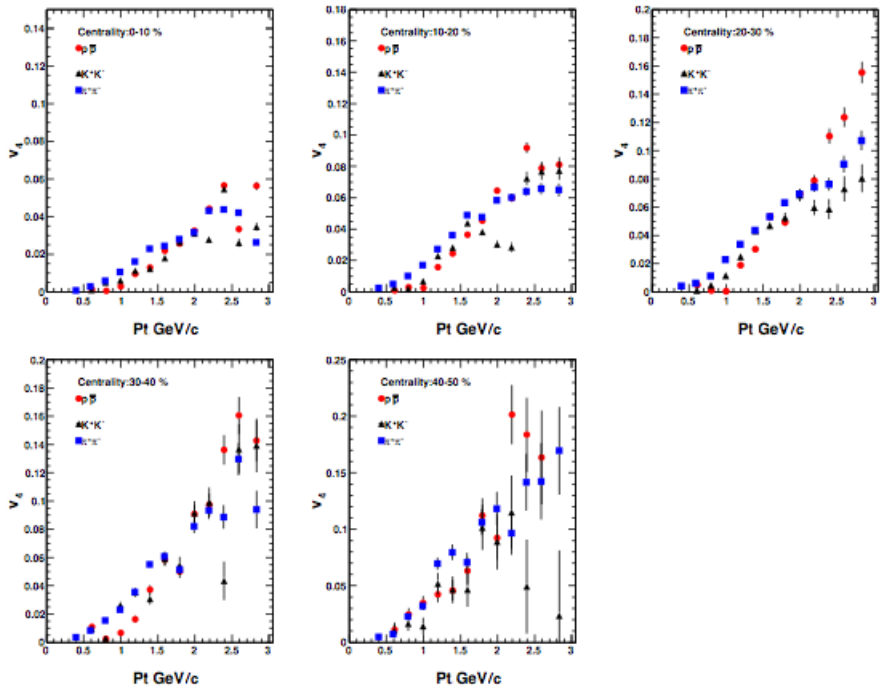


Figure 4.32: Particle IDentified $v_4$ results as a function of $p_T$ in various centrality slice for $Au + Au$ collision at $\sqrt{s_{NN}} = 200$ GeV. Results are shown in 10% centrality increments from left to right and then top to bottom, starting from 0-10% at top-left panel. **Note:only statistical errors are shown**

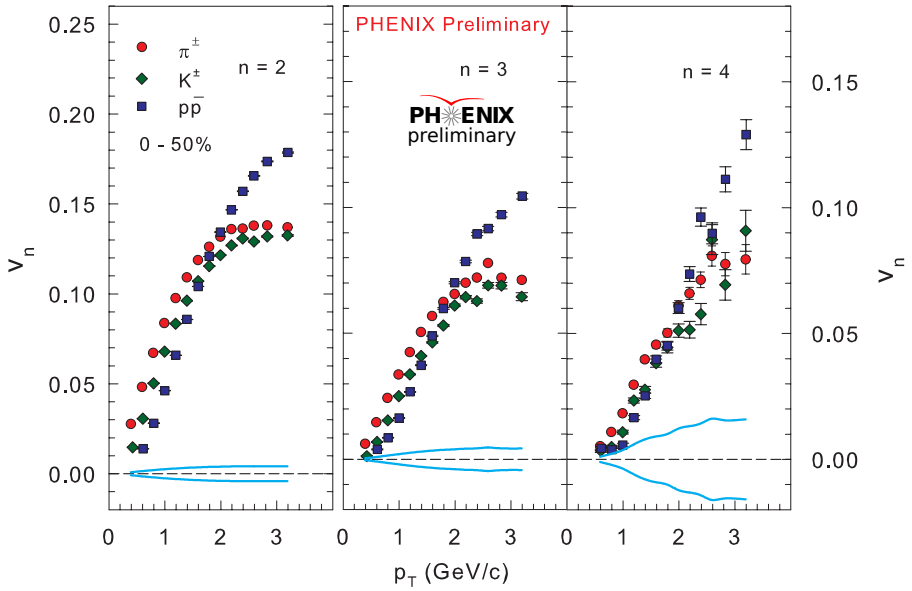


Figure 4.33: Partiel IDentifed $v_n$ (n=2,3,4) as a function of $p_T$ in 0-50% $Au+Au$ collisions at $\sqrt{s_{NN}}$ = 200 GeV. Cyan curves indicate the $p_T$-dependent systematic uncertainties for charged pions.

### Cross-check with Results via EP Method

For illustration purpose, the comparison made for charged pions $v_n$ (n=2,3,4) is shown in Fig.4.34, where we plot the $v_n$ (n=2,3,4) in 10% centrality step for $\pi^+, \pi^-$ from central to mid-central events, via both 2PC and EP method. The red dots are the $v_n$ values from long-range two-particle correlation method, and down-triangles are from EP analysis [118]. To avoid being too busy, only statistical uncertainties are indicated by error bars. Note that systematic uncertainties are comparable across these two methods, though they may differ a little depending on methodology-specific uncertainty estimate. It is striking to find that very good agreement is achieved in these two sets of $v_n$ results.

Similar studies were also performed for charged kaons and (anti-)protons $v_n$ (n=2,3,4) in 10% centrality step for central to mid-central events from 2PC and EP method. Again, we found remarkable consistencies in these cross-method comparisons, which may suggest the absence, or at least great suppression, of jet-biased non-flow contributions (mostly away-side jet) to flow measurements. In turn, such finding from comparisons indicates the domain we are looking at through these $v_n$ measurements is flow-dominated.

### Scaling Properties

It is shown [80] that an interesting test for the hydrodynamic pressure gradient-driven flow is to see the transverse kinentic energy $KE_T$-dependence of per constituent quark harmonic coefficient. The $KE_T$ is defined as $\sqrt{p_T^2 + m^2} - m$ ($m$ for hadron mass).

From Fig.1.7 in Section.1.2.4, the $v_2$'s of various hadron species scale to a single curve for $KE_T < 1$ GeV, a phenomenon usually referred to as "mass scaling". A clear separation is observed between baryons branch and mesons branch for $KE_T > 1$ GeV. The different scaling features below and above $KE_T \sim 1$ GeV indicate a possible transition from hydrodynamic flow description (eccentricity-driven) to jet-medium interaction description (suppression-driven) of QGP in different energy scale.

When the number of constituent quark (or valence quarks), $n_q$, is taken into account for each hadron species, as shown in Fig.1.11 panel (b), the per constituent quark $v_2$, $v_2/n_q$, scales with $KE_T/n_q$ well in the entire $KE_T$ range. This phenomenon is considered as a great evidence to support the proposition of partonic collectivity and the coalescence (recombination) mechanism of hadronization up to intermediate $p_T \lesssim 4$ GeV/c.

Similar studies were performed for our obtained $v_n$ (n=2,3,4) results in $Au + Au$ collisions at $\sqrt{s_{NN}} = 200$ GeV. Figure.4.35–4.37 show the number of constituent quark (NCQ) scaled $v_n$ (n=2,3,4) as a function of $KE_T/n_q$ in

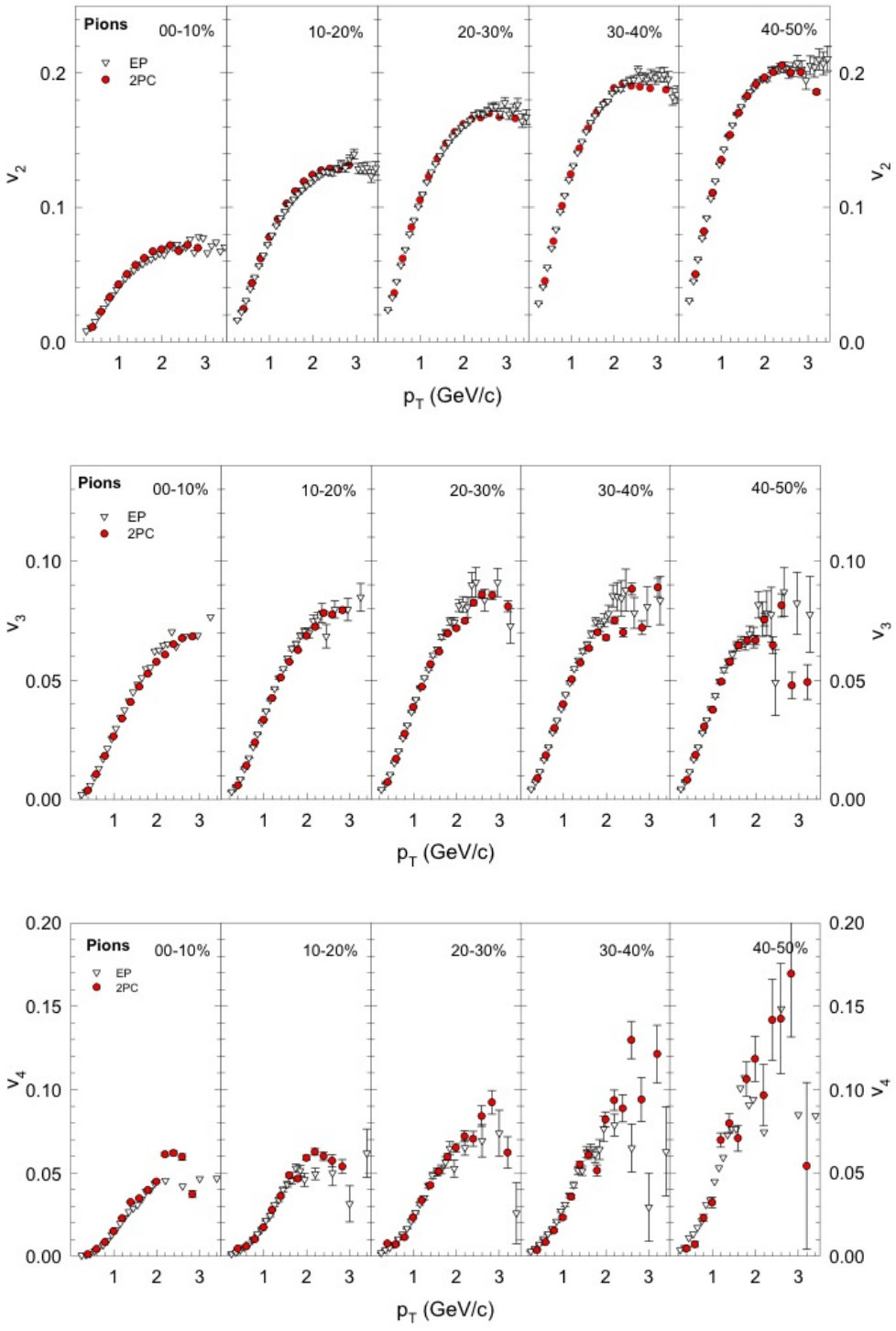


Figure 4.34: The comparison of charged pions $v_n$ (n=2,3,4) between 2PC and EP method.

various centrality slices.

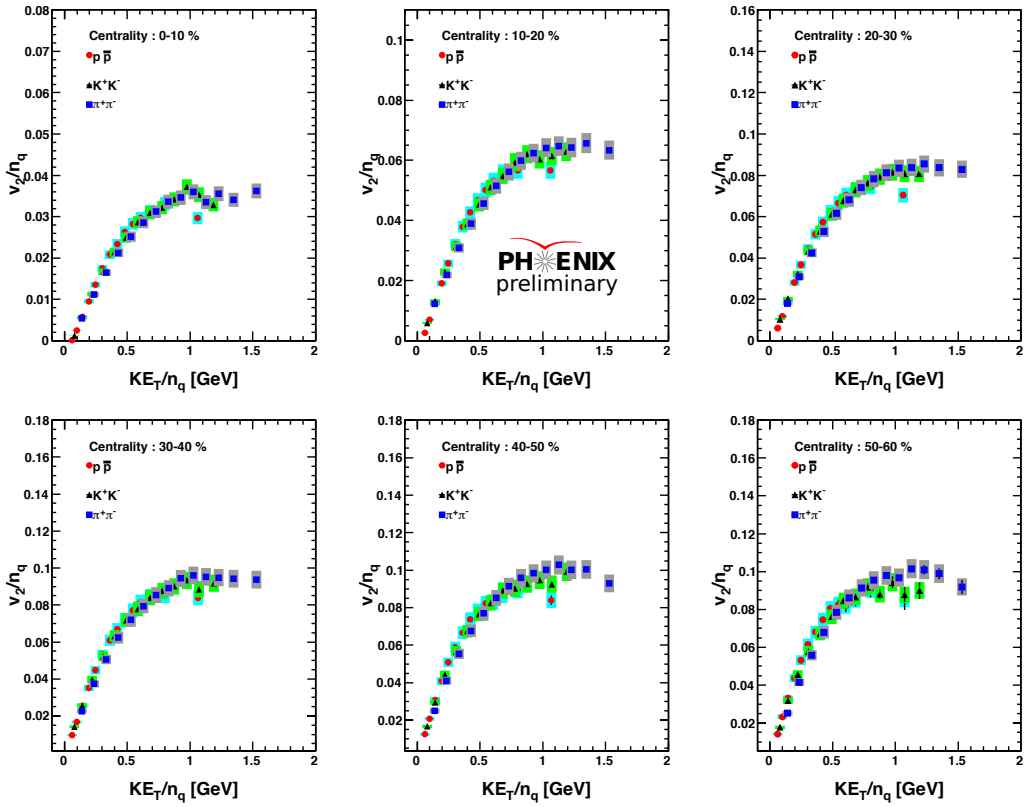


Figure 4.35: NCQ-scaling of $v_2$ as a function of $KE_T/n_q$ in various centrality slices for $Au + Au$ collisions at $\sqrt{s_{NN}} = 200$ GeV. Shaded bar indicates systematic uncertainties.

It is seen from the plots in Fig.4.35–4.37 presented above that not only the $v_2/n_q$, $v_4/n_q$ scales well with $KE_T/n_q$ within systematic uncertainties, the fluctuation-induced $v_3/n_q$ is also showing such scaling propterties. This is not hard to understand, considering the acoustic nature of QGP expansion in viscous horizon and its root in initial collision geometry through eccentricity [122], which will be discussed in great detail in Chapter Five.

### 4.4.2 Collisions at $\sqrt{s_{NN}} = 62.4$ and 39 GeV

Having looked at the $Au + Au$ collisions at full RHIC heavy ion beam energy at $\sqrt{s_{NN}} = 200$ GeV, let us move to the collisions at lower beam energies, *i.e.* $\sqrt{s_{NN}} = 62.4$ and 39 GeV.

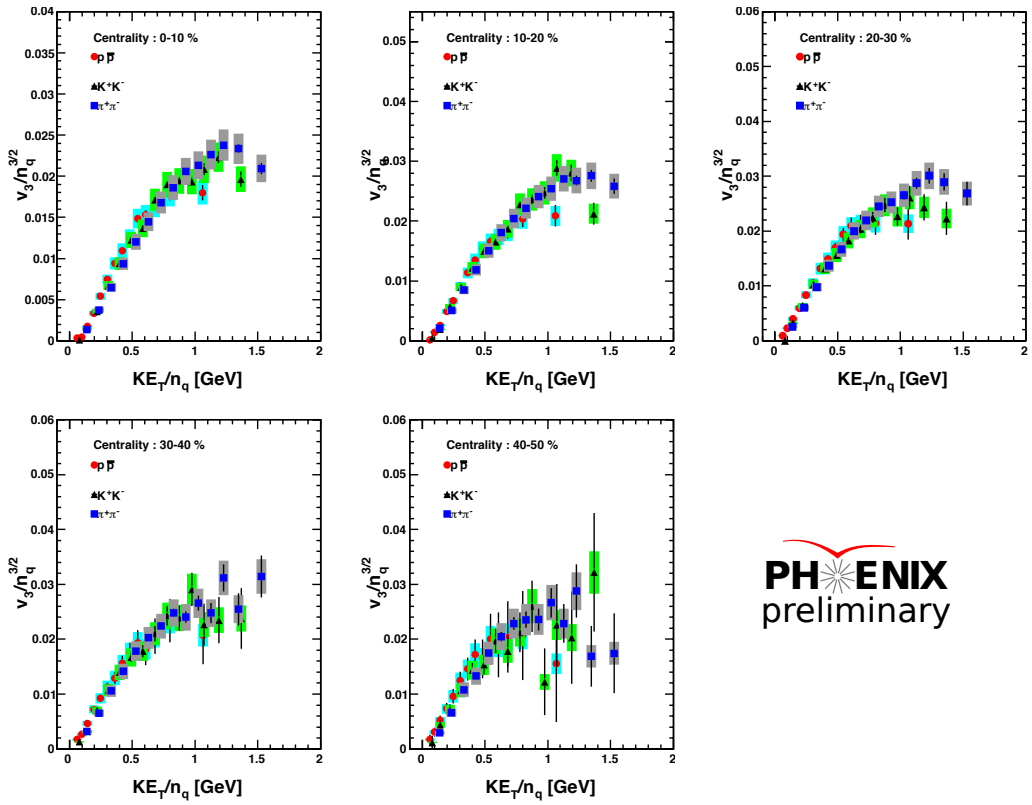


Figure 4.36: NCQ-scaling of $v_3$ as a function of $KE_T/n_q$ in various centrality slices for $Au + Au$ collisions at $\sqrt{s_{NN}} = 200$ GeV. Shaded bar indicates systematic uncertainties.

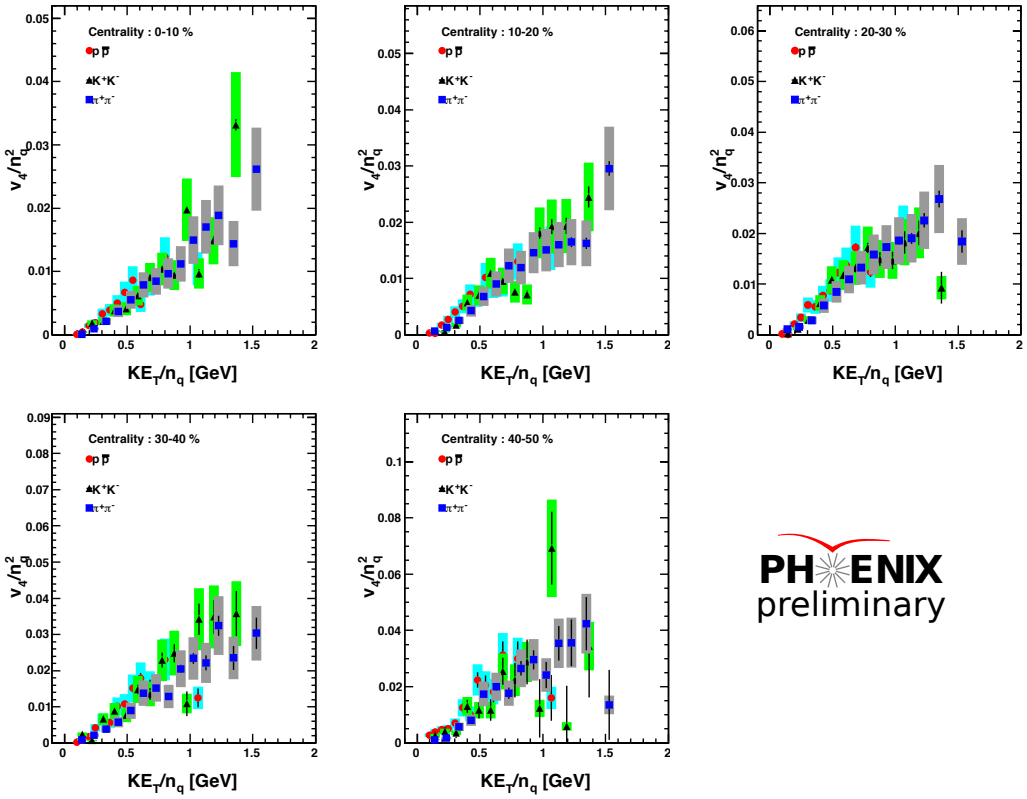


Figure 4.37: NCQ-scaling of $v_4$ as a function of $KE_T/n_q$ in various centrality slices for $Au + Au$ collisions at $\sqrt{s_{NN}} = 200$ GeV. Shaded bar indicates systematic uncertainties.

The analysis was performed with minimum-bias $Au + Au$ events from run year 2010. A total of ∼500M $Au+Au$ events at $\sqrt{s_{NN}} = 62.4$ GeV and ∼200M $Au + Au$ events at $\sqrt{s_{NN}} = 39$ GeV were used, subsequent to the rejection of bad runs based on QA studies and a ± 30 cm BBC z-vertex cut.

**QA**

The particle identification was performed using TOF East and TOF West detectors. The analysis is going to look at the flow coefficients $v_n$ (n=2,3) based on long-range two-particle correlation (2PC) method, as a function of $p_T$ and centrality.

All the data collected are used in this analysis except the following runs:

♢ Runs with very broad BBC-Z vertex distribution: 314025, 314026, 314033, 314034, 314042, 314604.

**Event and Track Selection**

Event and track selection are listed below:

Event Selection

♢ Centrality range: 0–60%

♢ $|bbcz|$ <30 cm - BBC vertex cut

Track Selection

♢ Momemtum cut: 0.1-6.0 GeV/c

♢ DCH Track Quality: 31 or 63

♢ $|zed| < 75$cm

♢ $n_0 \leq 0$ – RICH veto cut, to suppress conversion particles with wrong reconstructed momentum

♢ Track is projected to its expected hit location on TOF. We require tracks to have a hit on TOF within $\pm 2\sigma$ ("radial" matching cut) of the expected hit location in both the azimuthal and beam directions.

♢ $\pm 2\sigma$ radial matching on PC3, which is used to further suppress residual background

♢ Energy/Charge cut: $E_{tof}$ >0.002 for TOF-E, 30 <SumQ<600 for TOF-W at $\sqrt{s_{NN}}$ = 39 GeV and 60 <SumQ<600 for TOF-W at $\sqrt{s_{NN}}$ = 62.4 GeV

### Correlation Functions

Same as Section 4.4.1, the correlation functions were constructed following our standard practice of taking the ratio of two distributions:

$$C\left(\triangle\phi\right) = \frac{N_{pair,same}\left(\triangle\phi\right)}{N_{pair,mix}\left(\triangle\phi\right)}$$

where the numerator is the distribution of correlated pairs from same event and the denominator is the distribution of uncorrelated pairs from mixed events. These pairs were selected so as to have the same centrality, zvtx bin, etc, as for the correlated pairs. In current low energy $v_n$ analysis, the bbcz vertex is again partitioned into 10 bins within $|bbcz| < 30$ cm range, *i.e.*, 6 cm per zvtx bin. The centrality bin is selected at 10% increment.

- **Forward Track-Forward Track Correlations**

Following the same manner, we present the correlation functions from pair tracks from South-North forward detector (RxNP detector in our case). The inner south ring of RxNP detector was found pathologic when we performed 2PC analysis for inclusive charged hadron $v_n$ and this problematic $S_{in}$ sector in RxNP is always excluded in this analysis.

For illustration purpose, the $RxNP_{S_{out}}$ – $RxNP_{N_{in+out}}$ azimuthal correlation functions for the hits in the RxNP detector in $Au + Au$ collisions at $\sqrt{s_{NN}}$ = 62.4 and 39 GeV are shown in Fig.4.38 and 4.39, respectively.

- **Central Track-Forward Track Correlations**

For illustration purpose, the correlation functions built from charged pions in central arm full TOF acceptance (TOF-W + TOF-E) and RxNP particle hits in 20-30% centrality bin are shown in Fig.4.40, 4.41 for $Au+Au$ collisions at $\sqrt{s_{NN}}$ = 62.4 and 39 GeV, respectively. Again, it must be stressed that, on top of TOF acceptance in both east and west arm, there are three possible combinations of RxNP sectors for correlation function. They are, $RxNP_{S_{out}}$ with $RxNP_{N_{in+out}}$, $RxNP_{S_{out}}$ with $RxNP_{N_{out}}$ and $RxNP_{S_{out}}$ with $RxNP_{N_{in}}$.

Please note that correlation functions are also built for charged pions in TOF-W(E) acceptance only with various RxNP segment combinations. Similar studies were also performed for charged kaons and (anti-)protons.

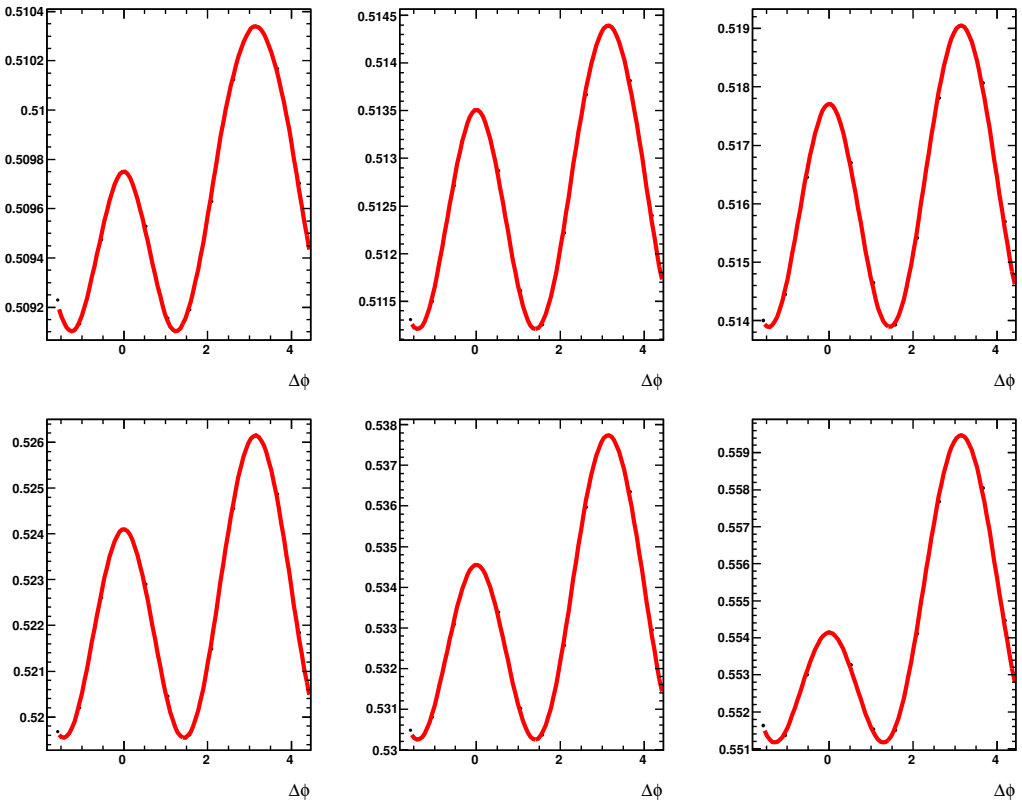


Figure 4.38: $RxNP_{S_{out}}$ – $RxNP_{N_{in+out}}$ azimuthal correlation functions for the hits in the RxNP detector for $Au+Au$ collisions at $\sqrt{s_{NN}} = 62.4$ GeV. Results are shown in 10% centrality increments from left to right and then top to bottom. Red curve in each panel is the harmonic fit to its correlation function.

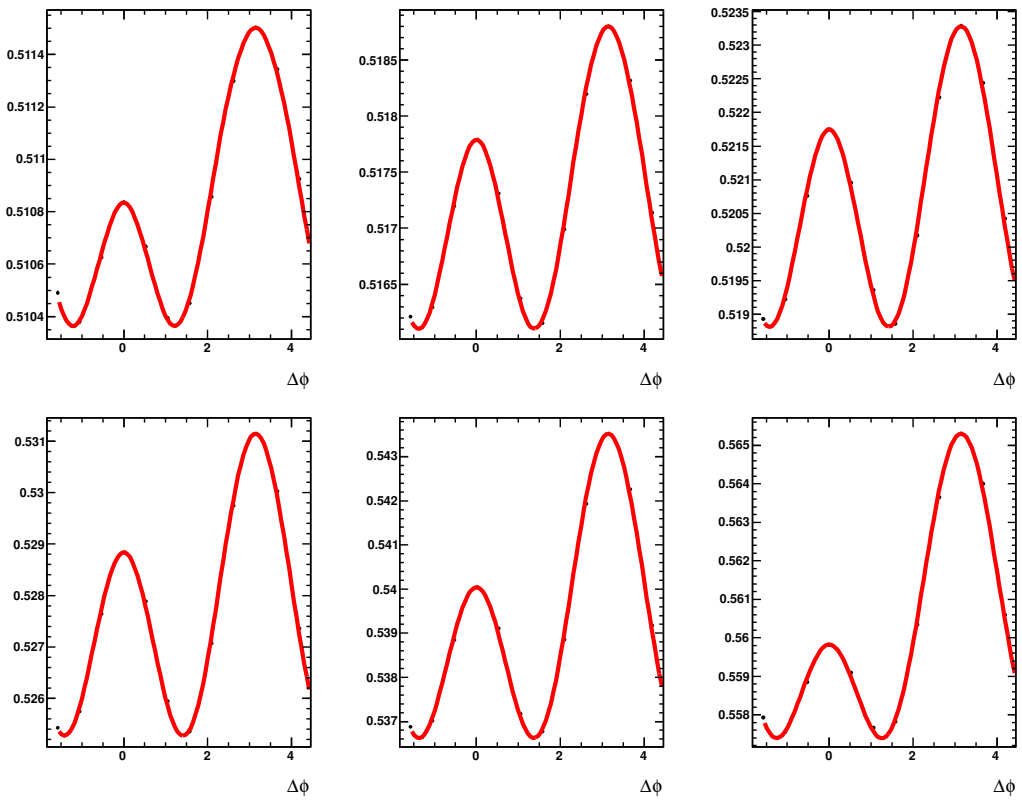


Figure 4.39: $RxNP_{S_{out}}$ – $RxNP_{N_{in+out}}$ azimuthal correlation functions for the hits in the RXN detector for $Au$+$Au$ collisions at $\sqrt{s_{NN}} = 39$ GeV. Results are shown in 10% centrality increments from left to right and then top to bottom. Red curve in each panel is the harmonic fit to its correlation function.

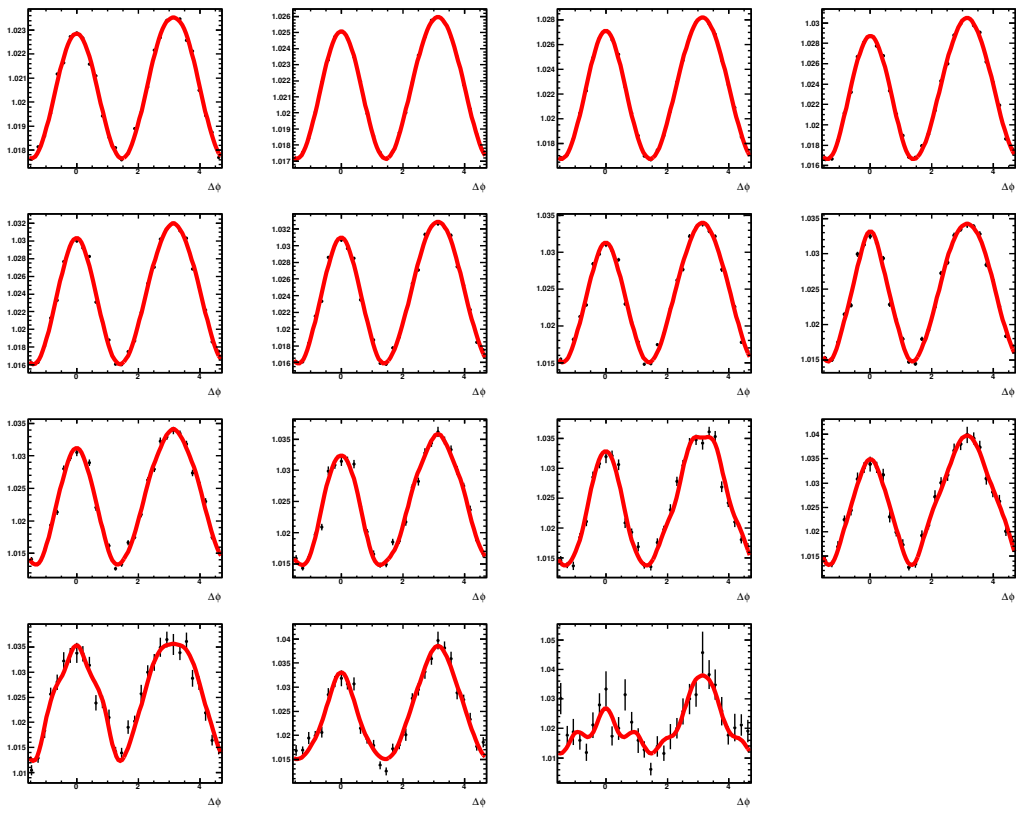

Figure 4.40: CNT-RxNP azimuthal correlation function for charged **Pions** within **TOF-W + TOF-E** in **10-20%** centrality, from $Au + Au$ collisions at $\sqrt{s_{NN}} = 62.4$ GeV. Results are shown in $p_T$ increments from left to right and then top to bottom. Red curve in each panel is the harmonic fit to its correlation function. Full RxNP acceptance is used, excludin the $S_{in}$ sector.

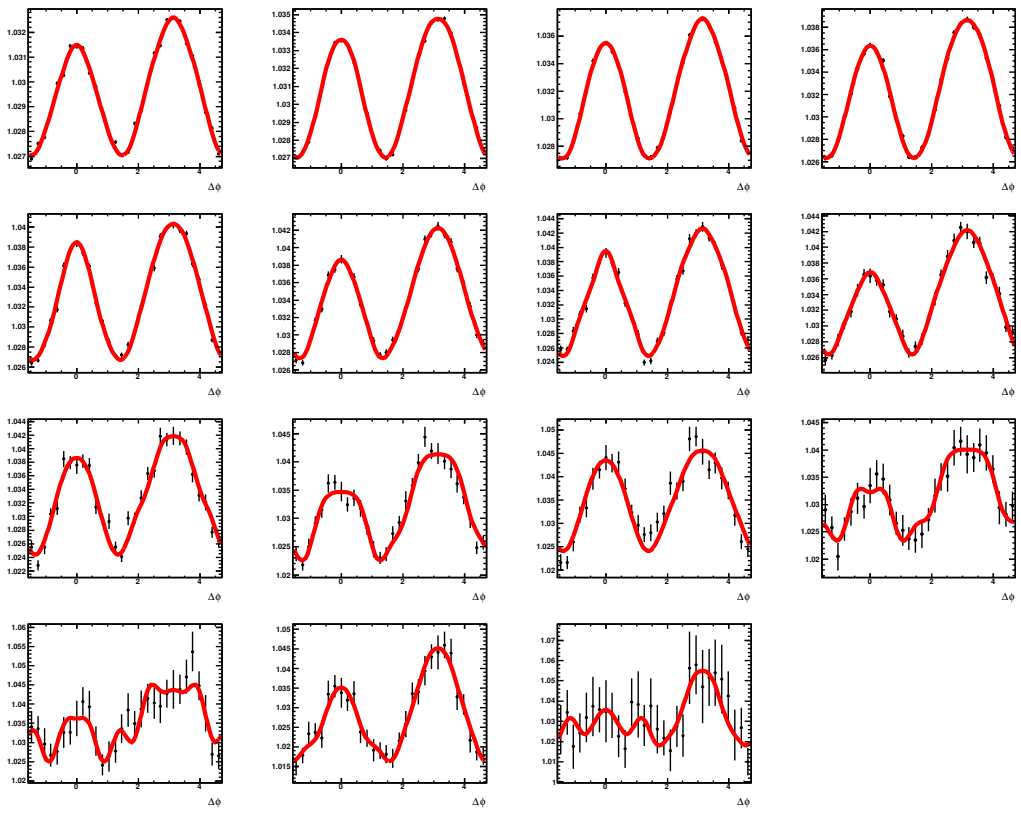

Figure 4.41: CNT-RxNP azimuthal correlation function for charged **Pions** within **TOF-W + TOF-E** in **10-20%** centrality, from $Au + Au$ collisions at $\sqrt{s_{NN}} = 39$ GeV. Results are shown in $p_T$ increments from left to right and then top to bottom. Red curve in each panel is the harmonic fit to its correlation function. Full RxNP acceptance is used, excludin the $S_{in}$ sector.

### Systematic Uncertainties

The systematic uncertainties are estimated based on the inclusive charged hadron $v_n$ in TOF acceptance, and study the possible variations induced from different detector acceptance (*i.e.* difference RxNP segment combinations) and TOF-E/W acceptance, following the same procedure as described in Section.4.4.1.

Figure.4.42 and 4.43 are for $v_2$ and $v_3$ of inclusive charged hadron in TOF acceptance in $Au + Au$ collisions at $\sqrt{s_{NN}} = 62.4$ GeV. The values obtained from various types of correlation functions are indicated in legend following the same color code in Section.4.4.1.

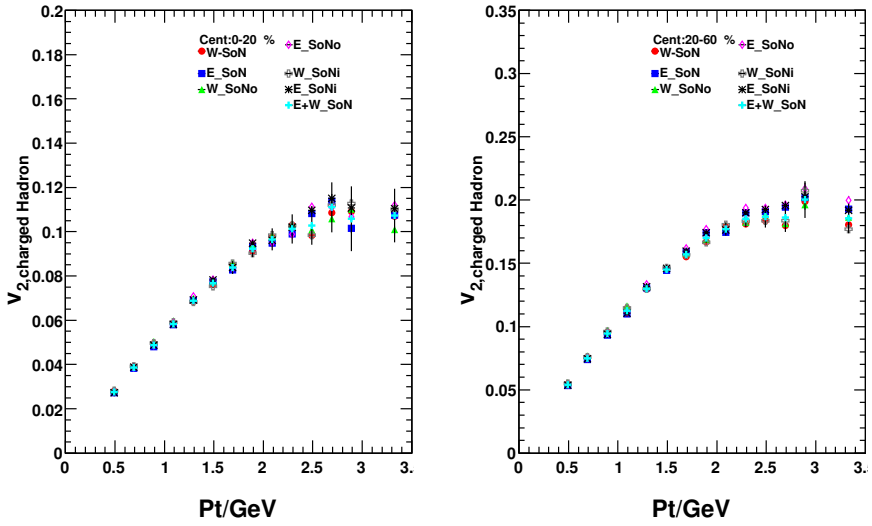


Figure 4.42: $v_2$ of inclusive charged hadron calculated from various TOF acceptance correlating with various RxNP segment combinations in $Au + Au$ collisions at $\sqrt{s_{NN}} = 62.4$ GeV. Results are shown in 0-20% and 20-60% centrality from left to right. Error bars are for statistical uncertainties only.

The corresponding ratio plots for inclusive charged hadron $v_n$ (n=2,3) within TOF acceptance in $Au + Au$ collisions at $\sqrt{s_{NN}} = 62.4$ GeV are shown in the Figure.4.44 and 4.45. To illustrate the possible statistical errors and to avoid being too busy, I just indicate the associated errors when taking the ratio of TOFE-$RxNPS_{out}N_{out}$ to our default setting.

Similar to Fig.4.42–4.45, the corresponding plots for $Au + Au$ collisions at $\sqrt{s_{NN}} = 39$ GeV are shown in Fig.4.46–4.49.

Systematic error estimates were obtained primarily via study of the dependence of $v_n$ on the separate TOF-W/E acceptance as well as on the choice of the RXN sub-detector used to generate the correlation functions. Since the

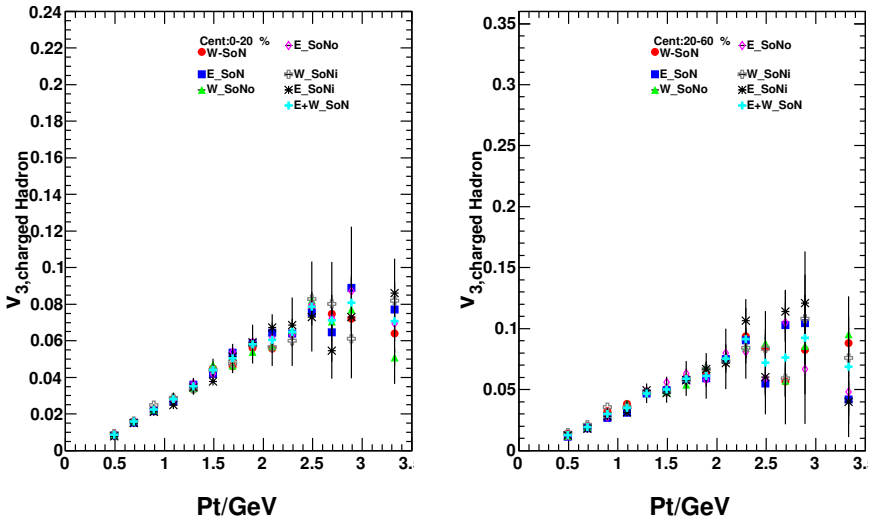


Figure 4.43: $v_3$ of inclusive charged hadron calculated from various TOF acceptance correlating with various RxNP segment combinations in $Au + Au$ collisions at $\sqrt{s_{NN}} = 62.4$ GeV. Results are shown in 0-20% and 20-60% centrality from left to right. Error bars are for statistical uncertainties only.

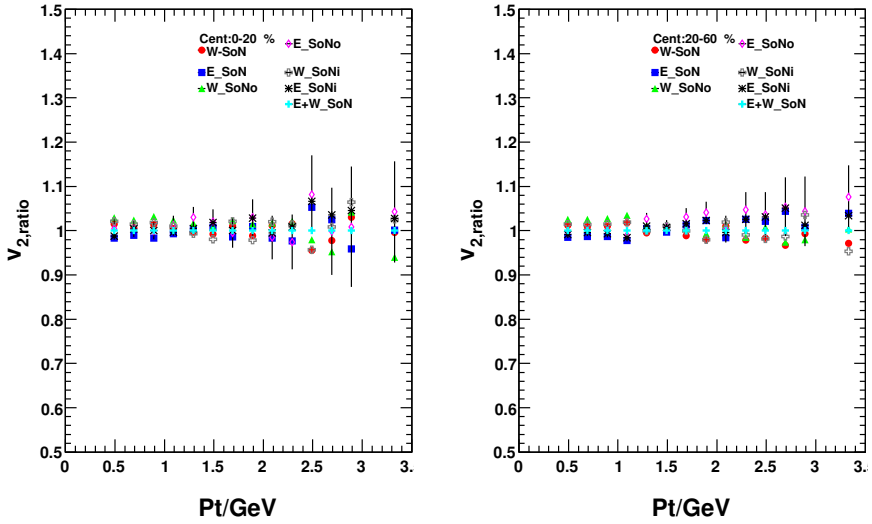


Figure 4.44: Ratio of inclusive charged hadron $v_2$ in $Au + Au$ collisions at $\sqrt{s_{NN}} = 62.4$ GeV within various TOF acceptance w.r.t $v_2$ calculated from default full TOF acceptance correlating with $RxNPS_{out}N_{in+out}$. Results are shown in 0-20% and 20-60% centrality from left to right. Error bars are for statistical only.

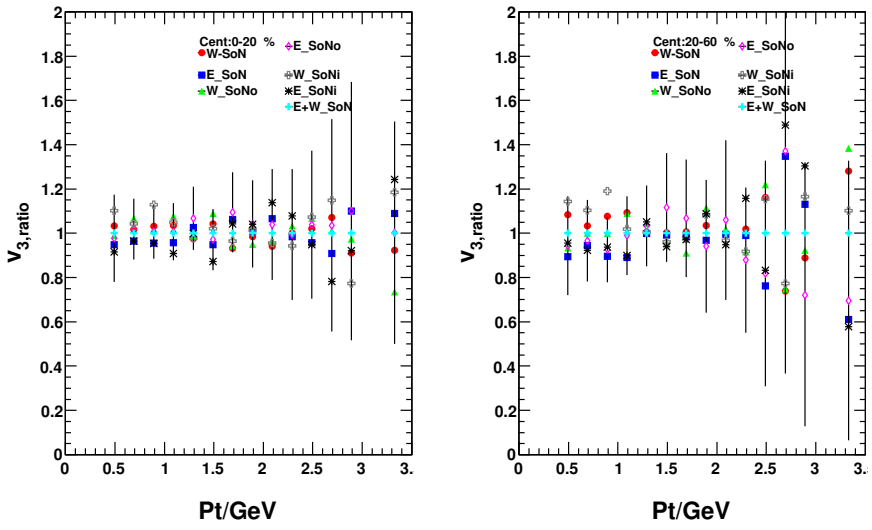


Figure 4.45: Ratio of inclusive charged hadron $v_3$ in $Au + Au$ collisions at $\sqrt{s_{NN}} = 62.4$ GeV within various TOF acceptance w.r.t $v_3$ calculated from default full TOF acceptance correlating with $RxNPS_{out}N_{in+out}$. Results are shown in 0-20% and 20-60% centrality from left to right. Error bars are for statistical only.

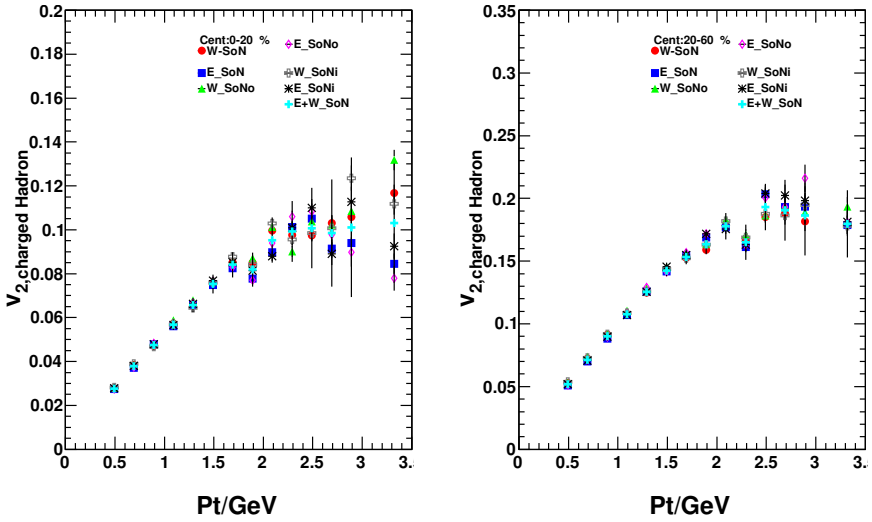


Figure 4.46: $v_2$ of inclusive charged hadron calculated from various TOF acceptance correlating with various RxNP segment combinations in in $Au + Au$ collisions at $\sqrt{s_{NN}} = 39$ GeV. Results are shown in 0-20% and 20-60% centrality from left to right. Error bars are for statistical uncertainties only.

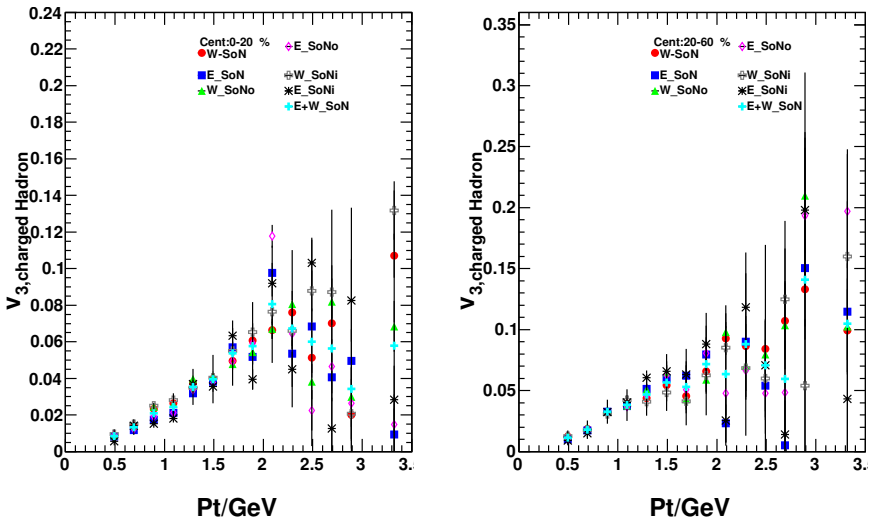


Figure 4.47: $v_3$ of inclusive charged hadron calculated from various TOF acceptance correlating with various RxNP segment combinations in $Au + Au$ collisions at $\sqrt{s_{NN}} = 39$ GeV. Results are shown in 0-20% and 20-60% centrality from left to right. Error bars are for statistical uncertainties only.

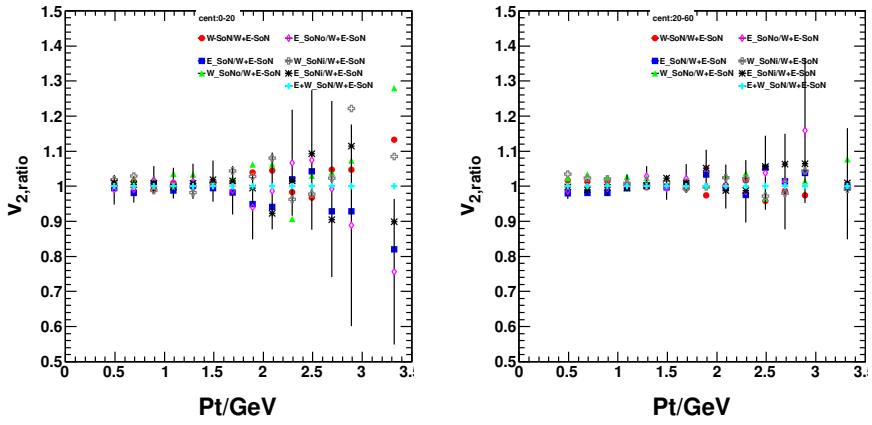


Figure 4.48: Ratio of inclusive charged hadron $v_2$ in $Au + Au$ collisions at $\sqrt{s_{NN}} = 39$ GeV within various TOF acceptance w.r.t $v_2$ calculated from default full TOF acceptance correlating with $RxNPS_{out}N_{in+out}$. Results are shown in 0-20% and 20-60% centrality from left to right. Error bars are for statistical only.

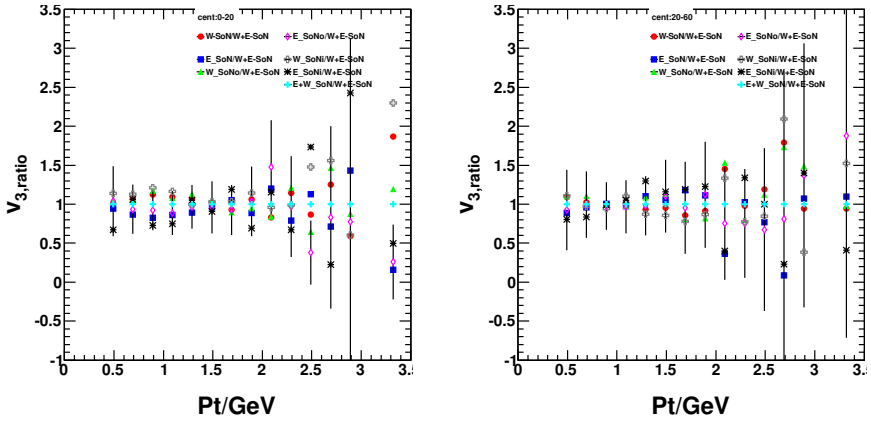


Figure 4.49: Ratio of inclusive charged hadron $v_3$ in $Au + Au$ collisions at $\sqrt{s_{NN}}$ = 39 GeV within various TOF acceptance w.r.t $v_3$ calculated from default full TOF acceptance correlating with $RxNPS_{out}N_{in+out}$. Results are shown in 0-20% and 20-60% centrality from left to right. Error bars are for statistical only.

inclusive charged hadron flow can be considered as the source of systematic uncertainties for PIDed case, and it is common to each particle species, the uncertainties associated with it can be viewed as the systematic errors that further propagate to pions, kaons and $p\bar{p}$. The ratio plots above show very little difference($\sim$ 5-8%) for $v_2$ but do show variations of $\sim$10–15% for $v_3$, depending on collision energies and centralities.

For $v_2$ in $Au + Au$ collisions at $\sqrt{s_{NN}}$ = 62.4 GeV, based on results of inclusive charged hadrons in TOF acceptance, as shown in Fig.4.42 and 4.44, we assign 5% for both 0-20% and 20-60% centrality.

For $v_2$ in $Au + Au$ collisions at $\sqrt{s_{NN}}$ = 39 GeV, the results at inclusive charged hadron level start being influenced by the statistics (please note that 2PC is a pair-distribution study), as shown in Fig.4.46 and 4.48. We carefully examined the results from various TOF acceptance and RXNP segment combinations, and assign 8% for 0-20% and 5% for 20-60% centrality.

For $v_3$ in $Au + Au$ collisions at $\sqrt{s_{NN}}$ = 62.4 GeV, based on results of inclusive charged hadrons in TOF acceptance, as shown in Fig.4.43 and 4.45, we assign 10% for 0-20%, and 12% for 20-60%.

For $v_3$ in $Au$+$Au$ collisions at $\sqrt{s_{NN}}$ = 39 GeV, based on results of inclusive charged hadrons in TOF acceptance, as shown in Fig.4.47 and 4.49, we assess the statistical uncertainties judiciously and exercise our best judgement. We assign 15% for both 0-20% and 20-60%.

In summary, the observations from the studies are quoted as systematic

uncertainty and tabulated in Table.4.4.2 and Table.4.4.2 for $Au+Au$ collisions at $\sqrt{s_{NN}} = 62.4$ and 39 GeV, respectively.

| Centraltiy (%) | 0–20 | 20–60 |
|---|---|---|
| $v_2$ (% err.) | 5 | 5 |
| $v_3$ (% err.) | 10 | 12 |

Table 4.3: Systematic uncertainties for PIDed $v_n$ results in $Au + Au$ collision at $\sqrt{s_{NN}} = 62.4$ GeV.

| Centraltiy (%) | 0–20 | 20–60 |
|---|---|---|
| $v_2$ (% err.) | 8 | 5 |
| $v_3$ (% err.) | 15 | 15 |

Table 4.4: Systematic uncertainties for PIDed $v_n$ results in $Au + Au$ collision at $\sqrt{s_{NN}} = 39$ GeV.

#### Cross-check with Results via EP Method

The same elliptic flow coefficients, $v_2$, for identified charged hadrons in $Au+Au$ collision at $\sqrt{s_{NN}} = 62.4$ and 39 GeV are measured by EP method, using the same data set collected in run year 2010. In this section, we are going to present the comparisons of $v_2$ across the two independent methods. The results in relatively wide centrality bin(0-20% and 20-60%) are achieved from multiplicity-scaled results of fine centrality bin. Only statistical uncertainties are indicated by error bars.

The comparison made for PIDed $v_2$ are shown in Fig.4.50 and 4.51 for $Au+Au$ collisions at $\sqrt{s_{NN}} = 62.4$ and 39 GeV, respectively. Please note that only particle identified elliptic flow $v_2$ is previously measured via EP method for the same dataset at same beam energies. The open symbols are the $v_2$ values from this 2PC analysis, and dark-grey dots are from EP analysis.

## 4.5 Beam Energy Dependence of $v_n$ Results

After few years of experiments at RHIC, the extensive set of flow measurements for various hadrons species became available. Having studied the $v_n$ at different RHIC collision energies, it is worthwhile looking at the beam energy

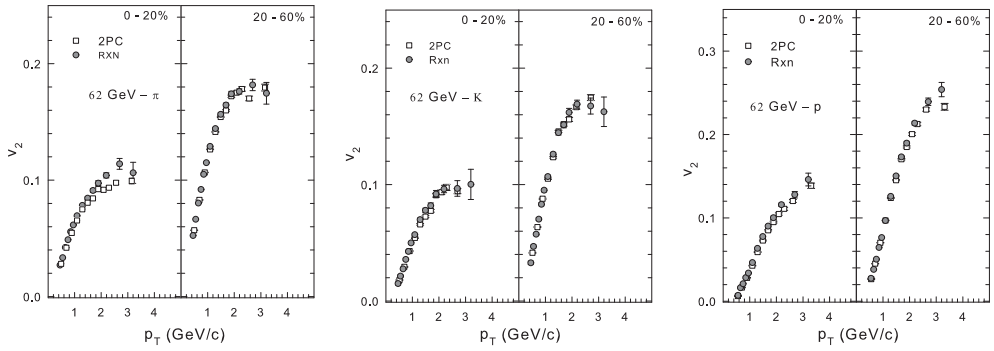


Figure 4.50: The comparison of PIDed $v_2$ between 2PC (this analysis) and EP method preliminary results[40] in $Au+Au$ collision at $\sqrt{s_{NN}} = 62.4$ GeV. The left panel is for charged pions $v_2$ comparison, middle panel for charged kaons and right panel for (anti-)protons. Error bars are for statistical only.

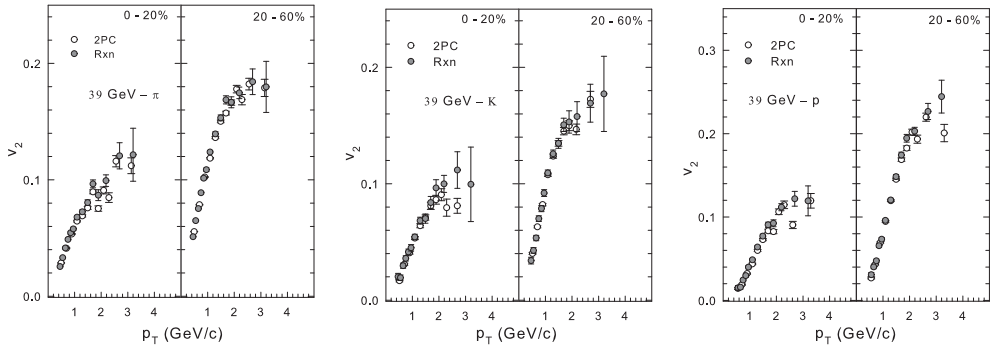


Figure 4.51: The comparison of PIDed $v_2$ between 2PC (this analysis) and EP method preliminary results[40] in $Au + Au$ collision at $\sqrt{s_{NN}} = 39$ GeV. The left panel is for charged pions $v_2$ comparison, middle panel for charged kaons and right panel for (anti-)protons. Error bars are for statistical only.

dependence of the $v_n$ (n=2,3) results. In this section, we present several plots showing the collision-energy dependence of the particle identified $v_n$ results we have obtained.

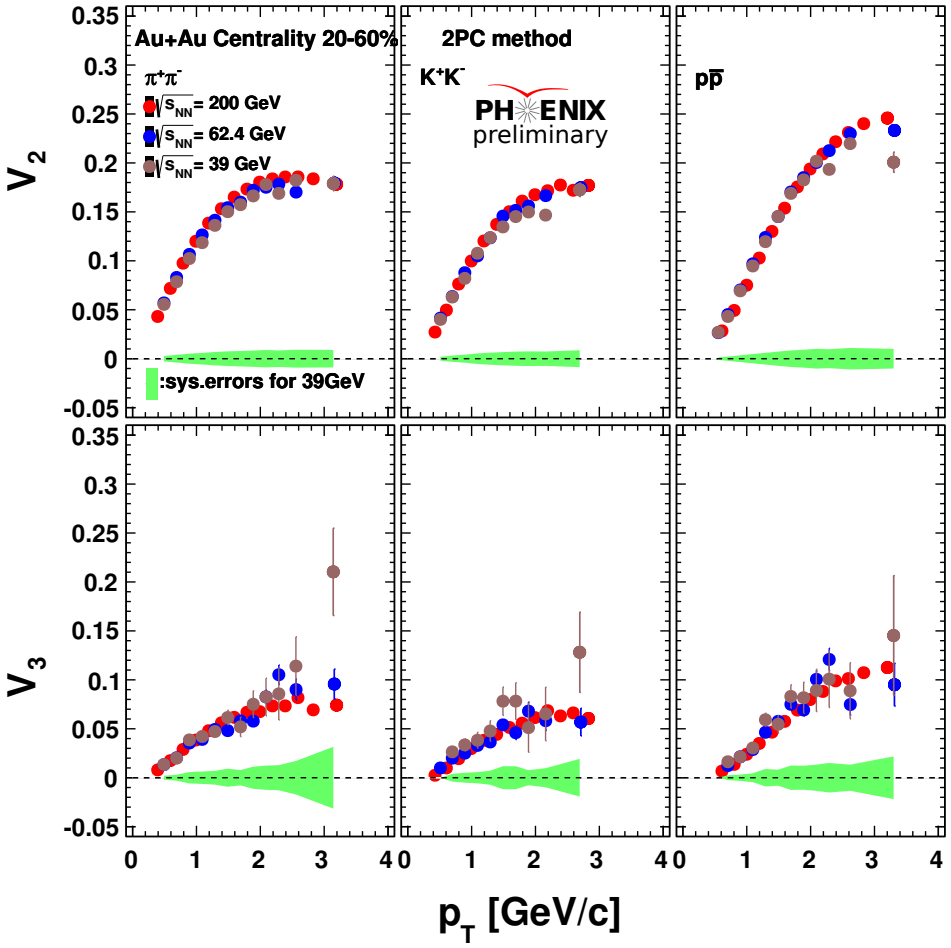


Figure 4.52: Collision-energy dependence of particle identified hadron $v_n$ (n=2,3) in 20-60% centrality. Green bands indicate systematic uncertainties at $\sqrt{s_{NN}} = 39$ GeV.

Figure.4.52,4.53 present the collision energy dependence of particle identified charged hadron $v_n$ (n=2,3) in 20-60% and 0-20% for $Au + Au$ collisions. To illustrate the level of systematic uncertainties, green bands sitting on the "zero" reference line represent the uncertainties at $\sqrt{s_{NN}} = 39$ GeV, where largest systematic uncertainties are expected. Within systematic uncertainties, $v_n$ (n=2,3) for three charged hadron species do not show significant difference

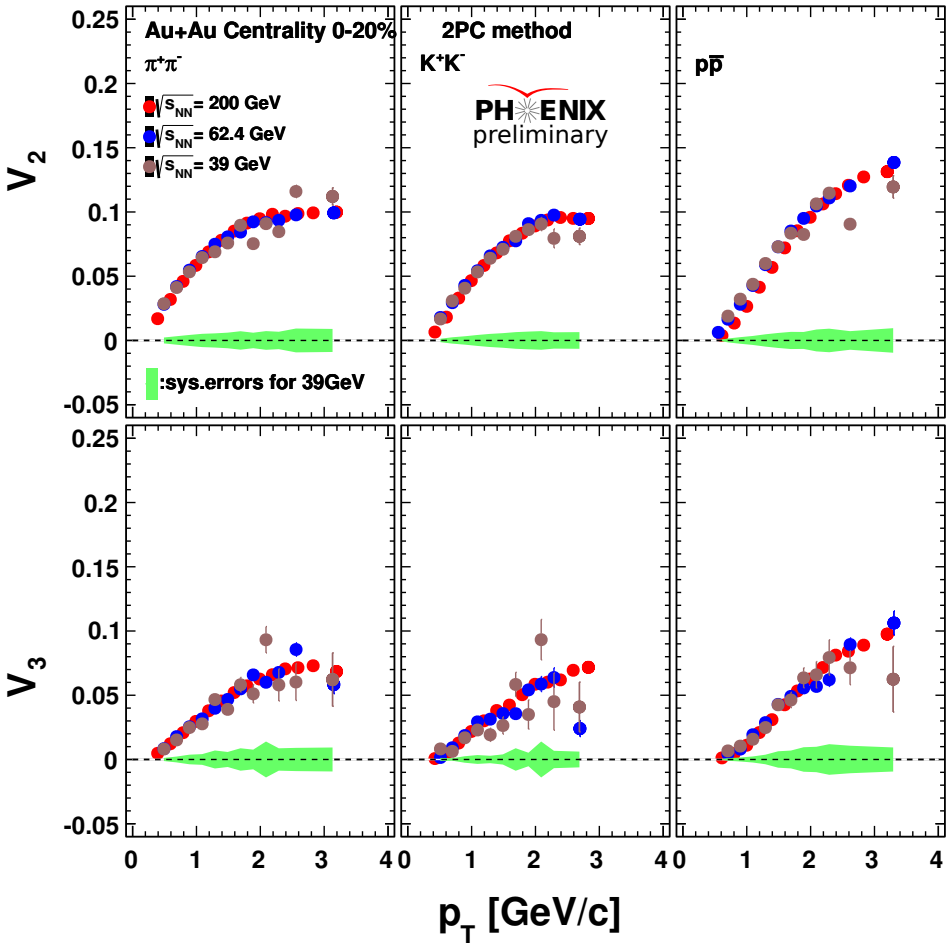


Figure 4.53: Collision-energy dependence of particle identified hadron $v_n$ (n=2,3) in 0-20% centrality slice. Green bands indicate systematic uncertainties at $\sqrt{s_{NN}} = 39$ GeV.

across RHIC beam energies in both central and mid-central events.

To test the eccentricity-driven hydrodynamic expansion in hadron flow development, the NCQ-scaling $v_n$ (n=2,3) are plotted, in Fig.4.54, 4.55, as a function of $KE_T/n_q$, where $n_q$ is the number of constituent quarks in a given hadron species.

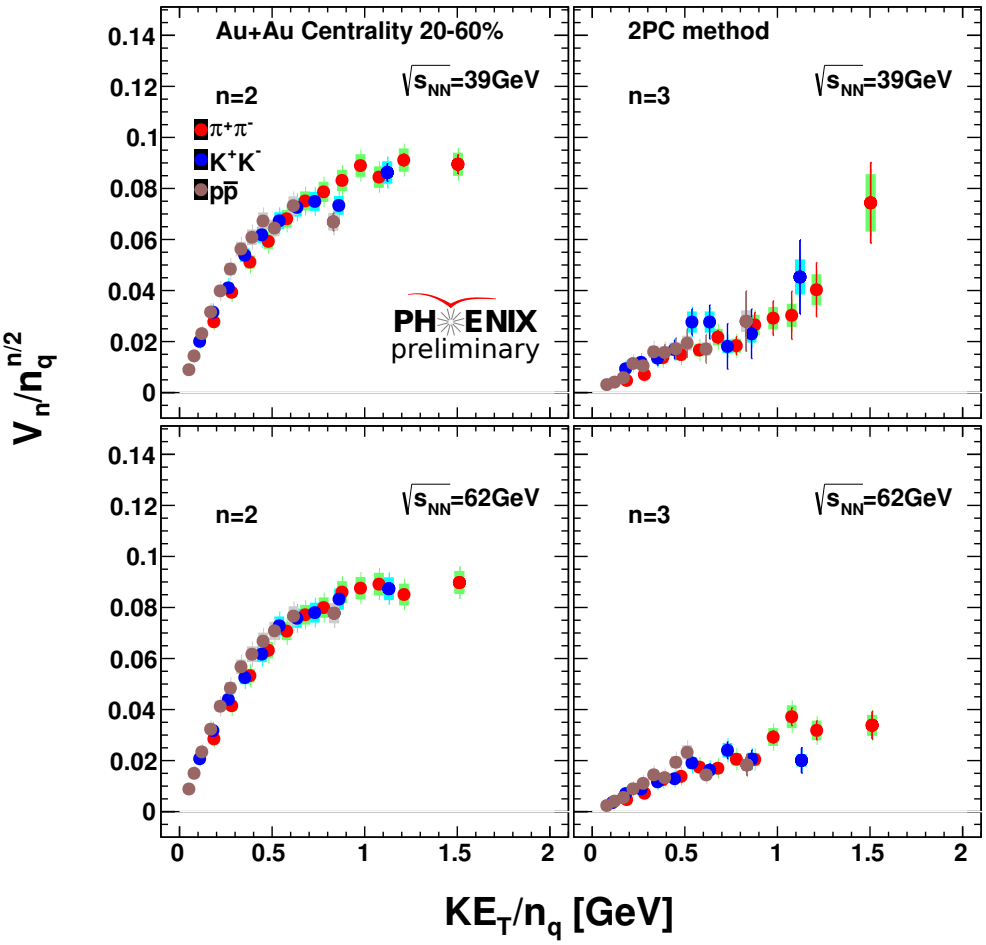


Figure 4.54: NCQ-scaling of particle identified hadron $v_n$ (n=2,3) in 20-60% centrality at $\sqrt{s_{NN}}$ = 39 and 62.4 GeV.

Again, the observation that both elliptic flow and triangular flow scale to a singal curve within the obtained $KE_T$ reach confirms the bulk of flow at RHIC energies is partonic, rather than hadronic, which can be well described by hydrodynamics.

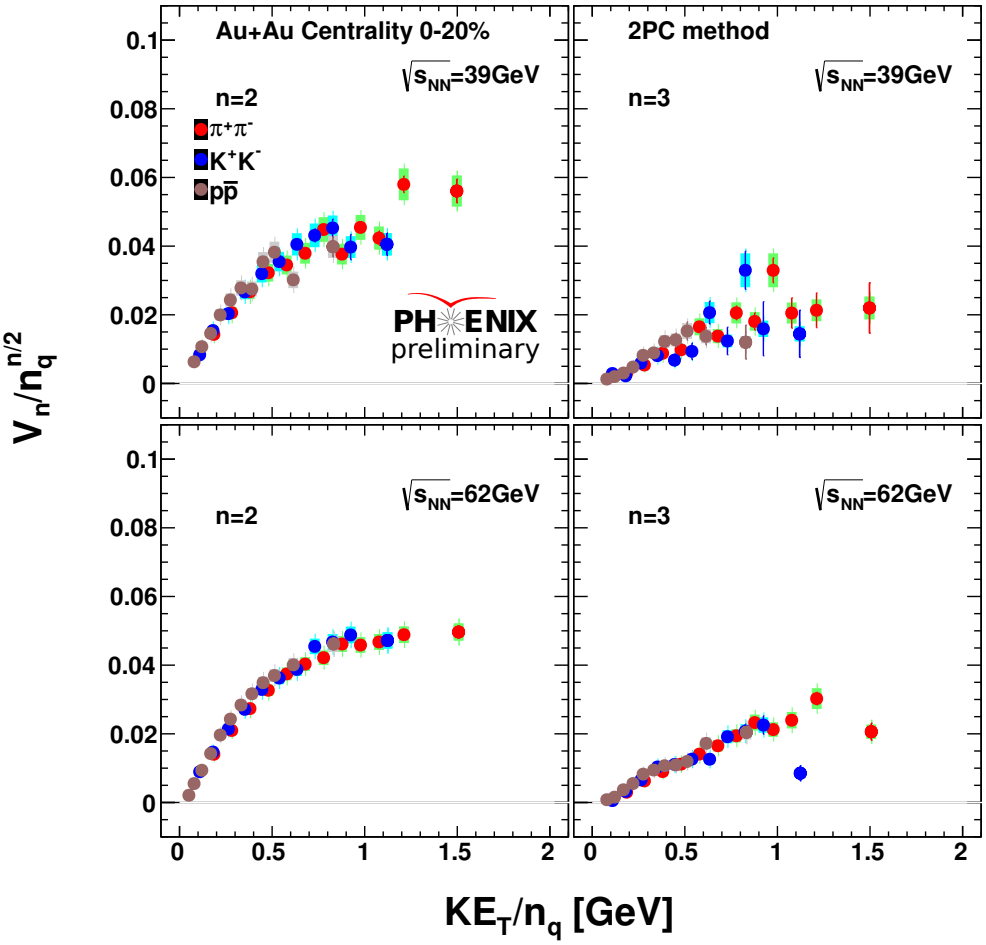


Figure 4.55: NCQ-scaling of particle identified hadron $v_n$ (n=2,3) in 0-20% centrality at $\sqrt{s_{NN}} = 39$ and 62.4 GeV.

## 4.6 Comparisons with LHC $v_n$ Results

Anisotropic flow measurements for charged hadrons are being pursued at both the RHIC and LHC. As stated in Section 1.2.6 in Chapter One, more than a factor of three increase in the measured energy density from RHIC to LHC could result in a change in the equation of state (EOS) and other transport properties of the hot and dense plasma produced in energetic heavy ion collisions, which in turn, would influence the magnitude and trend of anisotropic flow. An intriguing question is the extent to which flow measurements for charged hadrons differ from RHIC to LHC, and whether any difference in flow magnitude reflects the notable increase in energy density from RHIC to LHC?

It is noteworthy that the LHC $v_n$ measuremens can also be understood as the expansion of the QGP produced at a much higher energy density in $Pb + Pb$ collisions in the language of hydrodynamics. However, in constrast to RHIC results, tests for NCQ-scaling with LHC data for identified charged hadrons have indicated a breakdown of this scaling, unlike what is shown in the previous section of this manuscript [42]. In this section, I present comparisons of RHIC and LHC flow measurements for both unidentified and identified charged hadrons, to investigate whether the sizable increase in energy density from RHIC to LHC, signals a possible change in the expansion dynamics.

We start with the comparison of inclusive (unidentified) charged hadron $v_n(p_T)$ (n=2,3) obtained in RHIC [41] and LHC [39]. Figure 4.56 presents such comparison for several centrality selections. Although $v_2$ tends to show a slight variation from RHIC to LHC as centrality varies, in general, a good agreement between the magnitude and trends of both data sets for a broad range of $p_T$ and centralities, is achieved for $v_2$ and for $v_3$. It is noteworthy that the observed similarity between RHIC and LHC charged hadron flow measurements extends to the higher order harmonics.

Since $v_2(p_T)$ for inclusive charged hadrons are actually a weighted average of the values for identified charged hadron $v_2$ results, one can test for consistency between the measured values of $v_2(p_T)$ for identified and unidentified charged hadrons. Such a consistency check is shown for LHC data in Fig.4.57.

The left panel of Fig.4.57 shows the $v_2(p_T)$ for identified charged hadrons $(\pi^{\pm}, K^{\pm}, p\bar{p})$ and unidentified inclusive charged hadrons $(h)$, reported by ALICE and ATLAS collaboration respectively. A nice pattern of mass ordering is seen in the given 20-30% centrality bin. The right panel of Fig.4.57 shows that by averaging the individual $v_2$ values for $\pi^{\pm}, K^{\pm}$ and $p\bar{p}$ according to the measured $p/\pi$ and $K/\pi$ multiplicity ratios, the averaged values are essentially the same as those for $h$.

Before we continue our discussion, let us step back for a moment to see what we have obtained. We show in Fig.4.56 that there is not any significant

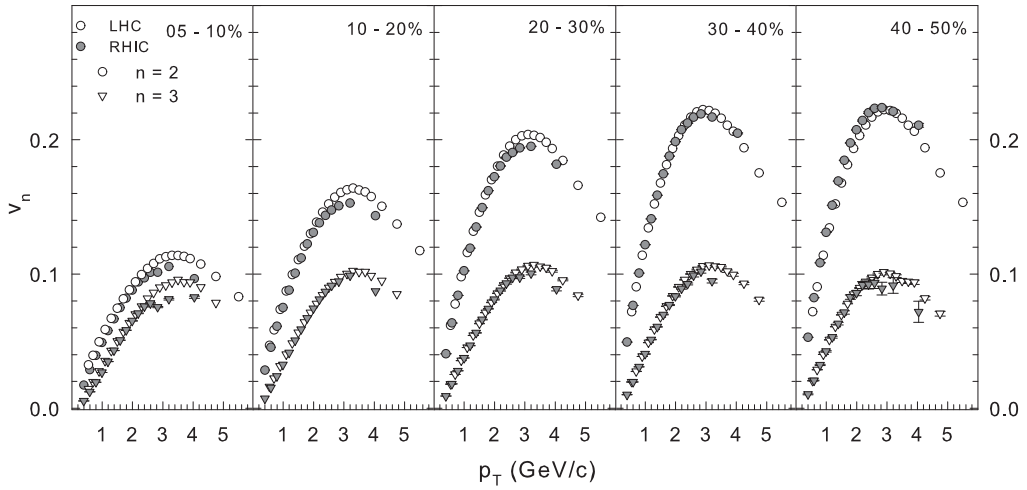


Figure 4.56: Comparison of $v_{2,3}(p_T)$ for inclusive (unidentified) charged hadrons obtained in $Au + Au$ collisions at $\sqrt{s_{NN}} = 200$ GeV (RHIC) and $Pb+Pb$ collisions at $\sqrt{s_{NN}} = 2.76$ TeV (LHC). The data are taken from Refs. [41] and [39]

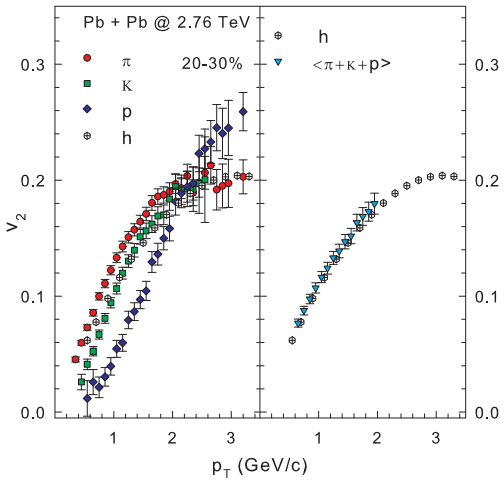


Figure 4.57: (a) Comparison of $v_2(p_T)$ vs. $p_T$ for charged pions, kaons, and (anti-)protons and unidentified charged hadrons $h$. (b) Comparison of $v_2(p_T)$ for $h$ and the weighted average of the values for pions, kaons and (anti-)protons. The data for identified and unidentified charged hadrons, are from the ALICE [42] and ATLAS [39] collaboration respectively. Results are shown for the 20-30% most central $Pb + Pb$ events.

difference in $v_n$ (n=2,3) measurements between RHIC and LHC at inclusive unidentified charged hadron level. We then, in Fig.4.57, show that the measured $v_2$ for unidentified charged hadrons can be understood as an appropriate averaging of the $v_2$'s for individual identified charged hadrons. Given the observed substantial differences between the LHC $v_2(p_T)$ values for $\pi^{\pm}, K^{\pm}$ and $p\bar{p}$, it is important and natural to ask whether the agreement between RHIC and LHC data for $h$ (Fig.4.56) translates to a similar agreement between RHIC and LHC measurements for $\pi^{\pm}, K^{\pm}$ and $p\bar{p}$ (respectively)?

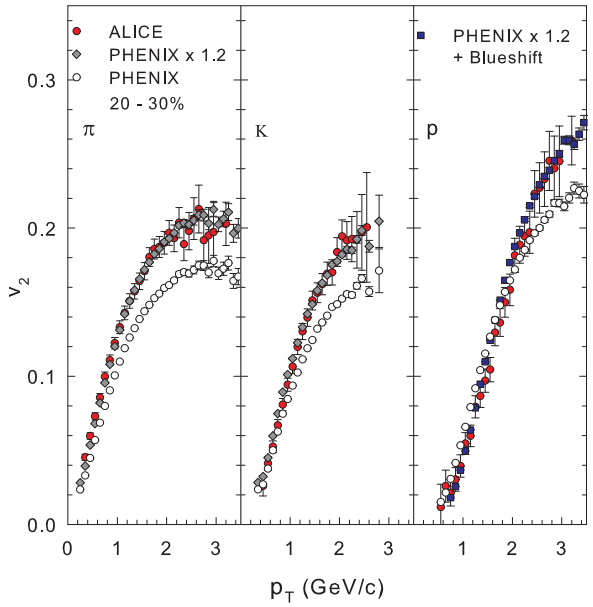


Figure 4.58: Comparison of PHENIX and ALICE data for $v_2(p_T)$ vs. $p_T$ for $\pi^{\pm}, K^{\pm}$ and $p\bar{p}$ as indicated. Results are shown for the 20-30% most central events.

Figure.4.58 compares the RHIC (open circles) and LHC (filled red circles) $v_2(p_T)$ values for $\pi^{\pm}, K^{\pm}$ and $p\bar{p}$ in the 20-30% most central collisions. The values for $\pi^{\pm}, K^{\pm}$ and $p\bar{p}$ indicate an approximate 20% increase from RHIC to LHC. This is confirmed by the excellent agreement between LHC measurements and RHIC measurements that are scaled up by a factor of $\sim 1.2$. (filled circles in left and middle panels of Fig.4.58).

For $p_T \gtrsim 2.5$ GeV/c, the observed $v_2$ results for $p\bar{p}$ shown in th right panel of Fig.4.58 also hint at a 20% difference between the rHIC and LHC values. For lower $p_T$ ($p_T \lesssim 2.0$ GeV/c) however, the RHIC $v_2(p_T)$ values appear to be larger than the LHC values. This inversion in $v_2$ trend can be attributed to a small blueshift of the LHC values, which has been observed in recent viscous hydrodynamical calculation for LHC collisions [123]. Such a blueshift can be

understood as a result of the sizable increase in the magnitude of radial flow generated in LHC collisions, especially in the hadronic phase. The effect from blueshift is again confirmed by the excellent agreement achieved between the $p\bar{p}$ measurements, when the RHIC data are scaled by the factor $\sim 1.2$ (as for $\pi^{\pm}, K^{\pm}$) and further blueshifted by $\sim 0.2$ GeV/c (filled squares in right panel of Fig.4.58. Similar good agreement between RHIC and LHC data were also obtained for other centrality selections, with essentially the same blueshift value. However, a large (smaller) scale factor was needed for more central (peripheral) collisions, as might be expected for the change in energy density with collision centrality.

The results from the comparisons shown in Fig.4.58 suggest that the agreement observed between the charged hadron measurements in Fig.4.56, is only one side of the story and may not convey all the essential information about the expansion dynamics. By constrast, the observed increase in $v_2(p_T)$ from RHIC to LHC for identified charged hadrons (Fig.4.58), suggests that the expansion dynamics in LHC collisions is driven by a larger mean sound speed $\langle c_s(T) \rangle$ for the plasma created in these collisions. Such an increase in $\langle c_s(T) \rangle$ could be due to the notable increase in energy density from RHIC to LHC.

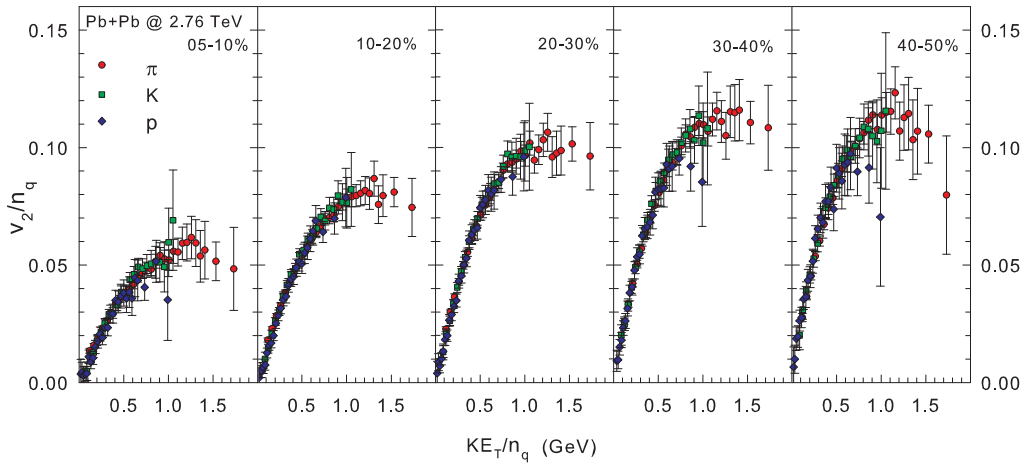


Figure 4.59: $v_2/n_q$ vs. $KE_T/n_q$ for $\pi^{\pm}, K^{\pm}$ and $p\bar{p}$, after the correction for blueshift is applied (see text). Results are shown for several centrality selections as indicated.

The blueshift inferred for $p\bar{p}$ $v_2(p_T)$ in LHC collisions results from the sizable increase in the magnitude of radial flow, thus it is incompatible with quark number scaling. Consequently, such blueshift provides a straightforward explanation for the observed failure of this scaling, when applied to LHC data for identified charged hadrons ($\pi^{\pm}, K^{\pm}$ and $p\bar{p}$). An appropriate correction for this

blueshift would lead to a restoration of quark number scaling. This is demonstrated for LHC data in Fig.4.59 for a broad range of centrality selections. In Fig.4.59, the $v_2(p_T)$ data for $p\bar{p}$ were redshifted, prior to quark number scaling is applied, by $\sim$ 0.2 GeV/c for each centrality selection to account for the blueshift (cf. right panel of Fig.4.58) with the same magnitude. Figure.4.59 shows that this procedure restores the excellent quark number of scaling of the LHC data for identified charged hadrons, and confirms that partonic flow still dominates for LHC collisions. However, the magnitudes of the quark number scaled values of $v_2/n_q$ are significantly larger than those observed at RHIC.

In summary, the particle identified hadron $v_2$ values show a sizable increase from RHIC to LHC, in constast to the agreement observed between the RHIC and LHC data sets for unidentified charged hadrons. This increase is compatible with the larger mean sound speed $\langle c_s(T)\rangle$, expected for the plasma created at a much higher energy density in LHC collisions. The comparisons also indicate a blueshift of LHC $p\bar{p}$ $v_2(p_T)$ relative to RHIC $p\bar{p}$ $v_2(p_T)$, which possibly arises from the notable growth of radial flow in the hadronic phase for LHC collisions. An excellent scaling of $v_2$ with the number of valence quarks is restored for each hadron species within a broad range of transverse kinetic energies and collision centralities, when the blueshift effect is properly addressed and accounted for. These results highlight the indispensable role of the measurements for identified particle species at both RHIC and the LHC, or studies of the temperature ($T$) dependence of the equation of state (EOS) and other transport properties.

# Chapter 5

# Acoustic Anisotropic Flow and Its Viscous Damping

In previous chapters, I have presented the methodologies of flow measurements as well as a set of results obtained via long-range two-particle correlation (2PC) method. The remarkable consistency achieved in flow measurements via event plane (EP) and 2PC method suggests possible absence, or at least great suppression, of the left-over contribution from back-to-back (away-side) jet, indicating a flow-domianted domain of flow measurements in PHENIX.

Based upon harmonic flow measurements, in this chapter we will be looking at a set of findings that would help us better understand the plasma created in heavy-ion collisions. It should be stressed that some of the data employed in this chapter are collected in $Pb+Pb$ collisions at LHC. However, the underlying physics message implied by those to-be-presented observations should, in principle, extend to RHIC. As shown in previous chapters, the relatively large uncertainties associated in higher order harmonics at RHIC make any stringent test, that requires precise measurement of flow harmonics, become much more difficult. To aid our studies, data taken from measurements by both the PHENIX and ATLAS collaboration for $Au+Au$ and $Pb+Pb$ collisions at $\sqrt{s_{NN}} = 0.2$ TeV and 2.76 TeV are used.

This chapter is organized as follows. In Section 5.1, we will re-visit the initial collision geometry, especially the eccentricity modeling within both the MC-Glauber and MC-KLN framework. We then, in Section 5.2, present a couple of studies, showing the acoustic nature of anisotropic flow development as well as the viscous damping of anisotropic flow. In Section 5.3, we will be exploring the various scaling properties of higher-order flow and investigate their possible implications of initial eccentricity.

## 5.1 Initial Eccentricity Fluctuations and Azimuthal Anisotropy

In Chapter Three, we present the Monte Carlo Glauber (MC-Glauber) model, one of two primary models currently employed for eccentricity ($\varepsilon_n$) estimates. The other model I skip back then is the so called factorized Kharzeev-Levin-Nardi (fKLN) model. Both of them are used to model the initial collision geometry. Aside of some qualitative similarities they share in modeling eccentricities, they do show some differences, which may influence the measured values of $v_n$.

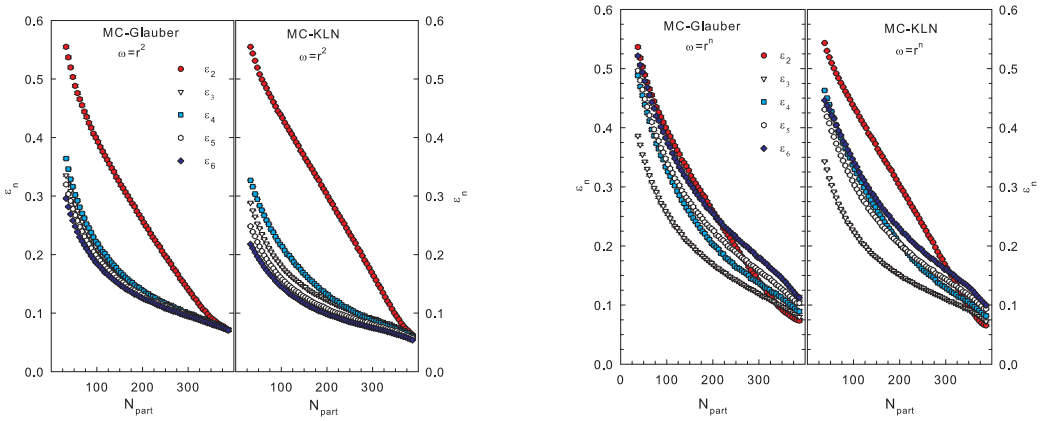


Figure 5.1: Calculated eccentricity $\varepsilon_n$ (n=2–6) as a function of $N_{part}$ for integral weight $\omega(\boldsymbol{r}_\perp) = {\boldsymbol{r}_\perp}^2$ and $\omega(\boldsymbol{r}_\perp) = {\boldsymbol{r}_\perp}^n$ in MC-Galuber and MC-KLN models.

Eccentricity ($\varepsilon_n$) is not experimentally measurable to date. Much efforts have been devoted to the theoretical modeling based on the "almond-shaped" collision zone, which is characterized by the impact parameter $b$ or the number of participating nucleons $N_{part}$. Because of limited number of participants and possible variations of their positions, the geometric fluctuations embedded in the collision zone would translate into the fluctuations of the participant plane and in turn, result in the initial eccentricities referenced to this plane.

Figure.5.1 shows the calculated eccentricity $\varepsilon_n$ (n=2–6) as a function of $N_{part}$ for integral weight $\omega(\boldsymbol{r}_\perp) = {\boldsymbol{r}_\perp}^2$ and $\omega(\boldsymbol{r}_\perp) = {\boldsymbol{r}_\perp}^n$ in MC-Galuber and MC-KLN models. For $\omega(\boldsymbol{r}_\perp) = {\boldsymbol{r}_\perp}^2$, $\varepsilon_n$ does not vary too much from n=3 to 6. $\varepsilon_2$'s magnitude is significantly larger than any $\varepsilon_n (n \geqslant 3)$, except in the very central events where geometry fluctuations dictate the $\varepsilon_n (n \geqslant 2)$. It is

also found that for ($n \geqslant 3$), $\varepsilon_n$ scales $\sim N_{part}^{-1/2}$. For weight $\omega(\boldsymbol{r}_\perp) = \boldsymbol{r}_\perp{}^n$, the calculated $\varepsilon(n \geqslant 3)$ show strong sensitivity to transverse density distributions. The overall magnitudes for $\varepsilon_3(n \geqslant 3)$ are larger than those calculated with $\omega(\boldsymbol{r}_\perp) = \boldsymbol{r}_\perp{}^2$. Also, it is noteworthy that this weighting leads to different values of $\varepsilon_n(n \geqslant 2)$ for MC-Glauber (a), MC-KLN (b) and the results with $\omega(\boldsymbol{r}_\perp) = \boldsymbol{r}_\perp{}^2$.

As shown in Fig.5.1, the magnitude of the eccentricity is of course, model dependent. For example, the second order eccentricity $\varepsilon_2$ obtained from the Glauber [124] model could differ, by as much as $\sim 25\%$ [125], from the $\varepsilon_2$ result in factorized Kharzeev-Levin-Nardi (fKLN) model.

For each collision, the colliding nuclei were generated according to the Woods-Saxon distribution (Eqn.3.1) and the values for $N_{part}$ the $N_{coll}$ were determined within the Glauber ansatz [124]. The eccentricities $\varepsilon_n$ were then calculated from the two-dimensional profile of the density of sources in transverse plane $\rho_s(\boldsymbol{r}_\perp)$, using modified versions of MC-Glauber and MC-KLN [126]. To be more specific, for each collision, the event shape vector $S_n$ is computed and the azimuth of the rotation angle $\Psi_n$ for $n^{th}$ order harmonic of the shape profile is obtained,

$$\begin{aligned} \boldsymbol{S_n} &= (S_{nx}, S_{ny}) \\ &= (S_n \cos(n\Psi_n), S_n \sin(n\Psi_n)) \\ &= \left( \int d\boldsymbol{r}_\perp \omega(\boldsymbol{r}_\perp)\rho_s(\boldsymbol{r}_\perp)\cos(n\phi), \int d\boldsymbol{r}_\perp \omega(\boldsymbol{r}_\perp)\rho_s(\boldsymbol{r}_\perp)\sin(n\phi) \right) \\ \Psi_n &= \tan^{-1}\left(\frac{S_{ny}}{S_{nx}}\right)/n \end{aligned} \tag{5.1}$$

where $\phi$ is the azimuth of each source and $\omega(\boldsymbol{r}_\perp)$ is the integral weight, which can be taken in form of $\boldsymbol{r}_\perp{}^2$ or $\boldsymbol{r}_\perp{}^n$. The eccentricities were then evaluated as $\varepsilon_n = \langle \cos n(\phi - \Psi_n) \rangle$, where "$\langle\ \rangle$" denotes averaging over all sources and events within a particular centrality or impact parameter range. The way we evaluate $\varepsilon_n$ is analog to $v_n$ measurments in that $\varepsilon_n$ is evaluated relative to the principal axis determined by maximizing the $n^{th}$ moment, while $v_n$ is measured with respect to the $n^{th}$ order event plane in experiments.

It is already shown by the studies of flow scaling properties in Chapter Four that a possible transition from flow-driven to suppression-driven anisotropy occurs in the intermediate transverse momenta. That is, for low transverse momenta ($p_T \lesssim 2$ GeV/c), the flow coefficients can be understood as partnoic interactions that drive the pressure gradients in the initial ellipsoid collision zone; for high transverse momenta ($p_T \gtrsim 5$ GeV/c), the flow coefficients are considered as the result from jet-medium ineractions (jet quenching), where

energetic scattered partons interact and lose energy in QGP before they fragment into hadrons.

Such transition may be picked up by the eccentricity-scaled anisotropy coefficients, $v_{2,4}(p_T, N_{part})/\varepsilon_{2,4}(N_{part})$. It is found [43, 128] that such eccentricity-scaled anisotropy coefficients can be analytically written as

$$\frac{v_{2k}(p_T)}{\varepsilon_{2k}} = \frac{v^h_{2k}(p_T)}{\varepsilon_{2k}} \left\{ \frac{1}{1 + [K^*(p_T)/K_0]} \right\}^k, \quad k = 1, 2, \ldots \tag{5.2}$$

where $K^*(p_T)$ reflects the magnitude of the viscous correction for a given $p_T$, $\frac{v^h_{2k}(p_T)}{\varepsilon_{2k}}$ are the eccentricity-scaled anisotropy coefficients in ideal hydrodynamics, $K_0$ is a constant of $0.7 \pm 0.03$ expected from a transport model in [129]

Figure.5.2 includes several studies on the eccentricity-scaled anisotropy coefficients, $v_{2,4}(p_T, N_{part})/\varepsilon_{2,4}(N_{part})$. The figues in the left panel show the comparison of $v_2/\varepsilon_2$ vs. $N_{part}$ for several $p_T$ seletions in ideal hydrodynamic (a) and viscous hydrodynamic (b) simulations of $Au + Au$ collisions. For perfect fluid, we expect to see flat $N_{part}$ dependence of $v_2/\varepsilon_2$; that is, the eccentricity-scaled anisotropy coefficient $v_2/\varepsilon_2$ does not show dependence on centrality. However, we could clearly read from panel (b) that viscous effect breaks such invariance suggested by simulations in the ideal case. It is noteworthy that these deviations away from the flat $N_{part}$ dependence can be used to evaluate the viscous corrections [130–132]. The figures in upper-right panel of Fig.5.2 show the experiment data of $v_2/\varepsilon_2$ (a) and $v_4/\varepsilon_4$ (b) as a function of $N_{part}$ for several $p_T$ selections, using MC-KLN model. The dashed curves indicate fits to the data with Eqn.5.2. Two sets of data show similar trends; that is for the lowest $p_T$ particles, an almost flat $N_{part}$ dependence is observed for both $v_2/\varepsilon_2$ and $v_4/\varepsilon_4$, indicating small eccentricity scaling violations. As $\langle p_T \rangle$ increases, the data are more "curved" with progressively upward slope. By contrast, the figure in bottom-right panel of Fig.5.2 exhibts an inverse trend, suggesting that the scaling violations decrease with increasing $p_T$ as $p_T$ is above $\sim 3$ GeV/c. Such interesting inversion in data trend might serve as an indication of suppresion-driven anisotropy that takes over and comes into play.

## 5.2 The Acoustic Anisotropic Flow and Its Visous Damping

The acoustic nature of anisotropic flow is rooted in its pressure gradient-driven mechanism. The fact that magnitude of $v_n(p_T, cent)$ drops as $n$ increases can be viewed as the dissipative effect that is analog to the attenuation of sound

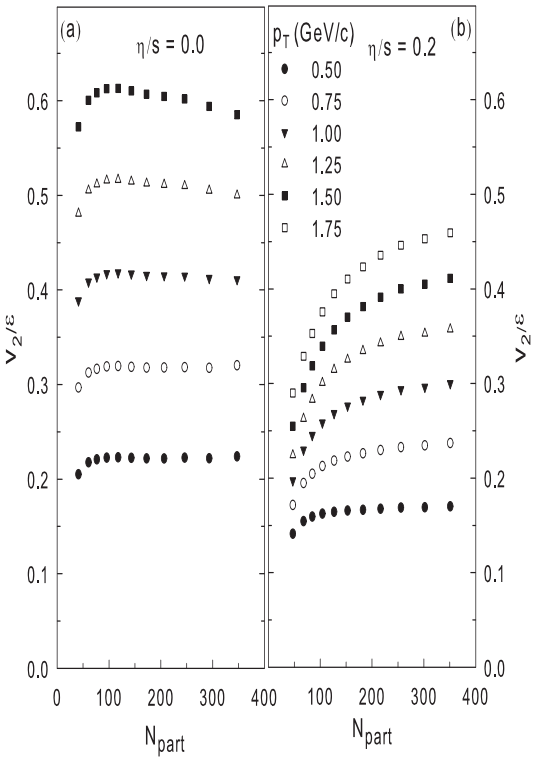


$v_2/\varepsilon_2$ vs. $N_{part}$ for several $p_T$ selections as indicated from (a) perfect fluid and (b) viscous hydrodynamic simulations of $Au + Au$ collisions [43].

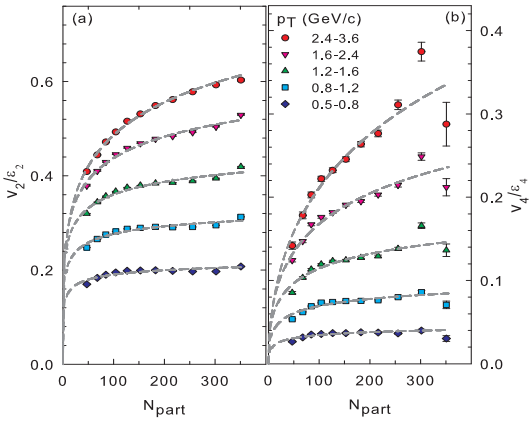


(a) $v_2/\varepsilon_2$ vs. $N_{part}$ (b) $v_4/\varepsilon_4$ vs. $N_{part}$ for several $p_T$ selections as indicated [127]. The dashed curves guide the fit to data in (a) and (b) with Eqn.5.2.

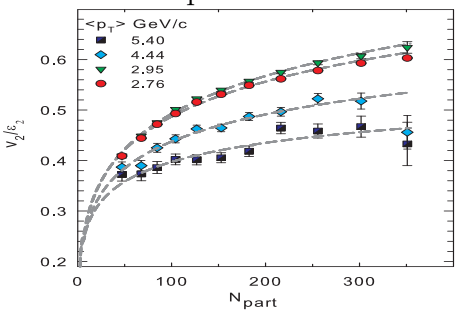


$v_2/\varepsilon_2$ vs. $N_{part}$ for several $\langle p_T \rangle$ values. The data are represented by different filled symbols, which are same as in upper figure panel (a). The dashed curves guide the fits to the data obtained with Eqn.5.2.

Figure 5.2: Various studies of $v_{2,4}/\varepsilon_{2,4}$ vs. $N_{part}$. Figure taken from [43]

waves in the plasma. Sound intensity is expected to be damped exponentially $\sim e^{-r/\Gamma_s}$. Here $\Gamma_s$ characterizes the sound attenuation length. This attenuation can be described in terms of a perturbation to the energy-momentum tensor $T_{\mu\nu}$,

$$\delta T_{\mu\nu}(n,t) = e^{-\beta n^2}\delta T_{\mu\nu}(0), \quad \beta = \frac{2}{3}\frac{\eta}{s}\frac{1}{\bar{R}^2}\frac{t}{T}, \tag{5.3}$$

where $\delta T_{\mu\nu}(0)$ reflects the spectrum of initial ($t = 0$) perturbations associated with the eccentricity moments that depict the collision geometry and its density driven fluctuations. $\beta$ is the viscous coefficient $\propto \eta/s$, $t \propto \bar{R}$ is the expansion time, $T$ is the temperature, $k = n/\bar{R}$ is the wave number (*i.e.* $2\pi\bar{R} = n\lambda$ for $n \geqslant 1$, $\lambda$ is the mean-free path) and $\bar{R}$ is the initial-state transverse size of the collision zone ($1/\bar{R} = (1/\sigma_x^2 + 1/\sigma_y^2)^{1/2}$).

A finite viscosity in the plasma may result in an asymmetry in the energy-momentum tensor which manifests as a correction to the local particle distribution ($f$) at freeze-out [132];

$$f = f_0 + \delta f(\tilde{p_T}), \quad \tilde{p_T} = \frac{p_T}{T}, \tag{5.4}$$

where $f_0$ is the quilibrium distribution and $\delta f(\tilde{p_T})$ is its purturbation correction to the first order, which leads to the $p_T-$dependent vicous coefficient $\beta'(\tilde{p_T}) \propto \beta/p_T^{\alpha}$. Here the $\alpha$'s magnitude is related to the relaxation time $\tau_R(p_T)$.

Equations 5.3 and 5.4 indicate that for a given centrality, the viscous corrections to the harmonic flow coefficients $v_n(p_T)$, grow exponentially as $n^2$; that is,

$$\frac{v_n(p_T)}{\varepsilon_n} \propto \exp\left(-\beta' n^2\right) \tag{5.5}$$

and the ratios of $v_n(p_T)$ and $v_2(p_T)$ can be written as,

$$\frac{v_n(p_T)}{v_2(p_T)} = \frac{\varepsilon_n}{\varepsilon_2}\exp\left(-\beta'(n^2-4)\right), \tag{5.6}$$

Equation 5.6 implies that higher order harmonics $v_n(p_T)$ ($n \geqslant 3$) can all be expressed in terms of the second order harmonic $v_2(p_T)$. The ratio between them only depends on the quotient of eccentricity and the relative viscous correction factors, as has been reported in [122]. Equation 5.5 can also be conveniently expressed in logarithm scale,

$$ln\left(\frac{v_n(p_T)}{\varepsilon_n}\right) \propto \frac{-\beta''}{\bar{R}}, \quad \beta'' = \frac{4}{3}\frac{n^2\eta}{Ts}, \tag{5.7}$$

which gives a characteristic system size dependence ($1/\bar{R}$) of the viscous cor-

rections. Note that $\beta'' \propto \eta/s$.

Note that the acoustic dissipative patterns summarized in Eqn.5.5,5.6, 5.7, if validated, suggest the possible extractions of $\alpha, \beta$ and $\varepsilon_n/\varepsilon_2$ from data. The multiple validation tests for these dissipative patterns as well as the their indicated eccentricity models are presented in the following Figures. **??**. The data employed in our analysis are taken from measurements by the ATLAS collaboration for $Pb+Pb$ collisions at $\sqrt{s_{NN}} = 2.76$ TeV. Figure 5.3 presents $v_n/\varepsilon_n$ as a function of $n$ for several $p_T$ selections in 20-30% most central collisions. The dashed curves are the exponential fits (cf. Eqn. 5.5) that reflect the viscous damping compatible with sound propagation in the plasma. The number of participants $N_{part}$ and $\varepsilon_n(cent)$ were computed via Monte Carlo Glauber (MC-Glauber) simulations based upon the two-dimensional profile of the density of sources in the transverse plane $\rho_s(\boldsymbol{r}_\perp)$. The weight $\omega(\boldsymbol{r}_\perp) = \boldsymbol{r}_\perp{}^n$ was used to compute $\varepsilon_n(cent)$.

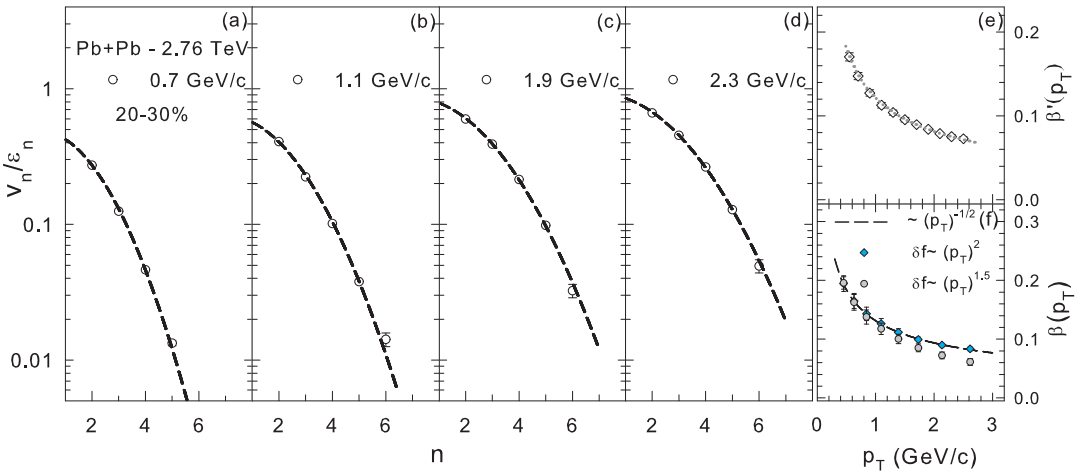


Figure 5.3: (a)–(d) $v_n/\varepsilon_n$ vs.$n$ for several $p_T$ selections in 20-30% most central $Pb+Pb$ events at $\sqrt{s_{NN}} = 2.76$ TeV [44]; (e) extracted $\beta'$ vs. $p_T$ for the same centrality selection; (f)$\beta'$ vs. $p_T$ from viscous hydrodynamical calculations [45] for $\delta f \propto p_T^2$ and $\delta f \propto p_T^{1.5}$.

Figure.5.3 confirms the expected exponential growth of the viscous corrections to $v_n$, as $n^2$. The $p_T-$dependent viscous coefficients $\beta'(\tilde{p_T})$ obtained from these fits, are summarized in Fig.5.3 (e), which confirms the expected $1/p_T^\alpha$ dependence in $\delta f(p_T)$. A similar dependence is also achieved for fits to the results of viscous hydrodynamical calculations, as shown in panel (f). The dotted curve in panel (e) indicates that good fit with $\alpha \sim 0.58$ and $\beta \sim 0.12$ could describe the trend fairly well. Similar results were obtained for a broad range of centrality selections.

Other interesting tests include ratios of the flow harmonics $v_n(p_T)/v_2(p_T)$ $(n \geqslant 3)$ (cf. Eqn.5.6) as well as the dependence of $v_n(p_T)/\varepsilon_n$ on the transverse size of the collision zone (cf. Eqn. 5.7). The open symbols in Fig.5.4 represent the measured ratios $v_n(p_T)/v_2(p_T)$ for $n = 3, 4, 5$ within indicated centrality selections. A simultaneous fit to these ratios was performed with Eqn.5.6 to extract parameter $\beta$ and $\varepsilon_n/\varepsilon_2$ at each centrality[1]. The filled symbols in Fig.5.4 show that the proposed fits describe data very well, which confirms the characteristic dependence of the viscous correction factors presented in Eqn.5.6. It is noteworthy that the good consistency achieved in Fig.5.4 also indicate that higher order harmonics are inherently related to $v_2$ via the "acoustic scaling" of the viscous corrections to anisotropic flow. The extracted values for $\varepsilon_n/\varepsilon_2$, $\alpha$ and $\beta$ are further studied and discussed below.

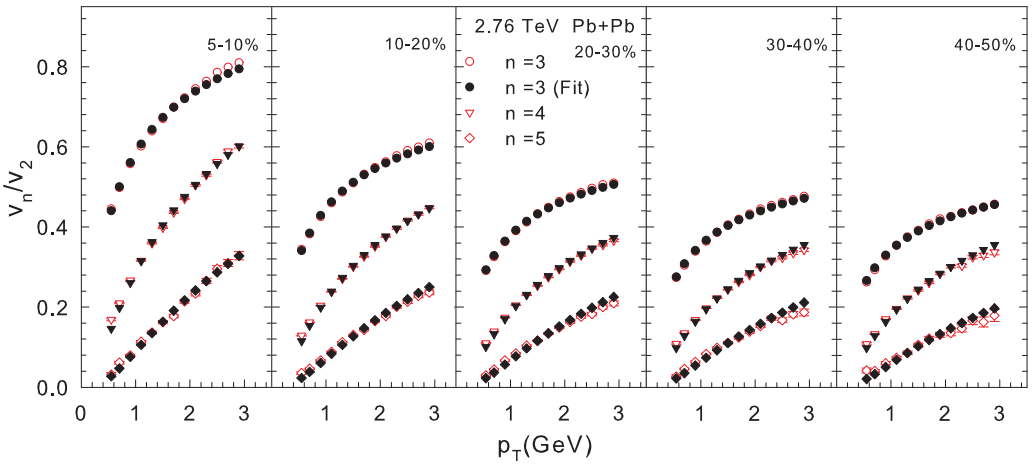


Figure 5.4: $v_n/v_2$ vs.$p_T$ for several centrality selections for $Pb + Pb$ collisions at $\sqrt{s_{NN}} = 2.76$ TeV. The open symbols represent the values from data; the filled symbols show the results of fits to these ratios with Eqn.5.6.

Figure.5.5 presents a direct study on the viscous correction and its relation with centrality (system size). The panel (a) in Fig.5.5 shows the $v_n$ (n=2,3) as a function of $N_{part}$ for $p_T \in (2, 3)$ GeV/c seletion. It is known from the plot that both $v_2$ and $v_3$ increases for $140 \lesssim N_{part} \lesssim 340$, a phenomenon considered as the result of an increase in $\varepsilon_2$ and $\varepsilon_3$ over same $N_{part}$ range. For more peripheral events with $N_{part}$ less than 140 however, the drecreasing of $v_2$ and $v_3$ contrasts with the increasing trends for $\varepsilon_2$ and $\varepsilon_3$, indicating that the viscous effects act to suppress $v_2$ and $v_3$ in much smaller collision profile. This interesting finding is further validated by the dashed curves in

[1] An initial value of $\alpha \sim 0.58$ from previous extraction was used to aid the convergence of these fits.

Fig.5.5 (b), where a linear dependence of $ln(v_n/\varepsilon_n)$ on $1/\bar{R}$ (cf. Eqn.5.7) is observed for the data shown in Fig.5.5 (a). Note as well that the slopes for n = 3 in Fig.5.5(b) are more than a factor of two larger than those for n = 2 as expected (cf. Eqn.5.7). Similar check is performed for other $p_T$ selections and same linear dependence is seen. Note that the slopes of these curves incorporate the information of viscosity via $\beta''$ ($\beta$).

Figure.5.5 (c)–(e) present a comparison between $\varepsilon_n/\varepsilon_2$ ratios (open symbols) extracted from the fits shown in Fig.5.4 and those obtained from model calculations (filled symbols). For the given 5-50% centrality range, the comparison shows good agreement between the extracted ratios and those obtained from MC-Glauber calculations with weight $\omega(\boldsymbol{r}_\perp) = \boldsymbol{r}_\perp{}^n$. However, an agreement is not achieved if the $\varepsilon_n/\varepsilon_2$ ratios are compared with model calculations from the factorized Kharzeev-Levin-Nardi (KLN) model. It can be also seen from the comparison that the extracted values of $\varepsilon_n/\varepsilon_2$ are larger than the values obtained from either eccentricity model in 0-10% centrality events. This difference could be due to the overestimate of $\varepsilon_2$ in most central events for the two eccentricity models involved.

The fits shown in Fig.5.4 give values for $\alpha$ and $\beta$, which are summarized in Fig.5.5(f) and (g); they are essentially centrality invariant. This suggests that within errors, the full data set for $v_n(p_T, cent)$ can be understood in terms of the eccentricity moments coupled to a single (average) value for $\alpha$ and $\beta$. Interestingly, this observation is compatible with recent viscous hydrodynamical calculations that are successful in reproducing $v_n(p_T, cent)$ measurements with a single $\delta f(\tilde{p_T})$ ansatz and an average value of $\eta/s$ [45, 133]

It is shown recently [134] that the characteristic linear dependence of $ln(v_n/\varepsilon_n)$ on $1/\bar{R}$ with slope $\beta'' \propto \eta/s$ holds across a borad range of beam energies across RHIC and the LHC. The fact that, the increase in $v_2$ from central to mid-central collisions followed by a decrease for peripheral collisions persists across the full range of collision energies, is considered as an indication that the transverse size of the collision zone plays a similar role in viscous damping across the full range of beam energies studied.

## 5.3 Scaling of Higher-order Flow and Its Implications

The coefficients $v_n(p_T, cent)$ (for odd and even $n$) are sensitive to both the initial eccentricity and the specific shear viscosity $\eta/s$. We have shown in previous chapters (cf. Section 1.3.2) that due to finite number of participants, the pervasive assumption of a smooth initial eccentricity profile may not be true in

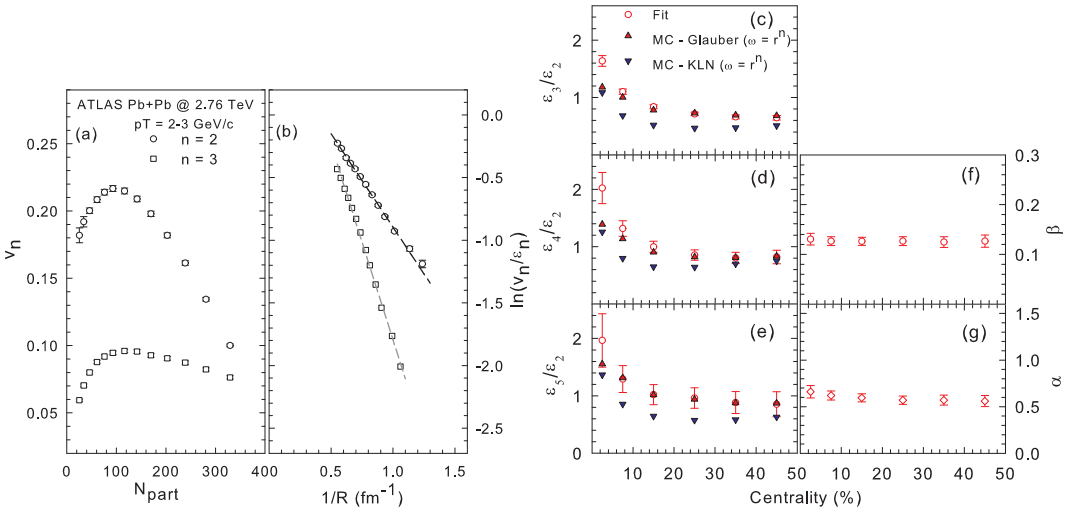


Figure 5.5: (a) $v_{2,3}$ vs.$N_{part}$ for $p_T \in (1,2)$ GeV/c; (b) $ln(v_n/\varepsilon_n)$ vs.$(1/\bar{R})$ for the data shown in (a); (c)–(e) $\varepsilon_n/\varepsilon_2$ vs. $N_{part}$. Open symbols are the values extracted from fits to $v_n(p_T)/v_2(p_T)(n \geqslant 3)$ with Eqn.5.6; filled symbols are from MC-Glauber and MC-KLN model calculations; (f) extracted values of $\beta$ vs. centrality; (g) extracted values of $\alpha$ vs. centrality.

real experiments. Instead, a rather "lumpy" transverse density distributions generated in actual collisions would result in the eccentricity profile that does not show particular spatial symmetry, so that odd-order harmonics are not necessarily zero from event to event.

Given Eqn.5.3 and the relation that $k = n/\bar{R}$, the viscous damping scales as $k^2$. The vsicous corrections for the higher-order eccentricity driven harmonics are then expected to scale as $n^2K$. Here, $K$ is the Knudsen number ($K = \lambda/\bar{R}$) ansatz (cf. Eqn.5.2). Therefore, the viscous corrections to higher-order harmonics can be expressed in terms of that for the second order flow harmonic,

$$K(n) = \left(\frac{n}{2}\right)^2 K(2), \tag{5.8}$$

suggesting a scaling in viscous damping process for $v_n(p_T)$ $(n \geqslant 3)$ and $v_2(p_T)$ within the same centrality class.

Figure.5.6 shows the ratios $v_3/(v_2)^{3/2}$ and $v_4/(v_2)^2$ as a function of $p_T$ [(a) and (b)] and $N_{part}$ [(c) and (d)] respectively. Figs.5.6 (a) and (b) show a flat $p_T$ dependence. However, Figs.5.6 (c) and (d) indicate much larger centrality dependence. The $p_T-$invariant feature of $v_3/(v_2)^{3/2}$ and $v_4/(v_2)^2$ within certain centrality class is considered as an indication of the $p_T-$independent contributions to the viscous corrections, which result from the dispersion relation

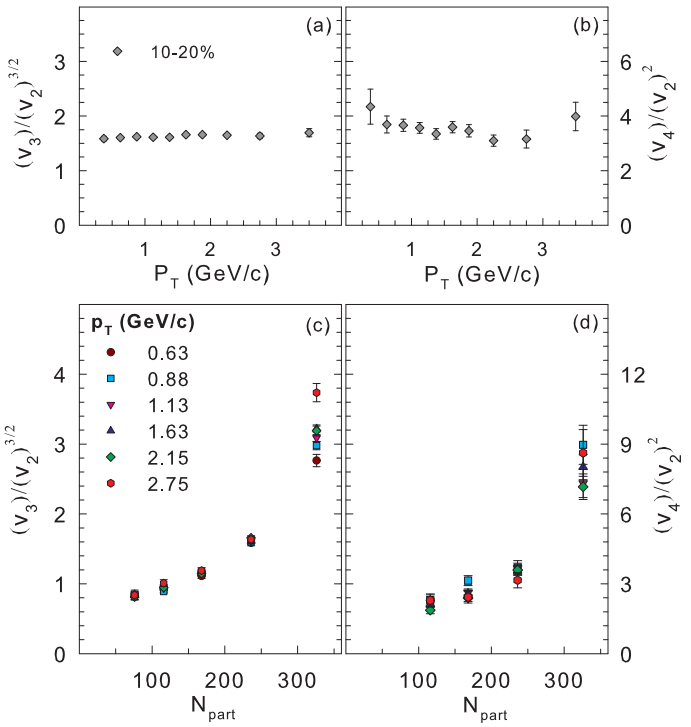


Figure 5.6: $v_3/(v_2)^{3/2}$ vs. $p_T$ (a) and $v_4/(v_2)^2$ vs. $p_T$ (b) for 10-20% most central $Au + Au$ collisions. The botton panels show $v_3/(v_2)^{3/2}$ vs. $N_{part}$ (c) and $v_4/(v_2)^2$ vs. $N_{part}$ (d) for several $p_T$ selections. Data are from Ref.[41].

for sound propagation [122]. Note that the overall viscous corrections do show $p_T$ dependence (cf. Fig.5.3 (e)). On the other hand, the flat $p_T$ dependence of $v_n/(v_2)^{n/2}$ suggests the acoustic $n^2K$ scaling relationship holds in viscous damping process for different order harmonics.

One striking feature of the observed $n^2K$ scaling (the $v_n/(v_2)^{n/2}$ scaling) is their potential distinguishing power of eccentricity models. It is suggested from $v_n/(v_2)^{n/2}$ scaling (*i.e.* $v_n/(v_2)^{n/2}$ does not show significant $p_T$ dependence within a given centrality class) that the $p_T-$dependent contributions to the viscous corrections would cancel out if we take the ratios $(v_n/\varepsilon_n)/(v_2/\varepsilon_2)^{n/2}$, and $v_n/(v_2)^{n/2}$ should behave like $\varepsilon_n/\varepsilon_2^{n/2}$. Figure.5.7 presents data comparison to the calculated ratios (a) $\varepsilon_3/(\varepsilon_2)^{3/2}$ vs. $N_{part}$ and (b) $\varepsilon_4/(\varepsilon_2)^2$ vs. $N_{part}$ for MC-Glauber and MC-KLN geomeotries in $Au+Au$ collisions. The $\varepsilon_n$ values for these ratios were evaluated as described in Section 5.1. The solid symbols are a representative set of experiment $v_n/(v_2)^{n/2}$ data (cf. Fig.5.6(c)(d)); the open symbols show the eccentricity ratios evaluated in two eccentricity models. A relatively good agreement between data and calculated $\varepsilon_n/(\varepsilon_2)^{n/2}$ indicate the possible discriminating ability of $v_n/(v_2)^{n/2}$ scaling in initial geometry model comparison.

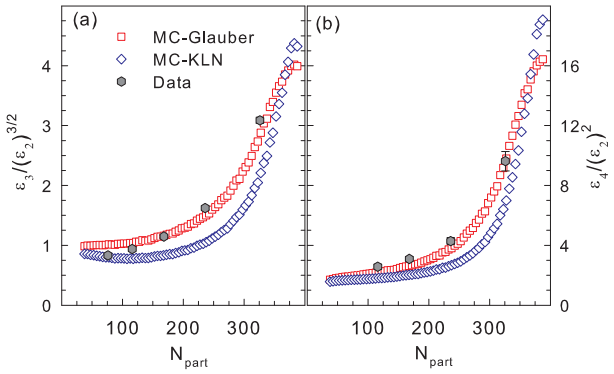


Figure 5.7: Data comparison to the calcualted ratios (a) $\varepsilon_3/(\varepsilon_2)^{3/2}$ vs. $N_{part}$ and (b) $\varepsilon_4/(\varepsilon_2)^2$ vs. $N_{part}$ for MC-Glauber and MC-KLN geomeotries in $Au+Au$ collisions. Figure taken from [122]

# Chapter 6

# Summary and Conclusions

Anisotropic flow is one of the most prominent bulk observables in heavy-ion collisions. This dissertation details the methodology and results of particle identified (PID) charged hadrons $v_n$ (n = 2,3,4) measurements, as a function of $p_T$, centrality and transverse kinetic energy, for $Au + Au$ collisions with PHENIX detector at $\sqrt{s_{NN}}$ = 200, 62.4 and 39 GeV, via long-range two-particle correlation (2PC) method. The obtained $v_2$ for charged pinos, kaons and (anti-)protons are consistent with results via event plane (EP) method at all collision energies studied. The higher order harmonics $v_3$ for all particle species at $\sqrt{s_{NN}}$ = 62.4 and 39 GeV are, for the first time, measured at PHENIX.

2PC method discussed in this manuscript correlates two sets of particle hits coming from separate $\eta$ ranges. We analyzed the azimuthal distributions for pairs in form of correlation functions, between central arm tracks and hits in one RxNP detector [(CNT,RxNP)], as well as correlations between hits in two RxNP sub-detectors, one on each side [(RxNP-N, RxNP-S)]. These correlation functions were then Fourier decomposed to extract event-averaged products $\left\langle v_n^{CNT} v_n^{RxNP} \right\rangle$ and $\left\langle v_n^{RxNP} v_n^{RxNP} \right\rangle$. The $v_n$ for central arm tracks were calculated as $v_n^{CNT} = \left\langle v_n^{CNT} v_n^{RxNP} \right\rangle / \sqrt{\left\langle v_n^{RxNP} v_n^{RxNP} \right\rangle}$. Data used were collected during the 2007 and 2010 run period by PHENIX collaboration.

The role of initial geometry fluctions was not realized until collisions of smaller nuclei ($Cu + Cu$) were carried out at RHIC in year 2005. It was found then the ratio $v_2/\varepsilon_2$ was surprisingly larger in this smaller system, compared to that in $Au + Au$ collisions. Moreover, the measured elliptic flow did not vanish in the most central events. One possible explanation to resolve this finding is the fluctuations in the initial state collision profile, which are considered more pronounced in smaller collision system. Since then, the pervasive assumption of a smooth eccentricity profile started to became questionable, and significant attention has been given to the full exploitation of the intial geometry

fluctuations and their link to odd order harmonics (especially $v_3$, $v_5$, etc).

The success measurement of higher order harmonics (for odd and even $n$) $v_n$ ($n \geqslant 3$) is a milestone in studies of the bulk properties of created plasma in heavy-ion collisions. Higher order harmonics will not only give more information about the transverse geometry fluctuations of the generalized eccentricities, but will also provide an important avenue for constraining different properties of the QGP. The measurements of particle identified charged hadrons $v_n$ would further extend our discussions into a new level, where a better insight on the expansion dynamics and more demanding tests for consituent quark number scaling for higher harmonics are expected.

Previous $v_2$ data for identified charged hadrons have shown a universal $v_2/n_q$ scaling for transverse kinetic energy $KE_T/n_q \lesssim 1$ GeV/c, *i.e.* quark number scaling. This observation is considered as an evidence for the partonic collectivity origin of ansitropic flow within indicated range of transverse kinentic energy. The higher order harmonics presented in this work show that such scaling is still valid. That is, $v_n/(n_q)^{n/2}$ vs. $KE_T/n_q$ gives a single curve for $\pi^{\pm}$, $K^{\pm}$ and $p\bar{p}$, evaluated within the same transverse kinetic energy $KE_T$ range. The universal scaling of data suggests that $v_n(p_T) \propto (v_2)^{n/2}$, which stems from the acoustic property of anisotropic flow.

A good consistency is found for $v_n$ results in cross-method (2PC and EP method) comparisons. The way we construct correlation functions in 2PC method requires a relative large pseudorapidity gap between selected hadron pairs. Such large $\eta$ separation should, in principle, suppress any near-side jet and short-range correlations as well as substantial amount of the away-side jets constributions. Indeed, the observed agreement between particle identified $v_n$ results via 2PC and EP method confirms the phase space we are looking at in anisotropy measurements presented in this work, is dominated by collective flow. That is, the left-over contributions from non-flow effects, if any, do not influence the azimuthal correlations significantly. Here, it must be emphasized that the observed agreement between 2PC flow measurement and the same quantity obtained via EP method does not indicate the absolute absence of non-flow correlations.

Another interesting study is the cross-experiment comparison of particle identified $v_n$ results, between RHIC (PHENIX) and the LHC (ALICE). The LHC $v_n$ measurements can be understood in terms of an eccentricity-driven hydrodynamic expansion of the QGP at a much higher energy density in heavy-ion ($Pb + Pb$) collisions. In spite of the striking similarity between RHIC and LHC $v_2(p_T)$ measurements for unidentified charged hadrons, tests for quark number scaling with LHC data for identified charged hadrons, have indicated an apparent breakdown of this scaling. To investigate whether the notable

increase in energy density from RHIC to LHC, signals a possible change in the expansion dynamics, I have compared the double differential measurements of $v_2(p_T, cent)$ for each identified charged hadron species. The $v_2(p_T)$ values for $\pi^{\pm}$ and $K^{\pm}$ are found approximately 20% larger than the RHIC values for the 20-30% most central events. On top of this "scale-up" effects that arise from much higher energy density at the LHC, the $v_2(p_T)$ data for $p\bar{p}$ at the LHC show a significant blueshift, which is also observed in recent viscous hydrodynamical calculations for LHC collisions. Such blueshift can be due to a sizable increase in the magnitude of the radial flow generated in LHC collisions, especially in the hadronic phase.

Several factors that could potentially influence the magnitude of azimuthal anisotropy are, for example, eccentricity, equation of state (EOS) and bulk shear viscosity. Much efforts have been devoted to theoretical modeling of the initial state eccentricity and equation of state as well as the possible extraction of shear viscosity of the plasma created in heavy-ion collisions. Because of the acoustic nature of anisotropic flow, the dissipative effects of the magnitude of $v_n(p_T, cent)$ as $n$ increases, is similar to the attenuation of sound waves in the plasma. In addition to the discriminating ability in eccentricity model comparisons, multiple empirical studies of acoustic scaling are also shown in [134, 135] to provide an avenue for extracting the specific shear viscosity $(\eta/s)$ of the quark-gluon plasma (QGP) produced in these collisions. A calibration of these scaling parameters via detailed viscous hydrodynamical model calculations, would give $(\eta/s_{QGP})$ estimates for the plasma produced in collisions of Au+Au ($\sqrt{s_{NN}} = 0.2$ TeV) and Pb+Pb ($\sqrt{s_{NN}} = 2.76$ TeV).

# Appendix A

# Tabulated Results for PIDed $v_n$ (n=2,3,4) in $Au + Au$ Collisions at $\sqrt{s_{NN}} = 200$ GeV

## A.1 Tabulated $v_2$ results

| $p_T$ (GeV/c) | Value | Stat. Errors ($\pm$) | Sys. Errors ($\pm$) |
|---|---|---|---|
| 0.393912 | 0.0108951 | 2.11646e-05 | 0.00054 |
| 0.590979 | 0.0223377 | 2.80841e-05 | 0.00111 |
| 0.789924 | 0.0329675 | 3.82833e-05 | 0.00165 |
| 0.990379 | 0.0424624 | 5.12695e-05 | 0.00212 |
| 1.19014 | 0.0503313 | 6.65545e-05 | 0.0015 |
| 1.39029 | 0.0570917 | 8.5745e-05 | 0.00171 |
| 1.59037 | 0.0622329 | 0.000110078 | 0.00187 |
| 1.79062 | 0.067128 | 0.000139275 | 0.00201 |
| 1.98994 | 0.0687986 | 0.000177396 | 0.00206 |
| 2.18952 | 0.0717099 | 0.000230081 | 0.00215 |
| 2.38952 | 0.067544 | 0.000296553 | 0.00202 |
| 2.5895 | 0.0719367 | 0.000398681 | 0.00216 |
| 2.82759 | 0.0697584 | 0.0004657 | 0.00209 |
| 3.19154 | 0.0748332 | 0.000610221 | 0.002245 |

Table A.1: Charged Pions $v_2$ in 0-10% centrality

| $p_T$ **(GeV/c)** | **Value** | **Stat. Errors** ($\pm$) | **Sys. Errors** ($\pm$) |
|---|---|---|---|
| 0.426667 | 0.0024002 | 0.000156647 | 0.00012 |
| 0.604826 | 0.01162 | 9.51817e-05 | 0.00058 |
| 0.796943 | 0.0226794 | 9.21916e-05 | 0.00113 |
| 0.994607 | 0.0333759 | 0.000104231 | 0.0017 |
| 1.19307 | 0.0427664 | 0.00012527 | 0.0013 |
| 1.39245 | 0.0497834 | 0.000155987 | 0.0015 |
| 1.59183 | 0.0572745 | 0.000195161 | 0.00171 |
| 1.79193 | 0.0615992 | 0.000249252 | 0.00184 |
| 1.99174 | 0.064267 | 0.000312289 | 0.00192 |
| 2.19005 | 0.0680189 | 0.000395092 | 0.0020 |
| 2.39072 | 0.0740449 | 0.000465202 | 0.0022 |
| 2.59118 | 0.0705769 | 0.000629877 | 0.00211 |
| 2.82875 | 0.067334 | 0.00064431 | 0.00202 |

Table A.2: Charged Kaons $v_2$ in 0-10% centrality

| $p_T$ **(GeV/c)** | **Value** | **Stat. Errors** ($\pm$) | **Sys. Errors** ($\pm$) |
|---|---|---|---|
| 0.612371 | 0.000474392 | 0.000113835 | 0.000024 |
| 0.80333 | 0.00741845 | 9.10273e-05 | 0.00037 |
| 0.999108 | 0.017132 | 9.12251e-05 | 0.00086 |
| 1.19618 | 0.0285581 | 0.000102482 | 0.000857 |
| 1.39462 | 0.040447 | 0.000122843 | 0.00121 |
| 1.59323 | 0.0522901 | 0.000152045 | 0.00157 |
| 1.79273 | 0.0624301 | 0.000190201 | 0.00187 |
| 1.9921 | 0.0699461 | 0.000239242 | 0.00210 |
| 2.19136 | 0.0787252 | 0.000303981 | 0.00236 |
| 2.3918 | 0.0843349 | 0.000392456 | 0.00253 |
| 2.59154 | 0.0885018 | 0.000496841 | 0.002655 |
| 2.83084 | 0.0932713 | 0.000545547 | 0.00280 |
| 3.20021 | 0.0984205 | 0.000648661 | 0.00295 |

Table A.3: (anti-)protons $v_2$ in 0-10% centrality

| $p_T$ **(GeV/c)** | **Value** | **Stat. Errors** ($\pm$) | **Sys. Errors** ($\pm$) |
|---|---|---|---|
| 0.39411 | 0.0244199 | 1.87067e-05 | 0.000122 |
| 0.591081 | 0.0436975 | 2.67738e-05 | 0.00218 |
| 0.790013 | 0.0618575 | 3.69997e-05 | 0.00309 |
| 0.990465 | 0.0777791 | 4.86597e-05 | 0.00389 |
| 1.19028 | 0.0913519 | 6.21716e-05 | 0.00274 |
| 1.39042 | 0.102953 | 7.88972e-05 | 0.00309 |
| 1.59054 | 0.112223 | 0.000100772 | 0.00337 |
| 1.79085 | 0.119715 | 0.000127724 | 0.00359 |
| 1.99015 | 0.124714 | 0.000164455 | 0.00374 |
| 2.18971 | 0.128314 | 0.000215467 | 0.00385 |
| 2.38976 | 0.129366 | 0.00028824 | 0.00388 |
| 2.58973 | 0.128579 | 0.000388829 | 0.003847 |
| 2.82805 | 0.131466 | 0.000460814 | 0.00394 |
| 3.19216 | 0.126746 | 0.000602295 | 0.00380 |

Table A.4: Charged Pions $v_2$ in 10-20% centrality

| $p_T$ **(GeV/c)** | **Value** | **Stat. Errors** ($\pm$) | **Sys. Errors** ($\pm$) |
|---|---|---|---|
| 0.427602 | 0.0118513 | 0.000114137 | 0.00059 |
| 0.605056 | 0.0263153 | 7.56557e-05 | 0.00131 |
| 0.797111 | 0.0457681 | 7.69206e-05 | 0.00229 |
| 0.994676 | 0.062795 | 8.93272e-05 | 0.00314 |
| 1.19319 | 0.077507 | 0.000108753 | 0.00233 |
| 1.39248 | 0.0905036 | 0.000136473 | 0.0027 |
| 1.59197 | 0.102115 | 0.000171142 | 0.00306 |
| 1.79207 | 0.109712 | 0.000216712 | 0.00329 |
| 1.9919 | 0.118713 | 0.000274959 | 0.00356 |
| 2.19024 | 0.124018 | 0.000350273 | 0.00372 |
| 2.3911 | 0.120698 | 0.000447469 | 0.00362 |
| 2.59159 | 0.122838 | 0.000600863 | 0.00369 |
| 2.82916 | 0.125717 | 0.000652926 | 0.00377 |

Table A.5: Charged Kaons $v_2$ in 10-20% centrality

| $p_T$ **(GeV/c)** | **Value** | **Stat. Errors** ($\pm$) | **Sys. Errors** ($\pm$) |
|---|---|---|---|
| 0.612566 | 0.0078406 | 8.58145e-05 | 0.00039 |
| 0.80328 | 0.0208955 | 7.1884e-05 | 0.00104 |
| 0.998981 | 0.0379813 | 7.38927e-05 | 0.00190 |
| 1.19614 | 0.0572126 | 8.539e-05 | 0.00171 |
| 1.39454 | 0.0771432 | 0.000103508 | 0.00231 |
| 1.59323 | 0.0964584 | 0.000129482 | 0.00289 |
| 1.79275 | 0.113757 | 0.000162708 | 0.00341 |
| 1.99218 | 0.127835 | 0.00020519 | 0.00383 |
| 2.19156 | 0.139934 | 0.000261768 | 0.00420 |
| 2.39183 | 0.150558 | 0.000337993 | 0.004517 |
| 2.59186 | 0.159751 | 0.000430003 | 0.00479 |
| 2.83123 | 0.167722 | 0.00047983 | 0.00503 |
| 3.20156 | 0.169967 | 0.000589494 | 0.00510 |

Table A.6: (anti-)protons $v_2$ in 10-20% centrality

| $p_T$ **(GeV/c)** | **Value** | **Stat. Errors** ($\pm$) | **Sys. Errors** ($\pm$) |
|---|---|---|---|
| 0.394178 | 0.0362553 | 1.97447e-05 | 0.00109 |
| 0.591095 | 0.0618754 | 2.73142e-05 | 0.00186 |
| 0.790023 | 0.0850946 | 3.74175e-05 | 0.00255 |
| 0.990485 | 0.105552 | 4.95888e-05 | 0.00317 |
| 1.19037 | 0.123074 | 6.45237e-05 | 0.00369 |
| 1.39051 | 0.136489 | 8.35726e-05 | 0.00409 |
| 1.59071 | 0.148226 | 0.000109404 | 0.00445 |
| 1.79101 | 0.156559 | 0.00014189 | 0.00470 |
| 1.99028 | 0.162557 | 0.000184449 | 0.00488 |
| 2.19008 | 0.166949 | 0.000243958 | 0.00501 |
| 2.3899 | 0.167581 | 0.000322874 | 0.00503 |
| 2.58985 | 0.170931 | 0.000440613 | 0.005128 |
| 2.82831 | 0.167481 | 0.000507397 | 0.00502 |
| 3.19338 | 0.165856 | 0.00067463 | 0.00498 |

Table A.7: Charged Pions $v_2$ in 20-30% centrality

| $p_T$ **(GeV/c)** | **Value** | **Stat. Errors** ($\pm$) | **Sys. Errors** ($\pm$) |
|---|---|---|---|
| 0.428055 | 0.020941 | 0.000122166 | 0.00063 |
| 0.605058 | 0.0405734 | 8.29707e-05 | 0.00122 |
| 0.797059 | 0.0647101 | 8.53321e-05 | 0.00194 |
| 0.994709 | 0.0868844 | 9.95737e-05 | 0.00261 |
| 1.19324 | 0.106295 | 0.00012204 | 0.00319 |
| 1.39254 | 0.122317 | 0.000153094 | 0.00367 |
| 1.59201 | 0.135442 | 0.000195479 | 0.00406 |
| 1.79215 | 0.145904 | 0.000247229 | 0.00438 |
| 1.99208 | 0.152651 | 0.000314659 | 0.00458 |
| 2.19062 | 0.158601 | 0.000401827 | 0.00476 |
| 2.39127 | 0.162857 | 0.000526825 | 0.00489 |
| 2.59192 | 0.161591 | 0.000669513 | 0.00485 |
| 2.82977 | 0.161467 | 0.000749166 | 0.00484 |

Table A.8: Charged Kaons $v_2$ in 20-30% centrality

| $p_T$ **(GeV/c)** | **Value** | **Stat. Errors** ($\pm$) | **Sys. Errors** ($\pm$) |
|---|---|---|---|
| 0.612643 | 0.0182019 | 9.04066e-05 | 0.000546 |
| 0.803063 | 0.0353357 | 7.81238e-05 | 0.00106 |
| 0.998741 | 0.0586692 | 8.16268e-05 | 0.00176 |
| 1.19583 | 0.0844739 | 9.48676e-05 | 0.00253 |
| 1.39437 | 0.110075 | 0.000115191 | 0.0033 |
| 1.5931 | 0.133209 | 0.000145161 | 0.00400 |
| 1.79269 | 0.154434 | 0.00018349 | 0.00463 |
| 1.99219 | 0.171815 | 0.000233556 | 0.00515 |
| 2.19152 | 0.187577 | 0.000300813 | 0.00563 |
| 2.39191 | 0.199973 | 0.000389253 | 0.00599 |
| 2.59184 | 0.211633 | 0.000497797 | 0.00635 |
| 2.83171 | 0.219564 | 0.00054967 | 0.00659 |
| 3.20237 | 0.223739 | 0.000676965 | 0.00671 |

Table A.9: (anti-)protons $v_2$ in 20-30% centrality

| $p_T$ **(GeV/c)** | **Value** | **Stat. Errors** ($\pm$) | **Sys. Errors** ($\pm$) |
|---|---|---|---|
| 0.394131 | 0.0451583 | 2.36626e-05 | 0.00135 |
| 0.590995 | 0.0746956 | 3.17999e-05 | 0.00224 |
| 0.789959 | 0.10122 | 4.372e-05 | 0.00304 |
| 0.990455 | 0.124584 | 5.90323e-05 | 0.00374 |
| 1.19036 | 0.14382 | 7.79617e-05 | 0.00431 |
| 1.39053 | 0.158803 | 0.000103157 | 0.00476 |
| 1.59075 | 0.170752 | 0.000137431 | 0.00512 |
| 1.79104 | 0.178111 | 0.000178452 | 0.00534 |
| 1.99046 | 0.188753 | 0.00023477 | 0.00566 |
| 2.19025 | 0.192001 | 0.000311006 | 0.00576 |
| 2.39004 | 0.190337 | 0.000417261 | 0.00571 |
| 2.59006 | 0.189627 | 0.000572156 | 0.00569 |
| 2.82862 | 0.188489 | 0.000668442 | 0.00565 |
| 3.1938 | 0.187408 | 0.000881212 | 0.00562 |

Table A.10: Charged Pions $v_2$ in 30-40% centrality

| $p_T$ **(GeV/c)** | **Value** | **Stat. Errors** ($\pm$) | **Sys. Errors** ($\pm$) |
|---|---|---|---|
| 0.428247 | 0.0284764 | 0.000152499 | 0.000854 |
| 0.604887 | 0.0510242 | 0.000104629 | 0.00153 |
| 0.796854 | 0.079472 | 0.000107739 | 0.00238 |
| 0.994566 | 0.104334 | 0.000127973 | 0.00313 |
| 1.19318 | 0.126431 | 0.000157814 | 0.00379 |
| 1.39255 | 0.14373 | 0.000198767 | 0.00431 |
| 1.59214 | 0.15576 | 0.000255103 | 0.00467 |
| 1.79226 | 0.167924 | 0.000322808 | 0.00504 |
| 1.9923 | 0.175242 | 0.000416564 | 0.00526 |
| 2.19096 | 0.180121 | 0.000527168 | 0.00540 |
| 2.39121 | 0.186656 | 0.000692087 | 0.00560 |
| 2.59182 | 0.177042 | 0.000885345 | 0.00531 |
| 2.8306 | 0.183552 | 0.000966393 | 0.00551 |

Table A.11: Charged Kaons $v_2$ in 30-40% centrality

| $p_T$ **(GeV/c)** | **Value** | **Stat. Errors** ($\pm$) | **Sys. Errors** ($\pm$) |
|---|---|---|---|
| 0.612497 | 0.0288868 | 0.000110653 | 0.000866 |
| 0.802638 | 0.05019 | 9.73025e-05 | 0.00151 |
| 0.998272 | 0.0766858 | 0.00010223 | 0.00230 |
| 1.19551 | 0.105644 | 0.000121684 | 0.00317 |
| 1.39409 | 0.134403 | 0.000149172 | 0.00403 |
| 1.59295 | 0.159736 | 0.0001879 | 0.00479 |
| 1.79256 | 0.182555 | 0.000239388 | 0.00548 |
| 1.99216 | 0.200645 | 0.000306042 | 0.00602 |
| 2.19175 | 0.215931 | 0.000400232 | 0.00648 |
| 2.39196 | 0.230966 | 0.000511647 | 0.00693 |
| 2.59196 | 0.244767 | 0.000653415 | 0.00734 |
| 2.83142 | 0.253456 | 0.000737077 | 0.00760 |
| 3.20328 | 0.256347 | 0.000910715 | 0.00769 |

Table A.12: (anti-)protons $v_2$ in 30-40% centrality

| $p_T$ **(GeV/c)** | **Value** | **Stat. Errors** ($\pm$) | **Sys. Errors** ($\pm$) |
|---|---|---|---|
| 0.393927 | 0.0501474 | 3.32114e-05 | 0.00150 |
| 0.590812 | 0.0820072 | 4.41388e-05 | 0.00246 |
| 0.789806 | 0.110697 | 6.11536e-05 | 0.00332 |
| 0.990356 | 0.135249 | 8.37677e-05 | 0.00401 |
| 1.19033 | 0.15376 | 0.00011227 | 0.00461 |
| 1.39051 | 0.170277 | 0.000151781 | 0.00511 |
| 1.59083 | 0.182792 | 0.000203067 | 0.00548 |
| 1.79112 | 0.191667 | 0.000266525 | 0.00575 |
| 1.99059 | 0.196588 | 0.000349231 | 0.00590 |
| 2.19025 | 0.200437 | 0.000468599 | 0.00601 |
| 2.39021 | 0.20558 | 0.00061544 | 0.00617 |
| 2.59022 | 0.20019 | 0.000843237 | 0.00601 |
| 2.82923 | 0.200696 | 0.000971767 | 0.00602 |
| 3.19443 | 0.185827 | 0.00126812 | 0.00557 |

Table A.13: Charged Pions $v_2$ in 40-50% centrality

| $p_T$ **(GeV/c)** | **Value** | **Stat. Errors** ($\pm$) | **Sys. Errors** ($\pm$) |
|---|---|---|---|
| 0.428145 | 0.0334025 | 0.000222649 | 0.00100 |
| 0.604506 | 0.0589453 | 0.000155766 | 0.00177 |
| 0.796611 | 0.0882861 | 0.000163052 | 0.00265 |
| 0.994384 | 0.113359 | 0.000193106 | 0.00340 |
| 1.19304 | 0.13499 | 0.000239005 | 0.00405 |
| 1.39249 | 0.15311 | 0.000301549 | 0.00460 |
| 1.59211 | 0.165123 | 0.000385999 | 0.00495 |
| 1.79215 | 0.178168 | 0.000492421 | 0.00535 |
| 1.99238 | 0.180574 | 0.000629165 | 0.00542 |
| 2.1909 | 0.185229 | 0.000811243 | 0.00556 |
| 2.39176 | 0.189189 | 0.00105081 | 0.00568 |
| 2.59212 | 0.185022 | 0.00132082 | 0.00555 |
| 2.83131 | 0.198179 | 0.00146304 | 0.00595 |

Table A.14: Charged Kaons $v_2$ in 40-50% centrality

| $p_T$ **(GeV/c)** | **Value** | **Stat. Errors** ($\pm$) | **Sys. Errors** ($\pm$) |
|---|---|---|---|
| 0.612094 | 0.037332 | 0.000158424 | 0.00112 |
| 0.802026 | 0.0624492 | 0.000141699 | 0.00187 |
| 0.997646 | 0.0924251 | 0.000154564 | 0.00277 |
| 1.19498 | 0.122511 | 0.000182464 | 0.00368 |
| 1.39366 | 0.152685 | 0.000224861 | 0.00458 |
| 1.59269 | 0.176392 | 0.00028714 | 0.00529 |
| 1.79226 | 0.199925 | 0.000372208 | 0.00599 |
| 1.99204 | 0.221174 | 0.000479741 | 0.00664 |
| 2.19162 | 0.234662 | 0.000625114 | 0.00704 |
| 2.3922 | 0.24636 | 0.000811383 | 0.00739 |
| 2.59191 | 0.248946 | 0.00104141 | 0.00747 |
| 2.83164 | 0.260661 | 0.00113322 | 0.00782 |
| 3.20357 | 0.268028 | 0.001403 | 0.00804 |

Table A.15: (anti-)protons $v_2$ in 40-50% centrality

| $p_T$ **(GeV/c)** | **Value** | **Stat. Errors** ($\pm$) | **Sys. Errors** ($\pm$) |
|---|---|---|---|
| 0.393611 | 0.0503898 | 5.49463e-05 | 0.00252 |
| 0.590525 | 0.0831583 | 7.2499e-05 | 0.004158 |
| 0.789565 | 0.111822 | 0.000101384 | 0.00560 |
| 0.990215 | 0.136172 | 0.000140277 | 0.00681 |
| 1.19023 | 0.15711 | 0.000192079 | 0.00786 |
| 1.39049 | 0.172762 | 0.000257674 | 0.00864 |
| 1.59082 | 0.183113 | 0.000349907 | 0.00916 |
| 1.79126 | 0.191307 | 0.000452036 | 0.00957 |
| 1.99065 | 0.196349 | 0.000602978 | 0.00982 |
| 2.19044 | 0.194023 | 0.000804019 | 0.00970 |
| 2.39039 | 0.203228 | 0.00107658 | 0.01016 |
| 2.59023 | 0.202389 | 0.0014391 | 0.01012 |
| 2.82862 | 0.198131 | 0.00167229 | 0.00991 |
| 3.19508 | 0.183982 | 0.00214622 | 0.00920 |

Table A.16: Charged Pions $v_2$ in 50-60% centrality

| $p_T$ **(GeV/c)** | **Value** | **Stat. Errors** ($\pm$) | **Sys. Errors** ($\pm$) |
|---|---|---|---|
| 0.427936 | 0.035607 | 0.000384716 | 0.00178 |
| 0.603978 | 0.0637016 | 0.000267261 | 0.00319 |
| 0.796157 | 0.0915651 | 0.000284918 | 0.00458 |
| 0.994184 | 0.115904 | 0.000337168 | 0.00580 |
| 1.19284 | 0.134533 | 0.000420848 | 0.00673 |
| 1.39244 | 0.15261 | 0.000532463 | 0.00763 |
| 1.59213 | 0.169441 | 0.000685718 | 0.00847 |
| 1.79215 | 0.173762 | 0.000871699 | 0.00869 |
| 1.99253 | 0.183984 | 0.00110084 | 0.00920 |
| 2.19107 | 0.176413 | 0.00142067 | 0.00882 |
| 2.39228 | 0.189095 | 0.0018188 | 0.00945 |
| 2.59248 | 0.1758 | 0.00230836 | 0.00879 |
| 2.83112 | 0.180391 | 0.00252362 | 0.00902 |

Table A.17: Charged Kaons $v_2$ in 50-60% centrality

| $p_T$ (GeV/c) | Value | Stat. Errors ($\pm$) | Sys. Errors ($\pm$) |
|---|---|---|---|
| 0.611409 | 0.0424926 | 0.000265333 | 0.00212 |
| 0.801114 | 0.0698292 | 0.000242278 | 0.00349 |
| 0.996909 | 0.0992944 | 0.000265468 | 0.00496 |
| 1.19442 | 0.13157 | 0.000319878 | 0.00658 |
| 1.39323 | 0.159745 | 0.000401338 | 0.00799 |
| 1.59233 | 0.185041 | 0.000517018 | 0.00925 |
| 1.79207 | 0.20443 | 0.000662928 | 0.01022 |
| 1.99203 | 0.224082 | 0.000862706 | 0.01120 |
| 2.19144 | 0.241531 | 0.00113257 | 0.01208 |
| 2.39196 | 0.248043 | 0.00145389 | 0.01240 |
| 2.59142 | 0.245968 | 0.00186868 | 0.01230 |
| 2.83203 | 0.25606 | 0.0020898 | 0.012803 |
| 3.20335 | 0.272236 | 0.00251687 | 0.01361 |

Table A.18: (anti-)protons $v_2$ in 50-60% centrality

## A.2 Tabulated $v_3$ results

| $p_T$ **(GeV/c)** | **Value** | **Stat. Errors** ($\pm$) | **Sys. Errors** ($\pm$) |
|---|---|---|---|
| 0.393912 | 0.00384747 | 4.37884e-05 | 0.000308 |
| 0.590979 | 0.0106236 | 5.96406e-05 | 0.000850 |
| 0.789924 | 0.0183298 | 8.58989e-05 | 0.00147 |
| 0.990379 | 0.0265027 | 0.000119822 | 0.00212 |
| 1.19014 | 0.034025 | 0.000157662 | 0.00272 |
| 1.39029 | 0.0408742 | 0.000201911 | 0.00327 |
| 1.59037 | 0.0473341 | 0.000255889 | 0.00379 |
| 1.79062 | 0.0527166 | 0.000317197 | 0.00422 |
| 1.98994 | 0.0577632 | 0.000397328 | 0.00462 |
| 2.18952 | 0.0607422 | 0.000500712 | 0.00486 |
| 2.38952 | 0.0651055 | 0.000637128 | 0.00521 |
| 2.5895 | 0.0675901 | 0.000840808 | 0.00541 |
| 2.82759 | 0.0683753 | 0.000985548 | 0.00547 |
| 3.19154 | 0.0641744 | 0.00129377 | 0.00513 |

Table A.19: Charged Pions $v_3$ in 0-10% centrality

| $p_T$ **(GeV/c)** | **Value** | **Stat. Errors** ($\pm$) | **Sys. Errors** ($\pm$) |
|---|---|---|---|
| 0.426667 | 0.000261103 | 0.00033181 | 0.0000209 |
| 0.604826 | 0.00434124 | 0.000199992 | 0.000347 |
| 0.796943 | 0.01017 | 0.00019323 | 0.000814 |
| 0.994607 | 0.0189361 | 0.000221629 | 0.00151 |
| 1.19307 | 0.026522 | 0.000268399 | 0.00212 |
| 1.39245 | 0.0346356 | 0.000337167 | 0.00277 |
| 1.59183 | 0.0387091 | 0.000418739 | 0.00310 |
| 1.79193 | 0.0483521 | 0.000534709 | 0.00387 |
| 1.99174 | 0.0535956 | 0.000667021 | 0.00429 |
| 2.19005 | 0.054522 | 0.000839721 | 0.00436 |
| 2.39072 | 0.0550458 | 0.000966148 | 0.00440 |
| 2.59118 | 0.0586983 | 0.00132733 | 0.00470 |
| 2.82875 | 0.0649071 | 0.00135987 | 0.00519 |

Table A.20: Charged Kaons $v_3$ in 0-10% centrality

| $p_T$ **(GeV/c)** | **Value** | **Stat. Errors** ($\pm$) | **Sys. Errors** ($\pm$) |
|---|---|---|---|
| 0.612371 | 0.00168907 | 0.00023918 | 0.000135 |
| 0.80333 | 0.0024784 | 0.000191193 | 0.000198 |
| 0.999108 | 0.00913482 | 0.00019242 | 0.000731 |
| 1.19618 | 0.0173257 | 0.000218212 | 0.00139 |
| 1.39462 | 0.0280467 | 0.000265791 | 0.00224 |
| 1.59323 | 0.0387415 | 0.000331696 | 0.00310 |
| 1.79273 | 0.0488442 | 0.000416319 | 0.00391 |
| 1.9921 | 0.0566478 | 0.000520683 | 0.00453 |
| 2.19136 | 0.0647453 | 0.000654348 | 0.00518 |
| 2.3918 | 0.0770726 | 0.000839474 | 0.00617 |
| 2.59154 | 0.0794414 | 0.00106102 | 0.00636 |
| 2.83084 | 0.0846979 | 0.00115577 | 0.00678 |
| 3.20021 | 0.0906904 | 0.00136202 | 0.00726 |

Table A.21: (anti-)protons $v_3$ in 0-10% centrality

| $p_T$ **(GeV/c)** | **Value** | **Stat. Errors** ($\pm$) | **Sys. Errors** ($\pm$) |
|---|---|---|---|
| 0.39411 | 0.00596408 | 5.1807e-05 | 0.000477 |
| 0.591081 | 0.0142231 | 7.66092e-05 | 0.00114 |
| 0.790013 | 0.0239317 | 0.000113454 | 0.00191 |
| 0.990465 | 0.0334588 | 0.000156485 | 0.00268 |
| 1.19028 | 0.0425775 | 0.000205427 | 0.00341 |
| 1.39042 | 0.0510835 | 0.000263655 | 0.00409 |
| 1.59054 | 0.0577268 | 0.000333781 | 0.00462 |
| 1.79085 | 0.0627093 | 0.000416884 | 0.00502 |
| 1.99015 | 0.0681652 | 0.000530334 | 0.00545 |
| 2.18971 | 0.0719375 | 0.000686254 | 0.00576 |
| 2.38976 | 0.076607 | 0.000906934 | 0.00613 |
| 2.58973 | 0.0757019 | 0.00120867 | 0.00606 |
| 2.82805 | 0.0779648 | 0.00142343 | 0.00624 |
| 3.19216 | 0.0730212 | 0.00182519 | 0.00584 |

Table A.22: Charged Pions $v_3$ in 10-20% centrality

| $p_T$ **(GeV/c)** | **Value** | **Stat. Errors** ($\pm$) | **Sys. Errors** ($\pm$) |
|---|---|---|---|
| 0.427602 | 0.00128348 | 0.000357405 | 0.000103 |
| 0.605056 | 0.00537682 | 0.000226208 | 0.000430 |
| 0.797111 | 0.0160405 | 0.000228783 | 0.00128 |
| 0.994676 | 0.0253234 | 0.000277189 | 0.00203 |
| 1.19319 | 0.0344337 | 0.000339961 | 0.00275 |
| 1.39248 | 0.0423801 | 0.000428152 | 0.00339 |
| 1.59197 | 0.0467535 | 0.000535008 | 0.00374 |
| 1.79207 | 0.0529172 | 0.000678172 | 0.00423 |
| 1.9919 | 0.0644337 | 0.000864538 | 0.00515 |
| 2.19024 | 0.0668378 | 0.00109955 | 0.00538 |
| 2.3911 | 0.0699068 | 0.00139276 | 0.00559 |
| 2.59159 | 0.0816638 | 0.00186256 | 0.006533 |
| 2.82916 | 0.0793201 | 0.00201362 | 0.00635 |

Table A.23: Charged Kaons $v_3$ in 10-20% centrality

| $p_T$ **(GeV/c)** | **Value** | **Stat. Errors** ($\pm$) | **Sys. Errors** ($\pm$) |
|---|---|---|---|
| 0.612566 | 0.00067653 | 0.000265997 | 0.000054 |
| 0.80328 | 0.00728463 | 0.000219409 | 0.000582 |
| 0.998981 | 0.0134499 | 0.000220844 | 0.00108 |
| 1.19614 | 0.0254339 | 0.00026697 | 0.00203 |
| 1.39454 | 0.0346512 | 0.000324233 | 0.00277 |
| 1.59323 | 0.0472874 | 0.000409708 | 0.00378 |
| 1.79275 | 0.0589447 | 0.000518395 | 0.00472 |
| 1.99218 | 0.0700647 | 0.000653326 | 0.00561 |
| 2.19156 | 0.0800068 | 0.000831729 | 0.00640 |
| 2.39183 | 0.0862644 | 0.00106277 | 0.00690 |
| 2.59186 | 0.090125 | 0.00134476 | 0.00721 |
| 2.83123 | 0.0940997 | 0.00149918 | 0.00753 |
| 3.20156 | 0.105609 | 0.00184279 | 0.00845 |

Table A.24: (anti-)protons $v_3$ in 10-20% centrality

| $p_T$ **(GeV/c)** | **Value** | **Stat. Errors** ($\pm$) | **Sys. Errors** ($\pm$) |
|---|---|---|---|
| 0.394178 | 0.00723808 | 6.87172e-05 | 0.000579 |
| 0.591095 | 0.0170251 | 9.81497e-05 | 0.00136 |
| 0.790023 | 0.0276114 | 0.000141871 | 0.00221 |
| 0.990485 | 0.0388014 | 0.000196139 | 0.00310 |
| 1.19037 | 0.0471845 | 0.000256146 | 0.00377 |
| 1.39051 | 0.0566184 | 0.00033398 | 0.00453 |
| 1.59071 | 0.0620735 | 0.000430125 | 0.00497 |
| 1.79101 | 0.069397 | 0.000551372 | 0.00555 |
| 1.99028 | 0.0713529 | 0.00071031 | 0.00571 |
| 2.19008 | 0.0750073 | 0.000931827 | 0.00600 |
| 2.3899 | 0.0812186 | 0.0012283 | 0.00650 |
| 2.58985 | 0.0851306 | 0.00166678 | 0.00681 |
| 2.82831 | 0.081911 | 0.00191063 | 0.00655 |
| 3.19338 | 0.0759322 | 0.00253534 | 0.00607 |

Table A.25: Charged Pions $v_3$ in 20-30% centrality

| $p_T$ **(GeV/c)** | **Value** | **Stat. Errors** ($\pm$) | **Sys. Errors** ($\pm$) |
|---|---|---|---|
| 0.428055 | 4.55615e-05 | 0.000456412 | 3.64e-06 |
| 0.605058 | 0.00904939 | 0.000303166 | 0.00072395 |
| 0.797059 | 0.0181156 | 0.000313975 | 0.00145 |
| 0.994709 | 0.0291194 | 0.000374559 | 0.00233 |
| 1.19324 | 0.0373951 | 0.00045981 | 0.00299 |
| 1.39254 | 0.0442322 | 0.000578587 | 0.00354 |
| 1.59201 | 0.051662 | 0.000740078 | 0.00413 |
| 1.79215 | 0.0576364 | 0.000936136 | 0.00461 |
| 1.99208 | 0.0636146 | 0.00118844 | 0.00509 |
| 2.19062 | 0.0699354 | 0.0015184 | 0.00560 |
| 2.39127 | 0.0641461 | 0.00198593 | 0.00513 |
| 2.59192 | 0.0738564 | 0.0025283 | 0.00591 |
| 2.82977 | 0.0687481 | 0.00282104 | 0.00550 |

Table A.26: Charged Kaons $v_3$ in 20-30% centrality

| $p_T$ **(GeV/c)** | **Value** | **Stat. Errors** ($\pm$) | **Sys. Errors** ($\pm$) |
|---|---|---|---|
| 0.612643 | 0.00479843 | 0.000337007 | 0.000384 |
| 0.803063 | 0.0118195 | 0.000288139 | 0.000946 |
| 0.998741 | 0.0208078 | 0.000304007 | 0.00167 |
| 1.19583 | 0.031118 | 0.000358676 | 0.00249 |
| 1.39437 | 0.0434425 | 0.000440109 | 0.0033 |
| 1.5931 | 0.0549205 | 0.000555985 | 0.00439 |
| 1.79269 | 0.0682989 | 0.000705593 | 0.00546 |
| 1.99219 | 0.0773912 | 0.000895176 | 0.00619 |
| 2.19152 | 0.0878961 | 0.00114959 | 0.00703 |
| 2.39191 | 0.100648 | 0.00148194 | 0.00805 |
| 2.59184 | 0.108558 | 0.00189267 | 0.00868 |
| 2.83171 | 0.110492 | 0.00207609 | 0.00884 |
| 3.20237 | 0.111257 | 0.00254698 | 0.00890 |

Table A.27: (anti-)protons $v_3$ in 20-30% centrality

| $p_T$ **(GeV/c)** | **Value** | **Stat. Errors** ($\pm$) | **Sys. Errors** ($\pm$) |
|---|---|---|---|
| 0.394131 | 0.0089409 | 9.44719e-05 | 0.000894 |
| 0.590995 | 0.0185367 | 0.000129664 | 0.00185 |
| 0.789959 | 0.0299474 | 0.000185242 | 0.00299 |
| 0.990455 | 0.0400404 | 0.000253759 | 0.00400 |
| 1.19036 | 0.0504502 | 0.000338995 | 0.00505 |
| 1.39053 | 0.0573717 | 0.000444393 | 0.00573 |
| 1.59075 | 0.0634254 | 0.000586372 | 0.00634 |
| 1.79104 | 0.0701572 | 0.000759628 | 0.00702 |
| 1.99046 | 0.0679654 | 0.000986187 | 0.00680 |
| 2.19025 | 0.0751914 | 0.00130378 | 0.00752 |
| 2.39004 | 0.0701233 | 0.00174148 | 0.00701 |
| 2.59006 | 0.0883109 | 0.00238226 | 0.00883 |
| 2.82862 | 0.0720927 | 0.00277861 | 0.00721 |
| 3.1938 | 0.0889957 | 0.00366813 | 0.00890 |

Table A.28: Charged Pions $v_3$ in 30-40% centrality

| $p_T$ **(GeV/c)** | **Value** | **Stat. Errors** ($\pm$) | **Sys. Errors** ($\pm$) |
|---|---|---|---|
| 0.428247 | 0.00365153 | 0.000631633 | 0.000365 |
| 0.604887 | 0.00893467 | 0.000431284 | 0.000893 |
| 0.796854 | 0.0197885 | 0.000447499 | 0.00198 |
| 0.994566 | 0.030291 | 0.000530062 | 0.00303 |
| 1.19318 | 0.0395702 | 0.000654495 | 0.00396 |
| 1.39255 | 0.0472529 | 0.000825244 | 0.00473 |
| 1.59214 | 0.0503917 | 0.00105677 | 0.00504 |
| 1.79226 | 0.0595118 | 0.00134638 | 0.00595 |
| 1.9923 | 0.0687511 | 0.00173543 | 0.00688 |
| 2.19096 | 0.0675556 | 0.00219262 | 0.00676 |
| 2.39121 | 0.0823364 | 0.00288755 | 0.00823 |
| 2.59182 | 0.0641834 | 0.00367353 | 0.00642 |
| 2.8306 | 0.0663952 | 0.00400935 | 0.00664 |

Table A.29: Charged Kaons $v_3$ in 30-40% centrality

| $p_T$ **(GeV/c)** | **Value** | **Stat. Errors** ($\pm$) | **Sys. Errors** ($\pm$) |
|---|---|---|---|
| 0.612497 | 0.00900625 | 0.000452326 | 0.00090 |
| 0.802638 | 0.0137406 | 0.000397446 | 0.00137 |
| 0.998272 | 0.0242495 | 0.000427808 | 0.00242 |
| 1.19551 | 0.0374331 | 0.000508482 | 0.00374 |
| 1.39409 | 0.0479258 | 0.000623281 | 0.00479 |
| 1.59295 | 0.0588676 | 0.000790151 | 0.00589 |
| 1.79256 | 0.0672287 | 0.00100432 | 0.00672 |
| 1.99216 | 0.0812693 | 0.00128583 | 0.00813 |
| 2.19175 | 0.091475 | 0.00167953 | 0.00915 |
| 2.39196 | 0.100904 | 0.00214217 | 0.01001 |
| 2.59196 | 0.0942937 | 0.0027237 | 0.00943 |
| 2.83142 | 0.106935 | 0.00308026 | 0.01069 |
| 3.20328 | 0.121793 | 0.00379706 | 0.01218 |

Table A.30: (anti-)protons $v_3$ in 30-40% centrality

| $p_T$ **(GeV/c)** | **Value** | **Stat. Errors** ($\pm$) | **Sys. Errors** ($\pm$) |
|---|---|---|---|
| 0.393927 | 0.00827061 | 0.000140008 | 0.000992 |
| 0.590812 | 0.0187225 | 0.00019162 | 0.00225 |
| 0.789806 | 0.0306183 | 0.000270258 | 0.00367 |
| 0.990356 | 0.0376817 | 0.00037068 | 0.00452 |
| 1.19033 | 0.0495288 | 0.000502956 | 0.00594 |
| 1.39051 | 0.0579526 | 0.00067234 | 0.00695 |
| 1.59083 | 0.0647987 | 0.000894963 | 0.00778 |
| 1.79112 | 0.0667854 | 0.0011659 | 0.00801 |
| 1.99059 | 0.0669204 | 0.00152672 | 0.00803 |
| 2.19025 | 0.0756044 | 0.00204621 | 0.00907 |
| 2.39021 | 0.0648127 | 0.00269006 | 0.00778 |
| 2.59022 | 0.0815989 | 0.00366638 | 0.00979 |
| 2.82923 | 0.0479352 | 0.00420133 | 0.00575 |
| 3.19443 | 0.0493633 | 0.00551236 | 0.00592 |

Table A.31: Charged Pions $v_3$ in 40-50% centrality

| $p_T$ **(GeV/c)** | **Value** | **Stat. Errors** ($\pm$) | **Sys. Errors** ($\pm$) |
|---|---|---|---|
| 0.428145 | 0.00333928 | 0.000966363 | 0. 000401 |
| 0.604506 | 0.0124261 | 0.00067234 | 0.00149 |
| 0.796611 | 0.0204196 | 0.000705714 | 0.00245 |
| 0.994384 | 0.0302295 | 0.000839442 | 0.00363 |
| 1.19304 | 0.0406112 | 0.00103997 | 0.00487 |
| 1.39249 | 0.0434843 | 0.00131152 | 0.00522 |
| 1.59211 | 0.055785 | 0.00168654 | 0.00669 |
| 1.79215 | 0.0506386 | 0.00214915 | 0.00608 |
| 1.99238 | 0.0602107 | 0.00274158 | 0.00723 |
| 2.1909 | 0.073762 | 0.00353839 | 0.00885 |
| 2.39176 | 0.0346726 | 0.00459201 | 0.00416 |
| 2.59212 | 0.0639839 | 0.00571281 | 0.00768 |
| 2.83131 | 0.0575259 | 0.00635529 | 0.00690 |

Table A.32: Charged Kaons $v_3$ in 40-50% centrality

| $p_T$ **(GeV/c)** | **Value** | **Stat. Errors** ($\pm$) | **Sys. Errors** ($\pm$) |
|---|---|---|---|
| 0.612094 | 0.00888694 | 0.000686812 | 0.00107 |
| 0.802026 | 0.0160084 | 0.000612537 | 0.00192 |
| 0.997646 | 0.027147 | 0.000667229 | 0.00326 |
| 1.19498 | 0.0382167 | 0.000787112 | 0.00459 |
| 1.39366 | 0.0500736 | 0.000986724 | 0.00601 |
| 1.59269 | 0.0648817 | 0.0012645 | 0.00779 |
| 1.79226 | 0.0758096 | 0.00162054 | 0.00910 |
| 1.99204 | 0.0897839 | 0.00208994 | 0.01077 |
| 2.19162 | 0.0855987 | 0.00270823 | 0.01027 |
| 2.3922 | 0.104209 | 0.00351891 | 0.01251 |
| 2.59191 | 0.0988778 | 0.00450897 | 0.01187 |
| 2.83164 | 0.106299 | 0.00495612 | 0.01276 |
| 3.20357 | 0.107721 | 0.00613268 | 0.01293 |

Table A.33: (anti-)protons $v_3$ in 40-50% centrality

## A.3 Tabulated $v_4$ results

| $p_T$ **(GeV/c)** | **Value** | **Stat. Errors** ($\pm$) | **Sys. Errors** ($\pm$) |
|---|---|---|---|
| 0.393912 | 0.000829132 | 0.000117225 | 0.000166 |
| 0.590979 | 0.00296822 | 0.000156538 | 0.000594 |
| 0.789924 | 0.00595174 | 0.000232048 | 0.00119 |
| 0.990379 | 0.0106157 | 0.000354134 | 0.00212 |
| 1.19014 | 0.016062 | 0.000504979 | 0.00321 |
| 1.39029 | 0.0229374 | 0.000698919 | 0.00459 |
| 1.59037 | 0.024521 | 0.000822865 | 0.00490 |
| 1.79062 | 0.028065 | 0.00100331 | 0.00561 |
| 1.98994 | 0.0316305 | 0.00122702 | 0.00633 |
| 2.18952 | 0.0431556 | 0.00162221 | 0.00863 |
| 2.38952 | 0.0437269 | 0.0019279 | 0.00875 |
| 2.5895 | 0.0420645 | 0.0023789 | 0.00841 |
| 2.82759 | 0.0262983 | 0.00262376 | 0.00526 |
| 3.19154 | 0.0354867 | 0.00342275 | 0.00710 |

Table A.34: Charged Pions $v_4$ in 0-10% centrality

| $p_T$ **(GeV/c)** | **Value** | **Stat. Errors** ($\pm$) | **Sys. Errors** ($\pm$) |
|---|---|---|---|
| 0.604826 | 0.000967809 | 0.000549452 | 0.000194 |
| 0.796943 | 0.00512364 | 0.000540105 | 0.00102 |
| 0.994607 | 0.00623864 | 0.000606987 | 0.00125 |
| 1.19307 | 0.0113189 | 0.000753242 | 0.00226 |
| 1.39245 | 0.012214 | 0.000924574 | 0.00244 |
| 1.59183 | 0.0181332 | 0.00117983 | 0.00363 |
| 1.79193 | 0.0265527 | 0.00153884 | 0.00531 |
| 1.99174 | 0.0309346 | 0.00191134 | 0.00619 |
| 2.19005 | 0.0278405 | 0.0023358 | 0.00557 |
| 2.39072 | 0.0546123 | 0.00287117 | 0.01092 |
| 2.59118 | 0.0262182 | 0.0036225 | 0.00524 |
| 2.82875 | 0.0346608 | 0.00365455 | 0.00693 |

Table A.35: Charged Kaons $v_4$ in 0-10% centrality

| $p_T$ **(GeV/c)** | **Value** | **Stat. Errors** ($\pm$) | **Sys. Errors** ($\pm$) |
|---|---|---|---|
| 0.80333 | 0.000575018 | 0.000526487 | 0.000115 |
| 0.999108 | 0.00286381 | 0.000527898 | 0.000573 |
| 1.19618 | 0.00943741 | 0.000622127 | 0.00189 |
| 1.39462 | 0.012872 | 0.00075525 | 0.00257 |
| 1.59323 | 0.0219263 | 0.000995095 | 0.00439 |
| 1.79273 | 0.0257466 | 0.00122537 | 0.00515 |
| 1.9921 | 0.0325431 | 0.00154668 | 0.00651 |
| 2.19136 | 0.044268 | 0.00199871 | 0.00885 |
| 2.3918 | 0.0565878 | 0.00257251 | 0.01132 |
| 2.59154 | 0.0332768 | 0.00292826 | 0.00666 |
| 2.83084 | 0.0562478 | 0.00334761 | 0.01125 |
| 3.20021 | 0.0827125 | 0.0040862 | 0.01654 |

Table A.36: (anti-)protons $v_4$ in 0-10% centrality

| $p_T$ **(GeV/c)** | **Value** | **Stat. Errors** ($\pm$) | **Sys. Errors** ($\pm$) |
|---|---|---|---|
| 0.39411 | 0.0024455 | 0.00022356 | 0.000489 |
| 0.591081 | 0.00513793 | 0.000324262 | 0.00103 |
| 0.790013 | 0.0101212 | 0.000532793 | 0.00202 |
| 0.990465 | 0.0170419 | 0.000833088 | 0.00341 |
| 1.19028 | 0.0271892 | 0.00127011 | 0.00544 |
| 1.39042 | 0.0361037 | 0.00169231 | 0.00722 |
| 1.59054 | 0.0489338 | 0.00228838 | 0.00979 |
| 1.79085 | 0.0475935 | 0.00243949 | 0.00952 |
| 1.99015 | 0.0582197 | 0.00307493 | 0.01164 |
| 2.18971 | 0.0601451 | 0.0035792 | 0.01203 |
| 2.38976 | 0.0639626 | 0.00439063 | 0.01279 |
| 2.58973 | 0.0657409 | 0.00549025 | 0.01315 |
| 2.82805 | 0.0648822 | 0.00628784 | 0.01298 |
| 3.19216 | 0.117968 | 0.00881798 | 0.02359 |

Table A.37: Charged Pions $v_4$ in 10-20% centrality

| $p_T$ **(GeV/c)** | **Value** | **Stat. Errors** ($\pm$) | **Sys. Errors** ($\pm$) |
|---|---|---|---|
| 0.605056 | 0.00270317 | 0.000945153 | 0.00054 |
| 0.797111 | 0.00210406 | 0.000939284 | 0.00042 |
| 0.994676 | 0.00684561 | 0.00110921 | 0.00137 |
| 1.19319 | 0.0227819 | 0.00160093 | 0.00456 |
| 1.39248 | 0.0281177 | 0.00200694 | 0.00562 |
| 1.59197 | 0.0437051 | 0.00274223 | 0.00874 |
| 1.79207 | 0.0381716 | 0.00309011 | 0.00763 |
| 1.9919 | 0.0303799 | 0.00363332 | 0.00608 |
| 2.19024 | 0.0284516 | 0.00451966 | 0.00569 |
| 2.3911 | 0.0722432 | 0.00630095 | 0.01445 |
| 2.59159 | 0.0766522 | 0.00812873 | 0.01533 |
| 2.82916 | 0.0771404 | 0.00875536 | 0.01543 |

Table A.38: Charged Kaons $v_4$ in 10-20% centrality

| $p_T$ **(GeV/c)** | **Value** | **Stat. Errors** ($\pm$) | **Sys. Errors** ($\pm$) |
|---|---|---|---|
| 0.80328 | 0.00289327 | 0.000900975 | 0.000579 |
| 0.998981 | 0.0023871 | 0.000910979 | 0.000477 |
| 1.19614 | 0.0156439 | 0.00121148 | 0.00313 |
| 1.39454 | 0.0245059 | 0.00159063 | 0.00490 |
| 1.59323 | 0.0363573 | 0.00214145 | 0.00727 |
| 1.79275 | 0.0452307 | 0.00269137 | 0.00905 |
| 1.99218 | 0.0644327 | 0.00361697 | 0.01289 |
| 2.19156 | 0.0597311 | 0.00402993 | 0.01195 |
| 2.39183 | 0.0917263 | 0.00558819 | 0.01835 |
| 2.59186 | 0.0786552 | 0.00622124 | 0.01573 |
| 2.83123 | 0.0810231 | 0.00679128 | 0.01620 |
| 3.20156 | 0.116571 | 0.00869706 | 0.02331 |

Table A.39: (anti-)protons $v_4$ in 10-20% centrality

| $p_T$ **(GeV/c)** | **Value** | **Stat. Errors** ($\pm$) | **Sys. Errors** ($\pm$) |
|---|---|---|---|
| 0.394178 | 0.00416588 | 0.000315308 | 0.00104 |
| 0.591095 | 0.00610078 | 0.000417047 | 0.00153 |
| 0.790023 | 0.0113345 | 0.000641888 | 0.00283 |
| 0.990485 | 0.0229353 | 0.00109641 | 0.00459 |
| 1.19037 | 0.0335884 | 0.00156711 | 0.00840 |
| 1.39051 | 0.0434979 | 0.00205694 | 0.01087 |
| 1.59071 | 0.052848 | 0.00259557 | 0.01321 |
| 1.79101 | 0.062919 | 0.00322043 | 0.01573 |
| 1.99028 | 0.0689785 | 0.00386631 | 0.01724 |
| 2.19008 | 0.0738705 | 0.00469965 | 0.01847 |
| 2.3899 | 0.0758068 | 0.0057668 | 0.01895 |
| 2.58985 | 0.0899277 | 0.00764048 | 0.02248 |
| 2.82831 | 0.106696 | 0.0088468 | 0.02667 |
| 3.19338 | 0.0732793 | 0.0108453 | 0.01832 |

Table A.40: Charged Pions $v_4$ in 20-30% centrality

| $p_T$ **(GeV/c)** | **Value** | **Stat. Errors** ($\pm$) | **Sys. Errors** ($\pm$) |
|---|---|---|---|
| 0.605058 | 0.00119419 | 0.00127518 | 0.000299 |
| 0.797059 | 0.00484769 | 0.00129958 | 0.00121 |
| 0.994709 | 0.0115733 | 0.00156584 | 0.00289 |
| 1.19324 | 0.024749 | 0.00207426 | 0.00619 |
| 1.39254 | 0.0431403 | 0.00286521 | 0.01079 |
| 1.59201 | 0.0467879 | 0.00349918 | 0.01170 |
| 1.79215 | 0.0524215 | 0.00431078 | 0.01311 |
| 1.99208 | 0.0680897 | 0.00553033 | 0.01702 |
| 2.19062 | 0.0594905 | 0.00664176 | 0.01487 |
| 2.39127 | 0.0583864 | 0.00847269 | 0.01460 |
| 2.59192 | 0.0726888 | 0.0107383 | 0.01817 |
| 2.82977 | 0.0800075 | 0.0120453 | 0.02000 |

Table A.41: Charged Kaons $v_4$ in 20-30% centrality

| $p_T$ **(GeV/c)** | **Value** | **Stat. Errors** ($\pm$) | **Sys. Errors** ($\pm$) |
|---|---|---|---|
| 0.803063 | 0.00120832 | 0.00119917 | 0.000302 |
| 0.998741 | 0.000454466 | 0.00123162 | 0.000114 |
| 1.19583 | 0.0187337 | 0.00160259 | 0.00468 |
| 1.39437 | 0.0301903 | 0.00209217 | 0.00755 |
| 1.5931 | 0.0529757 | 0.00300364 | 0.01324 |
| 1.79269 | 0.0490258 | 0.00337503 | 0.01226 |
| 1.99219 | 0.0690228 | 0.00445898 | 0.01726 |
| 2.19152 | 0.07828 | 0.00552625 | 0.01957 |
| 2.39191 | 0.10973 | 0.00734755 | 0.02743 |
| 2.59184 | 0.12301 | 0.00901942 | 0.03075 |
| 2.83171 | 0.154468 | 0.0103663 | 0.03862 |
| 3.20237 | 0.111035 | 0.0113052 | 0.02776 |

Table A.42: (anti-)protons $v_4$ in 20-30% centrality

| $p_T$ **(GeV/c)** | **Value** | **Stat. Errors** ($\pm$) | **Sys. Errors** ($\pm$) |
|---|---|---|---|
| 0.394131 | 0.00353906 | 0.000426833 | 0.00134 |
| 0.590995 | 0.00829049 | 0.000618965 | 0.00830 |
| 0.789959 | 0.0152222 | 0.000950362 | 0.00207 |
| 0.990455 | 0.0229762 | 0.00137012 | 0.005744 |
| 1.19036 | 0.0352647 | 0.00198612 | 0.00882 |
| 1.39053 | 0.0544592 | 0.00290778 | 0.01361 |
| 1.59075 | 0.0600586 | 0.00350959 | 0.01501 |
| 1.79104 | 0.0508083 | 0.00385696 | 0.01270 |
| 1.99046 | 0.0811513 | 0.00545356 | 0.02029 |
| 2.19025 | 0.0925535 | 0.00687514 | 0.02314 |
| 2.39004 | 0.0877138 | 0.0084781 | 0.02193 |
| 2.59006 | 0.128305 | 0.0117947 | 0.03208 |
| 2.82862 | 0.0930034 | 0.0129053 | 0.02325 |
| 3.1938 | 0.120043 | 0.016931 | 0.03001 |

Table A.43: Charged Pions $v_4$ in 30-40% centrality

| $p_T$ **(GeV/c)** | **Value** | **Stat. Errors** ($\pm$) | **Sys. Errors** ($\pm$) |
|---|---|---|---|
| 0.604887 | 0.00940933 | 0.00194194 | 0.00235 |
| 0.796854 | 0.0027522 | 0.00195804 | 0.000688 |
| 0.994566 | 0.0260981 | 0.0025445 | 0.00652 |
| 1.19318 | 0.0348286 | 0.00318914 | 0.00871 |
| 1.39255 | 0.030422 | 0.00381021 | 0.00761 |
| 1.59214 | 0.0584694 | 0.00523895 | 0.01462 |
| 1.79226 | 0.0536161 | 0.00631414 | 0.01340 |
| 1.9923 | 0.0905423 | 0.00851169 | 0.02264 |
| 2.19096 | 0.0980654 | 0.010493 | 0.02452 |
| 2.39121 | 0.0430453 | 0.0128876 | 0.01076 |
| 2.59182 | 0.135474 | 0.0171676 | 0.03387 |
| 2.8306 | 0.13796 | 0.0186039 | 0.03449 |

Table A.44: Charged Kaons $v_3$ in 30-40% centrality

| $p_T$ **(GeV/c)** | **Value** | **Stat. Errors** ($\pm$) | **Sys. Errors** ($\pm$) |
|---|---|---|---|
| 0.802638 | 0.00226853 | 0.00176698 | 0.000567 |
| 0.998272 | 0.00656933 | 0.00187997 | 0.00167 |
| 1.19551 | 0.0160624 | 0.00228579 | 0.00402 |
| 1.39409 | 0.0370052 | 0.00309303 | 0.00925 |
| 1.59295 | 0.0578627 | 0.00417502 | 0.01447 |
| 1.79256 | 0.0496446 | 0.00481942 | 0.01241 |
| 1.99216 | 0.08992 | 0.0067291 | 0.02248 |
| 2.19175 | 0.0963489 | 0.00836308 | 0.02409 |
| 2.39196 | 0.134813 | 0.0109466 | 0.03370 |
| 2.59196 | 0.158875 | 0.0136814 | 0.03972 |
| 2.83142 | 0.141125 | 0.0147666 | 0.03528 |
| 3.20328 | 0.205566 | 0.0187728 | 0.05139 |

Table A.45: (anti-)protons $v_4$ in 30-40% centrality

| $p_T$ **(GeV/c)** | **Value** | **Stat. Errors** ($\pm$) | **Sys. Errors** ($\pm$) |
|---|---|---|---|
| 0.393927 | 0.00444555 | 0.000999184 | 0.00111 |
| 0.590812 | 0.00680403 | 0.00134082 | 0.00170 |
| 0.789806 | 0.0220035 | 0.00266247 | 0.00550 |
| 0.990356 | 0.0308031 | 0.00372554 | 0.00770 |
| 1.19033 | 0.0666415 | 0.00712023 | 0.01666 |
| 1.39051 | 0.076266 | 0.00845591 | 0.01907 |
| 1.59083 | 0.0677012 | 0.00862977 | 0.01693 |
| 1.79112 | 0.101596 | 0.0123067 | 0.02540 |
| 1.99059 | 0.11324 | 0.0147078 | 0.02831 |
| 2.19025 | 0.0923695 | 0.0159872 | 0.02309 |
| 2.39021 | 0.135579 | 0.0218536 | 0.03389 |
| 2.59022 | 0.136318 | 0.0272742 | 0.03408 |
| 2.82923 | 0.162152 | 0.0315853 | 0.04054 |
| 3.19443 | 0.0517715 | 0.0365017 | 0.01294 |

Table A.46: Charged Pions $v_4$ in 40-50% centrality

| $p_T$ **(GeV/c)** | **Value** | **Stat. Errors** ($\pm$) | **Sys. Errors** ($\pm$) |
|---|---|---|---|
| 0.604506 | 0.00979534 | 0.00447532 | 0.00245 |
| 0.796611 | 0.0157508 | 0.00480028 | 0.00394 |
| 0.994384 | 0.0136745 | 0.0055626 | 0.00342 |
| 1.19304 | 0.049821 | 0.00824315 | 0.01246 |
| 1.39249 | 0.0444902 | 0.00951066 | 0.01112 |
| 1.59211 | 0.0446526 | 0.0117391 | 0.011163 |
| 1.79215 | 0.0972913 | 0.0168322 | 0.02432 |
| 1.99238 | 0.0854375 | 0.0196777 | 0.02136 |
| 2.1909 | 0.110208 | 0.0254229 | 0.02755 |
| 2.39176 | 0.0471602 | 0.0303152 | 0.01179 |
| 2.59212 | 0.264961 | 0.0451921 | 0.06624 |
| 2.83131 | 0.0227152 | 0.0416372 | 0.00568 |

Table A.47: Charged Kaons $v_4$ in 40-50% centrality

| $p_T$ (GeV/c) | Value | Stat. Errors ($\pm$) | Sys. Errors ($\pm$) |
|---|---|---|---|
| 0.802026 | 0.023672 | 0.00459653 | 0.00592 |
| 0.997646 | 0.0334007 | 0.00538637 | 0.00835 |
| 1.19498 | 0.0406896 | 0.00643442 | 0.01017 |
| 1.39366 | 0.043969 | 0.00762304 | 0.01099 |
| 1.59269 | 0.0605458 | 0.00999144 | 0.01514 |
| 1.79226 | 0.107207 | 0.0146916 | 0.02680 |
| 1.99204 | 0.0884125 | 0.0159565 | 0.02210 |
| 2.19162 | 0.192856 | 0.0255803 | 0.04821 |
| 2.3922 | 0.175763 | 0.0284393 | 0.04394 |
| 2.59191 | 0.156596 | 0.0330117 | 0.03915 |
| 2.83164 | 0.268747 | 0.041341 | 0.06719 |
| 3.20357 | 0.25818 | 0.0470368 | 0.06455 |

Table A.48: (anti-)protons $v_4$ in 40-50% centrality

## A.4 0-50% $v_n$ results

| $p_T$ **(GeV/c)** | **value** | **Stat. Errors** ($\pm$) | **Sys. Errors** ($\pm$) |
|---|---|---|---|
| 0.611263 | 0.0138809 | 5.0009e-05 | 0.000416 |
| 0.803177 | 0.0280884 | 4.18534e-05 | 0.000843 |
| 0.999121 | 0.0461806 | 4.35695e-05 | 0.00139 |
| 1.19613 | 0.0659145 | 5.08886e-05 | 0.00198 |
| 1.39457 | 0.0858192 | 6.23713e-05 | 0.00257 |
| 1.59316 | 0.104168 | 7.83356e-05 | 0.00313 |
| 1.79268 | 0.120827 | 9.85901e-05 | 0.00362 |
| 1.99201 | 0.134361 | 0.000124081 | 0.00403 |
| 2.19138 | 0.146737 | 0.00015815 | 0.00440 |
| 2.39177 | 0.157076 | 0.00020288 | 0.00471 |
| 2.59152 | 0.165619 | 0.000257142 | 0.00497 |
| 2.83079 | 0.173618 | 0.000283982 | 0.00521 |
| 3.20001 | 0.178631 | 0.000344846 | 0.00536 |

Table A.49: (anti-)protons $v_2$ in 0-50% centrality

| $p_T$ **(GeV/c)** | **value** | **Stat. Errors** ($\pm$) | **Sys. Errors** ($\pm$) |
|---|---|---|---|
| 0.611263 | 0.00389124 | 0.000153971 | 0.00023347 |
| 0.803177 | 0.00853245 | 0.000129824 | 0.000512 |
| 0.999121 | 0.0163767 | 0.000135157 | 0.000983 |
| 1.19613 | 0.0267578 | 0.00015922 | 0.00161 |
| 1.39457 | 0.0373278 | 0.000196782 | 0.00224 |
| 1.59316 | 0.0489669 | 0.000249311 | 0.00294 |
| 1.79268 | 0.059901 | 0.000315026 | 0.00359 |
| 1.99201 | 0.0701214 | 0.000396409 | 0.00421 |
| 2.19138 | 0.0785191 | 0.000504819 | 0.00471 |
| 2.39177 | 0.0894847 | 0.000647142 | 0.00537 |
| 2.59152 | 0.0916063 | 0.000818336 | 0.00550 |
| 2.83079 | 0.0971324 | 0.000908436 | 0.00583 |
| 3.20001 | 0.104512 | 0.00111615 | 0.00627 |

Table A.50: (anti-)protons $v_3$ in 0-50% centrality

| $p_T$ **(GeV/c)** | **value** | **Stat. Errors** ($\pm$) | **Sys. Errors** ($\pm$) |
|---|---|---|---|
| 0.803177 | 0.00385874 | 0.000643517 | 0.000772 |
| 0.999121 | 0.00567468 | 0.000686265 | 0.00113 |
| 1.19613 | 0.0165546 | 0.000825257 | 0.00331 |
| 1.39457 | 0.0251845 | 0.00101283 | 0.00504 |
| 1.59316 | 0.0397304 | 0.00136083 | 0.00795 |
| 1.79268 | 0.0451126 | 0.00174217 | 0.009023 |
| 1.99201 | 0.0601028 | 0.00213316 | 0.01202 |
| 2.19138 | 0.0736001 | 0.00290829 | 0.01472 |
| 2.39177 | 0.0962405 | 0.00359157 | 0.01925 |
| 2.59152 | 0.0898086 | 0.0041651 | 0.0180 |
| 2.83079 | 0.111225 | 0.00495655 | 0.02225 |
| 3.20001 | 0.128955 | 0.00596859 | 0.02579 |

Table A.51: (anti-)protons $v_4$ in 0-50% centrality

| $p_T$ **(GeV/c)** | **value** | **Stat. Errors** ($\pm$) | **Sys. Errors** ($\pm$) |
|---|---|---|---|
| 0.3924 | 0.0276865 | 1.10419e-05 | 0.000831 |
| 0.59071 | 0.0482937 | 1.64117e-05 | 0.00145 |
| 0.789872 | 0.0671707 | 2.30174e-05 | 0.00202 |
| 0.990376 | 0.083756 | 3.03909e-05 | 0.00251 |
| 1.19012 | 0.0976187 | 3.84593e-05 | 0.00293 |
| 1.39026 | 0.109201 | 4.81907e-05 | 0.00328 |
| 1.59036 | 0.118756 | 6.04689e-05 | 0.00356 |
| 1.79062 | 0.126184 | 7.55912e-05 | 0.00379 |
| 1.98956 | 0.131769 | 9.55757e-05 | 0.00395 |
| 2.18908 | 0.136044 | 0.000124039 | 0.00408 |
| 2.38917 | 0.136248 | 0.000161952 | 0.00409 |
| 2.58923 | 0.137932 | 0.000219156 | 0.00414 |
| 2.82739 | 0.138047 | 0.000255731 | 0.00414 |
| 3.19269 | 0.137028 | 0.000336194 | 0.00411 |

Table A.52: Charged Pions $v_2$ in 0-50% centrality

| $p_T$ **(GeV/c)** | **value** | **Stat. Errors** (±) | **Sys. Errors** (±) |
|---|---|---|---|
| 0.3924 | 0.00616658 | 3.06162e-05 | 0.000370 |
| 0.59071 | 0.0146416 | 4.6012e-05 | 0.000879 |
| 0.789872 | 0.0243241 | 6.87986e-05 | 0.00146 |
| 0.990376 | 0.0336098 | 9.59592e-05 | 0.00202 |
| 1.19012 | 0.0425198 | 0.000125948 | 0.00255 |
| 1.39026 | 0.0505017 | 0.000160974 | 0.00303 |
| 1.59036 | 0.05685 | 0.000204041 | 0.003411 |
| 1.79062 | 0.0624667 | 0.000255325 | 0.00375 |
| 1.98956 | 0.0655571 | 0.000323755 | 0.00393 |
| 2.18908 | 0.0701238 | 0.000419644 | 0.00421 |
| 2.38917 | 0.0721046 | 0.000551249 | 0.00433 |
| 2.58923 | 0.077887 | 0.000744846 | 0.00467 |
| 2.82739 | 0.0720779 | 0.000870282 | 0.00432 |
| 3.19269 | 0.0712164 | 0.00115127 | 0.00427 |

Table A.53: Charged Pions $v_3$ in 0-50% centrality

| $p_T$ **(GeV/c)** | **value** | **Stat. Errors** (±) | **Sys. Errors** (±) |
|---|---|---|---|
| 0.59071 | 0.0052293 | 0.000200882 | 0.00105 |
| 0.789872 | 0.0108237 | 0.000350734 | 0.00216 |
| 0.990376 | 0.0182327 | 0.000526467 | 0.00365 |
| 1.19012 | 0.0296074 | 0.000874533 | 0.00592 |
| 1.39026 | 0.0396482 | 0.00112205 | 0.00793 |
| 1.59036 | 0.0454903 | 0.00129327 | 0.00910 |
| 1.79062 | 0.0501997 | 0.00163262 | 0.01004 |
| 1.98956 | 0.0609807 | 0.00203164 | 0.01220 |
| 2.18908 | 0.0658899 | 0.00240315 | 0.01318 |
| 2.38917 | 0.0712976 | 0.00311303 | 0.01426 |
| 2.58923 | 0.0807794 | 0.00401863 | 0.01616 |
| 2.82739 | 0.0775281 | 0.00464842 | 0.01551 |
| 3.19269 | 0.0794154 | 0.00583586 | 0.01588 |

Table A.54: Charged Pions $v_4$ in 0-50% centrality

| $p_T$ **(GeV/c)** | **value** | **Stat. Errors** ($\pm$) | **Sys. Errors** ($\pm$) |
|---|---|---|---|
| 0.425434 | 0.0146884 | 6.97415e-05 | 0.00044 |
| 0.604645 | 0.0306243 | 4.47786e-05 | 0.00092 |
| 0.79693 | 0.0503107 | 4.54568e-05 | 0.00151 |
| 0.994525 | 0.0679718 | 5.31266e-05 | 0.00204 |
| 1.19296 | 0.083454 | 6.48535e-05 | 0.00250 |
| 1.39233 | 0.096206 | 8.08406e-05 | 0.00289 |
| 1.59167 | 0.107027 | 0.000101588 | 0.00321 |
| 1.79185 | 0.115449 | 0.000128264 | 0.00346 |
| 1.99164 | 0.121548 | 0.000161562 | 0.00365 |
| 2.18966 | 0.126981 | 0.000204827 | 0.00381 |
| 2.39025 | 0.130838 | 0.000257206 | 0.00393 |
| 2.59074 | 0.129117 | 0.000336852 | 0.00387 |
| 2.82883 | 0.131952 | 0.000364144 | 0.00396 |

Table A.55: Charged Kaons $v_2$ in 0-50% centrality

| $p_T$ **(GeV/c)** | **value** | **Stat. Errors** ($\pm$) | **Sys. Errors** ($\pm$) |
|---|---|---|---|
| 0.425434 | 0.00121871 | 0.000206634 | 0.0000731 |
| 0.604645 | 0.00686957 | 0.000134735 | 0.000412 |
| 0.79693 | 0.0154448 | 0.000137823 | 0.000927 |
| 0.994525 | 0.0250998 | 0.000165027 | 0.00151 |
| 1.19296 | 0.0336866 | 0.000203702 | 0.00202 |
| 1.39233 | 0.0410171 | 0.00025706 | 0.00246 |
| 1.59167 | 0.0464181 | 0.00032401 | 0.00279 |
| 1.79185 | 0.0531182 | 0.000412354 | 0.00319 |
| 1.99164 | 0.0611084 | 0.000523387 | 0.00367 |
| 2.18966 | 0.0643772 | 0.000666712 | 0.00386 |
| 2.39025 | 0.0628411 | 0.000856276 | 0.00377 |
| 2.59074 | 0.0690588 | 0.00111517 | 0.00414 |
| 2.82883 | 0.0689385 | 0.00123176 | 0.00414 |

Table A.56: Charged Kaons $v_3$ in 0-50% centrality

| $p_T$ **(GeV/c)** | **value** | **Stat. Errors** ($\pm$) | **Sys. Errors** ($\pm$) |
|---|---|---|---|
| 0.604645 | 0.00340053 | 0.000618255 | 0.000680 |
| 0.79693 | 0.00489004 | 0.000637086 | 0.000978 |
| 0.994525 | 0.0107645 | 0.000754362 | 0.00215 |
| 1.19296 | 0.0233912 | 0.00104826 | 0.00468 |
| 1.39233 | 0.0276747 | 0.00127454 | 0.00553 |
| 1.59167 | 0.0382504 | 0.00164336 | 0.00765 |
| 1.79185 | 0.0444564 | 0.00213802 | 0.00889 |
| 1.99164 | 0.0511145 | 0.00263238 | 0.01022 |
| 2.18966 | 0.0514669 | 0.00332194 | 0.01029 |
| 2.39025 | 0.0576625 | 0.00423368 | 0.01153 |
| 2.59074 | 0.0872584 | 0.00590972 | 0.01745 |
| 2.82883 | 0.069308 | 0.00606226 | 0.01386 |

Table A.57: Charged Kaons $v_4$ in 0-50% centrality

# Appendix B

# Tabulated Results for PIDed $v_n$ (n=2,3) in $Au + Au$ Collisions at $\sqrt{s_{NN}}$ = 62.4 and 39 GeV

## B.1 Tabulated PIDed $v_{2,3}$ results at $\sqrt{s_{NN}}$ = 39GeV.

| $p_T$ (GeV/c) | Value | Stat. Errors ($\pm$) | Sys. Errors ($\pm$) |
|---|---|---|---|
| 0.5118 | 0.0167129 | 0.000965696 | 1.3370e-03 |
| 0.697315 | 0.0308261 | 0.000871774 | 2.46609e-03 |
| 0.892768 | 0.040655 | 0.00104536 | 3.2524e-03 |
| 1.09154 | 0.0533362 | 0.00133575 | 4.2669e-03 |
| 1.29066 | 0.0639593 | 0.00173485 | 5.1167e-03 |
| 1.49012 | 0.0709832 | 0.00226799 | 5.6787e-03 |
| 1.69016 | 0.0810318 | 0.00309279 | 6.48254e-03 |
| 1.88992 | 0.0862661 | 0.00381769 | 6.9013e-03 |
| 2.08954 | 0.0905962 | 0.00511882 | 7.2477e-03 |
| 2.28915 | 0.0794533 | 0.0073666 | 6.3563e-03 |
| 2.6884 | 0.0810549 | 0.0064132 | 6.4844e-03 |

Table B.1: Charged Kaons $v_2$ in 0-20% centrality at $\sqrt{s_{NN}}$ = 39GeV.

| $p_T$ **(GeV/c)** | **Value** | **Stat. Errors** ($\pm$) | **Sys. Errors** ($\pm$) |
|---|---|---|---|
| 0.5118 | 0.00822233 | 0.00282174 | 1.2333e-03 |
| 0.697315 | 0.00629649 | 0.00252171 | 9.4447e-04 |
| 0.892768 | 0.0168872 | 0.00309055 | 2.5331e-03 |
| 1.09154 | 0.0229462 | 0.00396729 | 3.4419e-03 |
| 1.29066 | 0.0192347 | 0.00512301 | 2.8852e-03 |
| 1.49012 | 0.0264412 | 0.00669135 | 3.96618e-03 |
| 1.69016 | 0.0583883 | 0.00944956 | 8.7582e-03 |
| 1.88992 | 0.0350035 | 0.0113894 | 5.2505e-03 |
| 2.08954 | 0.0932476 | 0.0157284 | 0.01399 |
| 2.28915 | 0.045055 | 0.0222922 | 6.75825e-03 |
| 2.6884 | 0.0408488 | 0.0193779 | 6.12732e-03 |

Table B.2: Charged Kaons $v_3$ in 0-20% centrality at $\sqrt{s_{NN}} = 39$GeV.

| $p_T$ **(GeV/c)** | **Value** | **Stat. Errors** ($\pm$) | **Sys. Errors** ($\pm$) |
|---|---|---|---|
| 0.511253 | 0.0401535 | 0.000910213 | 2.00768e-03 |
| 0.697031 | 0.0630141 | 0.000856177 | 3.1507e-03 |
| 0.892843 | 0.0820856 | 0.00103329 | 4.1043e-03 |
| 1.09183 | 0.107725 | 0.00134771 | 5.3863e-03 |
| 1.29082 | 0.123706 | 0.00176444 | 6.1853e-03 |
| 1.49051 | 0.134636 | 0.00237404 | 6.7318e-03 |
| 1.69061 | 0.145179 | 0.00313577 | 7.25895e-03 |
| 1.8906 | 0.149855 | 0.00422713 | 7.49275e-03 |
| 2.15813 | 0.146701 | 0.00455449 | 7.33505e-03 |
| 2.69231 | 0.172515 | 0.00688768 | 8.62575e-03 |

Table B.3: Charged Kaons $v_2$ in 20-60% centrality at $\sqrt{s_{NN}} = 39$GeV.

| $p_T$ **(GeV/c)** | **Value** | **Stat. Errors** ($\pm$) | **Sys. Errors** ($\pm$) |
|---|---|---|---|
| 0.697031 | 0.0264347 | 0.00522874 | 3.9652e-03 |
| 0.892843 | 0.0335591 | 0.00625731 | 5.03387e-03 |
| 1.09183 | 0.0382776 | 0.00817176 | 5.7416e-03 |
| 1.29082 | 0.0477414 | 0.0105475 | 7.16121e-03 |
| 1.49051 | 0.0781851 | 0.0145088 | 0.01173 |
| 1.69061 | 0.078239 | 0.018852 | 0.01174 |
| 1.8906 | 0.0511833 | 0.0252838 | 7.6775e-03 |
| 2.15813 | 0.0651621 | 0.0274519 | 9.7743e-03 |
| 2.69231 | 0.128163 | 0.0409799 | 0.0192 |

Table B.4: Charged Kaons $v_3$ in 20-60% centrality at $\sqrt{s_{NN}} = 39$GeV.

| $p_T$ **(GeV/c)** | **Value** | **Stat. Errors** ($\pm$) | **Sys. Errors** ($\pm$) |
|---|---|---|---|
| 0.49078 | 0.0285945 | 0.00028089 | 2.2876e-03 |
| 0.68876 | 0.0412119 | 0.000385262 | 3.297e-03 |
| 0.8888 | 0.0534129 | 0.000529889 | 4.27303e-03 |
| 1.08926 | 0.0645125 | 0.000711864 | 5.161e-03 |
| 1.28899 | 0.0690208 | 0.00093245 | 5.5217e-03 |
| 1.48892 | 0.0758534 | 0.00127657 | 6.0683e-03 |
| 1.68948 | 0.0896617 | 0.00170453 | 7.17293e-03 |
| 1.88877 | 0.0753381 | 0.00227769 | 6.0270e-03 |
| 2.08888 | 0.0909118 | 0.00304245 | 7.2729e-03 |
| 2.2895 | 0.0846868 | 0.00413212 | 6.7749e-03 |
| 2.55752 | 0.115975 | 0.0048101 | 9.278e-03 |
| 3.13089 | 0.112097 | 0.00679461 | 8.968e-03 |

Table B.5: Charged Pions $v_2$ in 0-20% centrality at $\sqrt{s_{NN}} = 39$GeV.

| $p_T$ **(GeV/c)** | **Value** | **Stat. Errors** ($\pm$) | **Sys. Errors** ($\pm$) |
|---|---|---|---|
| 0.49078 | 0.00815268 | 0.00077958 | 1.223e-03 |
| 0.68876 | 0.0152037 | 0.00112571 | 2.2806e-03 |
| 0.8888 | 0.0248766 | 0.00179285 | 3.7315e-03 |
| 1.08926 | 0.0277356 | 0.0022162 | 4.1603e-03 |
| 1.28899 | 0.0466641 | 0.00338478 | 6.9996e-03 |
| 1.48892 | 0.0390072 | 0.00400856 | 5.8511e-03 |
| 1.68948 | 0.0581596 | 0.00570005 | 8.7239e-03 |
| 1.88877 | 0.0510965 | 0.00709604 | 7.66448e-03 |
| 2.08888 | 0.0931944 | 0.0102415 | 0.014 |
| 2.2895 | 0.0580251 | 0.0125168 | 8.7038e-03 |
| 2.55752 | 0.0602911 | 0.0143379 | 9.0437e-03 |
| 3.13089 | 0.062196 | 0.0208069 | 9.3294e-03 |

Table B.6: Charged Pions $v_3$ in 0-20% centrality at $\sqrt{s_{NN}} = 39$GeV.

| $p_T$ **(GeV/c)** | **Value** | **Stat. Errors** ($\pm$) | **Sys. Errors** ($\pm$) |
|---|---|---|---|
| 0.490676 | 0.0554962 | 0.000219875 | 2.7748e-03 |
| 0.688667 | 0.0786166 | 0.000305553 | 3.93083e-03 |
| 0.888828 | 0.102342 | 0.000438564 | 5.1171e-03 |
| 1.0893 | 0.118558 | 0.000613838 | 5.9279e-03 |
| 1.28906 | 0.136232 | 0.000863281 | 6.8116e-03 |
| 1.48918 | 0.150206 | 0.00120825 | 7.5103e-03 |
| 1.68937 | 0.157345 | 0.00165238 | 7.86725e-03 |
| 1.88897 | 0.166314 | 0.00227331 | 8.3157e-03 |
| 2.08865 | 0.177925 | 0.00320973 | 8.89625e-03 |
| 2.2891 | 0.168897 | 0.00441968 | 8.44485e-03 |
| 2.55712 | 0.182259 | 0.00500961 | 9.11295e-03 |
| 3.143 | 0.178985 | 0.00739771 | 8.94925e-03 |

Table B.7: Charged Pions $v_2$ in 20-60% centrality at $\sqrt{s_{NN}} = 39$GeV.

| $p_T$ **(GeV/c)** | **Value** | **Stat. Errors** ($\pm$) | **Sys. Errors** ($\pm$) |
|---|---|---|---|
| 0.490676 | 0.0135058 | 0.00138118 | 2.0259e-03 |
| 0.688667 | 0.0200406 | 0.00190337 | 3.0061e-03 |
| 0.888828 | 0.0386317 | 0.0028538 | 5.7948e-03 |
| 1.0893 | 0.0421341 | 0.00385456 | 6.3201e-03 |
| 1.28906 | 0.0471914 | 0.00531895 | 7.079e-03 |
| 1.48918 | 0.0615179 | 0.00746416 | 9.2277e-03 |
| 1.68937 | 0.0519897 | 0.010008 | 7.7985e-03 |
| 1.88897 | 0.0750639 | 0.0137376 | 0.01126 |
| 2.08865 | 0.0825103 | 0.0191611 | 0.01238 |
| 2.2891 | 0.0856448 | 0.026662 | 0.01285 |
| 2.55712 | 0.114037 | 0.0299968 | 0.01711 |
| 3.143 | 0.210331 | 0.0445936 | 0.03155 |

Table B.8: Charged Pions $v_3$ in 20-60% centrality at $\sqrt{s_{NN}} = 39$GeV.

| $p_T$ **(GeV/c)** | **Value** | **Stat. Errors** ($\pm$) | **Sys. Errors** ($\pm$) |
|---|---|---|---|
| 0.554277 | 0.014386 | 0.00132801 | 1.1509e-03 |
| 0.70533 | 0.0189497 | 0.000761996 | 1.516e-03 |
| 0.89854 | 0.0321476 | 0.000776471 | 2.5718e-03 |
| 1.09507 | 0.0437379 | 0.000896043 | 3.4990e-03 |
| 1.2927 | 0.0599153 | 0.00113618 | 4.793224e-03 |
| 1.49101 | 0.0729588 | 0.00145907 | 5.8367e-03 |
| 1.6909 | 0.0834799 | 0.00192619 | 6.6784e-03 |
| 1.8903 | 0.0824986 | 0.00251691 | 6.5999e-03 |
| 2.0897 | 0.106317 | 0.00334703 | 8.5054e-03 |
| 2.29066 | 0.114685 | 0.00455278 | 9.1748e-03 |
| 2.61775 | 0.0905265 | 0.00430251 | 7.24212e-03 |
| 3.29266 | 0.119494 | 0.0087125 | 9.5595e-03 |

Table B.9: (anti-)protons $v_2$ in 0-20% centrality at $\sqrt{s_{NN}} = 39$GeV.

| $p_T$ **(GeV/c)** | **Value** | **Stat. Errors** ($\pm$) | **Sys. Errors** ($\pm$) |
|---|---|---|---|
| 0.70533 | 0.00669161 | 0.00225746 | 1.0038e-03 |
| 0.89854 | 0.0104187 | 0.00225495 | 1.5628e-03 |
| 1.09507 | 0.0157476 | 0.00263129 | 2.36214e-03 |
| 1.2927 | 0.0248562 | 0.00335241 | 3.7284e-03 |
| 1.49101 | 0.0425657 | 0.00454986 | 6.3849e-03 |
| 1.6909 | 0.046296 | 0.00591438 | 6.9444e-03 |
| 1.8903 | 0.0635443 | 0.00779894 | 9.5316e-03 |
| 2.0897 | 0.065907 | 0.0102991 | 9.8861e-03 |
| 2.29066 | 0.0793627 | 0.013795 | 0.0119 |
| 2.61775 | 0.0713917 | 0.0132165 | 0.0107 |
| 3.29266 | 0.0624637 | 0.0255166 | 9.3696e-03 |

Table B.10: (anti-)protons $v_3$ in 0-20% centrality at $\sqrt{s_{NN}} = 39$GeV.

| $p_T$ **(GeV/c)** | **Value** | **Stat. Errors** ($\pm$) | **Sys. Errors** ($\pm$) |
|---|---|---|---|
| 0.554309 | 0.0269385 | 0.00117489 | 1.3469e-03 |
| 0.704482 | 0.0431465 | 0.000701656 | 2.15733e-03 |
| 0.89779 | 0.0693476 | 0.000730177 | 3.4674e-03 |
| 1.09455 | 0.0947245 | 0.000867528 | 4.7362e-03 |
| 1.29219 | 0.119573 | 0.00110305 | 5.9787e-03 |
| 1.491 | 0.145248 | 0.00147407 | 7.2624e-03 |
| 1.69046 | 0.168858 | 0.00198305 | 8.4429e-03 |
| 1.89061 | 0.18264 | 0.0026732 | 9.132e-03 |
| 2.0902 | 0.201786 | 0.00366374 | 0.0101 |
| 2.29048 | 0.193406 | 0.00489405 | 9.6703e-03 |
| 2.61841 | 0.21975 | 0.00490585 | 0.0110 |
| 3.29975 | 0.200735 | 0.0103712 | 0.0100 |

Table B.11: (anti-)protons $v_2$ in 20-60% centrality at $\sqrt{s_{NN}} = 39$GeV.

| $p_T$ **(GeV/c)** | **Value** | **Stat. Errors** ($\pm$) | **Sys. Errors** ($\pm$) |
|---|---|---|---|
| 0.704482 | 0.0163087 | 0.00432375 | 2.4463e-03 |
| 0.89779 | 0.0213719 | 0.00445718 | 3.2058e-03 |
| 1.09455 | 0.0303695 | 0.00525775 | 4.5554e-03 |
| 1.29219 | 0.0592341 | 0.00685772 | 8.8851e-03 |
| 1.491 | 0.0546362 | 0.00896839 | 8.19543e-03 |
| 1.69046 | 0.0830465 | 0.0119549 | 0.01246 |
| 1.89061 | 0.0817589 | 0.0159399 | 0.01226 |
| 2.0902 | 0.0892135 | 0.021669 | 0.01338 |
| 2.29048 | 0.100723 | 0.0290315 | 0.01511 |
| 2.61841 | 0.0888024 | 0.0287223 | 0.01332 |
| 3.29975 | 0.145275 | 0.0612065 | 0.02179 |

Table B.12: (anti-)protons $v_3$ in 20-60% centrality at $\sqrt{s_{NN}} = 39$GeV.

## B.2 Tabulated PIDed $v_{2,3}$ results at $\sqrt{s_{NN}} = 62.4$GeV.

| $p_T$ (GeV/c) | Value | Stat. Errors ($\pm$) | Sys. Errors ($\pm$) |
|---|---|---|---|
| 0.511815 | 0.0178984 | 0.00041447 | 8.9492e-04 |
| 0.6977 | 0.0293939 | 0.000372659 | 1.4697e-03 |
| 0.893422 | 0.042858 | 0.000441554 | 2.1429e-03 |
| 1.09221 | 0.0542557 | 0.000550546 | 2.7128e-03 |
| 1.29141 | 0.0658392 | 0.000704987 | 3.29196e-03 |
| 1.49043 | 0.0725006 | 0.000907333 | 3.625e-03 |
| 1.69059 | 0.077522 | 0.00119108 | 3.8761e-03 |
| 1.89047 | 0.0909216 | 0.001573 | 4.5461e-03 |
| 2.08913 | 0.0934949 | 0.00205591 | 4.67475e-03 |
| 2.28922 | 0.0975912 | 0.00261999 | 4.8796e-03 |
| 2.69543 | 0.0943814 | 0.00217679 | 4.7191e-03 |

Table B.13: Charged Kaons $v_2$ in 0-20% centrality at $\sqrt{s_{NN}} = 62.4$GeV.

| $p_T$ (GeV/c) | Value | Stat. Errors ($\pm$) | Sys. Errors ($\pm$) |
|---|---|---|---|
| 0.511815 | 0.00154817 | 0.00112396 | 1.548e-04 |
| 0.6977 | 0.00913697 | 0.00101897 | 9.137e-04 |
| 0.893422 | 0.0186379 | 0.00123669 | 1.864e-03 |
| 1.09221 | 0.0292769 | 0.00157101 | 2.923e-03 |
| 1.29141 | 0.0313733 | 0.0019566 | 3.137e-03 |
| 1.49043 | 0.0357477 | 0.00258154 | 3.5748e-03 |
| 1.69059 | 0.0356434 | 0.00334029 | 3.5643e-03 |
| 1.89047 | 0.0541774 | 0.00447778 | 5.4178e-03 |
| 2.08913 | 0.0587024 | 0.00583995 | 5.8702e-03 |
| 2.28922 | 0.063813 | 0.00752619 | 6.3813e-03 |
| 2.69543 | 0.024076 | 0.00615481 | 2.4076e-03 |

Table B.14: Charged Kaons $v_3$ in 0-20% centrality at $\sqrt{s_{NN}} = 62.4$GeV.

| $p_T$ **(GeV/c)** | **Value** | **Stat. Errors** ($\pm$) | **Sys. Errors** ($\pm$) |
|---|---|---|---|
| 0.511745 | 0.0414749 | 0.000411274 | 2.0737e-03 |
| 0.697447 | 0.063529 | 0.000385257 | 3.1765e-03 |
| 0.89333 | 0.0878561 | 0.000462178 | 4.3928e-03 |
| 1.09216 | 0.105075 | 0.000588022 | 5.2538e-03 |
| 1.29137 | 0.123501 | 0.000767556 | 6.1751e-03 |
| 1.49102 | 0.14568 | 0.00100289 | 7.284e-03 |
| 1.69071 | 0.151562 | 0.00133426 | 7.5781e-03 |
| 1.89079 | 0.155991 | 0.00175477 | 7.7996e-03 |
| 2.16063 | 0.16657 | 0.00184304 | 8.3285e-03 |
| 2.70939 | 0.174705 | 0.00254027 | 8.7353e-03 |

Table B.15: Charged Kaons $v_2$ in 20-60% centrality at $\sqrt{s_{NN}} = 62.4$GeV.

| $p_T$ **(GeV/c)** | **Value** | **Stat. Errors** ($\pm$) | **Sys. Errors** ($\pm$) |
|---|---|---|---|
| 0.511745 | 0.0100085 | 0.00226283 | 1.2010e-03 |
| 0.697447 | 0.0199901 | 0.00214218 | 2.3988e-03 |
| 0.89333 | 0.0251041 | 0.00249858 | 3.0125e-03 |
| 1.09216 | 0.0330069 | 0.00316886 | 3.9608e-03 |
| 1.29137 | 0.0365006 | 0.00412351 | 4.3801e-03 |
| 1.49102 | 0.0540006 | 0.00539858 | 6.4801e-03 |
| 1.69071 | 0.0460019 | 0.00711835 | 5.5202e-03 |
| 1.89079 | 0.0679992 | 0.00945042 | 8.1599e-03 |
| 2.16063 | 0.0582731 | 0.00998625 | 6.9928e-03 |
| 2.70939 | 0.0568391 | 0.013992 | 6.8207e-03 |

Table B.16: Charged Kaons $v_3$ in 20-60% centrality at $\sqrt{s_{NN}} = 62.4$GeV.

| $p_T$ **(GeV/c)** | **Value** | **Stat. Errors** ($\pm$) | **Sys. Errors** ($\pm$) |
|---|---|---|---|
| 0.491212 | 0.0281089 | 0.00012095 | 1.4054e-03 |
| 0.689152 | 0.0419533 | 0.000168161 | 2.0977e-03 |
| 0.889282 | 0.0547101 | 0.000230363 | 2.7355e-03 |
| 1.08973 | 0.065379 | 0.000303359 | 3.2690e-03 |
| 1.28942 | 0.074899 | 0.000394745 | 3.74495e-03 |
| 1.48946 | 0.080629 | 0.000518648 | 4.03145e-03 |
| 1.68977 | 0.0843418 | 0.000675513 | 4.21709e-03 |
| 1.88937 | 0.092323 | 0.000890275 | 4.6162e-03 |
| 2.08949 | 0.0917079 | 0.00117822 | 4.5854e-03 |
| 2.28918 | 0.093508 | 0.00158523 | 4.6754e-03 |
| 2.55968 | 0.0977423 | 0.0017379 | 4.8871e-03 |
| 3.15041 | 0.0993069 | 0.00241547 | 4.9653e-03 |

Table B.17: Charged Pions $v_2$ in 0-20% centrality at $\sqrt{s_{NN}} = 62.4$GeV.

| $p_T$ **(GeV/c)** | **Value** | **Stat. Errors** ($\pm$) | **Sys. Errors** ($\pm$) |
|---|---|---|---|
| 0.491212 | 0.00845412 | 0.000311446 | 8.4541e-04 |
| 0.689152 | 0.0177919 | 0.00050355 | 1.7792e-03 |
| 0.889282 | 0.0254506 | 0.000714924 | 2.5451e-03 |
| 1.08973 | 0.0316315 | 0.00094309 | 3.1632e-03 |
| 1.28942 | 0.0398734 | 0.00123181 | 3.9873e-03 |
| 1.48946 | 0.0467341 | 0.00163995 | 4.6734e-03 |
| 1.68977 | 0.0549517 | 0.00213551 | 5.4952e-03 |
| 1.88937 | 0.065842 | 0.00273161 | 6.5842e-03 |
| 2.08949 | 0.0600899 | 0.00341561 | 6.0090e-03 |
| 2.28918 | 0.0677608 | 0.00464083 | 6.7761e-03 |
| 2.55968 | 0.0855998 | 0.00522117 | 8.5600e-03 |
| 3.15041 | 0.0583048 | 0.00699182 | 5.8305e-03 |

Table B.18: Charged Pions $v_3$ in 0-20% centrality at $\sqrt{s_{NN}} = 62.4$GeV.

| $p_T$ **(GeV/c)** | **Value** | **Stat. Errors** ($\pm$) | **Sys. Errors** ($\pm$) |
|---|---|---|---|
| 0.491151 | 0.0570099 | 0.000100688 | 2.8505e-03 |
| 0.689015 | 0.0829862 | 0.000139639 | 4.1493e-03 |
| 0.889173 | 0.106574 | 0.000198187 | 5.3287e-03 |
| 1.08971 | 0.126461 | 0.000276466 | 6.3231e-03 |
| 1.28958 | 0.141468 | 0.000383511 | 7.0734e-03 |
| 1.48968 | 0.154297 | 0.000523517 | 7.7149e-03 |
| 1.6901 | 0.159911 | 0.000712046 | 7.9956e-03 |
| 1.88946 | 0.172079 | 0.000970306 | 8.6040e-03 |
| 2.08902 | 0.175152 | 0.00133066 | 8.7576e-03 |
| 2.28935 | 0.178284 | 0.00184464 | 8.9142e-03 |
| 2.55975 | 0.170174 | 0.00203832 | 8.5087e-03 |
| 3.15919 | 0.179534 | 0.00289801 | 8.9767e-03 |

Table B.19: Charged Pions $v_2$ in 20-60% centrality at $\sqrt{s_{NN}} = 62.4$GeV.

| $p_T$ **(GeV/c)** | **Value** | **Stat. Errors** ($\pm$) | **Sys. Errors** ($\pm$) |
|---|---|---|---|
| 0.491151 | 0.0133869 | 0.000554591 | 1.6064e-03 |
| 0.689015 | 0.0204002 | 0.000771038 | 2.4480e-03 |
| 0.889173 | 0.0354495 | 0.00111927 | 4.254e-03 |
| 1.08971 | 0.0391429 | 0.00152638 | 4.6971e-03 |
| 1.28958 | 0.0493461 | 0.00210753 | 5.9215e-03 |
| 1.48968 | 0.0481211 | 0.00285104 | 5.7745e-03 |
| 1.6901 | 0.0580756 | 0.00387753 | 6.9691e-03 |
| 1.88946 | 0.0578268 | 0.00526196 | 6.9392e-03 |
| 2.08902 | 0.0826659 | 0.00720469 | 9.9199e-03 |
| 2.28935 | 0.105242 | 0.00991783 | 0.0126 |
| 2.55975 | 0.0900726 | 0.0107659 | 0.01081 |
| 3.15919 | 0.0957186 | 0.0152109 | 0.01149 |

Table B.20: Charged Pions $v_3$ in 20-60% centrality at $\sqrt{s_{NN}} = 62.4$GeV.

| $p_T$ (GeV/c) | Value | Stat. Errors (±) | Sys. Errors (±) |
|---|---|---|---|
| 0.554278 | 0.00630355 | 0.000589248 | 3.1518e-04 |
| 0.705553 | 0.0165372 | 0.000334308 | 8.2686e-04 |
| 0.899073 | 0.0281633 | 0.000339055 | 1.4082e-03 |
| 1.09558 | 0.0427761 | 0.000392148 | 2.1388e-03 |
| 1.29324 | 0.0589674 | 0.000490062 | 2.9484e-03 |
| 1.49167 | 0.0728459 | 0.000622982 | 3.6423e-03 |
| 1.69131 | 0.0851809 | 0.000809242 | 4.2590e-03 |
| 1.89078 | 0.0949985 | 0.00106315 | 4.74992e-03 |
| 2.09071 | 0.104676 | 0.00140043 | 5.2338e-03 |
| 2.29066 | 0.110922 | 0.00185586 | 5.5461e-03 |
| 2.6189 | 0.120249 | 0.00177926 | 6.01245e-03 |
| 3.30428 | 0.138532 | 0.00325648 | 6.9266e-03 |

Table B.21: (anti-)protons $v_2$ in 0-20% centrality at $\sqrt{s_{NN}} = 62.4$GeV.

| $p_T$ (GeV/c) | Value | Stat. Errors (±) | Sys. Errors (±) |
|---|---|---|---|
| 0.705553 | 0.00422551 | 0.000915755 | 4.226e-04 |
| 0.899073 | 0.00808842 | 0.000922681 | 8.0884e-04 |
| 1.09558 | 0.0192614 | 0.00109491 | 1.9261e-03 |
| 1.29324 | 0.0287157 | 0.0013977 | 2.8716e-03 |
| 1.49167 | 0.0428998 | 0.00183162 | 4.2900e-03 |
| 1.69131 | 0.0491205 | 0.00234109 | 4.9121e-03 |
| 1.89078 | 0.0556877 | 0.00304503 | 5.5688e-03 |
| 2.09071 | 0.0568563 | 0.00396306 | 5.6856e-03 |
| 2.29066 | 0.0621132 | 0.00522934 | 6.2113e-03 |
| 2.6189 | 0.0894495 | 0.00517795 | 8.9450e-03 |
| 3.30428 | 0.106237 | 0.00927218 | 1.062e-02 |

Table B.22: (anti-)protons $v_3$ in 0-20% centrality at $\sqrt{s_{NN}} = 62.4$GeV.

| $p_T$ **(GeV/c)** | **Value** | **Stat. Errors** ($\pm$) | **Sys. Errors** ($\pm$) |
|---|---|---|---|
| 0.554268 | 0.0265979 | 0.000545051 | 1.3299e-03 |
| 0.704727 | 0.0450996 | 0.000327104 | 2.2550e-03 |
| 0.898328 | 0.0702264 | 0.000341178 | 3.5113e-03 |
| 1.09497 | 0.096921 | 0.000402323 | 4.8461e-05 |
| 1.29284 | 0.123886 | 0.000509968 | 6.1943e-03 |
| 1.49157 | 0.145186 | 0.00066225 | 7.2593e-03 |
| 1.69113 | 0.17031 | 0.000881674 | 8.5155e-03 |
| 1.89092 | 0.185052 | 0.00118232 | 9.2526e-03 |
| 2.09102 | 0.200448 | 0.00158339 | 0.0100 |
| 2.29089 | 0.212558 | 0.00211515 | 0.0106 |
| 2.62149 | 0.229939 | 0.00202001 | 0.0115 |
| 3.31277 | 0.23325 | 0.0040676 | 0.01167 |

Table B.23: (anti-)protons $v_2$ in 20-60% centrality at $\sqrt{s_{NN}} = 62.4$GeV.

| $p_T$ **(GeV/c)** | **Value** | **Stat. Errors** ($\pm$) | **Sys. Errors** ($\pm$) |
|---|---|---|---|
| 0.704727 | 0.0124326 | 0.00182191 | 1.4919e-03 |
| 0.898328 | 0.0213907 | 0.00187746 | 2.5669e-03 |
| 1.09497 | 0.0288345 | 0.00219123 | 3.46014e-03 |
| 1.29284 | 0.0464012 | 0.00276155 | 5.56814e-03 |
| 1.49157 | 0.057598 | 0.00358585 | 6.9118e-03 |
| 1.69113 | 0.0749947 | 0.0047775 | 8.9994e-03 |
| 1.89092 | 0.0692114 | 0.00630101 | 8.3054e-03 |
| 2.09102 | 0.100518 | 0.00843771 | 0.0121 |
| 2.29089 | 0.120835 | 0.0114097 | 0.0145 |
| 2.62149 | 0.0747739 | 0.0107969 | 8.9729e-03 |
| 3.31277 | 0.0950213 | 0.0217597 | 0.0114 |

Table B.24: (anti-)protons $v_3$ in 20-60% centrality at $\sqrt{s_{NN}} = 62.4$GeV.

# Bibliography


[1] Siegfried Bethke. Experimental Tests of Asymptotic Freedom. *Prog.Part.Nucl.Phys.*, 58:351–386, 2007, hep-ex/0606035. URL http://arxiv.org/abs/hep-ex/0606035.

[2] R.T. et al. 2007 Long Range Plan: The Frontiers of Nuclear Science, Report to the Nuclear Science Advisory Committee. URL http://science.energy.gov/~/media/np/nsac/pdf/20130201/2013_NSAC_Implementing_the_2007_Long_Range_Plan.pdf.

[3] F.Karsch. Lettice QCD at High Temperature and Density. In W. Plessas and L. Mathelitsch, editors, *Lectures on Quark Matter*, volume 583, of Lecture Notes in Physics, pages 209–249. Springer Berlin/Heidelberg, 2002.

[4] Peter Braun-Munzinger and Johanna Stachel. The Quest for the Quark Gluon Plasma. *Nature*, 448:302–309, 2007. URL http://www.nature.com/nature/journal/v448/n7151/full/nature06080.html#B65.

[5] A. Adare et al. (**PHENIX** Collaboration). Scaling properties of azimuthal anisotropy in Au+Au and Cu+Cu collisions at $\sqrt{s_{NN}} = 200$ GeV. *Phys.Rev.Lett.*, 98:162301, 2007, nucl-ex/0608033.

[6] B. B. Back et al. (**PHOBOS** Collaboration). Centrality and pseudorapidity dependence of elliptic flow for charged hadrons in au+au collisions at $\sqrt{s_{NN}} = 200$gev. *Phys. Rev. C*, 72:051901, Nov 2005. URL http://link.aps.org/doi/10.1103/PhysRevC.72.051901.

[7] Tetsufumi Hirano, Ulrich W. Heinz, Dmitri Kharzeev, Roy Lacey, and Yasushi Nara. Hadronic dissipative effects on elliptic flow in ultrarelativistic heavy-ion collisions. *Phys.Lett.*, B636:299–304, 2006, nucl-th/0511046.

[8] Tetsufumi Hirano, Naomi van der Kolk, and Ante Bilandzic. Hydrodynamics and Flow. *Lect.Notes Phys.*, 785:139–178, 2010, 0808.2684.

[9] Huichao Song. Causal Viscous Hydrodynamics for Relativistic Heavy Ion Collisions. 2009, 0908.3656.

[10] B. Alver et al. (**PHOBOS** Collaboration). Elliptic Flow Fluctuations in Au+Au Collisions at $\sqrt{s_{NN}} = 200$ GeV. *International Journal of Modern Physics E*, 16:3331–3338, November 2007.

[11] A. Adare, et al. (**PHENIX** Collaboration). Deviation from quark-number scaling of the anisotropyparameter $v_2$ of pions, kaons, and protons in Au+Au collisions at $\sqrt{s_{NN}} = 200$ GeV. *Phys.Rev.*, C85:064914, 2012, 1203.2644.

[12] B. Mohanty and N. Xu. Probe the QCD phase diagram with phi-mesons in high energy nuclear collisions. *J.Phys.*, G36:064022, 2009, 0901.0313.

[13] Shusu Shi. Recent Elliptic Flow Results from Beam Energy Scan at STAR. *Heavy Ion Collisions at LHC Era, Quy Nhon, Vietnam, 16-21 July 2012*. URL http://indico.cern.ch/getFile.py/access?contribId=4&sessionId=6&resId=0&materialId=slides&confId=163815.

[14] A. Adare, et al. (**PHENIX** Collaboration). Suppression Pattern of Neutral Pions at High Transverse Momentum in Au+Au Collisions at $\sqrt{s_{NN}} = 200$ GeV and Constraints on Medium Transport Coefficients. *Phys. Rev. Lett.*, 101:232301, Dec 2008. URL http://link.aps.org/doi/10.1103/PhysRevLett.101.232301.

[15] A. Adare, et al. (**PHENIX** Collaboration). Transverse momentum dependence of meson suppression $\eta$ suppression in Au+Au collisions at $\sqrt{s_{NN}} = 200$ GeV. *Phys.Rev.*, C82:011902, 2010, 1005.4916.

[16] A. Adare, et al. (**PHENIX** Collaboration). Identified charged hadron production in $p+p$ collisions at $\sqrt{s_{NN}} = 200$ and 62.4 GeV. *Phys.Rev.*, C83:064903, 2011, 1102.0753.

[17] A. Adare, et al. (**PHENIX** Collaboration). Production of $\omega$ mesons in $p+p$, d+Au, Cu+Cu, and Au+Au collisions at $\sqrt{s_{NN}} = 200$ GeV. *Phys.Rev.*, C84:044902, 2011, 1105.3467.

[18] A. Adare, et al. (**PHENIX** Collaboration). Measurement of Direct Photons in Au+Au Collisions at $\sqrt{s_{NN}} = 200$ GeV. *Phys.Rev.Lett.*, 109:152302, 2012, 1205.5759.

[19] A. Adare, et al. (**PHENIX** Collaboration). Nuclear modification factors of $\phi$ mesons in $d+Au$, $Cu+Cu$, and $Au+Au$ collisions at $\sqrt{s_{NN}} = 200$ GeV. *Phys. Rev. C*, 83:024909, Feb 2011. URL http://link.aps.org/doi/10.1103/PhysRevC.83.024909.

[20] J. D. Bjorken. Highly relativistic nucleus-nucleus collisions: The central rapidity region. *Phys. Rev. D*, 27:140–151, Jan 1983. URL http://link.aps.org/doi/10.1103/PhysRevD.27.140.

[21] Jeffery T. Mitchell. The RHIC Beam Energy Scan Program: Results from the PHENIX Experiment. *Nucl.Phys.*, A904-905:903c–906c, 2013, 1211.6139.

[22] S.S. Adler and others (**PHENIX** Collaboration). Systematic studies of the centrality and $\sqrt{s_{NN}}$ dependence of the $dE(T)/d\eta$ and $d(N(ch)/d\eta$ in heavy ion collisions at mid-rapidity. *Phys.Rev.*, C71:034908, 2005, nucl-ex/0409015.

[23] K. Adcox and others (**PHENIX** Collaboration). Measurement of the mid-rapidity transverse energy distribution from $\sqrt{s_{NN}} = 130$ GeV Au + Au collisions at RHIC. *Phys.Rev.Lett.*, 87:052301, 2001, nucl-ex/0104015.

[24] Constantin Loizides. Charged-particle multiplicity and transverse energy in Pb-Pb collisions at $\sqrt{s_{NN}} = 2.76$ TeV with ALICE. *J.Phys.*, G38: 124040, 2011, 1106.6324.

[25] Serguei Chatrchyan et al. Measurement of the pseudorapidity and centrality dependence of the transverse energy density in PbPb collisions at $\sqrt{s_{NN}} = 2.76$ TeV. *Phys.Rev.Lett.*, 109:152303, 2012, 1205.2488.

[26] M.M. Aggarwal et al. Scaling of particle and transverse energy production in Pb-208 + Pb-208 collisions at 158-A-GeV. *Eur.Phys.J.*, C18: 651–663, 2001, nucl-ex/0008004.

[27] Ranbir Singh, Lokesh Kumar, Pawan Kumar Netrakanti, and Bedangadas Mohanty. Selected Experimental Results from Heavy Ion Collisions at LHC. 2013, 1304.2969.

[28] Raimond Snellings. Elliptic Flow: A Brief Review. *New J.Phys.*, 13: 055008, 2011, 1102.3010.

[29] B. Alver, M. Baker, C. Loizides, and P. Steinberg. The PHOBOS Glauber Monte Carlo. 2008, 0805.4411.

[30] E. Richardson and others (**PHENIX** Collaboration). *Nucl. Instrum. Meth.*, A636:99, 2011, arXiv/1012.0873.

[31] K. Adcox et al. *Nucl. Instrum. Meth.*, A499:489, 2003.

[32] A. Milov. *Ph.D. thesis*, 2003.

[33] M. Aizawa et al. *Nucl. Instrum. Meth.*, A499:508, 2003.

[34] S.S. Adler et al. Identified charged particle spectra and yields in Au+Au collisions at $\sqrt{s_{NN}}$ = 200 GeV. *Phys.Rev.*, C69:034909, 2004, nucl-ex/0307022.

[35] R. Wei et al. *Analysis Note 768*, 2009.

[36] D. Reynolds et al. *Analysis Note 947*, 2010.

[37] S. Mahapatra et al. *Analysis Note 924*, 2010.

[38] X. Gong. *Ph.D. thesis*, 2012.

[39] Georges Aad et al. Measurement of the azimuthal anisotropy for charged particle production in $\sqrt{s_{NN}}$ = 2.76 TeV lead-lead collisions with the ATLAS detector. *Phys.Rev.*, C86:014907, 2012, 1203.3087.

[40] A. Taranenko. *Analysis Note 985*, 2011.

[41] A. Adare et al. Measurements of Higher-Order Flow Harmonics in Au+Au Collisions at $\sqrt{s_{NN}}$ = 200 GeV. *Phys.Rev.Lett.*, 107:252301, 2011, 1105.3928.

[42] Raimond Snellings. Anisotropic flow at the LHC measured with the ALICE detector . *J. Phys.*, G38:124013, 2011, 1106.6284.

[43] Roy A. Lacey, A. Taranenko, R. Wei, N.N. Ajitanand, J.M. Alexander, et al. Azimuthal anisotropy: transition from hydrodynamic flow to jet suppression. *Phys.Rev.*, C82:034910, 2010, 1005.4979.

[44] Jiangyong Jia. Measurement of elliptic and higher order flow from ATLAS experiment at the LHC. *J.Phys.*, G38:124012, 2011, 1107.1468.

[45] Bjorn Schenke, Sangyong Jeon, and Charles Gale. Higher flow harmonics from (3+1)D event-by-event viscous hydrodynamics. *Phys.Rev.*, C85: 024901, 2012, 1109.6289.

[46] David J. Gross and Frank Wilczek. Ultraviolet Behavior of Non-Abelian Gauge Theories. *Phys. Rev. Lett.*, 30:1343–1346, Jun 1973. URL http://link.aps.org/doi/10.1103/PhysRevLett.30.1343.

[47] Politzer, H. David. Reliable Perturbative Results for Strong Interactions? *Phys. Rev. Lett.*, 30:1346–1349, Jun 1973. URL http://link.aps.org/doi/10.1103/PhysRevLett.30.1346.

[48] J. D. Bjorken. Asymptotic Sum Rules at Infinite Momentum. *Phys. Rev.*, 179:1547–1553, Mar 1969. URL http://link.aps.org/doi/10.1103/PhysRev.179.1547.

[49] Stefan Scherer. Introduction to Chiral Perturbation Theory. *Adv.Nucl.Phys.*, 27:277, 2003, hep-ph/0210398. URL http://inspirehep.net/search?p=find+eprint+HEP-PH/0210398.

[50] Frithjof Karsch. Lattice QCD at High Temperature and Density. *Lect.Notes Phys.*, 583:209–249, 2002, hep-lat/0106019. URL http://inspirehep.net/search?p=find+eprint+HEP-LAT/0106019.

[51] Krishna Rajagopal and Frank Wilczek. The Condensed Matter Physics of QCD. 2000, hep-ph/0011333. URL http://arxiv.org/abs/hep-ph/0011333.

[52] Dirk H. Rischke. The Quark gluon plasma in equilibrium. *Prog.Part.Nucl.Phys.*, 52:197–296, 2004, nucl-th/0305030. URL http://inspirehep.net/search?p=find+eprint+NUCL-TH/0305030.

[53] Fodor, Z. and Katz, S.D. Critical Point of QCD atFfinite T and mu, Lattice Results for Physical Quark Masses. *JHEP*, 0404:050, 2004, hep-lat/0402006. URL http://arxiv.org/abs/hep-lat/0402006.

[54] P. Kolb and U. Heinz. In R. C. Hwa and X. N. Wang, editors, *Quark Gluon Plasma 3*, pages 1–59. World Scientific, Singapore, 2004.

[55] T.D. Lee and G.C. Wick. Vacuum Stability and Vacuum Excitation in a Spin-0 Field Theory. *Phys. Rev. D9*, page 2291, 1974.

[56] J. C. Collins and M. J. Perry. Superdense Matter: Neutrons or Asymptotically Free Quarks? *Phys. Rev. Lett.*, 34:1353, 1975.

[57] H. G. Baumgardt et al. Shock Waves and Mach Cones In Fast Nucleus-nucleus Collisions. *Z. Phys. A273*, pages 359–371, 1975.

[58] S. Nagamiya and M. Gyulassy. High-energy Nuclear Collisions. *Adv. Nucl. Phys.*, 13:201–315, 1984.

[59] J. W. Harris and B. Muller. The search for the quark-gluon plasma. *Ann. Rev. Nucl. Part. Sci.*, 46,71, 1996. URL http://arxiv.org/abs/hep-ph/9602235.

[60] U. W. Heinz and M. Jacob. *arXiv:nucl-th/0002042*.

[61] K. Adcox et al. (**PHENIX** Collaboration). *Nucl. Phys.*, A757:184–283, 2005. URL http://arxiv.org/abs/nucl-ex/0410003.

[62] J. Adams et al. (**STAR** Collaboration). *Nucl. Phys.*, A757:102–183, 2005. URL http://arxiv.org/abs/nucl-ex/0501009.

[63] B. B. Back et al. (**PHOBOS** Collaboration). *Nucl. Phys.*, A757:28–101, 2005. URL http://arxiv.org/abs/nucl-ex/0410022.

[64] I. Arsene et al. (**BRAHMS** Collaboration). *Nucl. Phys.*, A757:1–27, 2005. URL http://arxiv.org/abs/nucl-ex/0410020.

[65] M. Gyulassy and L. McLerran. *Nucl. Phys.*, A750:30, 2005. URL http://arxiv.org/abs/nucl-th/0405013.

[66] B. Muller and J. L. Nagle. *Ann. Rev. Nucl. Part. Sci.*, 56,93, 2006. URL http://arxiv.org/abs/nucl-th/0602029.

[67] L. D. McLerran and R. Venugopalan. Gluon Distribution Functions for Very Large Nuclei at Small Transverse Momentum. *Phys. Rev.*, D49: 3352–3355, 1994. URL http://arxiv.org/abs/hep-ph/9311205.

[68] D. Kharzeev, E. Levin and M. Nardi. *Nucl. Phys.*, A730:448, 2004. URL http://arxiv.org/abs/hep-ph/0212316.

[69] R. J. Glauber. *Phys. Rev. 100*, page 242, 1955.

[70] U. Heinz and P. Kolb. Early Thermalization at RHIC. *Nucl. Phys.*, A702:269–280, 2002. URL http://arxiv.org/abs/hep-ph/0111075.

[71] A. Adare et al. (**PHENIX** Collaboration). Detailed Measurement of the $e^+e^-$ Pair Continuum in $p$+$p$ and Au+Au Collisions at $\sqrt{s_{NN}} = 200$GeV and Implications for Direct Photo Production. *Phys. Rev. C81*, 2010. URL http://arxiv.org/abs/0912.0244.

[72] H. Song, S. Bass, U. Heinz, T. Hirano and C. Shen. Hadron Spectra and Elliptic Flow for 200 GeV Au+Au Collision from Viscous Hydrodynamcis Coupled to a Bolzmann Cascade. *Phys. Rev.*, C83:054910, 2011. URL http://arxiv.org/abs/1101.4638.

[73] P. Romatschke and U. Romatschke. Viscosity Information from Relativistic Nuclear Collisions: How Perfect is the Fluid Observed at RHIC. *Phys.Rev.Lett.*, 99:172301, 2007. URL http://arxiv.org/abs/0706.1522.

[74] Derek Teaney. The Effects of Viscosity on Spectra, Elliptic Flow, and HBT Radii. *Phys.Rev.*, C68:034913, 2003, nucl-th/0301099.

[75] S. Adler et al. (**PHENIX** Collaboration). Saturation of azimuthal anisotropy in Au + Au collisions at $\sqrt{s_{NN}} = 62$ GeV to 200 GeV. *Phys.Rev.Lett.*, 94:232302, 2005, nucl-ex/0411040.

[76] K. Adcox et al. (**PHENIX** Collaboration). Suppression of hadrons with large transverse momentum in central Au+Au collisions at $\sqrt{s_{NN}} = 130$ GeV. *Phys.Rev.Lett.*, 88:022301, 2002, nucl-ex/0109003.

[77] Gyulassy, Miklos and Vitev, Ivan and Wang, Xin-Nian and Zhang, Ben-Wei. Jet quenching and radiative energy loss in dense nuclear matter. 2003, nucl-th/0302077.

[78] Gyulassy, Miklos. The QGP discovered at RHIC. nucl-th/0403032.

[79] M. Gyulassy and L. McLerran. New forms of QCD matter discovered at RHIC. *Nucl. Phys.*, A750:30–63, 2005, nucl-th/0405013.

[80] M. Csanad, T. Csorgo, Andras Ster, B. Lorstad, N.N. Ajitanand, et al. Universal scaling of the elliptic flow data at RHIC. *Eur.Phys.J.*, A38:363–368, 2008, nucl-th/0512078.

[81] M. Csanad, T. Csorgo, R.A. Lacey, and B. Lorstad. Universal scaling of the elliptic flow at RHIC. 2006, nucl-th/0605044.

[82] P. K. Kovtun, D. T. Son, and A. O. Starinets. Viscosity in strongly interacting quantum field theories from black hole physics. *Phys. Rev. Lett.*, 94:111601, Mar 2005. URL http://link.aps.org/doi/10.1103/PhysRevLett.94.111601.

[83] Matthew Luzum and Paul Romatschke. Conformal relativistic viscous hydrodynamics: Applications to RHIC results at $\sqrt{s_{NN}} = 200$ GeV.

*Phys. Rev. C*, 78:034915, Sep 2008. URL http://link.aps.org/doi/10.1103/PhysRevC.78.034915.

[84] R. J. Fries, B. Müller, C. Nonaka, and S. A. Bass. Hadron production in heavy ion collisions: Fragmentation and recombination from a dense parton phase. *Phys. Rev. C*, 68:044902, Oct 2003. URL http://link.aps.org/doi/10.1103/PhysRevC.68.044902.

[85] S. Adler, et al. (**PHENIX** Collaboration). Elliptic Flow of Identified Hadrons in Au+Au collisions at $\sqrt{s_{NN}} = 130$GeV. *Phys. Rev. Lett.*, 91:182301, Oct 2003. URL http://link.aps.org/doi/10.1103/PhysRevLett.91.182301.

[86] Denes Molnar and Sergei A. Voloshin. Elliptic flow at large transverse momenta from quark coalescence. *Phys.Rev.Lett.*, 91:092301, 2003, nucl-th/0302014.

[87] Charles B. Chiu, Rudolph C. Hwa, and C. B. Yang. Azimuthal anisotropy: Ridges, recombination, and breaking of quark number scaling. *Phys. Rev. C*, 78:044903, Oct 2008. URL http://link.aps.org/doi/10.1103/PhysRevC.78.044903.

[88] A. Adare, et al. (**PHENIX** Collaboration). Identified charged hadron production in p+p collisions at $\sqrt{s_{NN}} = 200$ and 62.4 GeV. *Phys. Rev. C.*, 83:064903, Jun 2011. URL http://link.aps.org/doi/10.1103/PhysRevC.83.064903.

[89] B. Abelev et al. (**STAR** Collaboration). Identified Baryon and Meson Distributions at Large Transverse Momenta from Au+Au Collisions at $\sqrt{s_{NN}} = 200$ GeV. *Phys. Rev. Lett.*, 97:152301, Oct 2006. URL http://link.aps.org/doi/10.1103/PhysRevLett.97.152301.

[90] Johann Rafelski and Berndt Müller. Strangeness production in the quark-gluon plasma. *Phys. Rev. Lett.*, 48:1066–1069, Apr 1982. URL http://link.aps.org/doi/10.1103/PhysRevLett.48.1066.

[91] P. Koch and B. Muller and J. Rafelski. Strangeness in relativistic heavy ion collisions. *Phys. Rep.*, 142:167–262, 1096. URL http://www.sciencedirect.com/science/journal/03701573/142/4.

[92] Shor, Asher. $\phi-$Meson Production as a Probe of the Quark-Gluon Plasma. *Phys. Rev. Lett.*, 54:1122–1125, Mar 1985. URL http://link.aps.org/doi/10.1103/PhysRevLett.54.1122.

[93] Jean-Yves Ollitrault. Anisotropy as a signature of transverse collective flow. *Phys. Rev. D*, 46:229–245, Jul 1992. URL http://link.aps.org/doi/10.1103/PhysRevD.46.229.

[94] Serguei Chatrchyan et al. Azimuthal anisotropy of charged particles at high transverse momenta in PbPb collisions at $\sqrt{s_{NN}} = 2.76$ TeV. *Phys.Rev.Lett.*, 109:022301, 2012, 1204.1850.

[95] Sergei A. Voloshin, Arthur M. Poskanzer, and Raimond Snellings. Collective phenomena in non-central nuclear collisions. 2008, 0809.2949.

[96] Matthew Luzum. Flow fluctuations and long-range correlations: elliptic flow and beyond. *J.Phys.*, G38:124026, 2011, 1107.0592.

[97] B. Alver et al. System size, energy, pseudorapidity, and centrality dependence of elliptic flow. *Phys.Rev.Lett.*, 98:242302, 2007, nucl-ex/0610037.

[98] B. Alver and G. Roland. Collision geometry fluctuations and triangular flow in heavy-ion collisions. *Phys.Rev.*, C81:054905, 2010, 1003.0194.

[99] Nicolas Borghini and Jean-Yves Ollitrault. Momentum apectra, anisotropic flow, and ideal fluids. *Phys.Lett.*, B642:227–231, 2006, nucl-th/0506045.

[100] A. Adare and others (**PHENIX** Collaboration). Measurement of Higher order Flow Harmonics in $Au + Au$ collisions at $\sqrt{s_{NN}} = 200$ GeV. *Phys.Rev.Lett.*, 107:252301, 2011. URL http://link.aps.org/doi/10.1103/PhysRevLett.107.252301.

[101] Zhi Qiu and Ulrich W. Heinz. Event-by-event shape and flow fluctuations of relativistic heavy-ion collision fireballs. *Phys.Rev.*, C84:024911, 2011, 1104.0650.

[102] Nicolas Borghini, Phuong Mai Dinh, and Jean-Yves Ollitrault. Flow analysis from multiparticle azimuthal correlations. *Phys.Rev.*, C64: 054901, 2001, nucl-th/0105040.

[103] S. Aronson et al. *Nucl. Instrum. Meth.*, A499:480, 2003.

[104] G. Eppley J. Velkovska T. Chujo S. Huang B. Love H. Valle L. Ruan Z. Xu et al. W. Llope, T. Nussbaum. *Nucl. Instrum. Meth.*, A596:430, 2008.

[105] M. Aizawa et al. *Nucl. Instrum. Meth.*, A499:521, 2003.

[106] M. Chiu and others (**PHENIX** Collaboration). *AIP Conf. Proc.*, 915: 539, 2007, nucl-ex/0701031.

[107] M. Allen and others (**PHENIX** Collaboration). *Nucl. Instrum. Meth.*, A499:549, 2003.

[108] E. Garcia M. Murray H. Stroebele S. White C. Adler, A. Denisov. *Nucl. Instrum. Meth.*, A470:488, 2001.

[109] W. Anderson et al. 2011, arXiv/1103.4277.

[110] H. Akikawa and others (**PHENIX** Collaboration). *Nucl. Instrum. Meth.*, A499:537, 2003.

[111] M. Williams. *Nucl. Instrum. Meth.*, A525:168, 2004.

[112] K. Reygers et al. *Analysis Note 169*, 2003.

[113] J. Nagle et al. *Analysis Note 113.*

[114] Arthur M. Poskanzer and S.A. Voloshin. Methods for analyzing anisotropic flow in relativistic nuclear collisions. *Phys.Rev.*, C58:1671–1678, 1998, nucl-ex/9805001.

[115] Poskanzer, A. M. and Voloshin, S. A. Methods for analyzing anisotropic flow in relativistic nuclear collisions. *Phys. Rev. C*, 58:1671–1678, Sep 1998. URL http://link.aps.org/doi/10.1103/PhysRevC.58.1671.

[116] Jean-Yves Ollitrault. On the measurement of azimuthal anisotropies in nucleus-nucleus collisions. 1997, nucl-ex/9711003.

[117] S. Afanasiev and others (**PHENIX** Collaboration). Systematic Studies of Elliptic Flow Measurements in Au+Au Collisions at $\sqrt{s_{NN}}$= 200 GeV. *Phys.Rev.*, C80:024909, 2009, 0905.1070.

[118] Takahito Todoroki et al. *Analysis Note 1015*, 2012.

[119] Soumya Mahapatra. *Ph.D. thesis*, 2013.

[120] N. Borghini, P.M. Dinh, Jean-Yves Ollitrault, Arthur M. Poskanzer, and S.A. Voloshin. Effects of momentum conservation on the analysis of anisotropic flow. *Phys.Rev.*, C66:014901, 2002, nucl-th/0202013.

[121] A. Taranenko et al. *Analysis Note 760*, 2009.

[122] Roy A. Lacey, A. Taranenko, N.N. Ajitanand, and J.M. Alexander. Scaling of the higher-order flow harmonics: implications for initial-eccentricity models and the "viscous horizon". 2011, 1105.3782.

[123] Ulrich Heinz, Chun Shen, and Huichao Song. The viscosity of quark-gluon plasma at RHIC and the LHC. *AIP Conf.Proc.*, 1441:766–770, 2012, 1108.5323.

[124] M. Miller, K. Reygers, S.J. sanders, and P. Steinberg. Glauber Modeling in High-Energy Nuclear Collisions. *Ann. Rev. Nucl. Part. Sci.*, 57:205–243, 2007.

[125] T. Hirano, U. Heinz, D. Kharzeev, R. Lacey, and Y Nara. Hadronic dissipative effects on elliptic flow in ultrarelativistic heavy-ion collisions. *Phys. Lett. B*, 636:299–304, 2006.

[126] H. Drescher and Y Nara. Eccentricity fluctuations from the color glass condensate in ultrarelativistic heavy ion collisions. *Phys. Lett. C*, 76: 041903, 2007.

[127] A. Adare et al. Elliptic and hexadecapole flow of charged hadrons in Au+Au collisions at $\sqrt{s_{NN}} = 200$ GeV. *Phys.Rev.Lett.*, 105:062301, 2010, 1003.5586.

[128] H.-J. Drescher, A. Dumitru, C. Gombeaud, and Ollitrault J.-Y. *Phys. Lett. C*, 76:024905, 2007.

[129] Gombeaud C. and Ollitrault J.-Y. *Phys. Lett. C*, 77:054904, 20078.

[130] Huichao Song and Ulrich W. Heinz. Multiplicity scaling in ideal and viscous hydrodynamics. *Phys.Rev.*, C78:024902, 2008, 0805.1756.

[131] Roy A. Lacey, Arkadij Taranenko, and Rui Wei. Is the quark gluon plasma produced in RHIC collisions strongly coupled? 2009, 0905.4368.

[132] Kevin Dusling, Guy D. Moore, and Derek Teaney. Radiative energy loss and v(2) spectra for viscous hydrodynamics. *Phys.Rev.*, C81:034907, 2010, 0909.0754.

[133] Charles Gale, Sangyong Jeon, Bjoern Schenke, Prithwish Tribedy, and Raju Venugopalan. Initial state fluctuations and higher harmonic flow in heavy-ion collisions. *Nucl.Phys.A904-905*, 2013:409c–412c, 2013, 1210.5144.

[134] Roy A. Lacey, A. Taranenko, J. Jia, D. Reynolds, N.N. Ajitanand, et al. Beam energy dependence of the viscous damping of anisotropic flow. 2013, 1305.3341.

[135] Roy A. Lacey, D. Reynolds, A. Taranenko, N.N. Ajitanand, J.M. Alexander, et al. Acoustic scaling of anisotropic flow in shape-engineered events: implications for extraction of the specific shear viscosity of the quark gluon plasma. 2013, 1311.1728.